

THERMAL RADIATION CHARACTERISTICS
OF FLUIDIZED SOLIDS

by

David Anthony Lewin, B.Eng.

*A thesis submitted in fulfilment of the requirement
for the degree of Doctor of Philosophy*

THESIS
536.33 LEW
108996 26 NOV 1975

The University of Aston in Birmingham
Faculty of Engineering
Department of Mechanical Engineering

1 9 7 5

S U M M A R Y

Radiative heat transfer from an emulsion of high temperature fluidized solids is visualised, utilizing a continuum approach, as that from a volume emitter of voidage greater than zero. The initial considerations were of a simplified mathematical model which for an homogeneous constant property, emitting, absorbing and scattering medium may be described by the exact formulation for one dimensional, steady-state radiative transfer. From the analysis the dependancy of the emitted radiative flux levels upon the emissivity of the bed material emerged. Such observations were verified experimentally.

Following a study of the hydrodynamic behaviour of the bed surface, a model describing transient radiative transfer was evolved based upon the packet model with initial isothermal conditions. The small residence times of the surface eruptions, found experimentally, constrained the flux levels to be almost invariant with time.

The analysis was theoretically and experimentally extended to include the conductive heat transfer mode in consideration of surfaces immersed into a fluidized bed. Again, using the packet model the dominant conductive mode was apparent for early particle residence times. Radiation plays an increasingly significant role as the time history of the particle contact period proceeds. Contrary to previous suggestions, radiation contributes significantly to the overall energy transfer for the normal operating temperature range of fluidized bed heat exchangers, unless

sufficiently low particle or transfer surface emissivities are encountered.

Throughout the work a number of problems have been highlighted where further effort is required.

ACKNOWLEDGEMENTS

The author would like to thank and acknowledge:

Professor D E Elliott who suggested the topic of study and supervised the work;

Mr D C Hickson for his assistance with the computer programming and help in the preparation of the thesis;

Dr J Broughton and former colleagues at the University of Aston for their helpful discussions as the work progressed;

The British Gas Corporation for their financial support during the course of this study through the provision of a British Gas Corporation Scholarship;

The technical staff of the Department of Mechanical Engineering for their assistance with the experimental work;

Mrs J V Lloyd for the typing of the thesis;

Last, but not least, the assistance of his wife in the typing of the first draft and for her continuous encouragement throughout.

C O N T E N T S

<u>CHAPTER</u>		<u>PAGE</u>
1	AN INTRODUCTION TO THERMAL RADIATION WITHIN BEDS OF HIGH TEMPERATURE FLUIDIZED SOLIDS	
1.1	Introduction	1
1.2	Review of Previous Studies	2
1.2.1	The fluidized bed effective emissivity	3
1.3	The Equation of Radiative Transfer	6
1.4	Application of the Equation of Radiative Transfer to a Bed of Fluidized Solids - Description of Important Parameters	7
1.4.1	Description of important parameters encountered in the radiative transport equation	7
(i)	Scattering cross-section	8
(ii)	Extinction coefficient	9
(iii)	Phase function	10
(iv)	Scattering albedo	10
(v)	Optical thickness	11
1.4.2	Considerations of a simplification of the equation of radiative transfer	12
(i)	The alternate slab model	12
(ii)	The optically thick approximation	14
(iii)	The zone method	15
1.5	Concluding Remarks	15
2	ANALYSIS OF THE RADIATIVE TRANSFER EQUATION	
2.1	Introduction	17
2.2	Development of the Mathematical Model	17
2.3	Previous Solutions of the Radiative Transfer Equation	18

<u>CHAPTER</u>		<u>PAGE</u>
2.4	Analysis	20
	2.4.1 Boundary conditions	20
2.5	Discussion of Analytical Results	22
2.6	Conclusions	26
2.7	Suggestions of Areas for Further Study	26
3	DETERMINATION OF FLUIDIZATION AND RADIATIVE HEAT TRANSFER PARAMETERS	
3.1	Introduction	28
3.2	Minimum Fluidizing Velocity at High Bed Temperatures	28
	3.2.1 Experimental determination of U_{mf} at high bed Temperatures	29
	3.2.2 Discussion of results	31
	3.2.3 Conclusions	33
3.3	Determination of Particle Emissivity	33
	3.3.1 Manufacture of test samples	34
	3.3.2 Experimental procedure	35
	3.3.3 Discussion of results	39
	3.3.4 Conclusions	43
3.4	Determination of the Extinction Coefficient	44
	3.4.1 Experimental determination of bed pressure profiles	44
	3.4.2 Discussion of results	46
	3.4.3 Conclusions	49
3.5	Determination of the Time Average Temperature Gradient at the Surface of a Fluidized Bed	49
	3.5.1 Experimental determination of the surface temperature gradients	52
	3.5.2 Analysis of the shielded thermocouple probe	53
	3.5.3 Discussion of results	54

<u>CHAPTER</u>		<u>PAGE</u>
	3.6 Conclusions	57
4	EXPERIMENTAL DETERMINATION OF THE STEADY STATE RADIATIVE FLUXES EMITTED BY THE SURFACE OF A FLUIDIZED BED	
	4.1 Introduction	58
	4.2 The Experimental Program	58
	4.2.1 Instrumentation	58
	4.2.2 Experimental Procedure	61
	4.3 Discussion of Results	62
	4.3.1 Experimental observations	64
	4.3.2 Directional and hemispherical effective emissivities	72
	4.4 Further Studies of a Bed Composed of a Binary Mixture	74
	4.4.1 Experimental observations	74
	4.5 Application of the Analysis to Irradiation of a Remote Surface by a Fluidized Emulsion	77
	4.6 Conclusions and Suggestions for Further Study	77
5	A STUDY OF THE BEHAVIOUR OF A FREELY BUBBLING FLUIDIZED BED SURFACE	
	5.1 Introduction	80
	5.2 Particles Ejected by Single Isolated Bursting Bubbles	82
	5.2.1 A theoretical model	82
	5.2.2 Experimental study	85
	5.3 Discussion of Results	87
	5.3.1 Extension to a three-dimensional bed	89
	5.4 Conclusions	90
	5.5 Determination of Bubble Velocity in a Three Dimensional Bed	91
	5.5.1 Introduction	91

<u>CHAPTER</u>		<u>PAGE</u>
	5.5.2 Experimental procedure for the determination of bubble eruption diameters	91
	5.5.3 Film analysis and discussion of results	92
	5.6 Determination of the Surface Bubble Residence Time in Three Dimensional Beds	96
	5.7 Conclusions	97
6	TRANSIENT THERMAL RADIATION FROM HIGH TEMPERATURE FLUIDIZED SOLIDS	
	6.1 Introduction	99
	6.2 Analysis	100
	6.2.1 Numerical method of solution	102
	6.3 Discussion of Results	103
	6.4 Comparison with Experimental Observations	106
	6.5 Conclusions and Suggestions for Further Study	110
7	UNSTEADY COMBINED RADIATION AND CONDUCTION HEAT TRANSFER TO SURFACES IMMERSSED IN A FLUIDIZED BED	
	7.1 Introduction	113
	7.2 A Generalized Approach to Unsteady Combined Radiation and Conduction Heat Transfer	116
	7.2.1 Introduction	116
	7.2.2 Analysis	117
	7.2.3 Initial and boundary conditions	121
	7.2.4 A qualification for the use of a mean property gas boundary layer	123
	7.3 Discussion of Predicted Results	124
	7.3.1 Comparison of predicted with reported heat transfer data to an immersed probe	127
	7.3.2 Comparison of the instantaneous Nusselt- Fourier relationship for a coupled and uncoupled solution of conduction and radiation heat transfer to a plane surface	130

<u>CHAPTER</u>		<u>PAGE</u>
7.4	Experimental Determination of Heat Transfer to the Wall of a Quartz Glass Reactor	133
7.4.1	Experimental procedure	134
7.4.2	Discussion of results	135
7.5	Conclusions and Suggestions for Further Study	138

List of Tables

Table 1.1	8
Table 3.1	31
Table 3.2	41
Table 3.3	42
Table 3.4	43
Table 4.1	67
Table 4.2	69
Table 4.3	71
Table 6.1	108

REFERENCES	141
------------	-------	-----

DIAGRAMS

Appendices

A	The Effective Emissivity of a Fluidized Bed	151
B	The Equation of Radiative Transfer	152
C	The Two Flux Approximation of the Equation of Radiative Transfer	157
D	A Solution of the Radiative Flux Equation for Steady State Heat Transfer	160
E	(a) Determination of Exinction Coefficient from Bed Pressure Drop Distribution	164

	<u>PAGE</u>
E (b) Determination of Extinction Coefficient at a Plane Surface	165
F Operation of a Radiation Pyrometer (Radiometer) System	167
G A Solution of the Radiation Flux Equation for Unsteady Heat Transfer	171
H Computer Program for Steady and Unsteady Radiative Heat Transfer	173
I Unsteady Combined Conduction and Radiation Heat Transfer	175
J Computer Program for Unsteady Combined Conduction and Radiation Heat Transfer	179

NOMENCLATURE

A	Surface area
Bi	Biot number
C	Velocity of light
C_p	Specific heat capacity
C_D	Drag coefficient
$D(\tau)$	Non-dimensional function defined by equation (B.11)
D	Diameter
d	Object distance measured from radiation pyrometer
$E_n(x)$	Exponential integral defined by equation (2.1)
erf(x)	Error function
$F_{1,2}$	Non-dimensional boundary flux
F_{k-j}	View factor between surfaces k and j
f_o	Bubble voidage
G	Irradiation
g	Acceleration due to gravity
h	Height of rise of ejected particle cloud, heat transfer coefficient
H	Bed height
H_ω	'H'-function defined in [12]
I	Intensity of radiation
K	Coefficient, thermal conductivity
L	Thickness measured from bed surface, interparticle distance
m'	Defined by equation (1.3)
$N(x)$	Particle concentration distribution

n	Number of particles
N_λ	Steradiancy
Nu	Nusselt number
N_1	Conduction - Radiation number
$P(\theta)$	Phase function
P	Pressure
ppm	Parts per million
Q	Heat flow rate
q	Heat flux
Re	Reynolds number
T	Temperature, thermocouple
t	Absolute time
t'	Non-dimensional time
U	Velocity
V	Volume, velocity
W	Weight
\bar{x}	Particle diameters
x	Any position within the bed measured from the bed surface

Greek Symbols

α	Absorptivity
β	Angle
$\Delta t'$	Non-dimensional temperature increment
ΔP	Pressure difference
$\Delta \tau$	Optical depth increment
δ	Kronecker delta

ϵ	Emissivity, voidage
θ	Angle, non-dimensional temperature
λ	Wavelength
μ	Cos θ , viscosity
ρ	Density, reflectivity
σ	Stefan Boltzmann constant
τ	Optical depth, transmissivity
τ_0	Optical thickness
ϕ	Azimuthal Angle
ϕ_s	Sphericity
ψ	Angle
ψ_1	Defined by equation (1.2)
ω	Solid angle
ω_0	Scattering albedo
Ω	Solid angle
ν	Refractive index

Subscripts

1	Boundary 1
2	Boundary 2
a	Absorption
b	Bed, black body
c	Conduction
d	Directional, detector
e	Effective, emulsion
f	Fluid, fluidized
g	Gas

h	Hemispherical
i	Isothermal, instantaneous
m	Minimum, mean
n	Non-isothermal
p	Particle
r	Radiation
s	Sample, scattering
T	Thermocouple
t	Target, total
W	Wall
x	Region
y	Region

Superscripts

(')	Refers to a non-dimensional quantity or dummy variable of integration
u	Upper triangular matrix
L	Lower triangular matrix

CHAPTER 1

AN INTRODUCTION TO THERMAL RADIATION WITHIN BEDS OF
HIGH TEMPERATURE FLUIDIZED SOLIDS

1.1 Introduction

The analysis of radiative energy transport within and through beds of fluidized solids, or gas-solid emulsions, has received only limited attention during recent years. In the literature appears a wealth of information concerning the two modes of heat transfer in fluidized beds, namely conduction and convection, but for a number of reasons the radiative mode has escaped an equal degree of attention. With the advent of fluidized bed heat exchangers, particularly where combustion of a gas/air mixture takes place within the bed of fluidized solids, the temperatures encountered are of a sufficient level to warrant the inclusion of the thermal radiative component in the governing energy equation. The combustion of a gas/air mixture within a bed of fluidized solids takes place at temperatures much lower than the theoretical flame temperature of such a mixture. For this to occur the heat losses, which are predominantly radiative, from the upper, highly turbulent free surface of the bed must be large. In fact, of order 50% of the total heat capacity for a bed temperature of 1 000°C with a theoretical flame temperature of 2 000°C.

Heat transfer in any porous media (emulsion) is by gas and solid conduction as well as radiation. The mechanism of conduction through the gas and solid are similar, in a sense that the heat flux is proportional to thermal conductivity and local temperature gradient. Radiation on the other hand is a long range process

and must be treated accordingly. Local inhomogeneities in the emulsion affect the transmission of radiant energy. For example, radiation traversing the emulsion may (a) pass through voids in the porous bed, (b) be transmitted through the particles, (c) be absorbed by the particles and subsequently re-emitted (Kirchoff's Law) and (d) be scattered (re-orientated) by the particles. The emulsion can be considered to be homogeneous and continuous. This is justified if the gas voids and particles are essentially in equilibrium, and if the particle spacing is sufficiently small so that the temperature difference between adjacent particles is small compared to the absolute temperature.

Although the particular interest in this study is concerned with shallow fluidized bed heat transfer, the initial model of radiative transfer applies equally to beds of any depth. Unfortunately, no strict definition of a shallow fluidized bed exists and so, where necessary, a shallow bed is assumed to be one in which bubble coalescence does not have sufficient time to occur.

1.2 Review of Previous Studies

The limited amount of thermal radiative studies in fluidized beds that have been conducted have shown varying degrees of contradiction in a number of important fundamental areas. The levels of bed temperature below which the contribution of thermal radiation to the total energy exchange may be ignored is a first example. Yoshida and Kunii^[1] studied radiant heat transfer from a bed of fluidized solids to two kinds of heat exchange pipe,

one of a high emissivity 0.8 and one of a low emissivity 0.17, the bed walls having an emissivity of 0.8. The bed material was a microspherical catalyst of size distribution 0.149-0.210 mm and density 1 540 kg/m³. The authors concluded from this experimental study that the contribution due to radiation heat transfer was not significant (approximately 5%) below bed temperatures of 1 000°C - 1 200°C. A fundamental assumption based on the work of Zabrodsky^[2] and used in [1], was that the degree of blackness (effective emissivity) of the emulsion is equal to unity. In contrast to the work of [1], Vedamurthy and Sastri^[3] in a mathematical study of radiation and conduction heat transfer to the walls of a fluidized bed combustion concluded, for the case of coal burning within the combustor, that radiation contributed significantly (approximately 30%) to the overall heat transfer down to bed temperatures of 800°C. In this case the assumption was again that the emulsion effective emissivity was equal to unity although no mathematical justification was given. A number of further studies have been attempted but are concerned primarily with radiative heat transfer to immersed surfaces within a fluidized bed. These references are cited in studies reported later in this work.

1.2.1 The fluidized bed effective emissivity

In the previous section the term bed effective emissivity was introduced and requires a formal explanation. The term was introduced by Zabrodsky^[2] who recognised the fact that a particulate bed may have an effective emissivity of a somewhat different

value from the emissivity of the actual particle material. The term 'effective' is used to distinguish between the strict definition of emissivity of any isothermal surface emitter of voidage zero and a volume emitter (emulsion of fluidized solids) of voidage not equal to zero, with either isothermal or non-isothermal particulate boundaries. In the analysis, Zabrodsky^[2] approximated the emulsion of fluidized solids by a dusty gas cloud. Using the equation of energy attenuation (Beer's Law)

$$\frac{dI}{dx} = -K_a I \quad (1.1)$$

an expression for the effective emissivity was derived for the system. A complete description of this analysis appears in Appendix A. It was subsequently shown in [2] for a typical fluidized bed system that the effective emissivity ϵ_e was approximately unity in all cases. This is not a surprising conclusion as in addition to the high values of particle concentration a fundamental assumption of Beer's Law is that all particles are thermally black.

In contrast, the work of Rubstov and Syremyatnikov^[4] considered the problem of effective emissivity from an idealized model of the geometry of particles in contact with a plane vertical surface. A term

$$\psi_1 = \left[\frac{1}{m'} \right]^2 \quad (1.2)$$

$$\text{where } m' = (1 - \epsilon_b)^{-1/3} \quad (1.3)$$

and ϵ_b is the bed voidage was evolved as being the fraction of the surface overshadowed by the first row of particles. For n rows of particles the effective emissivity was derived as

$$\epsilon_e = \sum_1^n \epsilon_p \psi_K \quad \text{for } K = 1, \dots, n \quad (1.4)$$

and ϵ_p = particle material emissivity. It was concluded that ϵ_e may differ significantly from unity depending largely upon the value of ϵ_p .

In a discussion of [4] by Zabrodsky^[5] it was shown that the term $\psi = (1/m')^2$ was not strictly justified and, for spherical particles, must depend upon their packing arrangement, e.g. for loose cubic packing of spheres, the interparticle distance

$$L = 0.806 D_p (1 - \epsilon_b)^{-\frac{1}{3}} \quad (1.5)$$

and

$$\psi_1 = \frac{\pi D_p^2}{4L^2} = 1.2 \left[\frac{1}{m'} \right]^2 \quad (1.6)$$

Later experimental work by Pikashov *et al*^[6] in which a narrow angle radiometer probe was placed in a fluidized bed with the thin quartz protecting glass situated in the horizontal plane, supports the results of [4] and concludes that the effective emissivity must deviate from unity. However, in a similar experimental analysis by Ilchenko *et al*^[7], considerable cooling of the first row of particles in contact with the quartz protecting glass were observed. This would account for a reduction in the measured levels of effective emissivity.

Hence the 'state of the art' to date is confused being dependent on highly idealized systems and for this reason it is desirable to reconsider the problem of radiation heat transfer within an emulsion of fluidized solids using a physically and mathematically justifiable approach.

1.3 The Equation of Radiative Transfer

Considering Zabrodsky's^[2] earlier hypothesis of a dust cloud it is obvious from equation (1.1) that the energy attenuation on traversing the emulsion is due to the absorption properties of the emulsion alone. Consideration of a more complete equation, i.e. the equation of radiative transfer, introduces other factors into the analysis.

The equation of radiative transfer in non-dimensional form may be written as

$$\mu \frac{dI}{d\tau} = -I(\tau) + \frac{\omega_0}{4\pi} \int_{4\pi} I(\tau, \theta') P(\theta, \theta') d\Omega + (1 - \omega_0) I_b(\tau) \quad (1.7)$$

A more complete description of the derivation of equation (1.7) and its adaption for use with the governing energy equation appears in Appendix B. Briefly the equation describes energy (radiation intensity I) attenuation and augmentation when traversing a differential element of emulsion. The first term on the right-hand side of equation (1.7) describes energy attenuation due to absorption and scattering of the incident beam. The second term describes energy augmentation due to scattering (reorientation) of energy in the direction of the incident beam. The third term

accounts for the emission of the particles within the emulsion. Before proceeding to an analysis of equation (1.7), an explanation of the parameters appearing in the equation are now given in relation to a bed of fluidized solids.

1.4 Application of the Equation of Radiative Transfer to a Bed of Fluidized Solids - Description of Important Parameters

In a general sense any medium which absorbs, emits and scatters radiation, whether a particle seeded flame, thermal insulation material or a bed of fluidized solids may be equally described by the equation of radiative transfer. It is convenient here to consider the packet model of heat transfer described by Figure 1.1 in the case of an emulsion of fluidized solids through which radiative energy is transported. The packet model was first suggested and developed by Mickley and Fairbanks^[8] and used to describe conduction heat transfer between an emulsion and an immersed surface. A similar packet model is considered in this study where all particles are regarded as having zero relative motion, and heat is transferred only by the viewing (in a radiative sense) of a surface by a packet of emulsion which is constantly replenished with fresh particles. Obviously, conduction and convection heat transfer should be included into the analysis; however, the initial consideration is of radiation predominating.

1.4.1 Description of the important parameters encountered in the

radiative transport equation

(i) Scattering cross-section

The extent of scattering of an object (particle) is normally, particularly in the nuclear energy transport field, expressed in terms of a scattering cross-section. This is the apparent area that an object presents to an incident radiative beam in relation to the ability of the object to deflect (reorientate) radiative energy. This apparent area may be quite different from the physical cross-sectional area of the object as shown in Table 1.1 taken from Siegel and Howell^[9], depending upon the ratio of the particle size to the radiative wavelength of the incident beam, $\pi D_p / \lambda$. The ratio of the scattering cross-section to the actual geometric projected area of the particle is known as the efficiency factor.

TABLE 1.1 (Reproduced from [9])

BODY	PHYSICAL CROSS-SECTION mm ²	CONDITIONS	TYPE OF SCATTERING	SCATTERING CROSS-SECTION
Particles of Diameter D_p	$\frac{\pi D_p^2}{4}$	$\lambda \gg D_p$ single scattering	Rayleigh	Proportional to V^2 / λ^4
		$\lambda \approx D_p$	Mie	Varies widely
		$\lambda \ll D_p$	Fraunhofer and Fresnel diffraction plus reflection	$\sim 2 \left[\frac{\pi}{4} D_p^2 \right]$

(ii) Extinction coefficient

With reference to Section 1.3, attenuation of radiative energy is due to both scattering and absorption of an incident beam. In the radiative transfer equation (1.7) it is convenient to combine these two effects in terms of a single parameter, the extinction coefficient. With reference to Table 1.1 for a bed of fluidized particles, the ratio $\pi D_p \gg \lambda$ always applies and hence the absorption coefficient (K_a) is simply defined in this study as

$$K_a = \frac{N\pi D_p^2 \epsilon_p}{4} \quad (1.8)$$

from Hottel and Sarofim^[10] where ϵ_p is the particle material emissivity and N is the particle concentration. The particle concentration may be represented by a function of distance for a known distribution, but this refinement produces unnecessary complications at this stage of the work and so N is taken as a constant value throughout the emulsion field. The scattering coefficient K_s is similarly derived as the absorption coefficient and defined as

$$K_s = 2 \left[\frac{N\pi D_p^2 \rho_r}{4} \right] \quad (1.9)$$

where ρ_r is the reflectivity of the particle material from [10]. The multiplying factor of 2 in equation (1.9) accounts for the diffraction of energy around large particles where $\pi D_p \gg \lambda$ from [9]. The extinction coefficient is then simply $K_t = K_a + K_s$.

(iii) Phase function

A complete description of the phase function appears in [9]. Briefly, $P(\theta)$ is the intensity distribution, as a function of circumferential angle θ , of scattered energy. A number of different functions of $P(\theta)$ are described in [9] for various shapes and sizes of particles. In the case of fluidized particles with $\frac{\pi D}{P} \gg \lambda$ the phase function of energy scattered over 4π steradians is, for diffusely reflecting particles

$$P(\theta) = \frac{8}{3\pi} (\sin\theta - \theta\cos\theta) \quad (1.10)$$

The inclusion of such a phase function to account for anisotropic energy scattering, produces unnecessary complications in a solution of the radiative transfer equation. For this reason, all energy scattering is assumed to be isotropic and then $P(\theta) = 1$. A further justification of this fundamental assumption is shown in the work of Love *et al* [11], for a generalised absorbing and scattering medium, who concluded that anisotropic scattering accounts for 150% change in the overall emitted flux levels at $\tau_0 = 0.1$, to 30% at $\tau_0 = 2.0$.

However, the assumption of isotropic scattering is often valid in an optically thick medium, the difference in flux levels reducing as $\tau_0 \rightarrow \infty$.

(iv) Scattering albedo

The scattering albedo describes the amount of energy scattered to the total energy attenuated, i.e. $\omega_0 = K_s/K_t$.

Some workers, Chandrasekhar^[12] and Kourganoff^[13] use the value of

$$\frac{K_a}{K_t} = (1 - \omega_0) ,$$

the degree of darkening, in an astrophysical context.

(v) Optical thickness, τ_0

An important dimensionless parameter in any radiation absorbing, emitting and scattering medium is the optical thickness of the medium. In this present study a fundamental assumption is that all radiation is gray and independent of wavelength distribution. Another assumption is that all radiative properties of the fluidized emulsion are independent of temperature variation. It therefore follows that the extinction coefficient K_t is also independent of wavelength and temperature distribution. Hence the characteristic physical dimension (L) of the emulsion may be transformed into an optical dimension (photon penetration depth) as $\tau_0 = K_t L$. Physically, depending upon the constituents of the emulsion, the optical thickness may vary between zero, for a vacuum, and infinity for a solid object. In the case of a fluidized bed the passage, through an element of emulsion, of a beam of radiative energy is affected by other elements in close proximity. Hence the regime of application of optical thickness is for $\tau_0 \gg 1$, i.e. the emulsion is regarded as being optically thick. When considering the depth (x) of an emulsion of thickness (L), the term optical depth $\tau = K_t x$ is used.

1.4.2. Considerations of a simplification of the equation of radiative transfer

(i) The alternate slab model

In the analysis of [3], the equation of radiative transfer was not considered, the radiative flux appearing in the energy equation in a simplified form of $q'_T = \sigma T^4(x)$ with the assumption $\epsilon_p = 1$ or, in nondimensional form,

$$q'_T = \theta^4(x) \quad (1.11)$$

From Appendix B the radiative flux equation is given for a black body ($\omega_0 = 0$) emulsion, as

$$\begin{aligned} q'_T(\tau) = & 2F_1E_3(\tau) - 2F_2E_3(\tau_0 - \tau) + 2 \int_0^\tau \theta^4(\tau')E_2(\tau - \tau')d\tau' \\ & - 2 \int_\tau^{\tau_0} \theta^4(\tau')E_2(\tau' - \tau)d\tau' \end{aligned} \quad (1.12)$$

Equation (1.11) may be obtained from equation (1.12) by assuming the emulsion to be made up of finite slabs of solid material separated by interstices of negligible optical thickness, i.e.

$\tau = \tau_0 \rightarrow 0$. Hence equation (1.12) becomes

$$q'_T = 2F_1E_3(0) - 2F_2E_3(0)$$

and

$$q'_T = F_1 - F_2 \quad (1.13)$$

which is simply the radiative flux transfer between two black

parallel plates.

Again in [3] for use in a finite difference solution of the energy equation then (1.13) is recast in the form

$$q'_{r_i} = F_i - F_{i-1} \text{ for } i = 1, \dots, n \quad (1.14)$$

for the i^{th} and $(i-1)^{\text{th}}$ layers of the emulsion, or

$$q'_{r_i} = \theta_i^+ - \theta_{i-1}^+ \quad (1.15)$$

However, when considering the physics of the emulsion, equation (1.15) neglects the contribution to the flux at the i^{th} and $(i-1)^{\text{th}}$ layer of fluxes emitted by remote layers and passing through the intermediate interstices even though thermal radiative transfer is a long range (global) process. As (1.15) was obtained from assuming a negligible optical thickness between the layers it would seem reasonable to assume that the contribution of flux from adjacent and near adjacent layers is contributory. The simplification to obtain equation (1.15) is not consistent with the application of such an equation in a fluidized bed of $\epsilon_b > 0$. The emissivity of such a model is equal to that of the material considered and from a consideration of Figure 2.1 such a result would underestimate the subsequent radiative fluxes for all cases except $\epsilon_p = 1$.

In the work of Hill and Wilhelm^[49] a similar slab model was considered in a study of combined radiative and conductive heat transfer in a quiescent gas-solid bed. However, for a

generalized bed material of particle emissivity, ϵ_p , the bed was considered to be made up of either infinite parallel planes, concentric cylinders of infinite length, or concentric spheres, each surface considered gray and partially transparent. The allowance for the transparent nature of the surfaces (slabs), thought of as the effective fraction of free area, is an improvement over the model used by [3] accounting for the long range transfer of radiative energy. In addition, the effects of the reflectivity and absorptivity of the surfaces were included. The resulting equations were derived by applying an energy balance between successive surfaces and summing across the field. The radiative flux equations were similar, from a heat transfer point of view to those of Hamaker^[20] who considered a differential, rather than a finite slab approach to the problem. By way of interest the radiative flux equation obtained by [49] of

$$q'_r = \frac{\sigma(T_0^4 - T_{N+1}^4)}{\frac{1}{\alpha_0 A_0} + \frac{1 + \rho_r - \tau_t}{1 - \rho_r + \tau_t} \sum_{i=1}^N \frac{1}{A_i} + \frac{\rho_r}{\alpha_{N+1} A_{N+1}}} \quad (1.16)$$

simplifies to that of radiative transfer between two infinite parallel plates of temperatures T_0 and T_1 respectively i.e. the second term in the denominator disappears. The work of [49] and [20] are in fact different approaches to the derivation and solution of the radiative transfer equation.

(ii) Optically thick approximation

A more realistic approximation of radiative transfer within

fluidized beds is the optically thick approximation. From Sparrow and Cess^[26] it was shown that the radiative flux equation of Appendix B may be simplified in the case of $\tau_0 \gg 1$ of

$$q_r' = -\frac{4}{3} \frac{d\theta^4}{d\tau} \quad (1.17)$$

in nondimensional form and implies that radiative fluxes at a plane are affected by its near neighbours only, being a function of the local temperature gradient. Unfortunately, this assumption breaks down in the vicinity of a boundary for reasons given in [26] and explained in Chapter 2 of this work.

(iii) The Zone Method

Developed by Hottel and Sarofim^[10], this method consists of subdividing nonisothermal enclosures filled with a non-isothermal gas into areas and volumes that can be considered isothermal. An energy balance is then applied to each division leading to the solution of a set of simultaneous equations. The method is not mathematically elegant but forms a powerful practical tool having considerable advantage in multidimensional situations.

1.5 Concluding Remarks

From a consideration of the radiative transfer equation and its various components a number of approximate approaches to a solution have been considered. However, as the initial study forms a fundamental analysis of radiative transfer within and through emulsions of fluidized solids, an application of the exact

radiative transfer equation is desired. Where appropriate, comparisons are made with the approximate solutions. From the subsequent application of the radiative transfer equation it is convenient to model the fluidized bed as that of a packet of gas-solid emulsion with appropriate mean physical properties.

CHAPTER 2

ANALYSIS OF THE RADIATIVE TRANSFER EQUATION

2.1 Introduction

Applications of radiant transport theory has received considerable attention over recent years, and appears in the literature of astrophysics [12] and [13], optics, Gumprecht *et al.*^[14], chemistry, Chu and Churchill^[15] and nuclear energy, Davison^[16]. One of the most thorough and clear presentations is given by Viskanta^[17] who emphasized the heat transfer point of view. The work in [17] is particularly relevant to the present study of fluidized solid radiative transfer and for this reason [17] and subsequent studies by the same author are constantly cited throughout this text.

2.2 Development of the Mathematical Model

As a first step a simplified physical model of a fluidized emulsion is assumed along the lines of the packet model of [8]. A plane, gray layer of the emulsion packet is bounded by plane, parallel, gray, diffusely emitting - reflecting boundaries, according to the configuration of Figure B1 in Appendix B. In addition, a number of further simplifying assumptions are made and summarised as follows:

1. One-dimensional radiative heat transfer
2. Constant fluid and solid properties
3. Fluid and solid in local thermal equilibrium
4. Steady-state
5. Fluid and solid in dynamic equilibrium

6. Constant absorption and scattering coefficients
7. Isotropic scattering
8. Emulsion, homogenous and isotropic and of constant voidage

With consideration of later experimental studies, the emulsion is further visualized as a homogeneous slab exchanging energy, by radiation only, with a remote heat transfer surface (detector).

2.3 Previous Solutions of the Radiative Transfer Equation

The equation of radiative transfer has been applied to a similar model as previously described and solved using a number of different techniques. Edwards and Bobco^[18] in a generalized study of dispersion emission used a modified diffusion method of solution. This technique was based upon the method of moments used in an application of the equation of radiative transfer to nuclear transport problems. The particular application of [18] is in the field of radiation exchange from a seeded rocket engine exhaust plume to some remote heat transfer surface (e.g. engine base). An interesting and relevant feature of this analysis is the use of free boundary conditions which occur equally in the case of rocket engine exhaust plumes and beds of fluidized solids. The free boundary is applicable whenever an inward directed radiative flux on the emulsion boundary has a negligible influence on the temperature and radiative flux distribution within the emulsion. Further conclusions from [18] of a fundamental nature were the concept of radiative intensity, when non-dimensionalised

to the emulsion black body intensity, being equivalent to directional emissivity and that isotropic scattering does not lead to the classical Lambert diffuse emission at an emulsion boundary. Even in an emulsion of $\tau_0 \rightarrow \infty$ the latter case is not met. This conclusion emphasizes the care which must be taken in interpreting experimental results when using a narrow angle (field of view) radiometer to view such an emulsion. Finally, the relation between an area formulation and a volume formulation of the problem was indicated to show that any scattering system may be solved as a field problem and the results used with an area configuration factor to obtain the irradiation at some remote surface. Alternatively, the irradiation may be obtained directly by application of the volume formulation as shown in [17] without introduction of a configuration factor concept.

In a study of radiation through a foggy (scattering) atmosphere, Schuster^[19] introduced the now well-known two flux method of approximate solution of the radiative transfer equation. This method was extended for use in heat transfer systems by Hamaker^[20] and consists of reducing the non-linear, integrodifferential equation to two simultaneous, linear differential equations, which in a simple plane parallel system are amenable to a closed form solution.

In a similar study area as [18], Morizumi and Carpenter^[21] used a statistical probability approach to solve the radiative transfer equation. However, only the first term on the right-hand side of the equation was considered and similar to the equation used in [2]. The multiple scattering of radiative

energy was allowed for by the probability functions derived for an incident beam traversing a differential slab of emulsion. Comparisons of the analytical predictions with subsequent experimental results, using a narrow angle radiometer and a spectrometer, resulted in an average difference of 17% between the two.

2.4 Analysis

The equation of radiative transfer in conjunction with the energy equation in Appendix B is now amenable to a closed form solution and hence a numerical technique is employed. The solution is complicated by the fact that the exponential integral $E_1(|\tau - \tau'|)$ appearing in the energy equation is singular at the origin. This problem is overcome by approximating the temperature distribution $\theta^h(\tau)$ and the scattering function $D(\tau)$, with finite polynomial expansions, as suggested by Leung and Edwards^[22] in a study of solar heat shields and solar heat collectors. This method was also used in a non-scattering system for the temperature distribution in a time dependant radiative heat transfer study by Viskanta and Bathla^[23] and by Krishna Prasad and Hering^[24] in a similar investigation.

After spacial discretization of the plane parallel layer of emulsion, bounded by gray, diffusely emitting, black boundaries, the problem is reduced to one of solving for unknown coefficients using a matrix method applied across the field.

2.4.1. Boundary conditions

As discussed previously, the free boundary of a fluidized

bed emulsion may be regarded for radiative heat transfer purposes as one in which the incoming boundary radiative flux has negligible effect on the temperature and flux distribution within the emulsion. This being the case, the free boundary condition used in this analysis is taken as equivalent to a black plane wall at either zero absolute temperature with $F_1 = \theta_1^4 = 0$, or at atmospheric temperature with θ_1^4 of order 0.002 for a bed temperature at 1 000°C. This boundary condition is obviously idealized and suggests a temperature discontinuity at the free surface of the emulsion. In reality, conduction and convection heat transfer will occur in addition to radiation heat transfer to eliminate the apparent discontinuity. The idealized boundary condition used here is not physically justifiable but is used as a mathematical expedience. A similar problem was observed by Deissler^[25] in a study of radiative heat transfer to parallel plates from an absorbing, emitting and scattering medium. The case of an optically thick medium was taken, resulting in an approximation to the radiative flux equation of

$$q'_r = - \frac{4}{3} \frac{d\theta^4}{dT}$$

from [25] and [26]. Appropriate boundary conditions were evaluated to account for the apparent discontinuity when conduction was absent from the analysis. This technique is commonly referred to as the radiation slip method.

The second boundary condition, deep within the emulsion, is taken to be equivalent to a plane, black, diffusely radiating

surface at the bed temperature. This is in accordance with the configuration of Figure B.1 of Appendix B, and Figure 1.1. The assumption of such a black boundary was chosen to simulate the radiative flux emitted from the volume of emulsion beyond a depth of $\tau = 10$. Hence from Appendix B, $F_2 = \theta_2^4 = 1$. With the exponential integral $E_3(\tau) = 0.0000038302$ for $\tau = 10$, the effects of such an assumption are sensed only in the immediate vicinity of this boundary.

With reference to Figure B.1 and Figure 1.1, solutions were obtained for fluxes emitted in the negative x direction.

2.5 Discussion of Analytical Results

The method of solution of the energy equation is described in Appendix D. The exponential integrals $E_n(\tau)$ encountered in the solution of the radiative transfer equation from [9] are described briefly as

for positive real arguments

$$E_n(\tau) = \int_0^1 \mu^{n-2} e^{-\tau/\mu} d\mu \quad (2.1)$$

or

$$E_n(\tau) = \int_0^1 \mu^n \mu^{-2} e^{-\tau/\mu} d\mu \quad (2.2)$$

and

$$E_n(\tau) = \frac{1}{\tau} \int_0^1 \mu^n d(e^{-\tau/\mu}) \quad (2.3)$$

integrating by parts the recurrence relation is obtained as

$$nE_{n+1}(\tau) = e^{-\tau} - \tau E_n(\tau) \quad n \geq 1 \quad (2.4)$$

and

$$\int E_n(\tau) d\tau = -E_{n+1}(\tau) \quad n \geq 1 \quad (2.5)$$

From Appendix D the lowest case of exponential integral encountered is $E_2(\tau)$. Using the recurrence relation of equation (2.4) with values of $E_1(\tau)$ obtained from a computer algorithm, all higher cases of $E_n(\tau)$ may be obtained.

The solutions of Appendix D were tested for convergence using polynomial expansions for $\theta^4(\tau)$ and $D(\tau)$ of order 4 and 6, with a spacial step size reduced from 0.1 to 0.05 and to 0.02. For the convenience of studies, reported later, of a transient analysis of radiative transfer a spacial size less than 0.05 required a large amount of computer memory and exceeded the capacity of University of Aston ICL 1905E computer. Again, for a transient analysis computational time was also excessive. For these reasons the 1906A/CDC7600 installation at the University of Manchester Regional Computer Centre was utilized.

This technique, although not of a closed form as the analysis given in [18], is sufficiently flexible to account for possible non-isothermal conditions. It was not subject to the anomalies of [18], where in some cases ϵ_e exceeded unity.

From the theory developed in [18] and [21] the curves of effective emissivity against optical thickness are shown in Figure 2.1 for an isothermal slab, along with results obtained using the two flux method of [19] in Appendix C. The value of effective emissivity from each method reaches an asymptotic value

for large values of optical thickness. It is apparent from these curves that only a particulate material of emissivity equal to unity will produce an effective emulsion emissivity of unity at large emulsion optical thicknesses. It appears possible, in most cases, to have an effective emulsion emissivity of a higher value than the particulate material emissivity. This may be explained by consideration of the work reported in [26] on radiation from cavities. As a bundle of radiative energy traverses a cavity (or void in a fluidized bed of particles), the multiple reflections occurring within the cavity act to augment the emissive power of the cavity relative to that of a plane surface of identical temperature and material emissivity. In practice, the cavity effect is used in the design of black bodies. Because of the asymptotic nature of the curves in Figure 2.1 and for reasons which are later justified experimentally, the slab of emulsion is considered to be optically thick and an optical thickness of $\tau_0 = 10$ is taken as being representative of the depth over which the changes of temperature and hence radiative flux may extend, but not exceed. The solutions of Appendix D were initially for an isothermal emulsion. However, as a non-isothermal system is more realistic, due allowance was made in the analysis to make possible the inclusion of a temperature distribution.

Results were obtained for a number of scattering albedo values ω_0 . The curves are shown in Figure 2.2 along with curves derived from those of Figure 2.1.

Also shown on Figure 2.2 are exact values of ϵ_e (hemispherical) with $\tau_0 = \infty$. These results were reported in [18] and derived from

the work of [12]. Briefly, the analysis is taken from a solution of the radiative transfer equation in the discipline of astrophysics [12] and adapted in [18] for use in a heat transfer context. Radiative intensities may be defined in terms of H_{ω} functions which are tabulated in [12] for a range of ω_0 and θ values.

The value of ϵ_e (hemispherical) requires values of the first moments of the H_{ω} functions again reported in [12]. The points of hemispherical emissivity taken from [18] and plotted in Figure 2.2 show a favourable comparison with the results obtained by the present analysis thus justifying its use.

Again, in Figure 2.2 the results obtained in the present analysis are greater than those from the work in [18] by up to 6.1%. As reported in [18], these results would underestimate the exact solution. Hence it is reasonable to assume that the analysis presented in this study is an improved approximation to the exact solution.

The curves of Figure 2.2 show conclusively the effect of particle material emissivity, through the scattering albedo ω_0 on the emulsion effective emissivity. This is in contrast with the findings in [2] who concluded that $\epsilon_e = \text{unity}$ in all cases but supports the postulation in [4] and [5]. The curves of Figure 2.3 demonstrate how the effective emissivity of absorbing, emitting and scattering media exceed the value of particle emissivity. As a comparison the effective emissivity of a diffusely emitting conical groove, from [26], is given emphasizing the effect of scattering.

2.6 Conclusions

The equation of radiative transfer is not amenable to closed form solution and a numerical technique, subject to initial simplifying assumptions, has been developed. The variation of effective emissivity, of an emulsion of fluidized solids, with change of scattering albedo is shown. The results compare favourably with the results of other authors and show the dependence of ϵ_e upon the type of particle material used. The limitation of the Zabrodsky model [2] originates in the neglect of the effects of energy scattering and energy emission of a particulate emulsion. The consequence is an overshadowing of the important features highlighted only by a solution of the complete equation of radiative transfer.

2.7 Suggestions of Areas for Further Study

The solution of the radiative transfer equation may be achieved by alternative methods such as the statistical Monte Carlo method developed for use in heat transfer systems by Howell and Perlmutter^[27]. However, this technique requires considerable computer time and storage capacity and for this reason the classical differential approach is used in the present study. Another method of solution is a numerical technique based upon Gaussian quadrature and a matrix eigenvector application developed by Hsia^[28] and Love^[29] used in a study of steady-state radiative transfer with an-isotropic scattering. The work by Weston and Hauth^[30] in a study of the transient cooling of an absorbing, emitting and isotropic scattering medium for the case of combined

radiation and conduction used a similar approach. Solutions based on this approach would be useful in order to compare and justify the technique used in the present study. In this work of an emulsion of fluidized solids, a number of simplifying assumptions were made and listed. The assumption of steady state is one which may be readily relaxed and solutions obtained for the more realistic situation of transient radiative transfer. In theory, the analysis may also be extended to include conduction heat transfer for the case of energy exchange to a surface immersed within a fluidized bed. However, before these extensions to the work are undertaken, it is desirable to conduct an experimental programme to justify the results so far obtained.

CHAPTER 3

DETERMINATION OF FLUIDIZATION AND RADIATIVE HEAT
TRANSFER PARAMETERS

3.1 Introduction

Before proceeding to an experimental programme of radiative flux determination from emulsions of fluidized solids, it is necessary to describe a few fundamental fluidizing parameters in addition to those arising due to radiative heat transfer considerations.

3.2 Minimum Fluidizing Velocity at High Bed Temperatures

A fundamental property of any bed of fluidized solids is the minimum fluidizing velocity, U_{mf} . It is a basic parameter used in mathematical models of fluidization and used extensively in the two phase theory of fluidization of Davidson and Harrison^[31]. Values of U_{mf} may be determined for any bed temperature using the classical Ergun equation, Ergun^[32] of

$$\frac{1.75}{\phi_s \epsilon_{mf}^3} \left[\frac{D_p U_{mf} \rho_g}{\mu} \right]^2 + \frac{150(1-\epsilon_{mf})}{\phi_s^2 \epsilon_{mf}^3} \left[\frac{D_p U_{mf} \rho_g}{\mu} \right] = \frac{D_p^3 \rho_g (\rho_p - \rho_g) g}{\mu^2} \quad (3.1)$$

resulting in the solution of a quadratic for U_{mf} . Equation (3.1) for particle Reynolds numbers of less than 20 may be simplified to

$$U_{mf} = \frac{(\rho_p - \rho_g) g}{\mu} \frac{\phi_s^2 D_p^2}{150} \frac{\epsilon_{mf}^3}{(1-\epsilon_{mf})} \quad (3.2)$$

The two parameters, sphericity ϕ_s and voidage at minimum fluidizing velocity ϵ_{mf} are not well tabulated for a comprehensive range of

particle types. To overcome this problem, a paper by Broughton^[34] described a technique in a study of high temperature effects on U_{mf} which resulted in rewriting of equation (3.2) in the form

$$U_{mf} = \frac{(\rho_p - \rho_g)g D_p^2 \phi_s^2}{\mu_g f(\epsilon_{mf})} \quad (3.3)$$

where

$$f(\epsilon_{mf}) = \frac{150(1 - \epsilon_{mf})}{\epsilon_{mf}^3} = C \phi_s^2 \quad (3.4)$$

hence

$$U_{mf} = \frac{(\rho_p - \rho_g)g D_p^2}{C \mu_g} \quad (3.5)$$

[34] cited values of C used by other workers ranging from 1 233, Davidson and Harrison^[35] to 1 650, Kunii and Levenspiel^[36] and suggested in the absence of experimental data that a value of 1 440 be used producing an expected error range of up to 15%. Again [34] cites a number of references where equation (3.5) was used with acceptable results, although correlation was poor, with a value for C of 1420, in the work of Mii, Yoshida and Kunii^[37] resulting in errors of up to 100% compared with experimental values of U_{mf} .

3.2.1. Experimental determination of U_{mf} at high bed temperatures

An experimental programme was set up in which bed pressure drops were measured at incremental gas flow velocities. Due to the low gas flow rates required in such experiments, it was not possible to use a conventional type of fluidized bed as combustion

becomes unstable. For this reason an 80 mm diameter x 300 mm high, mild steel fluidized bed reactor was designed and is shown in Figure 3.1. The incoming air was heated by a 2 kilo-watt 'cooker element' situated below the 2 in thick ceramic distributor plate. The position of the heating element, on heating the distributor plate, reduced considerably the thermal gradients which would normally occur in a fluidized bed just above a relatively cool distributor plate. Hence, the gas velocity remains constant throughout the total height of bed, an important criterion for U_{mf} measurements. Particles of a number of materials were sieved in a narrow size range. In order to achieve good fluidization, bed heights of up to 140 mm were used. If shallow beds are used in U_{mf} experiments, i.e. of less than approximately 100 mm in a bed diameter 80 mm, there is a possibility that the total weight of solids will not be fully supported by the fluidizing medium at or above minimum fluidizing conditions. This phenomenon is particularly noticeable at high bed temperatures, and demonstrated in the later experiments of Section 3.4 in which shallow beds of height 25 mm were used. The bed pressure drop levels were measured using an inclined liquid manometer from a pressure tapping just above the distributor plate and another tapping above the bed of solids. The experimental procedure was to lower the gas flow rate from an initially well fluidized bed while measuring the pressure drop at suitable intervals. This was then repeated for increasing gas velocities, again measuring pressure levels, up to a well fluidized condition. Repeated raising and lowering of the gas flow rates resulted in the typical curves shown in Figure 3.2

from which U_{mf} was determined in the normal way.

3.2.2. Discussion of results

For the materials used in these experiments, the curves of U_{mf} against bed temperatures are shown in Figure 3.3 (a, b & c). Unfortunately, it was not possible to raise the bed temperatures above 600°C using the electrical heating method. The normal bed temperature range of interest for radiation flux measurements is 800°C to 1 100°C. In order to compare the experimental results of U_{mf} with those obtained using both equation (3.1) and equation (3.5), the voidage at minimum fluidizing velocity was determined from

$$\epsilon_{mf} = 1 - \frac{W_b}{A_b \rho_p H_{mf}} \quad (3.6)$$

where H_{mf} was measured during the experiments, using a steel ruler immersed in the bed. This technique was rather crude as the true bed height was difficult to determine due to localized bubbling around the ruler as U_{mf} was reached. Over the range of bed temperatures used the value of H_{mf} changed by only 2 mm to 3 mm resulting in a small variation of the calculated ϵ_{mf} values. For the purpose of substitution in equation (3.1) and (3.5) a mean of ϵ_{mf} over the bed temperature range was taken. Values of sphericity ϕ_s were obtained using the paper of Rittenhouse^[33] who tabulated diagrams of typical ranges of two-dimensional particle sphericity. Using a microscope and these tables, subjective estimates of sphericity were obtained. The results of ϵ_{mf} and

TABLE 3.1

MATERIAL: SILICA SAND; TEMPERATURE: 300 K; ρ_p : 2 630 kg/m ³				
ϕ_s	ϵ_{mf}	D_p mm	C	Re_{mf}
0.83	0.44	0.354	1431.4	2.086
0.85	0.424	0.55	1568.8	6.637
0.83	0.416	0.777	1766.3	14.86
MATERIAL: SILICON CARBIDE; TEMPERATURE: 300 K; ρ_p : 3 179 kg/m ³				
ϕ_s	ϵ_{mf}	D_p mm	C	Re_{mf}
0.75	0.47	0.354	1361.3	2.63
0.72	0.455	0.55	1674.1	7.51
0.75	0.45	0.777	1609.5	18.89
MATERIAL: ALUMINA; TEMPERATURE: 300 K; ρ_p : 3 850 kg/m ³				
ϕ_s	ϵ_{mf}	D_p mm	C	Re_{mf}
0.67	0.52	0.354	1140.7	3.74
0.69	0.501	0.55	1250.2	11.46
0.69	0.49	0.777	1365.8	25.1
MATERIAL: MAGNESIA; TEMPERATURE: 300 K; ρ_p : 3 820 kg/m ³				
ϕ_s	ϵ_{mf}	D_p mm	C	Re_{mf}
0.71	0.49	0.354	1289.9	3.45
0.71	0.482	0.55	1376.5	10.64
0.73	0.471	0.777	1425.1	24.76

sphericity are shown in Table 3.1 for the bed materials used along with the values of constant C and particle Reynolds number for each case. A wide range of values for C were obtained emphasizing the effect of particle sphericity and hence ϵ_{mf} on the resulting U_{mf} levels. Comparison of the sphericity and ϵ_{mf} results obtained here with the curves of Brown *et al*^[41] shown in Figure 3.4 shows that all points were bounded by the curves of loose packing and normal packing. As these two quantities are subject to experimental error the favourable comparison with the expected curve of loose packing for the case of a fluidized bed places this error within acceptable limits.

The comparison of theoretical with experimental $U_{mf} V_s$ temperature curves of Figure 3.3 (a, b and c) are reasonable in most cases showing least deviation for U_{mf} calculated from equation (3.5). The discrepancy with values calculated from equation (3.1) and equation (3.5) were most obvious at ambient temperature. This fact is reflected in the values of particle Reynolds numbers at ambient and high temperatures. In some cases, Re_{mf} was large and hence equation (3.5) was used at or approaching its limit of applicability. Although the greatest discrepancy between theoretical and experimental U_{mf} values occurred at ambient temperatures, at high bed temperatures of up to 600°C the error was acceptable and the trend is assumed to continue to bed temperatures of up to 1100°C. The use of either equation (3.1) or equation (3.5) with a known value of C would give acceptable results at high bed temperatures in the absence of sphericity and ϵ_{mf} values. The use of C = 1440 in equation (3.5) as suggested by [34] gives maximum difference at 600°C of 16% in the case of 0.354 mm diameter

alumina particles and of 4% for 0.777 mm diameter sand particles.

3.2.3 Conclusions

For all particle sizes and materials used in the later experimental studies of this work, U_{mf} was measured for bed temperatures up to 600°C. The correlations with equation (3.1) and equation (3.5) with a predetermined value for constant C in each case were reasonable. The greatest discrepancy occurred at ambient temperature but rapidly diminished as the bed temperature was increased. As stated in [34] the use of $C = 1440$ in equation (3.5) is expected to give errors of up to 16% for high temperature beds. It is assumed that the results can be extrapolated to bed temperatures of up to 1100°C and equation (3.1) or equation (3.5) used with confidence.

3.3 Determination of Particle Emissivity

As emphasized by the results of Chapter 2, Figure 2.2, the effective emissivity of an optically thick medium which absorbs and scatters radiation is strongly dependant upon particle emissivity. As described in Table 3.3 values of ϵ_p for the materials used in this study vary considerably. Such variations are understandable when the large number of parameters which effect emissivity measurements are considered. Some examples of these parameters are grain structure, transmissivity, wavelength dependency, trace additives and surface roughness. The problem has also been aggravated by the inadequate description given by many investigators of the materials studied. An additional difficulty arises due

to emission originating at considerable depths below the material surface, e.g. refractory oxides, wood and fibrous materials, where absorption and scattering of energy are significant parameters.

In order to have reasonable estimates of the particle emissivities used in this study it was necessary to produce test samples of the various materials and conduct an experimental programme of measurement.

3.3.1 Manufacture of test samples

The most suitable samples for emissivity measurements are solid slabs of equivalent material. Unfortunately, no such samples were available and so special test samples were produced from the readily available particulate material.

An initial consideration was given to the possible use of slabs made from compacted fine particulate material. However, all that is really achieved is a packed bed of solids which is essentially a volume emitter rather than the required surface emitter. Hence, a different method was considered where particles of each material in the size range 0.71 mm to 0.85 mm were embedded in a single layer on the surface of a sub-layer of suitable material. In order to reduce the contribution to the overall surface emitted flux of this sub-layer, a material of low emissivity was chosen, i.e. pure silver.

Using a firebrick mould which also acted as a support for the test sample, a small amount of silver was melted using a propane/air burner. Immersed in this melt was a Cr.AL thermocouple. A diagram of the sample configuration is shown in Figure 3.5. As the

silver became molten, a few particles were sprinkled onto the surface. The particles in direct contact with the surface became embedded and on subsequent cooling in air remained intact. All the loose particles then remaining were blown off using a compressed air jet. The resulting surface as described in Figure 3.5 revealed closely spaced particles interspaced by silver. The molten silver developed a small meniscus and with the lower density particles protruding from the silver the appearance of the surface was far from ideal. However, subsequent grinding of the surface completely removed the embedded particles and so was not continued. Although a source of error, for the purpose of analysis, such a sample surface was regarded as being flat. The size of each sample, as described by Figure 3.5 was chosen as $\frac{1}{8}$ in diameter x $\frac{1}{4}$ in deep for the field of view of the radiation pyrometer subtended a circular area of 0.25 ins diameter at a target distance of 24 ins. Hence, the field of view was always filled by the sample.

3.3.2 Experimental procedure

The experimental configuration is described schematically in Figure 3.5. To reduce the losses of radiative flux from the system and to ensure energy interchange between pyrometer and sample surface only, the inner surface of the pyrometer extension tube was covered with aluminium foil. This highly reflecting surface, in reducing the temperature gradients at the test sample surface, also reduced the error incurred in assuming that the immersed thermocouple measured this surface temperature. In similar experiments conducted by Sully, Brandes and Waterhouse^[72], coats

of powdered refractories of known thickness were applied to metal strips. The surface temperature gradients were corrected by taking emissivity measurements for a range of coating thicknesses and extrapolating back to a zero thickness. However, absorption and scattering of energy within and at the surface of these coatings becomes significant and should be allowed for. In the work of Pattison^[73], solid cylindrical test samples were heated on the outer surface by a propane/oxygen flame and measurements of material emissivity obtained by viewing through this flame. In the subsequent analysis due allowance was made for the effect of flame emissivity. In this way the surface temperature was known accurately, being obtained from a radiation pyrometer viewing a 0.25 in diameter x 1 in deep hole bored in the specimen acting as a black body source.

Various measurement techniques have been cited in the literature, the most comprehensive of which appears in [43]. However, a few simple methods were considered, Pirani^[74], plotted the decay of radiation with time using a total radiation receiver and extrapolated back to zero time to obtain the sample emissivity. This method being dependant upon the response time of the measuring instrument was not considered. Michaud^[75] used a similar technique to [73]. This method of a flame directly heating the surface to be measured was not desirable in this study. With the sample temperature measured just below the surface of the silver sub-layer the true value of surface temperature could not be determined with any reasonable degree of certainty. Ideally, a furnace was required to heat the sample. However, this was not readily available and

the test sample in this study was heated on its reverse side by a propane-air burner. Each sample was raised in temperature in steps up to a maximum of about 860°C. With the melting point of silver determined at approximately 935°C, it was not advisable to raise the sample temperature any further. For each steady value of sample temperature measured via a digital voltmeter, the pyrometer output was recorded. From the output fluctuations the error of the pyrometer output was estimated at ±5 K. Such experiments were repeated a number of times by constantly raising and lowering the sample temperature. A further sample of pure silver with no other material present was like-wise studied.

From the conservation of energy, particle emissivity ϵ_p may be simply obtained from the equation

$$q_{o,particle} A_p + q_{o,silver} A_s = q_{i,detector} A_{target} \quad (3.7a)$$

From a consideration of the system, neglecting radiative exchange with the pyrometer extension tube, then generally

$$\sum_{j=1}^N [\delta_{kj} - (1 - \epsilon_k) F_{k-j}] q_{o,j} = \epsilon_k \sigma T_k^4 \quad (3.7b)$$

with

$$\delta_{kj} = \begin{cases} 1 & \text{when } k = j \\ 0 & \text{when } k \neq j \end{cases}$$

where $q_{o,j}$ is the radiosity of surface j

$\{ q_{i,j}$ is the irradiation of surface i }

then

$$q_{o,p} - (1 - \epsilon_p) F_{p-d} q_{o,d} = \epsilon_p \sigma T_p^4 \quad (3.7c)$$

$$q_{o,s} - (1 - \epsilon_s) F_{s-d} q_{o,d} = \epsilon_s \sigma T_p^4 \quad (3.7d)$$

and with

$$q_{o,d} = \sigma T_d^4 \Rightarrow \text{negligible}$$

Then equations (3.7c) and (3.7d) simplify to give with equation (3.7a)

$$\epsilon_p = \frac{T_{\text{measured}}^4}{T_{\text{sample}}^4} \frac{A_{\text{target}}}{A_{\text{particle}}} - \epsilon_{\text{silver}} \frac{A_{\text{silver}}}{A_{\text{particle}}} \quad (3.8)$$

The number of particles within the 0.25 inch diameter field of view of the pyrometer were counted with the aid of a microscope. Great care was exercised in ensuring correct alignment of the sample and pyrometer. However, the exact position, relative to the sample centre line of the area of view could not be precisely determined. Hence the number of particles within an area of 0.25 in diameter were counted for this area centred at different positions over the sample surface. A mean value was then obtained.

From a few initial experiments it appeared that ϵ_p predicted from the overall energy balance, gave values greater than unity, particularly when A_p/A_t was small. Such an energy balance predicts an inverse relationship between ϵ_p and the ratio A_p/A_t . In order to investigate the validity of this relationship the initial experiments were repeated for a number of A_p/A_t values. The experimental

technique eventually used was to initially measure the emissivity of a sample of pure silver defined as

$$\epsilon_{\text{silver}} = \frac{T_{\text{pyrometer}}^4}{T_{\text{sample}}^4}$$

from Appendix F. The sample was then remelted and a few particles added to the molten surface. The emissivity of this sample was then determined for a range of sample temperatures along with the ratio A_p/A_t . This procedure was repeated for increasing values of A_p/A_t .

3.3.3 Discussion of Results

Typical experimental values of ϵ_{sample} against sample temperature are given in Figure 3.6a for each particle material and A_p/A_t value along with the curve of ϵ_{silver} for silver alone. As expected for non metallic solids, the value of ϵ_{sample} decreased with increase of sample temperature. This fact is well known and reported in [9] and [10]. For silver, the curve predicts a similar trend; however, as reported in [9] and [10] for metals, an opposite trend was observed. The reason for this discrepancy may be attributed to the formation of an oxide at the surface of the silver sample, which would hence exhibit the trend reported for a non-metallic material. At high sample temperatures, a levelling out of ϵ_{sample} was observed for all the materials studied. Hence it was a simple matter to extrapolate the results to higher temperatures to the levels encountered in fluidization, i.e. up to 1100°C.

The effects on ϵ_{sample} of varying the ratio A_p/A_t are shown

in Figure 3.6b. The curves were drawn, simply by inspection, through the results of ϵ_{sample} and extrapolated to a value of $A_p/A_t = \text{unity}$.

Hence the method of ϵ_p determination was to take $\epsilon_p = \epsilon_{\text{sample}}$ at the extrapolated point of $A_p/A_t = 1$, when the sample is totally covered by particulate material. An explanation of this non-linearity effect lies in the effects of the scattering of radiative energy by the essentially particulate surface. The true surface area of the radiating particles is much larger than the cross-sectional area assumed in equation (3.7a) and tends towards a hemispherical surface. Hence considerable particle to particle radiation takes place resulting in a multiple scattering system.

This method is simple but approximate in that the temperature of the particles are assumed to reach the measured silver sublayer temperature. Realistically temperature gradients are in evidence and it is therefore expected that the results underestimate the true values of ϵ_p . An extension of the technique, although not considered in this study, was described by [72] in which increasing particle depths were used. This would be useful in estimating the effects of surface temperature gradients.

TABLE 3.2

Material	ϵ_p	Temperature Range K	Reference and Notes
Al ₂ O ₃	0.55 - 0.45	1 000 - 13 000	[9]
Al ₂ O ₃	0.35 - 0.53	1 473	[10] - Grain size 2 - 120 μ m
Al ₂ O ₃	0.42 - 0.25	750 - 1 000	[42]
Al ₂ O ₃	0.41	1 200	[43]
Al ₂ O ₃	0.45 - 0.25	1 273	[21]
MgO ₃	0.5 - 0.45	1 000 - 13 000	[9]
MgO ₃	0.3 - 0.48	1 473	[10] - Grain size 1 - 120 μ m
MgO ₃	0.3 - 0.2	1 000 - 2 200	[42]
MgO ₃	0.2	1 200	[43] - Pressed and sintered measured in argon
MgO ₃	0.45	1 200	[45]
SiO ₂	0.62 - 0.46	1 173 - 1 573	[42] - Grain size 70 - 600 μ m
SiO ₂	0.75	1 300	[43] - Fused specimen 0.33 cm thick measured in vacuum 10 ⁻⁹ mm Hg
SiC	0.96 - 0.8	1 300	[45]
Fire clay	0.75	1 273	[42]

TABLE 3.3

Material	k_p kW/m K	ρ_p kg/m ³	C_p kJ/kgK	ϵ_p Range	ω_o Range	ϵ_e Range
Silica Sand	0.00187	2360	0.8374	0.46 - 0.75	0.71 - 0.4	0.78 - 0.82
Silicon Carbide	0.018	3179	0.714	0.8 - 0.96	0.34 - 0.09	0.94 - 0.99
Alumina	0.0061	3850	0.714	0.25 - 0.55	0.86 - 0.63	0.62 - 0.82
Magnesium Oxide	0.007	3820	0.714	0.2 - 0.5	0.89 - 0.68	0.55 - 0.79
Fire Clay	0.00128	2600	1.172	0.75	0.4	0.91
Carbon	0.005	2300	0.952	~1.0	0	1.0

The predicted results of ϵ_p and corresponding values of ω_o along with ϵ_{ei} determined from Figure 2.3 are tabulated below in Table 3.4.

TABLE 3.4

	Silica Sand	Alumina	Magnesia	Silicon Carbide
ϵ_p	0.64	0.37	0.57	0.77
ω_o	0.529	0.773	0.601	0.374
ϵ_{ei}	0.87	0.71	0.84	0.93

3.3.4 Conclusions

Test samples from which particle emissivity was determined were produced from slabs of silver into the surface of which particles were embedded. Varying the number of particles per unit area the values of sample emissivity were observed to increase non-linearly with increase in A_p/A_t . The value of ϵ_p was then determined by extrapolation to $A_p/A_t = 1$. The method is essentially approximate and for the reasons described would tend to underestimate the true values of ϵ_p . However, the advantages of the technique lay in its simplicity of what is essentially a complex problem. It is expected that the results of ϵ_p so predicted enable values of fluidized emulsion effective emissivities to be predicted with greater confidence.

3.4 Determination of the Extinction Coefficient

In order to determine the extinction coefficient it was necessary to know the value of particle concentration within the emulsion. In the context of the assumptions so far postulated for a fluidized emulsion, the constant voidage extends to the free surface. As this free surface is assumed to be in dynamic equilibrium, i.e. the gas and particles are motionless relative to one another, and furthermore that at no time is the surface disturbed by the passage of bubbles, then it is possible to derive an equation of particle concentration which will be a time mean value. The derivation of this particle concentration equation in terms of the vertical pressure drop profile within the emulsion is shown in Appendix E(a). The analysis is then extended to include the radiative parameters of particle emissivity and reflectivity resulting in the final equation for extinction coefficient K_t . The unknown pressure profile existing within the emulsion, being essentially a time-mean value, particularly in the vicinity of the free surface, had to be determined experimentally. The resulting pressure profile may then be approximated for purposes of analysis by a least squares polynomial curve fitting procedure.

3.4.1 Experimental Determination of Bed Pressure Profile

The experimental configuration shown in Figure 3.7a of a 143 mm diameter x 100 mm high mild steel fluidized bed reactor, was used with a supply of propane/air mixture. Bed pressure drop profiles were determined, for a number of particle sizes, (sieved to a narrow size range), materials, fluidizing velocity and bed

temperature, measured by an unshielded copper constantan thermocouple, immersed in the bed. As the characteristics of shallow beds are of particular interest in this study only bed heights of up to 25 mm, measured at atmospheric pressure, were studied.

To measure the pressure drop distribution, a 0.5 mm diameter stainless steel pitot tube was traversed through the total depth of the bed with pressure levels recorded at incremental heights. In reality the pitot tube remained fixed while the bed was traversed vertically. The pressure levels of such shallow beds are small and difficult to measure quickly using a liquid manometer, with a long response time of the liquid column and connecting tube. Hence a 'Kistler' differential pressure transducer, type 7251, capable of resolution to 4 Pascals was used. The output from the transducer was processed in a charge amplifier type 5001 and finally recorded on an Ultra Violet Recorder (U-V-R). The differential transducer is basically a dynamic pressure measuring instrument but may also be used to measure quasi-static pressure levels, as required in these experiments. To achieve this mode of operation the transducer was connected to the pressure probe via a three-way pneumatic switch. The configuration is shown in Figure 3.7b. By means of this switch the reference (zero) differential pressure is applied to the transducer. Releasing this switch, and with the charge amplifier in the 'Long' time constant mode, the required differential pressure level was then applied to the transducer. A typical output signal traced from the U.V.R. paper is shown in Figure 3.8. In Figure 3.9 is shown the simple resistance matching network used to match the high impedance transducer amplifier with the low impedance

U.V. recorder.

3.4.2. Discussion of Results

In the vicinity of the free bubbling surface, the experimental points were difficult to obtain, a transducer signal to noise ratio of unity was approached. Hence in this region the pressure drop curves were extrapolated to zero at an 'observed' mean bed height, i.e. the height of the bed taken when the pressure probe became visible. This extrapolated distance was in most cases of order 3 mm to 4 mm and constituted a small proportion of the overall bed height. Examples of the experimental pressure profiles are shown for a few of the cases studied in Figure 3.10 through Figure 3.12. The curves resulted from a least squares fit of the experimental points.

In most cases it was observed that the total bed pressure drop measured at the distributor plate was not equal to the weight of solids in the bed, i.e. $PA/W_b \neq 1$, even at high values of $U-U_{mf}$. This suggests that the whole of the bed was not fully supported by the fluidizing gas and may be explained from a consideration of what occurs in the first few particle diameters just above the distributor plate. Over the first few particle diameters of the bed large temperature gradients occur. As a result, this portion of the bed will not be fluidized constituting a measurable proportion of the total height of bed, e.g. 20% for a 25 mm deep bed of particle size 0.50 mm and entrance region extending over $10 D_p$. In very deep beds this entrance region effect constitutes only a small percentage of the total bed height and being difficult to measure could be

considered as an experimental error. Further to this explanation the work of Hiby^[45] who measured oscillation frequencies in the region just above the distributor plate of beds up to 150 mm deep, concludes that the first 10 D_p of the bed perform a periodic oscillation coherent over the bed cross-section. This oscillation of about the ten lowest layers within a deep bed continues and acts as the origin for periodic gas bubble formation. Extension of the work of [45] by Verloop and Heertjes^[46] in shallow gas fluidized beds, showed that the bed would oscillate homogeneously, i.e. the particles moved in phase, only when the height of bed was smaller than some critical height, e.g. for $D_p = 0.55$ mm, $U/U_{mf} = 3$, $\epsilon_b = 0.52$ and from [46] $H_c = 79$ mm.

Hence even though the bed is well fluidized with $1 < U/U_{mf} < 3$ for a height of less than 79 mm, a fully supported condition is not reached. Although the studies of [45] and [46] were at ambient temperature, extensions of the hypothesis to higher bed temperatures appear to be valid.

From the pressure profiles so obtained, along with values of the appropriate particle emissivity and reflectivity given in Table 3.4, values of extinction coefficient K_t may be obtained corresponding to values of optical depth $\tau = 10$ shown on the pressure distribution curves. The pressure curves were generally of an approximately linear relationship up to optical depths of $\tau = 10$, and the errors due to non-linearities in deriving subsequent values of K_t from $K_t \sim 10/nD_p$ are small. The curves of K_t against change of excess gas velocity $(U-U_{mf})$ are most appropriate to this work and are shown in Figure 3.13 through Figure 3.21.

The curves were obtained from a least squares polynomial fit of the experimental points. No attempt was made to correlate the effect of bed temperature variation as only three values were studied. Values of K_t required at intermediate bed temperature levels were obtained by simple interpolation. As may be expected increasing bed temperatures and increasing gas velocities produce incremental bed expansions resulting in lower particle concentrations and hence lower values of K_t .

These experimental values of K_t for a fluidized emulsion have not, to the author's knowledge, been determined previously. However, studies on radiatively semi-transparent materials such as Dydydium glass by Melamed [38] in which the assumption of optical thickness, $\tau_0 = \infty$ was made, show values of absorption coefficient K_a of a comparative level. Also from the analysis of Yokoburi [39] levels of K_t occurring in a particle seeded gas for carbon particles of size typically $D_p = 0.77$ mm gives $K_t = 1\ 500\ m^{-1}$. These results compare favourably with values for K_t using particles, i.e. silicon carbide found in this work. As a contrast, values of K_a are given for non-seeded hydrogen at 100 atmospheres and 1 680 K of $10^{-5} m^{-1}$ from Williams *et al* [40]. This was a study of the wavelength dependency of K_a in sub-micrometre particle flames. For non-seeded CO_2 , a value of K_a of approximately $10\ m^{-1}$ at atmospheric pressure and 700 K was reported in [26]. In addition, [40] gave an approximate value for K_a of $1\ 000\ m^{-1}$ for $1\ \mu m$ diameter carbon at 2 200 K with a dispersion density (weight of particles per unit volume of emulsion) of $0.2\ kg/m^3$, which emphasizes how the radiative properties are improved when solid particles are added to a

hot gas.

3.4.3. Conclusions

Time average particle concentration levels may be estimated experimentally in the vicinity of a freely bubbling fluidized bed surface from a determination of the time mean static pressure distribution throughout the height of the bed. From such an analysis the important radiative parameter of extinction coefficient follows. The levels of K_t reported are comparable to those of similar systems in semi-transparent materials and particle seeded gases reported in the literature. The K_t values of a fluidized emulsion are as expected; some orders of magnitude greater than reported values of non seeded gases such as hydrogen and CO_2 .

As $\tau = 10$ extends to appreciable physical depths within the bed, i.e. $x = 14.16$ mm for 0.354 mm diameter sand particles at 1050°C , it is expected that radiative cooling will produce temperature gradients to similar physical depths.

3.5 Determination of the Time Average Temperature Gradient at the Surface of a Fluidized Bed

As stated in Chapter 1.4.1(v), all properties of the emulsion are assumed to be independent of temperature distribution. From the analysis of Chapter 2 an initial solution was of an isothermal slab of emulsion. However, a more realistic model is one in which thermal gradients exist at the bed surface due to radiative cooling of the particles. The existence of such surface

temperature gradients is a reasonable hypothesis if the heat transfer by radiation and convection to and from a single particle in a hot gas stream is considered.

For example, consider a single particle in a hot gas stream, initially at 1 323°K and suddenly exposed (radiatively) to an atmosphere at ambient temperature. Use of the lumped capacity technique is justified for a Biot number of less than 0.2. For a silicon carbide particle in air, the solid and fluid properties are:

$D_p = 0.55 \text{ mm}$	$\rho_f = 0.2715 \text{ kg/m}^3$
$k_p = 1.87 \text{ W/m K}$	$\mu_f = 4.86 \times 10^{-5} \text{ Ns/m}$
$\rho_p = 3 179 \text{ kg/m}^3$	$k_f = 8.35 \times 10^{-2} \text{ W/m K}$
$c_p = 0.714 \text{ kJ/kg K}$	$T_\infty = 300 \text{ K}$
$\epsilon_p = 0.92$	$C_{pf} = 1.188 \text{ kJ/kg.K}$
$T_o = 1 323 \text{ K}$	

Using the Rantze-Marshall correlation for low Reynolds numbers:

$$h_c = 2 \frac{k_f}{D_p} = 0.3036 \text{ kW/m}^2 \text{ K} \quad (3.9)$$

$$h_r = \sigma \epsilon_p (T_o^2 + T_\infty^2) (T_o + T_\infty) = 0.1558 \text{ kW/m}^2 \text{ K} \quad (3.10)$$

$$Bi = \frac{(h_r + h_c) D_p}{2k_p} = 0.068 \quad (3.11)$$

and

$$\frac{T(t) - T_\infty}{T_o - T_\infty} = e^{-\left[\frac{h_r + h_c}{\rho_p \cdot C_p} \right] \frac{6}{D_p} t} \quad (3.12)$$

for $t = 0.06$ secs, a typical residence time for particles above

the bed. Then

$$T(0.06) = 1196.07 \text{ K}$$

and

$$\frac{T(0.06)}{T_o} = 0.904 \quad (3.13)$$

In the analysis of a fluidized bed gas to particle heat transfer by [36], the heat transfer coefficient was determined for both steady and unsteady conditions from a simple heat balance equation, neglecting any radiative transfer. The important parameters in the resulting relationship were the temperatures of the inlet and exit gas and the temperature of the solids within the bed, assumed equal to the gas temperature throughout the bed. The temperature distribution throughout the bed implies significant losses from the bed surface by radiative heat transfer and the radiative term should be included in the overall heat balance equation. A paper by Juveland *et al*^[44] attempted to measure this distribution for a number of fluidizing conditions in very shallow beds of heights up to 13.3 mm. A suction pyrometer was used to measure the gas temperature profile above the bed. Due to blockage of the pyrometer by entrained particles, temperatures less than $\frac{1}{4}$ in from the bed surface were not obtained. By back extrapolation from the resulting profiles the gas temperature at the bed surface was determined. In all cases the gas exit temperature was less than the bed temperature by up to 150°C. With these results and the assumption of [36] that the particles and gas at exit are in local thermal equilibrium, the resulting thermal radiation levels

emitted by the bed surface are accordingly reduced from the purely isothermal case.

3.5.1. Experimental Determination of the Surface Temperature Gradients

The measurement of the temperature distribution at the highly bubbling free surface of the bed is complicated by the large turnover rate of particles and all that may be hoped for is a time mean estimation of the gradients. One method of observation would be to view the bed in the horizontal plane with a narrow angle radiation pyrometer and traverse the instrument through the total height of bed. However, two major difficulties arise; that of the unknown effective emissivity of the dense bed coupled with, as the pyrometer views the diffuse cloud above the dense phase, an unknown configuration factor, i.e. the field of view of the pyrometer may not be completely filled at all times. For reasons of the above complications, this method was not pursued and a contact measuring instrument was selected. Firstly, a suction pyrometer was used and traversed through a 143 mm dia x 100 mm high mild steel bed of bed depths 25 mm as in Section 3.3. To ensure sufficiently low pyrometer suction rates compared with the total throughput of propane-air mixture, a fraction not exceeding 10%, a small entrance bore of 1.5 mm diameter was used. Unfortunately, the fine hole tended to block, as in [44], so consistently that results were only possible in the void region above the bed. For this reason a shielded Cr.AL thermocouple probe was constructed from twin bore alumina tubing and shown in Figure 3.22. The shielded thermocouple probe measures essentially the temperature

of the gas flowing over the thermocouple bed. Gas exhaust holes were provided behind the thermocouple bead to induce such a flow. For use in the thermal balance equation, a thermocouple was inserted in the wall of the tube to monitor T_w .

Vertical traverses of the probe, both up and down, were achieved by actually traversing the bed, supported on a 'Griffin Labjack' maintaining the probe in a fixed position. A range of bed temperatures, excess gas velocities ($U - U_{mf}$), particle materials and particle sizes were used in the experiments to determine as far as possible the effects on the resulting temperature profiles of as many variables as practicable. The bed was traversed relative to the fixed probe well into the free board above the bed; the observed bed height determined at the point where the end of the probe emerged from the bed.

3.5.2. Analysis of the Shielded Thermocouple Probe

A simple heat balance on the probe of Figure 3.22 gives

$$h_c A_T (T_g - T_T) = h_r A_T (T_T - T_w) + \sigma A_T F_{\infty T} (T_T^4 - T_\infty^4) + \text{conduction losses} \quad (3.14)$$

From [9] $F_{\infty T}$, the view factor between the thermocouple bead and the open end of the probe, is small and may be neglected. Then equation (3.14) becomes:

$$T_g = T_T + \frac{h_r}{h_c} (T_T - T_w) + C \quad (3.15)$$

From the Rantze-Marshall correlation for low Reynolds number flow:

$$h_c = \frac{2K_f}{D_T} \quad (3.16)$$

Assuming concentric cylinders:

$$h_r = \frac{\sigma(T_T^2 + T_W^2)(T_T + T_W)}{\frac{1}{\epsilon_T} + \frac{A_T}{A_W} \left[\frac{1}{\epsilon_W} - 1 \right]} \quad (3.17)$$

which underestimates the exact value of h_r by less than 3%

with $\epsilon_T = 0.8$ for an oxidised thermocouple head

$\epsilon_W = 0.5$ for alumina

In equation (3.15) the conduction losses in the thermocouple wires may be neglected. Assuming the wires to be fins protruding 3 mm from the base of the alumina tubing, the temperature correction was of order 10 K introducing an error of 1% in the temperature ratio θ .

3.5.3. Discussion of Results

The measured temperature levels were non-dimensionalised to the bed temperature plotted against probe position relative to the observed surface of the bed. This vertical distance, x , was transformed into an optical depth $\tau = K_t x$ and the experimental results are shown in Figure 3.23 through Figure 3.25. Appropriate values of K_t were obtained from the earlier reported results in Chapter 3, linearly interpolating between the plotted curves where necessary. It was desirable to check the repeatability of a few of the experimental results. However, this was subject to the

ability of repeating the precise air and gas flow rates to achieve the same bed temperature value measured at the same position within the bed. It was not thought that the test rig or for that matter, the method of gas temperature measurement justifies too rigorous a check. Hence, experiments were repeated in the sense that similar conditions were set up for each repeated test run and a range of further results obtained.

The scatter of the experimental points shown in Figure 3.23 through Figure 3.25 were reasonable, of order $\pm 5\%$ for the bed temperatures considered. However, it was observed that temperature profiles obtained at bed temperatures below 850°C fell well outside the general range of experimental scatter resulting from studies at higher bed temperatures. At bed temperatures below 850°C , incomplete combustion within the bed causes considerable gas bubble explosions to occur at or near the bed free surface resulting in high noise levels and higher than bed temperature gas levels. Hence, studies for such unstable conditions resulting from these low bed temperature levels were considered to give unrepresentative results. For later analytical use it was convenient to obtain a mathematical relationship between θ and τ and for this reason a least squares polynomial curve fitting procedure was undertaken using a fourth degree polynomial in line with the analysis of Chapter 2. The striking observation which was a consistent feature of these experiments is the high curvature of the temperature distribution curve deep within the bed, close to the point of maximum temperature. Below this portion of the bed the temperature decreases due to the cooling effect of the

distributor plate. At the other extremity of the bed close to the free surface, the curvature is less severe with the gradient reducing gradually into the free board above the bed surface. The point of inflexion is an indication of the 'effective' surface of the bed above which cooling of the gas by relatively cold particles has no effect. The shape of the fitted polynomial approximations of Figure 3.23 through Figure 3.25 support this observation.

A further observation was that particles of a high emissivity, i.e. silicon carbide, tended to show a pronounced temperature gradient whereas for particles of a low emissivity the slope of the temperature curve was significantly reduced. This fact is simply explained from a consideration of the particle radiative heat transfer coefficient being dependant on the value of particle emissivity from equation (3.8).

The degree of cooling of the bed surface is significant and extends to large optical depths within the bed, e.g. in the case of 0.777 mm silicon carbide the curve extends to $\tau = 6$, resulting in an actual depth of $x = 16.63$ mm. For a shallow bed of total depth 25 mm (measured at ambient temperature), the depth of penetration of this time mean cooling curve represents 66.6% of the total bed height. The assumption of an isothermal shallow bed is far from reasonable.

In deep beds, although this percentage may become insignificant, the assumption of an isothermal bed still does not hold as the important parameter is optical depth. With the initial assumption of an optical thickness of $\tau_0 = 10$; the cooling curves

are seen to extend in most cases almost to this depth and hence flux levels emitted from the surface are reduced accordingly. The fluxes originating at large optical depths deep within the bed are reduced exponentially on passing through the emulsion producing insignificant effects at the free surface - a point discussed earlier in Chapter 2.

3.6 Conclusions

Using a somewhat crude method it has been possible to measure the time averaged gas temperature gradients in the vicinity of the free surface of a fluidized bed. Although subject to uncertainties, the nature of the results obtained produce some interesting observations, particularly the depth within the bed to which cooling of the gas and particles extends. At this stage it is reasonable although not strictly true to assume that particles and gas remain, on a time average basis, at the same temperature. It is now feasible incorporating the results of this and previous chapters to set up a programme of experiments to measure the steady state radiative fluxes emitted by the surface of a fluidized bed.

CHAPTER 4

EXPERIMENTAL DETERMINATION OF THE STEADY STATE RADIATIVE
FLUXES EMITTED BY THE SURFACE OF A FLUIDIZED BED

4.1 Introduction

As the free surface of a fluidized bed is readily accessible it lends itself to the experimental determination of emitted radiative fluxes by simply viewing it with a suitable instrument. It has the major advantage over studies of heat transfer to immersed surfaces within the bed in that no disturbance to particle motion is imposed. The analysis of Chapter 2 may, in principle, be applied to a study of radiative heat transfer to a surface within the bed. In previous chapters essentially steady state or time average processes have been analysed and the assumption is continued in this study. Throughout the experimental study the radiative fluxes are assumed to emanate only from the particulate solids. The contribution of the air/gas (propane) mixture is taken to be negligible due to the relatively low emissivity of the combustion products. A short study of the NO_x levels produced during fluidized bed combustion of natural gas and air was carried out at the British Gas Corporation, Midlands Research Station. Using variable gas/air mixtures at bed temperatures from 900°C to 1080°C , the maximum NO_x level observed was 9.7 ppm for a bed of 0.354 mm diameter sand particles at a temperature of 900°C , combustion taking place with 10% excess gas.

4.2 The Experimental Programme

4.2.1 Instrumentation

For the determination of the essentially fluctuating radiative flux levels emitted from the bed surface it was desirable to use an instrument with a fast response time. As will be described in Chapter 5, the residence times of particles at the bed surface ranged from approximately 0.02 seconds to 0.1 seconds. Hence, an instrument response time considerably less than 0.02 seconds was required. Radiometers of the required response time are available utilizing a variety of detectors, e.g. uncooled thermistor bolometers or cooled Indium Antimonide detectors held in an evacuated chamber. The output signal from such instruments is essentially d.c. and in order to improve the amplification of the signal a mechanical chopper, positioned in front of the instrument viewing aperture, converts the radiative flux signal to a.c. A full description of such instruments appears in Smith, Jones and Chasmar^[47]. In addition such instruments are capable of wavelength dependant radiative flux investigations through the use of narrow band filters.

Unfortunately, the cost of such instruments became prohibitive and a radiation pyrometer manufactured by 'Land Pyrometers' was purchased for the study. A schematic diagram of this instrument in its operating position is shown in Figure 4.1b. The instrument utilizes a thermopile detector sensitive by virtue of the arsenic trisulphide protecting glass, to a wavelength range of 0.8 μm to 11 μm . Held in an evacuated chamber and with auxilliary electronics, the detector has a response time of 0.06 seconds to 98% of input signal. The distance of the lens from the thermopile was 6.325 in, the focal length of the lens being 5.007 in. The instrument field

of view varied with distance from the target, i.e. from 1.4 ins diameter at zero pyrometer to target distance, to 0.25 ins diameter at a target distance of 24 ins. The narrow field of view of 1/100 radian was an advantageous requirement enabling a study to be made of a small area of the bed surface at any one time. The pyrometer is essentially a temperature measuring device over the range of 300°C to 1 200°C, i.e. 0-5 volts signal output. The output is normally non-linear but a linearising circuit was used to simplify calibration. An emissivity control via an operation amplifier is a standard addition on this instrument providing for a range of target emissivity of between 0.5 and 1.0. Its normal use is when the target emissivity is known, which is not the case in a fluidized bed. On the contrary, it is this 'effective emissivity' as described in Chapter 1 that is to be determined, being equivalent to the non-dimensional radiative flux analysis of Appendix B. Hence it is necessary to consider the operation of a radiation pyrometer for use as an 'effective emissivity' measuring device. Such an analysis is confined to Appendix F, and simply defines $\epsilon_e = T_{\text{pyrometer}}^4 / T_{\text{target}}^4$ with $T_{\text{target}} = T_{\text{bed}}$ in this case. The instrument emissivity control was maintained at a value of 1.

Because of the fluctuating nature of the input/output signal the temperature levels from the pyrometer were monitored on an Ultra Violet recorder using a galvanometer having a natural frequency of 160 Hz. For matching of the high impedance pyrometer with the low impedance U.V. recorder, the network of Figure 3.9 was again utilized. To improve the accuracy of this measuring

system the pyrometer output signal was amplified. To achieve this the pyrometer was operated over small voltage ranges, i.e. a 1.8 volt change giving full scale deflection of the galvanometer, by offsetting the general voltage level via a series connected battery and only allowing the variable signal through to the U.V.R. In this way the variable signal was amplified without recourse to a d.c. amplifier. The output U.V.R. trace was then calibrated by simply imposing a known voltage to the pyrometer input circuit. This was a technique provided for by the instrument manufacturer along with calibration of the pyrometer against a black body source.

4.2.2 Experimental Procedure

The experimental configuration was as shown in Figure 4.1a,b. With the bed surface exposed to atmosphere, large temperature gradients occur at the free surface, described in Chapter 3.4 and as a consequence, these have to be minimised in order to apply the isothermal analysis of Appendix B. To achieve a near isothermal condition, the radiative losses from the bed surface were reduced using a 1 inch thick ceramic plate placed above the reactor. In the plate was cut a 15 mm wide slot extending over half the plate width. The bed was then viewed by the pyrometer through this slot. In this configuration there is a possibility that the bed and top surface will provide a hohlraum condition, i.e. the pyrometer would view a black body. However, a condition of a hohlraum is that all surfaces of the enclosure remain isothermal irrespective of surface emissivity, otherwise the second

law of thermodynamics would be contravened. To check this possibility the inside surface of the top ceramic plate was continuously monitored, always remaining some 200°K-300°K below the temperature of the bed. This bed temperature was measured by a bare CrAL thermocouple located deep in the bed at the position of maximum temperature. A check on the isothermal nature of the bed was carried out by comparing the radiation pyrometer output signal with and without the top ceramic plate in position. Typical U.V. recorder traces are shown in Figure 4.2 showing clearly, for the case of an isothermal bed, the signal to noise ratio of order unity. With this experimental configuration using a 143 mm dia x 100 mm deep mild steel reactor, a number of experiments were carried out for variable fluidizing conditions and different particle materials sieved in narrow size ranges of 0.31 - 0.42 mm, 0.5 - 0.6 mm and 0.71 - 0.82 mm. Geometric means of the particle size ranges were then obtained. A photograph of the overall experimental rig is given in Figure 4.1a.

4.3 Discussion of Results

An initial study of the horizontal variations to check for any localised characteristics of emitted flux were determined by traversing the bed in the horizontal plane across the field of view of the pyrometer. The results indicated only significant variations near the wall of the reactor where cooler particles of longer average residence times reside. The invariant nature of the results are taken also to be an indication of even fluidization over the bed surface. Following this, a further study was carried

out to determine the effect on emitted flux levels of a variation in bed height. As the object was to study shallow beds, the flux levels were measured for a number of heights up to 50 mm. The results are given in Figure 4.3 in terms of the standard deviation of temperature fluctuations obtained from the U.V. traces for various bed heights and temperatures. The differences of standard deviation did not present significant variations in mean temperature, and subsequently a bed height of $H_{mf} = 25$ mm (measured at ambient temperature) was used throughout.

Using the experimental conditions previously described, results of surface temperatures ($T_{\text{pyrometer}}$) were determined for both an isothermal (ϵ_{ei}) and a non-isothermal (ϵ_{en}) (top ceramic plate removed) bed. The mean surface temperatures along with the standard deviations obtained from the recorded U.V.R. traces were determined from up to 100 values of temperature taken at small intervals over a 150 mm length of paper trace. With $\epsilon_e = T_{\text{pyrometer}}^4 / T_{\text{bed}}^4$, results for the variable material and fluidizing parameters are given in Figure 4.4 through Figure 4.11. The theoretical curves for ϵ_{ei} and ϵ_{en} shown also in Figure 4.4 through Figure 4.11 are derived using the analysis of Appendix B and Appendix D. These theoretical predictions are dependant upon appropriate values of particle emissivity ϵ_p . In the case of an isothermal bed, values of ϵ_{ei} may be read directly from Figure 2.2 for an appropriate range of albedo values. In the case of a non-isothermal bed, values of ϵ_{en} were obtained from Appendix D after making due allowance for the surface temperature gradients using the appropriate curves reported in Figure 3.23 through Figure 3.25.

The measured mean surface temperatures obtained from the U.V.R. traces for an isothermal bed resulted in insignificant values of standard deviation. However, for a non-isothermal bed these values of standard deviation increased appreciably. A typical value of standard deviation equal to 14 K for the case of 0.55 mm sand particles at a bed temperature of 1 000°C and a $(U-U_{mf})$ value of 338.6 mm/s was recorded.

4.3.1 Experimental Observations

Referring to Figure 4.4 through Figure 4.11 it was observed that at low values of $(U-U_{mf})$, approximately 150 mm/s, the value of effective emissivity ϵ_e reduced particularly when the top plate above the bed was removed. This fact is most probably due to poor particle mixing and particle turn-over, both at the surface and deep within the bed. This results in particles residing far longer than normal at the bed surface. Being exposed to atmosphere, significant cooling by radiation ensues. Increasing the value of $(U-U_{mf})$ tended to improve the particle mixing and particle turn-over rate at the bed surface resulting in an initial increase and final levelling out of the effective emissivity values. Also, an increase in gas/air velocity would tend to expand the bed as a whole. An observation was that combustion within the bed improved whereas in the somewhat 'slumped' state of the bed at low gas/air velocities, combustion appeared unstable with an increase in the emitted noise level. At relatively high values of $(U-U_{mf}) \sim 450$ mm/s a tendency for the effective emissivity values to fall was observed. However, the trend was far from consistent and no further conclusions

may be drawn.

As expected, the effective emissivity or non-dimensional flux varied considerably from unity being strongly dependant on particle emissivity. Comparison of the experimental points with the theoretical predictions is complicated by the fact that at this stage theory does not allow for any variation of ϵ_e with change of excess gas velocity ($U-U_{mf}$).

For the case of sand and alumina particles the experimental points of Figure 4.4 through Figure 4.7 for high $U-U_{mf}$ values fall reasonably close to the predicted values for the isothermal bed. Theory tends to overpredict experiment by up to 6% for bed temperatures exceeding about 900°C but underpredict for less than 900°C. Similar trends were observed also for magnesia particles whereas for silicon carbide particles excellent agreement with theory was obtained.

With the bed surface open to atmosphere and due allowance made in the predictions for the surface temperature gradients present, using the curves of Figure 3.23 through Figure 3.25, comparison with experiment was generally poor. Such discrepancies are understandable considering the method by which the surface temperature gradients were obtained and the uncertainties associated with the resulting profiles. For an optically dense medium the surface emitted flux tends to follow the proportionality $q_T(o) \propto \theta^4(o)$. Hence any small error in determining the surface temperature will be amplified by raising this surface temperature up to the power four. Such experiments confirm the inadequacy of the method used for the temperature gradient measurements described

in Chapter 3.

A comparison of the predictions for an isothermal bed with the essentially non-isothermal emulsion overpredicts by up to 50%.

As will be shown in Chapter 5, the response time of the radiation pyrometer is of the same order as the residence time of the surface ejected bubbles. Hence the results of ϵ_e which are strictly fluctuating may be significantly damped because of this time lag between physical occurrence and subsequent measurement. Ideally, a fast response instrument is required with a small field of view to follow the instantaneous evolution of radiative flux from single isolated bursting bubbles. However, the discrepancies between theory and experiment are still too large to be accounted for by the time lag of the measuring instrument. It is evident that considerable surface eruption interaction takes place with increased particle residence times at the bed surface resulting in significant surface temperature gradients.

Only three particle sizes were used although covering a reasonable size range. In all experiments no obvious effect on the results of varying particle size was observed.

With the reported discrepancies between prediction and experiment the results, at this stage, are useful to a thermal designer only in an empirical sense. For convenience the results may be reported by taking mean values at high $U-U_{mf}$ values. From such results particle emissivity may then be predicted for comparison with Table 3.4. Such mean values of ϵ_{ei} are reported in Table 4.1.

TABLE 4.1

	Silica Sand	Silicon Carbide	Alumina	Magnesia
ϵ_{ei}	0.82	0.92	0.67	0.76
ϵ_p	0.54	0.76	0.31	0.43

Experimentally, it was further observed that the effective emissivity changed significantly as the bed temperature was lowered. At bed temperatures less than 850°C the value of ϵ_e began to increase from the values observed at higher bed temperatures. For relatively high values of $(U-U_{mf})$ this fact was most prominent and reported in Figure 4.4 and Figure 4.8 for all particle materials at bed temperatures of 825°C. To check this observation further experiments were carried out using a high value of $(U-U_{mf}) = 340$ mm/s for both isothermal and non-isothermal bed conditions. Varying the bed temperature the previous observations were supported and the results recorded in Figure 4.12 and plotted as in [7] as a radiative flux (rather than effective emissivity) against bed temperature. The cross-hatched area encompasses the experimental results of [7] in which a similar deviation away from the absolute black body curve with increases in bed temperature was reported. The comparison is one in principle only and is not strictly valid as in the experiments of [7] a radiometer probe was immersed into the bed. In this case other factors should be considered, particularly the cooling of the particles in contact with the radiometer protecting glass which, as a consequence, would reduce the recorded

flux levels.

In a discussion of the work reported in [7] a recent paper, [5], quoted a table of particle emissivities and effective (measured) bed emissivities for the bed materials used in [7]. It was suggested in [5] that the radiometer quartz protection glass used in [7] was not cooled to the levels anticipated, i.e. 100°C-200°C, and in most cases would approach the temperature of the bulk of the bed. Hence it is fair to assume an almost isothermal emulsion radiating through a glass wall. Below in Table 4.2. are given the particle and effective emissivities taken from [5] via [7]. For comparison, values of ω_o were calculated from the reported values of ϵ_p and values of ϵ_e then predicted from Figure 2.3. A comparison between ϵ_e from this study and $\epsilon_e^{[5]}$ from [5] are extremely close, shown by the percentage difference column of Table 4.2. Hence with an accurate knowledge of particle material emissivity and isothermal conditions prevailing, emitted radiative flux levels may be simply predicted with reasonable accuracy.

Theoretically, according to the analysis of Chapter 2, the curves of radiative flux against bed temperature remain parallel to the absolute curve for a black body. The trend away from this parallelism shown in the experimental points of Figure 4.12 being due to the fact that at bed temperatures below 850°C, combustion within the bed was not complete and occurred in the gas bubbles at or near the bed surface. This fact was noted in the surface temperature profile measurements of Chapter 3.3 resulting in higher local particle temperatures than were measured deep within the bed. This fact was further observed in the work

TABLE 4.2. Taken from [5] and [7]

BED MATERIAL	Dp mm	U/U _{mf}	Tb °C	ϵ_p	ϵ_e [5]	ω_o	ϵ_e	$\frac{\epsilon_e - \epsilon_e^{[5]}}{\epsilon_e^{[5]}} \%$
River Sand	1 - 1.5	1.2 - 3.0	500 - 1 100	0.6	0.85	0.58	0.85	0
Chamotte	1 - 1.5	1.2 - 3.0	450 - 1 100	0.6	0.8	0.58	0.85	+6.25
Zirconium Dioxide	0.25 - 1	1.2 - 4.0	600 - 1 150	0.23	0.59	0.88	0.57	-3.38
Corundum (Alumina)	1.5 - 2	1.2 - 3.0	800 - 1 450	0.27	0.59	0.85	0.63	+6.78

of Sadilov and Baskakov^[48] in an attempt to determine the temperature of the gas within the bubbles bursting at the bed surface. From the results of [48] this gas bubble temperature was up to 900 K higher for a bed of 0.32 mm diameter alumina particles at a gas velocity of 0.3 m/s than the measured bed temperature of 800°C. As the bed temperature was increased this temperature difference reduced rapidly to almost zero at a bed temperature of 1100°C. For this reason only experimental results in beds above 900°C are regarded as being representative.

It is interesting at this point to compare the results of this study with those of Szekely and Fisher^[71] who reported a study of bed to wall radiation heat transfer in which a fluidized bed of particles was heated by a radiant heater at 650 K through the glass walls of the bed. From strategically positioned thermocouples a heat balance was established over the whole system and heat transfer coefficients were determined. The theoretical analysis considered the radiative heat transfer to a single particle and after certain simplifying assumptions a simple relationship of

$$Q_r = F \sigma \pi D_p^2 (T_s^4 - T_p^4) \quad (4.1)$$

was reported, with

T_s = heater temperature

T_p = particle temperature

Included in F is the emissivity of the particulate material along with the view factor between a triangular array of particles and a plane surface. In all cases the predicted values of radiative

flux underestimated the experimental values of Q_R by a factor of about 1.5. As noted in [71] the simple analysis did not take account of reflection or reradiation from adjacent particles or for any additional heat absorbed by subsequent layers of particles. For this purpose the problem should be described by the exact integro-differential equations.

To this end, using the experimental conditions reported in [71], values of Q_R were predicted using the analysis of Appendix B and C; the calculated values are reported in Table 4.3 along with the predicted and experimental results from [71]. In this analysis with the bed heated through the transparent walls by an externally radiating source, the boundary conditions from [71] were $\theta_1^4 = 9.222$ with $T_1 = 650$ K and $T_b = 373$ K.

TABLE 4.3

	Silicon Carbide	Porous Alumina	Iron Shot	
ϵ_p	0.94	0.9	0.6	} From [71]
Predicted Q_R watts	~95	~90	~110	
Experimental Q_R watts	~160	~140	~135	} Present Study
ω_o	0.12	0.18	0.58	
Predicted Q_R watts	124.7	109.4	65.2	

where $Q_R = q_R \pi DL$

$D = 0.061$ m

$L = 0.067$ m

From Table 4.3 a significant increase in the predicted values of Q_T are observed for Silicon Carbide and Alumina using the present analysis. However, the discrepancy is still too large to be attributed to experimental error. For the case of iron shot particles the present analysis predicts results even smaller than those predicted in [71]. Unfortunately, no details are given in [71] of the source of particle emissivity determination. It is possible in the case of iron shot that the value of ϵ_p is much larger than 0.6. Interestingly with $\epsilon_p = \text{unity}$, theory predicts $Q_T = 138.5$ watts.

With the unacceptably large discrepancy between prediction and experiment, it would be useful to repeat similar experiments and qualify the results reported in [71].

4.3.2 Directional and Hemispherical Effective Emissivities

Both experimentally and theoretically according to the analysis of Chapter 2, the reported values of emulsion effective emissivity are, by definition, hemispherical. Functionally, the directional emissivity of any emitter is defined as

$$\epsilon_{ed} = \epsilon_{ed}(\theta, \tau_o, \omega_o)$$

In the analysis of Appendix B the radiative flux, and hence effective emissivity, is assumed to be invariant with respect to angle θ , where θ is measured from the normal to the emulsion surface shown in Figure 4.1. Through subsequent integration, the effective emissivity becomes

$$\epsilon_e = \epsilon_e(\tau_o, \omega_o) = \epsilon_{eh}$$

In the work of [18] the directional effect of emissivity was shown to deviate from Lambert's Cosine Law, significantly at large values of angle θ , particularly in media of a low optical thickness. This variation was shown to be less marked for optically dense media. In the work of [7] where a radiometer was immersed in the bed, Lambert's Law was assumed to hold but not strictly justified. To check the angular variation of effective emissivity in the case of a fluidized bed where an optical measuring instrument with a narrow field of view was used, an experimental programme was carried out.

The radiation pyrometer supported on a simple traversing mechanism was moved along a hemispherical path above the bed. Using a 143 mm diameter x 50 mm high mild steel reactor, the pyrometer viewed the bed surface to within 10° of the horizontal plane through a 15 mm wide x 20 mm high slot cut into the side of the bed. During operation a few particles were ejected through this slot but this did not produce any detrimental effects. Using the same bed materials as in previous experiments, and for similar fluidizing conditions, results of effective emissivity were obtained with and without the top ceramic plate in position. The results are shown in Figure 4.13 through Figure 4.20. The deviation from Lambert's Cosine Law is small as suggested in [18] and confirms the earlier assumption of this work that hemispherical emissivity may be used throughout with the introduction of only a small error.

Strictly, for comparison with experiment, a two-dimensional analysis of the surface emitted fluxes should be conducted, a similar study of which was carried out in the work of Bobco^[50].

However, in the interest of simplicity and to a first approximation, an analysis of the angular variation of emitted flux was taken from [18]. This analysis was essentially a modified diffusion approximation to the radiative transfer equation.

The comparison of experiment and prediction was expectedly poor in some cases. The important trend away from Lambert's Cosine Law was sustained, though not of a sufficiently significant level to invalidate the assumption made previously of ϵ_{ed} invariant with angle θ .

4.4 Further Studies of a Bed Composed of a Binary Mixture

The previous experiments were idealized in that particles of a very narrow size range were used. Industrial applications of fluidized bed heat exchangers normally use particulate material comprising a large size range. As an extreme of this condition, the effect on emitted radiative flux levels in beds of binary mixtures were studied. When using a binary mixture segregation of the bed occurs. Segregation, according to the work of Cheung, Nienow and Rowe^[51] and of Gibilaro and Rowe^[52], depends largely upon the density ratio of the particles using and to a lesser degree upon the diameter ratio of the particles. In this work only the particle diameter ratio effects are considered as in heat exchangers it is unlikely that particles of different type (density) are used.

4.4.1 Experimental Observations

The experimental configuration and method of radiative flux

measurement has been described earlier in this Chapter and need not be elaborated here. The results of two such experiments for a non-isothermal bed using Silica Sand and Silicon Carbide are reported in Figure 4.21 for a range of percentage fines content.

On start-up the bed segregated readily with combustion taking place in the fluidized upper portion of the bed made up of fines with the lower portion of large particles remaining unfluidized. As the temperature of the lower portion rose above 750°C this also became fluidized. The two segregated regions then became increasingly mixed as the temperature of the lower portion increased further. With combustion taking place deep within the lower portion, at a temperature 950°C for sand particles and 935°C for Silicon Carbide particles, a number of effective emissivity results were observed for a range of $(U-U_{mf})$ values. The values of minimum fluidizing velocity for the mixture were derived from the correlation of [51] as $U_{mf\text{ mix}} = (U_{mfL}/U_{mfS})^{a_L} U_{mfS}$, with subscript L and S referring to Large and small particles respectively. The term a_L is the fraction of large particles present, i.e. $a_L + a_S = 1$. In a segregated bed the above correlation does not hold except perhaps in the interface between the upper and lower portions. For a low percentage fines content, mixing at the interface of the upper and lower portions was significant although a major proportion of the fines remained virtually suspended above the bed surface.

As suspected, the measured results of effective emissivity showed a marked drop of order 5% compared with the previous results for a narrow particle size range. The suspended fines, having

extremely long residence times at the bed surface, were cooled significantly by radiation to atmosphere and also acted as an attenuator of the radiative fluxes emitted by the lower portion of large particles. Similar trends to those experienced on beds of a narrow particle size range were observed for increasing $(U-U_{mf})$ values, i.e. a sharp increase in effective emissivity with a final levelling off. However, as the percentage fines content was increased, different results were observed at low $(U-U_{mf})$ values. With more fines added a sufficient volume of small particles encouraged combustion to take place in the upper portion of the bed and at the interface. This was verified by traversing a thermocouple through the total height of the bed and noting the point of maximum temperature. At low $(U-U_{mf})$ values with combustion taking place near to the bed surface, the lower portion became defluidized (similar to start-up conditions). Hence the upper portion acted as a single bed with a high turn-over rate of small particles thereby producing higher emitted radiative flux levels. Increasing $(U-U_{mf})$ encouraged a shift downwards of the combustion zone, this once more fluidizing the lower portion, improving the mixing of the two regimes near the bed surface. With small particles thus virtually suspended the radiative flux levels were reduced. These results were general for both silica sand and silicon carbide, although for silicon carbide the shift of the combustion zone to the lower portion occurred at a lower percentage fines content than for silica sand.

The experiments were not continued further. Nevertheless, they demonstrate that in an industrial design of a thermal heat

exchanger where large particle size ranges are to be used, the effect of segregation may have a significant effect upon the expected radiative flux levels emitted from the bed surface.

4.5 Application of the Analysis to Irradiation of a Remote Surface by a Fluidized Emulsion

The analysis so far has been concerned with the determination of the surface emergent radiative flux levels from a fluidized bed. Of interest to the thermal designer is the irradiation of a surface, remote from the bed, but nevertheless exchanging radiative energy with the bed. The solution of the radiative transfer equation has by nature transformed the problem of radiation from a volume emitter to one of transfer from an effective surface, i.e. with a corresponding value of effective emissivity. Hence irradiation of a remote surface is reduced to a geometrical problem when the appropriate emissivity and temperature of the remote surface are included in the solution of the radiative transfer equation. The analysis becomes essentially that of radiative transfer between opaque surfaces involving a determination of the relevant view factor.

4.6 Conclusions and Suggestions for Further Study

Radiative flux levels from the free surface of a fluidized bed have been obtained both theoretically and experimentally with the assumption of steady state heat transfer made throughout. An important parameter is the particle material emissivity and, due to the range of values reported in the literature, may be a source

of large discrepancy between predicted and experimental results. However, values of particle emissivity reported in Chapter 3 produce a reasonable comparison between theoretical and experimental values of emulsion effective emissivity for a closely controlled study of an isothermal bed surface. The variations of particle emissivity with the range of temperatures used in this work do not appear to be large (from Chapter 3) and hence the assumption of invariance in this study is not expected to be a major source of error.

Further studies on beds radiating to atmosphere showed how the complex, time-dependent, surface temperature gradients considerably reduced the emitted fluxes compared with the controlled isothermal case.

An attempt has been made to estimate these temperature profiles using a shielded thermocouple probe reported in Chapter 3. Unfortunately, such a method leads to large uncertainties as to the accuracy of the resulting profiles which on substitution into the theoretical analysis show considerable discrepancy with experiment emphasizing the emitted flux dependence upon the type of remote boundary present. With the emitted fluxes being proportional to the surface temperature raised to the fourth power of any optically dense medium, then the accurate determination of this surface temperature is essential.

Further experiments studying the hemispherical variation of the surface emitted flux show a deviation from Lambert's Cosine Law. Although such variations occur over a small lower portion of the hemisphere, they are not considered significant in this study

of an emulsion with $\tau_0 \gg 1$.

As industrial designers are concerned with beds of a large particle size range a few experiments were conducted to show the effect on surface emitted flux levels from binary mixtures. Although such experiments are somewhat ideal, they do show interesting trends which should be further studied for a variety of mixture types and fluidizing conditions. However, as many fundamental problem areas still remain, this line of approach was not continued.

Theoretically, the study has established that radiative flux determination from a volume emitter may be recast as an effective surface emitter, the transfer from which depends only upon the geometry (view factor) between the relevant surfaces and the thermal gradients present at the bed surface.

So far the analysis has been verified experimentally only under controlled laboratory conditions where the surface temperature gradients have been significantly reduced and isothermal conditions maintained throughout the bed. In order to predict the emitted flux levels for a variety of remote boundary conditions further study is required on the behaviour of the bubbling surface and its effect upon the emitted fluxes.

The assumption of a steady state process maintained throughout this study is an over-simplification of the real conditions, and a study of the fluctuating nature both thermally and hydrodynamically of single isolated erupting bubbles is desired to eliminate any surface interactions.

CHAPTER 5

A STUDY OF THE BEHAVIOUR OF A FREELY BUBBLING FLUIDIZED
BED SURFACE

5.1 Introduction

Before proceeding to an unsteady analysis of radiative transfer, a study of the behaviour of particles at the bed surface is necessary. Any study of the surface is complicated by the apparent non-periodic nature of bubbling. However, according to the hypothesis of [45], the observed periodic nature of bubble nucleation just above the distributor plate gives rise to similar pressure fluctuations measured at this position. To a first approximation it may be considered that these periodic fluctuations are due to a subsequent periodic bursting of bubbles at the bed surface. Following this initial premise, a simple model of bubble and particle motion may be derived which enables representative, if not exact, results to be obtained. From the point of view of radiative heat transfer at the freely bubbling surface, such an energy exchange is rendered unsteady not by the direct variation of radiative intensity (as this term in the radiative transfer equation is multiplied by the reciprocal of the velocity of light, i.e.

$$\frac{1}{c} \frac{dI}{dt}),$$

but directly by the radiation cooling of the particles subject to a residence time of exposure. Hence a first consideration in the study of surface behaviour is to establish a residence time, or residence time distribution of particles ejected by bursting bubbles.

It was shown earlier in Chapter 3 that on a time average basis temperature gradients extended deep into the bed to optical depths of order 10. Consideration of the temperature fluctuations at the surface suggests two alternatives. First, of all a model of an isothermal packet of emulsion brought to the surface at zero time and exposed thereby producing a temperature distribution for all times greater than zero may be assumed. Alternatively, as there may be a significant time lapse between one bubble arriving at the surface ejecting a packet of particles, and the next bubble plus ejected packet, the subsequently exposed surface would cool by radiation. A temperature distribution would be imposed at the surface which in the model suggests that at zero time the emulsion packet is not isothermal. Of course in a freely bubbling bed as distinct from a single isolated bursting bubble, considerable bubble interaction and lateral particle mixing takes place. Thus neither of the two alternatives would strictly hold, although the second one appears closer to reality.

One important assumption inherent in the two suggestions is that particles ejected into the free board above the bed originate from or near to the bed surface. From extensive studies of bubbles in fluidized beds reported in [31], it appears that particles ejected into the free board may well originate at the bed surface. However, these may also be augmented by a proportion of particles brought from deep within the bed, carried in the wake of the bubble. Again the observations reported in [31] confirm that considerable particle mixing takes place within the bubble wake as the bubble passes through the bed. If this is the case, then particles ejected

in this manner into the free board would be considerably hotter than particles ejected from the surface, given their momentum by the diffusion of gas from the bubble as it reaches the surface. It is a point of conjecture whether or not bubbles occur at all in shallow fluidized beds which for the purposes of this study are defined as beds in which bubbles may grow but do not have sufficient time to coalesce. Again referring to the work of [45] and from the observations of shallow bed pressure drops reported in Chapter 3, it is quite feasible to imagine bubbles originating at, or a few particle diameters below, the bed surface. This is particularly so when the overall bed height approaches $10 D_p$. So in any study of the behaviour of a freely bubbling bed surface the above postulations should be considered.

For the convenience of any initial study where a limited amount of work has been previously reported, the simplest approach is usually the most desirable. In this work the obvious starting point was to study the behaviour of single isolated bursting bubbles and build up a model to include further complexities if initial observations allow. To this end with a consideration of the previous postulations, a programme of experiments was conducted in which single bubbles were injected into an incipiently fluidized bed and the ensuing events recorded on film.

5.2 Particles Ejected by Single Isolated Bursting Bubbles

5.2.1 A Theoretical Model

An initial study of the appropriate equations of particle motion at the bed surface was made in the light of the work on

particle ejection and entrainment by Zenz and Weil^[55] and later by Do, Grace and Clift^[56]. In particular, the work of [56] postulated a simple model based on three simplifying assumption and it is this analysis that is used in this study. Assumptions:

- [1] Particles are ejected from the surface of the bed with an initial velocity V_i related to, but not necessarily the same as, the velocity of the bubble causing the particle ejection
- [2] The subsequent particle motion is determined by a balance between gravity and drag forces, with

$$C_D = \frac{24}{Re} (1 + 0.15 Re^{0.687}) + \left[\frac{0.42}{1 + 4.25 \times 10^4 Re^{-1.16}} \right] \quad (5.1)$$

- [3] The gas in the free board has a uniform superficial velocity, U .

The equation of motion may be written from a consideration of assumption [2]; i.e.

$$\frac{dV}{dt} = \frac{-3}{4} \frac{C_D \rho_g V_r |V_r|}{\rho_p D_p} - \frac{(\rho_p - \rho_g)g}{\rho_p} \quad (5.2)$$

where $V = dh/dt$ is positive in the upwards direction, and

$$V_r = V - U, \text{ and}$$

h is the height of the particle measured from its ejected position, i.e. the dome of the erupting bubble.

Equation (5.2) may be solved numerically with boundary conditions of $V = V_i$ and $h = 0$ at $t = 0$.

The above theoretical model is similar to that of [55] but allows for the more exact form of drag coefficient. [55] used the standard relationship of

$$C_D = \frac{37.5}{Re} \quad (5.3)$$

A computer program using a Kutta-Merson numerical integration procedure was written to solve equation (5.2) and checked with the reported results of [56] using their initial boundary and flow conditions. The predicted particle trajectory curves as a function of time are described in [56]. These curves suggest observations which may be expected from later experimental studies. It appears that large particles are generally projected higher for the same initial conditions and have longer residence times in the free board than smaller particles, although very fine particles may be immediately entrained and carried away if their terminal settling velocity is exceeded. Further predictions by [56] suggest that increasing the superficial gas velocity U increases the height and residence time of any size of particle. Also, that if particles return to the bed and are not entrained away, the maximum height of rise is strongly dependant on the initial ejection velocity V_i , with

$$\frac{h_{\max}}{D_p} = \rho \frac{D_p V_i}{\mu 28.125} \left[1 - \frac{1}{V} \log_e (1 + V) \right] \quad (5.4)$$

where $V = V_i / (V_t - U)$

V_t = terminal settling velocity.

5.2.2 Experimental Study

In the work of [56] an experimental programme was conducted to verify the previously described mathematical model. A 'two dimensional' fluidized bed was used, constructed from plexiglass sheet 560 mm wide x 10 mm thick x 2 440 mm high. Although not given in the report, it would appear that a deep bed of glass beads was used for the study. As this present work is concerned with shallow beds, i.e. less than 100 mm, it was necessary to repeat such experiments and compare the results with the analytical predictions. A similar 'two-dimensional' fluidized bed was constructed from perspex sheet 600 mm wide x 10 mm thick x 600 mm deep. Sand particles of three sizes, i.e. 0.354 mm, 0.55 mm and 0.777 mm (geometric means) were used. The depth of particles within the bed was maintained at 65 mm, measured at minimum fluidization conditions, throughout the experiments. A schematic diagram is shown in Figure 5.1 describing the lighting arrangement similar to that employed in [56] for purposes of a photographic study of the bubble rise and subsequent bursting at the bed surface. Intense rear lighting of the bed enabled the two dimensional bubbles to be seen clearly. Above the bed a black matt screen (cardboard) was used with front illumination to allow sufficient contrast for particles ejected into the free board to be seen. The horizontal screen at the front of the bed was designed to allow illumination of ejected particles and prevent front illumination of the lower portion of the bed. The superficial gas velocity was set at $1 - 1.2 U_{mf}$ for the particles used, the incoming air bubbled through a humidifier to minimise any

electrostatic effects.

With a solenoid valve controlled by a rotating cam, a series of bubbles were ejected through a 1 mm diameter bore stainless steel tube, positioned at 10 mm above the distributor plate. The frequency of bubble generation was simply controlled by changing the speed of rotation of the cam. The bubble rise bursting at the bed surface, followed by particle ejection, was recorded for a number of experiments using an electrically driven 'Hycam' high speed camera operated at 200 frames per second. A pulse marker appeared on the film every 10 seconds as a check of frame speed. Sufficiently clear resolution of particles was obtained using a 75 mm telephoto lens. The velocity of bubbles and ejected particle trajectories were measured from a frame by frame analysis of the films.

Using the bubble nose as the point of reference, its mean rise velocity was obtained from a measurement of distance travelled divided by time of travel. The mean ejection velocity of particles at the surface of the bed was also obtained from the motion of the dome shaped surface disturbance as the bubble broke the surface. The determination of this velocity was made difficult by having to measure very short disturbance distances. However, use of the high speed camera and subsequent enlargement of each frame by an order 4.4 : 1 when viewed on a screen made it at least possible, although the measurements may be subject to a small error. The position with respect to time of the upper surface of the ejected cloud of particles was observed as the cloud rose and then returned to the bed surface.

5.3 Discussion of Results

As an example of the bubble rise and particle ejection, a sequence of photographs are shown in Figure 5.2. It was observed that on initial injection of a volume of gas into the bottom of the bed, an immediate disturbance was sensed at the bed surface shown in Figure 5.2a. Figure 5.2b and Figure 5.2c show clearly the rising bubble with its well defined wake. During examination of this bubble motion, the particles within the wake being interchanged with particles from the main emulsion could be clearly observed. Figure 5.2d shows the bubble approaching the bed surface. Clearly the bubble here reduces in size as gas from its interior diffuses rapidly through the small depth of emulsion of reduced resistance above it. Figure 5.2e and Figure 5.2f then describe the subsequent rise and fall of the ejected particulate cloud.

As observed in [56], the initial ejection velocity V_i of the particles exceeds the mean bubble rise velocity by typically 15%, whereas in this work it is between 15% and 25%. It appears that this extra velocity may be caused by the diffusion of gas from the bubble interior as the bubble breaks the surface supporting the evidence of Grace and Harrison^[57].

Predicted and observed particle cloud trajectories are described in Figure 5.4 through Figure 5.6 with $V_i = 1.25 U_b$ for the different cases studied. In all cases the comparisons are reasonable and justify the theoretical analysis in application to shallow fluidized beds for single isolated bubbles. Also shown in Figure 5.3 are the predicted cloud trajectories for high temperature conditions. The experimental results, although observed at ambient temperature,

compare favourably with the high temperature predicted curves. Such comparisons are reasonable as the only variables in the predicted results are gas properties with bubble velocity taken from ambient conditions. Although the gas viscosity increases by an order of two from 20°C to 1 000°C, the gas density reduces by an order of four.

In a freely bubbling shallow fluidized bed considerable interaction between bubbles at the surface along with lateral mixing of particles takes place. For this reason films were taken of a freely bubbling system and typically shown in Figure 5.3. The analysis of these films proved difficult and only a study of the local variations occurring at the surface were possible. It is highly unlikely that such local variations could be generalised to occur across the whole of the bed surface. However, such studies are interesting in that they show another extreme of surface disturbance particularly when two bubbles coalesce near the surface just before bubble eruption. As the shallow bed is considered for the purpose of this study to be one in which bubble coalescence within the bed does not have sufficient time to take place, only the occurrence of bubble coalescence at the surface was considered. The important observations were that the initial ejection velocity V_i is increased considerably by up to twice the measured bubble velocity, i.e. $V_i = 2U_b$. This effect was also reported by Botterill, George and Basford^[57] in a study of coalescing three dimensional bubbles. As the occurrence of bubble coalescence at the surface reduces as the bed height is reduced, the study of such phenomena was not pursued but is reported as an

observation which should receive further attention. As the bed heights used for purposes of radiative heat transfer were only up to 30 mm, it seems reasonable to assume that the initial analysis of single isolated bubbles may be applied to these beds.

Again from the point of view of radiation transfer an important observation was the origin of the particles within the ejected cloud. It appeared that for a single isolated bubble, the wake fraction of the bubbles did not burst through the bed surface as has been suggested by Basov *et al*^[58] and Kehoe^[59], but particles within the cloud originated at the bed surface. However in a freely bubbling bed where bubble coalescence near the bed surface took place the wake, through increased momentum due to the acceleration of the now larger bubble, did break the surface and spout to an appreciable height. Again this was an infrequent occurrence and to a first approximation was not considered. According to this observation it seems reasonable that at all times a temperature gradient exists at the bed surface, confirming the experiments of Chapter 3, and hence a purely isothermal assumption would overestimate the resulting radiative flux levels.

From the theoretical analysis the residence time of the projected cloud of particles is simply determined from the maximum time of cloud rise and fall.

5.3.1 Extension to a Three-Dimensional Bed

The studies have been concerned with an experimental study of a two-dimensional bed. Such beds are convenient for experimental study in that bubbles may be readily photographed from their

nucleation stage through to their bursting at the bed surface and subsequent collapse. For the more realistic case of a three-dimensional bubbling bed, Rowe, in the section on experimental properties of bubbles in [31] expressed doubt as to the great value of two-dimensional behaviour. Although this remains an area of uncertainty, it was assumed for the purpose of this study that the two-dimensional experimental verification of equation (5.2) applies to three-dimensional beds.

5.4 Conclusions

Using a simple analytical approach, the particle ejection heights and mean residence times may be predicted for single, isolated bursting bubbles. The analysis has been verified by experiment using a two-dimensional bed and it was assumed to represent the three-dimensional case. As beds of interest in this work are essentially shallow, the extra projected heights of particle clouds due to coalescence of bubbles at the bed surface are not considered. It appears that the majority of ejected particles constituting the particle cloud above the bed originate from the surface of the bed and hence it is reasonable to assume that large temperature gradients exist at all times within the cloud. It is expected that determination of the actual temperature gradient will be complicated by the lateral, unsteady mixing of particles within the cloud.

At elevated bed temperatures, using bubble velocities obtained at ambient conditions, the predicted cloud trajectories did not show any large variation over those predicted at room temperature.

However, in order to verify this fact it is desirable to determine bubble velocities in three-dimensional beds at elevated temperatures.

5.5 Determination of Bubble Velocity in a Three-Dimensional Bed

5.5.1 Introduction

Bubble velocities within three-dimensional beds are difficult to study and the work of Rowe and Everett^{[60],[61],[62]} have resorted to an elegant method using an x-ray technique. Less elegant methods have been used by Werther^[63] in which a miniature capacitance probe was immersed in beds of varying sizes. It was pointed out in [63] that the technique of photographing the bubbling surface of the bed and relating bubble eruption size to bubble velocity may lead to large errors, being restricted to studies at relatively low ($U-U_{mf}$) values. However, such a technique was used by Kassim^[64] in a study of the effects in deep beds of various types of distributor plate design. Unfortunately, at high bed temperature no other method appears forthcoming and hence experiments were conducted using shallow beds, i.e. up to 70 mm height measured at ambient temperatures.

5.5.2 Experimental Procedure for the Determination of Bubble Eruption Diameters

Filming of the bed surface was carried out using a highly reflecting plate placed above the bed and inclined at an angle of 45° to the bed surface. A schematic diagram of the experimental arrangement is shown in Figure 5.7. A Bolex Camera operated at

64 frames per second was used with 75 mm lens. A previous study of the bubble eruption diameters occurring in shallow fluidized beds at ambient temperatures of heights less than 70 mm is reported in McGrath and Streatfield^[65]. For comparison, initial experiments at ambient temperature used a square bed of dimensions 153 mm x 153 mm x 200 mm high, constructed from 4 mm thick perspex sheet. For a range of $(U-U_{mf})$ values using 0.15 mm sand particles, films were taken and bubble eruption diameters obtained from a frame by frame analysis. Only one particle size was used, the assumption being made from the two-phase theory of fluidization^[35] that the governing parameters are the physical and fluidization properties of solids and gas.

The experiments were repeated at a bed temperature of 900°C using a 143 mm diameter x 150 mm high mild steel reactor with 0.354 mm sand particles. With combustion taking place within the bed the 'red glow' of emitted light did not give sufficient contrast to clearly define individual bubbles. However, by shining an angled photoflood lamp on to the bed surface, the sand particles appeared a similar colour to the studies at ambient temperature. This technique made it possible to obtain bubble eruption diameters at a number of $(U-U_{mf})$ values although at relatively high superficial gas velocities film analysis became impossible.

5.5.3 Film Analysis and Discussion of Results

The films were projected on to a screen for analysis, producing a 4.4:1 enlargement. Bubble eruption diameters D_{be} were measured across the horizontal diameter. An alternative, and

perhaps more accurate method, was that of [64] in which the maximum and minimum diameter were measured and $D_{be} = \sqrt{D_{be \max} \cdot D_{be \min}}$. In this study the diameter D_{be} of each bubble over the bed surface was measured. In order to avoid measuring the same bubble at different stages of its rise and fall, only every fourth frame was analysed. The number of bubbles of a given size for each of over 50 frames were plotted on a bubble size distribution diagram. A typical diagram is given in Figure 5.8 emphasizing the 'bell-shaped' normal distribution curve. From such diagrams log-probability curves were drawn to determine the mean bubble eruption diameters at appropriate values of $(U - U_{mf})$. The probability co-ordinate was determined from a cumulative summation of all bubble eruption diameters. Such typical curves are reported in Figure 5.9 through Figure 5.12 for ambient bed temperatures and Figure 5.13 through Figure 5.16 for elevated bed temperatures. Mean bubble eruption diameters are then obtained from these curves corresponding to the 50% probability line.

It was observed in the previous studies of [64] and [65] of bubbles in two-dimensional beds that the bubble diameter was related to its eruption diameter by $D_{be} = \frac{3}{2} D_b$, where all diameters are now mean values. With this relationship, the bubble velocity within a three-dimensional bed may be determined from the simple equation of

$$U_b = U - U_{mf} + 0.711\sqrt{gD_b} \quad (5.5)$$

derived from the two-phase theory of fluidization of [35]. From

the results of mean D_b so obtained a plot of D_b (mean) against $H_{mf} \cdot (U - U_{mf})$ for the range of experiments studied is described in Figure 5.17. Curve ① was determined from experiments at ambient temperatures whereas curve ② was obtained at elevated temperatures of $900^\circ\text{C} \pm 20^\circ\text{K}$ using a least squares polynomial fit. Interestingly, the work of Kato and Wen^[65] for deep beds confirmed the relationship of

$$D_b = 1.4 \rho_p D_p \frac{U}{U_{mf}} H \quad (5.6)$$

This relationship compared with the experimental results observed in this study for shallow beds at ambient temperatures tended to underestimate D_b . In fact, comparison was improved to a maximum difference of 5% by changing the constant in equation (5.6) to 2.8. In the reported study of [65] bubble eruption diameters at ambient temperatures were plotted against excess gas velocity $(U - U_{mf})$ for a number of bed heights.

Comparison of the results of [65] with those of curve ① and equation (5.6) show considerable discrepancy. It was observed by [65] that appreciable bubbling occurred at minimum fluidizing velocities with reported eruption diameters of up to 50 mm. It is possible in such studies that due to distributor plate design local fluidization occurred at low superficial gas velocities rather than homogeneous fluidization. The possibility of local fluidization occurring in the present study was reduced by using a high pressure drop distributor plate. The occurrence of local fluidization in [65] was further supported by the reported curves of a number of

surface eruptions against excess gas velocity. For a shallow bed of height 13 mm, up to 45 surface eruptions were reported at minimum fluidizing conditions, rising to a maximum of 80 eruptions at $(U-U_{mf}) = 120$ mm/sec. Thereafter the number of eruptions fell linearly with further increase of excess gas velocity. However, as pointed out by [65] for particles less than 0.2 mm diameter the bubble velocity exceeds the superficial gas velocities and a large cloud occurs around such bubbles. Hence at the surface such bubbles disperse their cloud and give too high a figure for the measured eruption diameter. The method of eruption diameter determination in [65] was to fluidize the bed with a 1 mm thick layer of fine powdered alumina outlining the bursting bubble which was subsequently measured with a ruler. At high excess gas velocities the gas flow was shut off for bubble measurement. It is possible at such velocities, particularly in the deep beds, that considerable bubble coalescence occurred at the bed surface.

With such large discrepancies no comparisons were possible.

In the present study at elevated temperatures, no reasonable correlation of the form of equation (5.6) was observed. A convenient form of presentation was to obtain a polynomial plot, using a least squares curve fitting technique of D_b against $H_{mf}(U-U_{mf})$. This curve is only suitable for use within the range of H_{mf} and $U-U_{mf}$ values used in its determination, i.e. to values of $H_{mf}(U-U_{mf})$ of 10×10^3 mm²/s. However, from inspection the relationship appears to approach a maximum and may be reasonably extrapolated to values of $H_{mf}(U-U_{mf})$ of 20×10^3 mm²/s; thereafter large errors are introduced.

The asymptotic nature of curve (2) is reasonable as at elevated temperatures gas viscosity levels become appreciable and the seemingly linear relationship of curve (1) at ambient temperature does not hold. Also the indicated finite size of bubble diameter when $H_{mf} = 0$ is reasonable as, at the distributor plate, the bubble size approaches the size of the distributor plate holes. As described in [64], equation (5.6) should be modified to

$$D_b = D_{bd} + 1.4 \rho_p D_p \frac{U}{U_{mf}} H \quad (5.7)$$

where D_{bd} is related to the size of distributor plate holes. Curve (1) of Figure 5.17 should also be modified in a similar way.

5.6 Determination of the Surface Bubble Residence Time in Three-Dimensional Beds

With the analysis derived in Section 5.2, the mean bubble residence times may be obtained with the boundary condition of initial ejection velocity V_i related to bubble velocity as

$$V_i = 1.25 U_b \quad (5.8)$$

$$V_i = 1.25 \left[(U - U_{mf}) + 0.711 \sqrt{g D_p} \right] \quad (5.9)$$

Values of mean D_b are taken from the polynomial expression of $D_b = f(h_{mf}, U - U_{mf})$ described in Figure 5.17 and may be applied with $H_{mf}(U - U_{mf})$ not greater than $20 \times 10^3 \text{ mm}^2/\text{s}$.

Figure 5.18 describes the predicted particle cloud trajectories

of a freely bubbling bed of 0.354 mm silica sand particles operating at a $(U-U_{mf})$ value of 100 mm/s and a bed temperature of 1 000°C. The influence of bed height on the resulting trajectory profiles are as expected, i.e. with deeper beds D_b increases, V_i therefore increases and hence h_{max} increases along with residence time t_r . From the curves of Figure 5.18 the predicted particle cloud residence times were obtained and are reported in Figure 5.19 with residence time t_r defined as the time for the cloud to rise and subsequently return to the bed surface. Hence for any solid material and fluidizing conditions, the particle cloud residence times may be predicted in a similar manner.

The foregoing analysis has ignored the residence time distribution of individual particles, assuming to a first approximation that all particles reside for the same time. Such an extension of the work is not justified while the uncertainties introduced by the method of bubble velocity measurement remain.

5.7 Conclusions

Using an approximate technique a method of predicting mean residence times of surface erupted particle clouds has been established. Experimental mean bubble sizes are combined with the solutions of the equations of motion of surface ejected particle clouds. Being approximate in nature as the method is subject to experimental limitations, all that may be expected at this stage is a reasonable order of size of the mean cloud residence times. There are many areas in which further work or even a completely different approach are justified, particularly in bubble velocity

determination. The object of such a study is to enable an analytical solution of unsteady radiative heat transfer to proceed. As no previous studies are forthcoming, this chapter is regarded as a first step which has of necessity been kept as simple as possible. An unsteady solution although limited to varying degrees by the above-mentioned considerations is nevertheless approached and reported in the next chapters.

CHAPTER 6

TRANSIENT THERMAL RADIATION FROM HIGH TEMPERATURE
FLUIDIZED SOLIDS

6.1 Introduction

Transient thermal radiation heat transfer in generalized media which absorb, emit and scatter energy has been a subject of considerable interest in recent years. Viskanta and Bathla^[23] used the exact formulation to study the radiative heating and cooling of a plane layer of stagnant gas in which the scattering mode was neglected, i.e. $K_t = K_a$. Nemchinov^[66] used the two flux approximation to study the transient cooling by radiation of a semi-infinite volume of gas. A number of other solutions, Onufriev^[67], Adriankin^[68], along with Viskanta and Lall^[69] examined the problem for a spherical mass of gas. Recently, Prasad and Hering^[24] used the exact formulation to study the transient heating of a plane layer of non-scattering, grey medium between parallel black plates.

Particular interest in this work is in the radiative energy transfer from the freely bubbling surface of a fluidized bed of solids to a remote heat transfer surface for a number of different bed materials. In this configuration radiative transfer is the predominant mode of energy exchange and hence in the subsequent analysis the conduction and convection heat transfer modes are neglected. As in the steady state approach of Chapter 2 the time dependant problem studied here is essentially one of energy transfer from an optically thick medium (emulsion) in which the scattering of radiative energy may be significant. The exact formulation given in Appendix B is employed and a technique developed in

Appendix C is used along with a finite difference approximation of the energy equation.

6.2 Analysis

A plane parallel layer of a constant voidage absorbing, emitting and scattering medium (emulsion) is confined between uniform temperature, gray, diffusely emitting and reflecting boundaries shown in Figure B1 of Appendix B. From the analysis of Appendix B, the one dimensional energy equation may be written as

$$\frac{\partial \theta}{\partial t'} = - \frac{\partial q'_r}{\partial \tau} \quad (6.1)$$

as defined in Appendix G, where the equation of radiative flux q'_r is given by equation (B.10) of Appendix B. The model is of the emulsion and boundaries initially at the same temperature (isothermal) or with some known initial temperature distribution imposed on the emulsion. At time zero the emulsion is subject to a step change of temperature at one boundary (designated 1) in Figure 1.1, the other boundary (designated 2) held at a constant temperature throughout. Hence, fluxes are emitted in the negative x direction with reference to Figure 1.1 and Figure B1. Equation (6.1) is then subject to initial conditions of

$$t' = 0, \quad \theta(\tau, 0) = \begin{bmatrix} 1 \\ \theta(\tau) \end{bmatrix} \quad (6.2)$$

and boundary conditions of

$$\tau = 0, \quad \theta(0, t') = \theta_1, \quad t' > 0 \quad (6.3)$$

$$\tau = \tau_0, \quad \theta(\tau_0, t') = 1, \quad t' > 0 \quad (6.4)$$

along with the radiative boundary conditions of

$$F_1 = \epsilon_1 \theta_1^4 + 2(1 - \epsilon_1) \left[F_2 E_3(\tau_0) + \int_0^{\tau_0} [(1 - \omega_0) \theta^4(\tau, t') + \frac{\omega_0}{4} D(\tau', t')] E_2(\tau') d\tau' \right] \quad (6.5)$$

and

$$F_2 = \epsilon_2 \theta_2^4 + 2(1 - \epsilon_2) \left[F_1 E_3(\tau_0) + \int_0^{\tau_0} [(1 - \omega_0) \theta^4(\tau, t') + \frac{\omega_0}{4} D(\tau', t')] E_2(\tau_0 - \tau') d\tau' \right] \quad (6.6)$$

6.2.1 Numerical Method of Solution

The energy equation, being a partial, non-linear, integro-differential equation, is not amenable to a closed form solution in its present form. A numerical technique is used which has been previously described for the steady state solution in Appendix D so will not be repeated here. However, as the time dependant nature of the solution is now required, the extension of the numerical method to allow for this is described in Appendix G. Briefly, the solution is one of a finite difference approximation of the energy equation by computational means using the U.M.R.C.C. CDC7600/1906A installation. At each time interval a least squares polynomial curve fitting procedure is used to describe the temperature distribution. An independant check on this part of the program revealed agreement with its exact counterpart to the sixth significant figure

or less. The computer program developed for this analysis is reported in Appendix H. For the steady state solutions of Chapter 2, the same program was used but with the time dependant flux solution not included, i.e. simply the same as a solution at time zero.

6.3. Discussion of Results

An initial check of the computed results was made with the reported curves of the instantaneous time dependant radiative flux of [23]. Unfortunately, the reported analysis was only concerned with a zero scattering ($\omega_0 = 0$) medium and as no other solutions for $\omega_0 > 0$ are available to the author's knowledge, this single comparison will have to suffice. Figure 6.1 describes the comparison of the present solution with that of [23] for an initially isothermal emulsion, i.e. $\theta(\tau, 0) = 1$ a maximum difference of order 1.4% was observed in the flux predictions. Further solutions for $0 \leq \omega_0 \leq 1$ remained convergent and are assumed correct to a similar order of magnitude.

Surface radiative flux levels and temperature distributions were obtained for a number of scattering albedo values typical of fluidized solid materials and described in Figure 6.2 and Figure 6.3 for idealized boundary conditions. In all cases an optical thickness of $\tau_0 = 10$ is assumed as being representative of the depth of the emulsion over which the variation of temperature and flux may extend. In Figure 6.2 an important observation is the reduced cooling rate of the emulsion as the scattering albedo is increased from zero. This is reasonable as the albedo is a function of

particle emissivity and with a reduced particle emissivity the emulsion cannot emit or re-absorb energy at the same rate as a black body. However for large times, solutions converge irrespective of albedo value. This reduced cooling rate is reflected in the temperature distribution curves of Figure 6.3. Further solutions are reported in Figure 6.4 and Figure 6.5 showing the effects of varying the initial boundary temperature θ_1 and of the boundary emissivity ϵ_1 on an initially isothermal emulsion $\theta(\tau,0) = 1$. As may be expected an increase in the free boundary temperature θ_1 reduces the initial overall radiative flux exchange. The emulsion then cools from this initial level but at a reduced rate. Similar effects are observed as the free boundary emissivity ϵ_1 is reduced from a value of unity. For low values of ϵ_1 energy in the vicinity of the boundary is reflected back to the emulsion where it is re-absorbed thus reducing the cooling rate. For values of ϵ_1 approaching 0.5 with the reduced cooling rate, the change with time of temperature distribution was exceedingly small and this set a limit on the accuracy of the numerical solution. In fact, the solution began to diverge for these low values of ϵ_1 , the recommended range of applications being $0.6 \leq \epsilon_1 \leq 1$. The term appearing in the non-dimensional time, i.e. $\rho C_p(1 - \epsilon_b)/K_t \sigma T_b^3$, characterises the time to radiate the entire energy of the volume of emulsion at a temperature T_b . Solutions were obtained by this method up to non-dimensional times of 0.1 after which actual computing time became prohibitive. For completeness an approximate approach applicable for long time solutions, i.e. for $t' \gg 1$ was employed, the dashed lines of Figure 6.2 and Figure 6.3 drawn joining the two solutions.

Using the optically thick approximation, i.e. $\tau_0 \rightarrow \infty$ described elsewhere [9] and [26], the energy equation becomes

$$\frac{\partial \theta}{\partial t'} = \frac{16}{3} \frac{\partial^2 \theta}{\partial \tau^2} \quad (6.7)$$

subject to boundary conditions of

$$\tau = 0, \quad \theta = \theta_1 + \left[\frac{1}{\epsilon_1} - \frac{1}{2} \right] \frac{16}{3} \frac{\partial \theta}{\partial \tau}, \quad t' > 0 \quad (6.8)$$

$$\tau \rightarrow \infty, \quad \theta = 1, \quad t' > 0 \quad (6.9)$$

and an initial condition of

$$t' = 0, \quad \theta = 1, \quad \tau > 0 \quad (6.10)$$

An analytical solution may be obtained from Carslaw and Jaeger^[70] page 71, as

$$\theta(\tau, t') = \operatorname{erf} \frac{\tau}{8\sqrt{\frac{3}{t'}}} + \exp \left[\frac{3\tau}{16 \left[\frac{1}{\epsilon_1} - \frac{1}{2} \right]} + \frac{3}{16} \frac{t'}{\left[\frac{1}{\epsilon_1} - \frac{1}{2} \right]^2} \right] \operatorname{erfc} \left[\frac{\tau}{8\sqrt{\frac{3}{t'}}} + \frac{3}{4} \left[\frac{1}{\epsilon_1} - \frac{1}{2} \right] \sqrt{\frac{t'}{3}} \right] \quad (6.11)$$

where

$$\theta(\tau, t') = \frac{T(\tau, t') - T_1}{T_b - T_1} \quad (6.12)$$

and

$$q'_R(0, t') = \frac{1}{4} \frac{\theta(0, t') (\theta_1^4 - 1)}{\left[\frac{1}{\epsilon_1} - \frac{1}{2} \right]} \quad (6.13)$$

which may be readily solved. Equation (6.11) is only applicable for a long time solution as the optically thick approximation does not hold in the vicinity of any boundary (space or time). As predicted by equation (6.11) all solutions converge after a sufficient time lapse irrespective of scattering albedo or of initial boundary conditions. As qualified later, such long time solutions constitute what is essentially an academic exercise as only short time solutions are applicable to the freely bubbling surface.

6.4 Comparison with Experimental Observations.

Experimental determination of the surface emitted radiative fluxes have already been described in Chapter 4. The results, due to the limitations of the radiation pyrometer, were essentially time average measurements. In order to compare predictions from the time solution with the experimental results it is necessary to consider the residence time and residence time distribution of the ejected particle clouds. A simplification appearing in the approach of this problem described in Chapter 5 is to assume a uniform residence time distribution of the ejected cloud. Hence on a time average basis, the emitted radiative fluxes may be described by the equation

$$q_{rm}(0, t_m) = \frac{1}{t_m} \int_0^{t_m} q_R(0, t) dt \quad (6.14)$$

where $q_r(0,t)$ is the instantaneous radiative flux. The results of this approach are described in Figure 6.6 for the different bed materials used in this study. Figure 6.6a describes the time variation of instantaneous radiative flux with the uniform initial temperature distribution shown in the inset, and Figure 6.6b describes the time mean variation of the flux obtained by use of equation (6.12). Such curves were plotted only to a maximum non-dimensional time (t') of 0.1. From an initial consideration of the particulate cloud residence times such a range of (t') appeared to cover all possible cases. A striking feature of these curves is the small variation of radiative flux with non-dimensional time. These curves imply, depending on mean residence time values, that the time mean radiative fluxes emitted by the bed surface are essentially invariant with change of $(U-U_{mf})$. The curves of Figure 6.7 and Figure 6.8 substantiate these predictions, being essentially equivalent to the corresponding curves of Figure 4.5, Figure 4.7, Figure 4.9 and Figure 4.11 found from the steady state analysis. In order to obtain the curves of Figure 6.7 and Figure 6.8 appropriate particle cloud residence times were obtained from Figure 5.19 along with values of K_t reported in Figure 3.13 through Figure 3.21, H_{mf} in all cases being 25 mm (measured at ambient temperatures).

Table 6.1 illustrates typical values of the appropriate parameters for non-dimensional time determination for the case of Silicon Carbide particles.

As may be observed from Table 6.1, although particle size was not directly included in the analysis the effects appear in

TABLE 6.1

Silicon Carbide; $\rho = 3\,179\text{ kg/m}^3$; $C_p = 0.714\text{ kJ/kg}$				
(a) $U-U_{mf} = 100\text{ mm/s}$; $H_{mf} = 25\text{ mm}$ (at 20°C)				
	$D_p\text{ mm}$			$T_b\text{ }^\circ\text{C}$
	0.354	0.55	0.777	
K_t	960	670	780	925
ϵ_b	0.55	0.46	0.41	
t_m	0.09	0.09	0.09	
t'_m	0.00825	0.00479	0.00511	
K_t	900	600	600	1 050
t_m	0.09	0.09	0.09	
t'_m	0.0104	0.00578	0.00529	
(b) $U-U_{mf} = 400\text{ mm/s}$				
K_t	660	560	400	925
ϵ_b	0.71	0.59	0.51	
t_m	0.2	0.2	0.2	
t'_m	0.0196	0.0117	0.00701	
K_t	600	510	360	1 050
t_m	0.2	0.2	0.2	
t'_m	0.0239	0.0144	0.00849	

the non-dimensional time predictions through the value of extinction coefficient K_t and emulsion voidage ϵ_b . Experimentally, the effects of particle size appear in the value of minimum fluidizing velocity although from Figure 6.7 and Figure 6.8, no consistent characteristic was observed. An important variable affecting the value of t_m' is bed voidage. Using the relationship given in Leva *et al*^[76] of

$$\frac{1 - \epsilon_b}{\epsilon_b^3} = \frac{U_{mf}}{U} \left[\frac{1 - \epsilon_{mf}}{\epsilon_{mf}^3} \right] \quad (6.15)$$

the bed voidage may be written in terms of the cubic equation.

$$\epsilon_b^3 \alpha + \epsilon_b - 1 = 0 \quad (6.16)$$

where

$$\alpha = \left[\frac{1 - \epsilon_{mf}}{\epsilon_{mf}^3} \right] \left[1 - \frac{U - U_{mf}}{U} \right]$$

Now from the analysis of Chapter 3, equation (3.4)

$$\left[\frac{1 - \epsilon_{mf}}{\epsilon_{mf}^3} \right] = \frac{C \phi^2}{150} \quad (6.17)$$

with $C = 1\,440$ as validated by the high temperature correlations of U_{mf} determination reported in Figure 3(a,b,c). The appropriate values of ϵ_b reported in Table 6.1 are assumed invariant for the temperature ranges of interest. In all cases values of t_m' are 0.01 or less, thus the values of radiative flux predict an almost

invariant change with time. The effects of the initial temperature distribution using appropriate temperature profiles from Figure 3.23 through Figure 3.25 on the predicted radiative flux levels are described in Figure 6.9(a,b). No comparison is made with experimental results because as reported earlier in Chapter 4, considerable discrepancies were observed. This being the case, Figure 6.9(a,b) are presented for academic interest only. The initial temperature distribution reduces the cooling rate of the emulsion as evidenced by Figure 6.10 and Figure 6.11 compared with an equivalent emulsion subject to an initial uniform distribution. Such an effect is similar to the results encountered from an increase in the scattering albedo ω_0 .

6.5 Conclusions and Suggestions for Further Study

Within the limitations of experimentally predicting particle cloud residence times, the essentially time dependant radiative fluxes emitted by an ejected isothermal emulsion are independant of excess gas velocity ($U-U_{mf}$). This invariance is also predicted experimentally although the response time of the measuring instrument (radiation pyrometer) may have limited these observations.

The transient analysis considers radiative transfer from a single bursting isothermal bubble and ejected particle cloud, with no interaction between adjacent bubbles at or near the bed surface. In reality considerable interaction does occur, particularly at high ($U-U_{mf}$) values, hence further studies are required on single bursting bubbles. However, even for considerably long residence times the change of radiative flux is not expected to be large.

The initial temperature distribution was assumed uniform. However, results indicate that depending upon the boundaries present, a temperature distribution will always be imposed upon the ejected cloud. With a high emissivity, low temperature boundary, the ejected cloud residence times and surface interaction of bubbles are sufficient to impose an initial significant temperature distribution. At the other extreme a boundary of low emissivity or high emissivity and high temperature the initial temperature variation is not large. Hence further analysis must be considered with this boundary dependant temperature distribution more adequately described.

An important observation is that when a heat transfer surface is brought into contact with the bed and energy exchange by conduction must be considered, radiative transfer plays an increasingly significant role as the residence time of the emulsion packet increases. However, for short residence times conduction heat transfer will be the predominant mode.

The model of transient radiative transfer developed in this chapter has certain shortcomings. Its verification by experimentation is far from complete and further improvement must be left until a suitable radiometer or alternative measuring instrument is available. Further uncertainties remain in the determination of extinction coefficient values. The values of K_t used in this transient model were obtained from a time averaged approximation, and further effort is required in determining more reliable values of K_t applicable in this transient model. The residence time of the ejected cloud of particles was obtained in a somewhat idealised

and simple way and requires further investigation, particularly for the case when surface interaction of bubbles occur.

In essence, the attempt of such a transient study has, in providing for further study, evolved a number of areas where further knowledge is desired even though the model has of necessity been kept as simple as possible.

CHAPTER 7

UNSTEADY COMBINED RADIATION AND CONDUCTION HEAT TRANSFER
TO SURFACES IMMERSSED IN A FLUIDIZED BED

7.1 Introduction

During the history of fluidized bed heat transfer considerable attention has been focused on the mechanism controlling heat energy exchange between the bed and either the walls of the reactor or some immersed surface. Various workers^[1] and Baskakov and Goldobin^[83] immersed two surfaces of a high and low emissivity into a hot bed to determine the radiative heat transfer component. Overall heat transfer coefficients were obtained to an immersed spherical, copper calorimeter by Karchenko and Markhorin^[84], although the size of the probe of 60 mm diameter was too large to apply the lumped capacity method of heat transfer with Biot numbers exceeding 0.2. Hence unaccounted for errors are expected in the reported values of heat transfer coefficient. As a contrast the work of Baskakov *et al*^[85] used a radiometer probe immersed in the bed to measure the radiative fluxes and presented the variation of effective emissivity of the bed with change of temperature of the radiometer quartz protection glass. Such curves showed the influence of the cooling of the first row of particles in contact with the glass by conduction and radiation, reflected in a lowering of the measured radiative fluxes. These results may be compared with those of [6] where no such allowance for particle cooling was made, and further confirmed by the observations of [7].

In all the above analysis, the combined modes of conduction and radiation heat transfer are present. To date no reasonable

comparisons between existing theories and experiment are available. The most comprehensive theoretical solution, without at present any experimental data, was performed by [3]. Unfortunately in the analysis no values of wall temperature was reported and hence a comparison with the solution presented in this chapter is not forthcoming.

At low bed temperatures where the predominant mode of heat transfer is by conduction a number of studies have been performed, a notable one of which is that of Kubie and Broughton^[82] who found excellent agreement with controlled residence time data available in the literature. In essence the theoretical solutions presented in [82] were based on the packet theory first established in [8] which was modified to account for the local voidage and property variations in the vicinity of a flat surface. An equation relating bed voidage and non-dimensional distance was reported as

$$\epsilon(\bar{x}) = 1 - 3(1 - \epsilon_b)(\bar{x} - \frac{2}{3}\bar{x}^2) \text{ for } \bar{x} < 1$$

and

$$\epsilon(\bar{x}) = \epsilon_b \text{ for } \bar{x} > 1$$

where \bar{x} = number of particle diameters.

Although not strictly correct in that conduction and radiation must be solved simultaneously, the curves reported in Figure 7.1 are taken from the analysis of Chapter 6 for a purely radiating system and from [82] for a purely conducting system. As the simultaneous solution of both modes of heat transfer are expected to produce a mutual weakening of each component, the curves of

Figure 7.1 would tend to over predict the correct results. A further assumption for the radiative curve of Figure 7.1 is that no property variations occur which would again tend to over predict. Also a constant temperature boundary condition was used in the present analysis, whereas in [82] a constant flux boundary condition was considered. However, the interesting feature of such curves is the obvious predominance of conduction for short emulsion residence times. Radiation plays an increasingly significant role as the time history of the emulsion packet proceeds. This fact was pointed out by Lick^[77] in an asymptotic approach for short and long time solutions of the combined modes of heat transfer in a plane absorbing slab. Also in evidence is the dependance of radiative particle Nusselt number ($h D_p / K_{be}$) on particle size and bed temperature. These results imply that the radiative heat transfer coefficient is independant of particle size although an indirect dependance appears in the non-dimensional time through the extinction coefficient K_t . Such a result contrasts with the pure conduction results where the heat transfer coefficient is strongly dependant on particle size and reported elsewhere^{[83], [84]} and ^[85]. Hence with these different regimes of dependance a general representation of conductive and radiative Nusselt numbers is impractical and only solutions for specific conditions may be reported.

In the absence of sufficient experimental data on radiation and conduction heat transfer pertaining to the case of a fluidized emulsion, a programme of experimentation was designed in which the bed was viewed through the wall of a quartz glass reactor with a

radiation pyrometer. However, before such experiments are described a mathematical model of the system is first evolved and solutions compared with some existing data.

7.2 A Generalized Approach to Unsteady Combined Radiation and Conduction Heat Transfer

7.2.1 Introduction

Simultaneous conductive and radiative transfer under transient conditions, although a complex phenomenon, has become a subject of considerable technical interest in recent years. Initial solutions were subject to simplifications and approximations to the non-linear, partial, integro-differential energy equation. The two flux approximation was used in [66] and a linearisation, combined with an exponential Kernel approximation to the radiative flux equation was used in [77] for short and long asymptotic time solutions. Heinisch and Viskanta^[78] used a similarity solution utilizing the optically thick approximation for radiative flux and Hazzah and Beck^[79] used a rigorous differential method to predict energy transfer for the limiting cases of an optically thin and thick medium. Recently the studies in [30] and Doornink and Hering^[80] utilised the exact formulation of the radiative transfer equation. [80] assumed a non-scattering medium contained between black parallel boundaries and utilized the function approximation technique essentially used in this study and described in Appendix D. Scattering effects were included in the analysis described in [30] where the study of a similar plane layer problem also allowed for reflecting boundaries using for solution the

method of idempotents discussed by [29]. In all the previous analyses a gray medium, homogeneous in nature and contained between plane parallel boundaries was assumed. In this study a model of similar geometry is assumed as being most relevant and of a simple configuration for the study of heat transfer to the walls of a fluidized bed reactor or to a probe immersed therein.

7.2.2 Analysis

The simultaneous transport of energy from a stationary emulsion may be described in terms of the geometry of Figure B1 and Figure 1.1. The assumptions according to the emulsion are again as described in the steady state analysis of Chapter 2. The radiative flux equation is described in Appendix B, and for a fluidized packet of emulsion in accordance with the analysis of [82] for a variable property boundary layer, may be written in the energy equation as

$$\frac{\partial}{\partial x} \left[K(x) \frac{\partial T}{\partial x} \right] - \frac{\partial q_r}{\partial x} = \rho(x) C_p(x) \frac{\partial T}{\partial t} \quad (7.1)$$

The physical model described by equation (7.1) requires that the radiative flux term q_r be written also in variable property form. Such a term would result in unnecessary complications in solutions at this stage and would not be consistent with the assumptions initially written into the mathematical model. To reduce the complexity of equation (7.1) in keeping with the non-variable property radiative flux term, a mathematical expedience described by Wicke and Fetting^[81] may be utilised. The proposed model of [81] suggests

that heat is transferred through a gas film separating the emulsion packet from the bed wall or immersed surface. The packet originates from deep within the bed, resides at the wall for a specific time and is then replaced by a fresh packet. In this analysis with such a gas film attached to the heat transfer surface assuming mean property values, equation (7.1) may be simplified to

$$\frac{\partial^2 \theta}{\partial \tau^2} - \frac{1}{4N_1} \frac{\partial q_r}{\partial \tau} = \frac{\partial \theta}{\partial \tau}, \quad (7.2)$$

where in the two regimes value N_1 assumes a mean constant value, i.e.

for the gas film:

$$N_1 = N_{1g} = \frac{K_{tg} K_g}{4 \sigma T_b^3} \quad (7.3)$$

for the emulsion:

$$N_1 = N_{1e} = \frac{K_{tb} K_b}{4 \sigma T_b^3} \quad (7.4)$$

The term N_1 is referred to in the literature as the conduction-radiation parameter with $N_1 \rightarrow \infty$ for pure conduction and $N_1 \rightarrow 0$ for pure radiation.

As described in [9] the parameter N_1 does not directly give the relative values of conduction to emission as the ratio of these values depends also upon both the temperature difference and temperature level in addition to the value of N_1 . Described in [80] is the relative importance of the term N_1/τ_0^2 . Radiative transfer

does not significantly effect the temperature distribution for $N_1/\tau_0^2 > 5.0$ and conduction predominates. As N_1/τ_0^2 or N_1 decreases, greater interaction of radiative and conductive transfer occurs.

For $\tau_0 > 1$, radiative transfer effects are dominant when $N_1 < 0.005$.

Also pointed out in the work of [30] was the warning of interpreting

t' as a measure of absolute time in comparing results for differing

values of N_1 , e.g. for a fixed optical thickness $\tau_0 = 1$ increasing

N_1 by 10^2 implies increasing thermal conductivity by a factor of

10^2 . However, absolute time is inversely proportional to thermal

conductivity, hence for $N_1 = 0.005$ and $t' = 0.001$, the corresponding

comparison for $N_1 = 0.5$ should be at $t' = 0.1$. In this study the

situation arose where non-dimensional time relating to the gas

layer and the emulsion packet were not equivalent because of the

difference in the corresponding values of N_1 (gas layer) and N_1

(emulsion packet). However, the two non-dimensional times of

$$t'_g = \frac{K_{tg}^2 K_g t}{(\rho C_p)_g} \quad (7.5)$$

and

$$t'_b = \frac{K_{tb}^2 K_b t}{(\rho C_p)_b} \quad (7.6)$$

may be related by equating through the absolute time t . Hence

$$t'_b = \frac{K_{tb}^2}{(\rho C_p)_b} \frac{(\rho C_p)_g t'_g}{K_{tg}^2 K_g} \quad (7.7)$$

In the analysis a weighted mean value of $(\rho C_p)_g$ was taken as

$$(\rho C_p)_{ge} = \frac{(\rho C_p)_g + (\rho C_p)_b}{2} \quad (7.8)$$

and

$$(\rho C_p)_b = (\rho C_p)_p (1 - \epsilon_b) \quad (7.9)$$

In finite difference form equation (7.7) becomes

$$\Delta t'_b = \frac{K_{tb}^2 K_b (\rho C_p)_g}{(\rho C_p)_b K_{tg}^2 K_g} \Delta t'_g \quad (7.10)$$

It was convenient for computation of equation (7.2) to impose a value $\Delta t'_b$ in the finite difference approximation and hence the corresponding value of $\Delta t'_g$ was then determined. The value of $\Delta t'_b$ (the time increment) was set using a fixed spacial step size in equation (7.2) and convergence obtained with $\Delta\tau = 0.02$ and $\Delta t'_b = 0.0001$. From [82] the voidage variation of the emulsion packet takes place over one particle diameter. However, as the major property variation occurs over the first $0.5 D_p$ the depth of the gas layer in this study is taken equal to $0.5 D_p$. With the assumption of an optically thin gas layer which is transparent and offers no resistance to radiation transport from the bulk of the emulsion packet and bed wall, the extinction coefficient in the gas layer, K_{tg} is

$$K_{tg} = \frac{\tau_0}{0.5 D_p} \quad \text{with } \tau_0 = 0.1 \quad (7.11)$$

The effective conductivity of the gas layer was taken as a mean between K_g and K_b , i.e.

$$K_{ge} = \frac{K_g + K_b}{2} \quad (7.12)$$

The thermal conductivity within the emulsion packet was determined from the analysis of Kunii and Smith^[86] who derived a relationship for the effective conductivity of a porous medium in terms of the voidage and the solid and gas conductivities. Hence

$$\frac{K_{be}}{K_g} = \epsilon_b + \frac{\beta(1 - \epsilon_b)}{\phi_1 + \gamma \frac{K_g}{K_p}}$$

where constant $\beta = 1$ and $\gamma = \frac{2}{3}$ for $0.476 \leq \epsilon_b \leq 1.0$. The constant ϕ_1 is reported graphically by [86] as a function of K_p/K_g . The curve of Figure 7.2 of K_{be}/K_g against ϵ_b was derived for the particulate material used in this study.

7.2.3 Initial and Boundary Conditions

In accordance with the simple model of an isothermal packet of emulsion arriving at the plane boundary at zero time, and heat transfer taking place with incremental time, the initial condition may be written

$$\theta(\tau, 0) = \left\{ \begin{array}{l} 1 \\ \theta(\tau) \end{array} \right\}, \quad \tau \geq 0 \quad (7.13)$$

with boundary conditions of

$$\theta(0, t') = \theta_1, \quad t' \geq 0 \quad (7.14)$$

and

$$\theta(\tau_0, t') = 1.0, \quad t' > 0 \quad (7.15)$$

along with the radiative boundary conditions of

$$F_w = \epsilon_w \theta_w^4 + (1 - \epsilon_w) (F_w - q_r(0)) \quad (7.17)$$

and

$$F_2 = \epsilon_2 \theta_2^4 + (1 - \epsilon_2) (F_2 + q_r(\tau_0)) \quad (7.18)$$

As the gas layer is defined as an optically thin medium a simplification to equation (7.2) results in a modified energy equation for the optically thin limit of

$$\left. \frac{\partial^2 \theta}{\partial \tau^2} \right|_{\tau=\tau_{og}} + \frac{(1 - \omega_0)}{2N_1 g} [F_w + F_e - 2\theta^4(\tau_{og}, t')] = \left. \frac{\partial \theta}{\partial t'_g} \right|_{\tau' = \tau_{og}} \quad (7.19)$$

For non-black boundaries F_w and F_e , the wall flux and emulsion flux respectively may be found from the equations relating incident, emitted and reflected radiative energy, hence

$$F_w = \frac{\epsilon_w \theta_w^4 + (1 - \epsilon_w) q'_{re}}{[1 - (1 - \epsilon_w)(1 - \epsilon_e)]} \quad (7.20)$$

and

$$F_e = \frac{q'_{re} + (1 - \epsilon_e) \epsilon_w \theta_w^4}{[1 - (1 - \epsilon_e)(1 - \epsilon_w)]} \quad (7.21)$$

with q'_{re} the non-dimensional radiation from the emulsion packet and ϵ_e the effective emissivity of the surface of the emulsion packet

designated $\epsilon_e = q'_{re}$. As q'_{re} changes with time of exposure of the packet, the value of ϵ_e is also time dependant. Using the optically thin limit for the energy equation, (7.19) simplifies the starting solution at each time interval of the finite difference approximation of equation (7.2). If equation (7.2) had not been modified to account for the optically thin gas layer a difficulty arises in determining with sufficient confidence the gradient $\partial q'_r / \partial \tau$ at $\tau = \tau_{og}$.

Within the emulsion packet the energy equation (7.2) is applied across the field at each time interval in explicit finite difference form. A complete analysis of the finite difference equations used to solve equation (7.2) and equation (7.19) appear in Appendix I along with the computer programme written for this purpose. The time solution of the radiative flux equation was based upon the method used for the transient, pure radiative model of Chapter 6 with appropriate modifications to include the conductive heat transfer mode.

7.2.4 A Qualification for the Use of a Mean Property Gas Boundary Layer

An initial study of the effects upon the predicted results of varying the effective properties of the gas layer between a gas value, e.g. $K_{ge} = K_g$ and a mean value, e.g.

$$K_{ge} = \frac{(K_g + K_b)}{2}$$

produced an insignificant change in the radiative flux distribution

with time but reduced the conductive flux level by a factor of almost 3. As the conductive values predicted, using a mean property gas layer, compared favourably with the results of [82], such a boundary layer approximation was used throughout.

7.3 Discussion of Predicted Results

In order to determine appropriate values of K_t for the emulsion packet in the vicinity of a flat surface, the simple analysis reported in Appendix E(b) was used in accordance with the boundary property variations of [82]. Curves of these values are plotted in Figure 7.3 for the particulate material studied. K_{tb} in the emulsion was then taken from the invariant portion of the curves from $D_p = 1$ onwards.

The variation of bed voidage ϵ_b with $U - U_{mf}$ was derived from the equation

$$\epsilon_b^3 \alpha + \epsilon_b - 1 = 0$$

where

$$\alpha = \frac{(1 - \epsilon_{mf})}{\epsilon_{mf}^3} \left[1 - \frac{U - U_{mf}}{U} \right]$$

and

$$\left[\frac{1 - \epsilon_{mf}}{\epsilon_{mf}^3} \right] = \frac{C \phi_s^2}{150} \quad \text{with } C = 1440$$

discussed earlier in Chapter 3 and Chapter 6. Values of K_{tb} varying

with $U-U_{mf}$ were then determined and reported in Figure 7.4 through Figure 7.6.

Throughout the analysis an emulsion optical thickness of $\tau_0 = 10$ is assumed along with a black boundary condition at $\tau = \tau_0$ simulating the flux from deep within the bed, i.e. $F_2 = F_b = 1$. The instantaneous radiative and conductive heat transfer coefficients are defined as

$$h_r(t') = \frac{q_r(0,t')}{T_b - T_w} \quad (7.21)$$

and

$$h_c(t') = \frac{q_c(0,t')}{T_b - T_w}$$

with

$$q_c(0,t') = -K_{ge} \left. \frac{\partial \theta}{\partial \tau} \right|_{\tau=0}$$

Using a uniform residence time distribution function $\psi(t') = 1$ of emulsion packets at the wall, time average heat transfer coefficients are defined as

$$h_{rm}(t'_m) = \frac{1}{t'_m} \int_0^{t'_m} h_r(t') \psi(t') dt' \quad (7.23)$$

and

$$h_{cm}(t'_m) = \frac{1}{t'_m} \int_0^{t'_m} h_c(t') \psi(t') dt' \quad (7.24)$$

In order to derive suitable values of the absolute emulsion packet

mean residence times, t_m , the expression of Gelperin and Einstein reported in [31] was used. With

$$t_m = \frac{H_{mf}^2}{0.711H_f^2} \frac{(U - U_{mf})}{1.5 g} \left[\frac{H_{mf}}{H_f - H_{mf}} \right]^2 \quad (7.25)$$

Using the relations

$$\frac{1 - \epsilon_b}{\epsilon_b^3} = \frac{U_{mf}}{U} \left[\frac{1 - \epsilon_{mf}}{\epsilon_{mf}^3} \right] \quad (7.26)$$

$$H_f = H_{mf} \left[\frac{1 - \epsilon_{mf}}{1 - \epsilon_b} \right] \quad (7.27)$$

equation (7.25) may be transformed to

$$t_m = \frac{U - U_{mf}}{10462.365} \left[\frac{1 - \epsilon_b}{1 - \epsilon_{mf}} \right]^2 \quad (7.28)$$

with $(U - U_{mf})$ in mm/s.

An assumption in the analysis is that heat is transferred from the inner surface of the gas bubbles attached to the surface by radiation only. Hence to find the view factor between an assumed hemispherical bubble and the wall consider radiation between a gray heat source (inner bubble surface) and a gray heat sink (wall) completely enclosed in a radiating enclosure (surrounding emulsion). Then

$$\frac{1}{A_b F_{bw}} = \frac{1}{A_b F_{bw}} + \frac{1}{A_b} \left[\frac{1}{\epsilon_e} - 1 \right] + \frac{1}{A_w} \left[\frac{1}{\epsilon_w} - 1 \right] \quad (7.29)$$

with

$$A_b = \frac{\pi D_b^2}{2}, \quad A_w = \frac{\pi D_b^2}{4}$$

and $F_{wb} = 1.0$, then $F_{bw} = \frac{1}{2}$. Then

$$\frac{1}{\bar{F}_{bw}} = \frac{1}{\epsilon_e} + \frac{2}{\epsilon_w} - 1 \quad (7.30)$$

Hence

$$h_{re}(t'_m) = h_{rm}(t'_m)[1 - f_o] + h_{rm}(t'_m) \frac{A_b}{A_w} \bar{F}_{bw} f_o \quad (7.31)$$

and consequently

$$h_{ce}(t'_m) = h_{cm}(t'_m)[1 - f_o] \quad (7.32)$$

with

$$h_t(t'_m) = h_r(t'_m) + h_c(t'_m) \quad (7.33)$$

where

$$f_o = 1 - \frac{[1 - \epsilon_b]}{[1 - \epsilon_{mf}]} \quad (7.34)$$

7.3.1 Comparison of Predicted with Reported Heat Transfer Data to an Immersed Probe

Unfortunately, very little experimental data exists in the literature which may be suitably compared with the present analysis. The work of [83], however, does provide for an initial and suitable

comparison. Using the reported physical properties for fireclay given in [83] of probe surface emissivity $\epsilon_w = 0.8$, particle emissivity $\epsilon_p = 0.75$ and for two particle sizes namely 0.35 mm and 0.63 mm, theoretically predicted curves of radiative and total heat transfer coefficient are reported in Figure 7.7(a,b) and compared with the experimental data from [83]. A list of appropriate values used in the analysis are given below in Table 7.1.

TABLE 7.1

Fireclay $(\epsilon_p = 0.75 \quad T_b = 1\,123 \text{ K})$
 $(\omega_o = 0.4 \quad \epsilon_w = 0.8)$

			Units
D_p	0.35	0.63	mm
ϵ_b	0.72	0.55	-
K_{be}	0.0002	0.00027	kW/m K
ρ_p	2600	2600	kg/m ³
C_p	1.1724	1.1724	kJ/kg K
K_{tg}	114.3	95.7	m ⁻¹
K_{tb}	1500	1400	m ⁻¹
N_{1g}	0.0504	0.1747	-
N_{1b}	0.934	1.177	-
f_o	0.589	0.34	-

The probes used in [83] were spherical, one of a high and one of a low emissivity. The analysis presented here considers transfer between plane surfaces and may account for a certain level of error. The predicted radiative heat transfer coefficients of Figure 7.7a compare favourably with the data from [83], particularly for a particle size of 0.35 mm diameter. A further improvement between the results is observed if the contribution to radiative transfer from the inner surface of the bubble is neglected. However, such neglect is unreasonable and would lead to an even poorer comparison for the total heat transfer coefficient of Figure 7.7b than is already observed. The trend observed experimentally for total heat transfer to increase with reduced particle size is supported by the predicted results due to increased contribution from conduction with smaller particles.

With the varying opinions voiced in the literature on the significance of radiative transfer in fluidized beds it is interesting to note that in the predicted results of this study at a bed temperature of 1 123 K the percentage of radiative to total (conduction plus radiation) heat transfer coefficient varied from 12.7% at a probe wall temperature of 200°C to 28.3% at a wall temperature of 800°C. The experimental data from [83] gave 4.5% and 20% respectively. Hence, radiation appears to be a significant contributor to the total heat transfer even with a comparatively low temperature bed of 1 123 K (850°C).

It was reported in [3] and [7] that cooling within the emulsion extended up to $1.5 D_p$ after a suitable residence time. From the results of this study cooling was observed to extend up

to $\sim 4 D_p$ for 0.35 mm particles at a probe wall temperature of 200°C after a residence time of 0.138 seconds.

7.3.2 Comparison of the Instantaneous Nusselt-Fourier Relationship for a Coupled and Uncoupled Solution of Conduction and Radiation Heat Transfer to a Plane Surface

Reported in Figure 7.1 are the instantaneous conductive and radiative Nusselt number ($h D_p / K_{be}$) variation with instantaneous Fourier number

$$\frac{K_{be} t}{\rho_p C_p (1 - \epsilon_b) D_p^2}$$

The non-dimensional time, referring to the pure radiation and combined conduction and radiation cases, were transformed for convenience into equivalent Fourier numbers. With

$$F_o = \frac{K_{be} t'}{D_p^2 K_{tb} \sigma T_b^3}$$

for pure radiation and

$$F_o = \frac{t'}{K_{tb}^2 D_p^2}$$

for the combined mode. As previously stated these curves were obtained by uncoupling the conductive and radiative components of the energy equation and solving separately. Figure 7.8 in contrast to Figure 7.1 describes the results obtained from a simultaneous solution of the coupled radiation and conduction energy equation and compared with the curves taken from Figure 7.1. Unfortunately,

computational time became excessive and only coupled solutions to a value of $F_0 = 1.0$ were predicted. The interesting feature of these curves is the small but noticeable reduction in the radiative Nusselt numbers for the combined solution, emphasizing the mutual weakening of each component when solved simultaneously. These observations are further qualified by the temperature profiles of Figure 7.12 which show considerably more cooling of the emulsion layer adjacent to the boundary when conduction is present compared with the case when conduction is neglected. Also in evidence are the depths of penetration of the cooling curves, in both cases exceeding the value of $1.5 D_p$ proposed by [3] and [7].

Referring to Figure 7.8 the conductive Nusselt number appears to underestimate at early times the curve interpolated from the predictions of [82] and overestimate for longer times. However, such a comparison is not strictly valid as the analysis of [82] considered a constant flux boundary condition whereas this study considers a constant temperature boundary condition. Also the curves obtained from [82] were interpolated for the materials used in this study. Similar curves to Figure 7.8 may be drawn for other materials and different boundary conditions. A few such curves are described in Figure 7.9 and Figure 7.10 for sand particles and varying boundary conditions. As expected, increasing the wall temperature and decreasing the wall emissivity significantly change the value of radiative Nusselt number although no change in the conductive Nusselt number was observed. Figure 7.11 for silicon carbide particles shows a marked fall in both conductive and radiative Nusselt numbers compared with sand particles.

This may be attributed to the fact that silicon carbide has a higher thermal conductivity than sand and becomes the influencing term in the Nusselt number ($h D_p / K_{be}$) even though the heat transfer coefficients (both radiative and conductive) have been significantly increased.

Such curves of instantaneous Nusselt-Fourier number variations are at this stage used only to predict and understand the important trends of combined conduction and radiative heat transfer to a plane boundary. In the predicted case of heat transfer to a surface immersed in a fluidized bed, the emulsion residence time, residence time distribution and bubble to wall heat transfer must be considered. Hence for other materials and boundary (wall) conditions the predicted results may be summarised as follows:

- (a) For bed materials of high particle emissivity, i.e. $\omega_0 \rightarrow 0$, the contribution of radiation to the total heat transfer is significant in fluidized beds operating at normal temperatures, i.e. $800^\circ\text{C} - 1100^\circ\text{C}$ when the irradiated surface has an emissivity approaching unit. As $\omega_0 \rightarrow 1$ the emitted flux levels are reduced accordingly.
- (b) For low wall emissivities the contribution of radiation decreases significantly, i.e. by an order of 50% for a wall emissivity of 0.5.
- (c) The radiative heat transfer coefficient is independent of particle size although an increase of particle size is reflected in an increase in the radiative Nusselt number through the term (D_p / K_{be}), multiplying the heat transfer

coefficient h . The converse is true for conduction with the heat transfer coefficient dependant and Nusselt number independant of particle size.

- (d) Conduction is independant of temperature level and only dependant on temperature gradient. On the other hand, radiation depends solely on the relative temperature levels between the fluidized bed and containing walls or immersed surface.
- (e) Within the normal range of emulsion packet residence times occurring in fluidized beds, the conductive mode of heat transfer is predominant over the initial period of contact with radiation becoming more prominent as time proceeds. Furthermore, the simultaneous solution of combined conduction and radiation provides an insignificant weakening of the radiative component compared with the solution of the uncoupled energy equation. This reduces the complexity of solving the energy equation and simplifies the predictions of radiative transfer.

7.4 Experimental Determination of Heat Transfer to the Wall of a Quartz Glass Reactor

To augment the previously reported results of heat transfer to probes immersed in a fluidized bed where both conduction and radiation are important, an experimental programme was designed in which the radiation pyrometer described in Chapter 4 was positioned in the horizontal plane viewing the bed through the glass wall of the fluidized bed reactor. A schematic diagram of the experimental

configuration is described in Figure 7.13. The pyrometer extension tube was covered internally with aluminium foil to reduce energy exchange with the bed and also directed cooling air to the glass wall, the flow of which could be varied to maintain a constant glass wall temperature. The temperature of the glass wall was constantly monitored by two Cr.Al thermocouples embedded into two small holes bored into the glass wall. These thermocouples were strategically positioned above and below the pyrometer viewing area of 0.25 in diameter. To reduce heat losses from the bed the whole reactor was heavily lagged. Also to reduce radiative transfer prior to the measuring section through the glass wall to the insulation, a strip of aluminium foil was placed just below the pyrometer viewing area. This technique enhanced the probability of an isothermal packet being brought into the viewing area, an assumption upon which the analysis is based, rather than one with an imposed thermal gradient. In all experiments bed heights of 70 mm were used.

7.4.1 Experimental Procedure

Unfortunately it was not possible with the present system to maintain low wall temperatures, i.e. of order 100°C - 200°C. Hence, as an attenuation of the fluxes may be expected at high glass wall temperatures along with a contribution from the glass itself an initial study of the overall attenuation effects of the quartz glass was performed. This was achieved by viewing the bed free surface alternately through a sample of the quartz glass and then with the glass sample removed. The attenuation was estimated

at a number of glass temperatures and found to reduce the true radiative flux by $14\% \pm 3\%$ over a temperature range of 600°C to $1\ 000^{\circ}\text{C}$.

Beds of silica sand, magnesia, alumina and silicon carbide particles with three different particle sizes of geometric means $0.354\ \text{mm}$, $0.55\ \text{mm}$ and $0.777\ \text{mm}$ were used. Initially the bed temperature was set at around $1\ 000^{\circ}\text{C}$, With the wall temperature then controlled to a fixed value by the air flow over the outer surface of the glass wall, pyrometer output was recorded for increasing values of $(U-U_{mf})$. Low values of $(U-U_{mf}) < 100\ \text{mm/s}$ were difficult to obtain as the bed tended to become poorly fluidized and combustion of the propane/air mixture became unstable. However, with care and speed reasonably repeatable results were obtained by quickly lowering the superficial air velocity to some fixed level and recording the pyrometer output before combustion became unstable and the bed temperature began to fall. The air velocity was then rapidly increased to establish stable conditions and a steady bed temperature.

7.4.2 Discussion of Results

As in this study a radiatively transparent wall was used, the boundary conditions in the analysis previously described in this chapter had to be modified. For the purpose of conduction heat transfer determination the wall temperature was taken as measured experimentally.

However, the radiative boundary condition simulating transfer to the radiation pyrometer was obtained by taking the temperature

and emissivity as ambient and unity respectively, e.g. $F_1 = 0.00238$ and with $F_2 = 1$ at $T_b = 1\ 000^\circ\text{C}$. The results of these experiments along with the theoretically predicted values are described in Figure 7.14 through Figure 7.16 are typical time average radiative flux curves from which the predicted curves of Figure 7.17 through Figure 7.20 were obtained for a range of $(U-U_{mf})$ values.

For the case of silica sand and silicon carbide particles, comparison of experiment with the predicted results are reasonable although for the case of alumina and magnesia a significant deviation may be observed. The analysis predicts a definite dependency of emitted radiative flux on particle size with q'_{rm} increasing for a decrease in particle size. As pointed out earlier, the opposite is true for conduction heat transfer. However, experimentally such trends were difficult to observe.

The general shape of the predicted curves were obtained experimentally with lower emitted fluxes at high emulsion packet residence times, i.e. low values of $(U-U_{mf})$. The fluxes increase rapidly at first as $(U-U_{mf})$ was steadily increased with a levelling out towards a maximum value. The fraction of bubbles present within the bed from the previously described analysis of f_o predicts a steady increase as $(U-U_{mf})$ and bed voidage increases. If this is the case then at increasingly shorter packet residence times the emitted flux should tend to decrease due to the predominance of radiation from the inner bubble surface over that from the emulsion. However, in reality this is not the case as shown in [36] the bubble fraction f_o attains a maximum at an

optimum value of $(U-U_{mf})$ after which it decreases. Hence, with this mechanism the emitted radiative fluxes should continue to increase as the proportion emitted by the bubble gives way to that emitted from the emulsion packet. Such effects were not studied experimentally and are only analytically predicted observations. At very high values of $(U-U_{mf})$ slugging of the bed would tend to occur along with a reduced bubble fraction and a different mechanism of particle motion takes place. In this case a reduced particle residence time at the wall may again become the dominant feature.

Without the advantage of controlled residence time and bubble fraction experiments, the predicted solutions are limited by the highly idealised equations which are used to determine t_m and f_o . From the pyrometer output trace a peak much greater than the general levels was observed at infrequent periods irrespective of $(U-U_{mf})$ values. It was apparent that such peaks were due to passing bubbles which had a 'hotter glow' than the surrounding emulsion suggesting that gas combustion was taking place at the bubble boundary thereby raising the particles in its near vicinity to levels above the general bed level. For this reason the applicability of transfer to the wall of the equation used to predict f_o becomes questionable. Its use may in fact be reasonable away from the wall or at a surface immersed within the bed, but not necessarily at the bed wall. Such observations are supported by the work of Donsi *et al*^[87] who reported that solids flow tends to be vertically downwards at the bed wall and upwards in the core of the bed, and that a limitation on solids exchange

normal to the wall is related to a continuous curtain of particles confining the bubble on the wall side. Such a curtain of particles would shield the effects of direct bubble to wall radiative transfer.

7.5 Conclusions and Suggestions for Further Study

The general analysis of combined conduction and radiative heat transfer from an optically dense emulsion has been applied to the case of a surface immersed within the bed compared with the data obtained by other workers. The results are reasonable as the size of probe used by some workers was too large to give sufficiently small Biot numbers and was spherical with the analysis developed in this study strictly applicable only to plane surfaces.

A purely analytical approach was undertaken initially to predict the instantaneous values of conductive and radiative Nusselt numbers comparing the results obtained from the coupled energy equation with the uncoupled solutions. Insignificant mutual weakening of either mode was observed for the coupled solution.

The work has been extended experimentally to measure the radiative fluxes in contact with the wall of a glass reactor. In many ways this is similar to the studies of [6] where a radiometer probe was immersed into a bed and the fluxes measured from the particles in contact with quartz protecting glass. The advantage of this study is the direct allowance given in the analysis to the conductive transfer between glass and contacting particles, although a disadvantage was the inability of the system to maintain a sufficiently low glass wall temperature. In the analysis

of the previous study of [6] this was not carried out.

The experimental results, although far from comparing satisfactorily with theory in some cases, show similar distinct trends. Unfortunately, the analysis is still subject to areas of large uncertainty, particularly the values of residence time of emulsion packets at the wall and of bubble fraction determination. For both these unknowns standard expressions were used to give representative results. However, further studies are desirable on single bubbles or bubble chains with the residence time and bubble fraction controlled, in contrast to the freely bubbling bed studied here. For this purpose and to facilitate a transient radiative study, a radiometer with a much shorter response time is required than the one used in the present study. As particle motion at the bed wall and at the bed axis tends to be different, i.e. particles move downward at the wall and upward at the centre of the bed, then heat transfer results measured experimentally or postulated analytically may be significantly different for the two regions. Further effort is required in this direction with a radiometer probe, utilizing a water-cooled quartz protecting glass placed at both positions.

The theoretical analysis retains a physically unjustified approximation; that of a gas film between the first row of particles and the wall or immersed surface. Such an approximation is used at this stage as a mathematical expedience. It was shown in [82] that a physically justifiable variable property boundary layer could be used to good effect for the case of conduction heat transfer only. Further work is now necessary to solve the

energy equation including the radiative term utilizing such a variable property boundary layer.

REFERENCES

REFERENCES

- [1] YOSHIDA, K, UENO, T and KUNII, D (1974). "Mechanism of Bed-Wall Heat Transfer in a Fluidized Bed at High Temperatures". Chemical Engineering Science, Vol.29, pp 77-82.
- [2] ZABRODSKY, S S (1963). "Hydrodynamics and Heat Transfer in Fluidized Beds".
- [3] VEDAMURTHY, V N and SASTRI, V M K (1974). "An Analysis of the Conductive and Radiative Heat Transfer to the Walls of Fluidized Bed Combustors". Int.J.Heat & Mass Transfer, Vol.17, pp 1-9.
- [4] RUBSTOV, G K and SYREMYATNIKOV, N I (1963). "Emissivity and Calculated Surface Radiation in a Fluidized Bed". IZV. Vuzov Emerget, No.5.
- [5] ZABRODSKY, S S (1973). "Compound Heat Exchange Between a High Temperature Gas Fluidized Bed and a Solid Surface". Int.J.Heat & Mass Transfer, Vol.16, pp 241-248.
- [6] PIKASHOV, V S, ZABRODSKY, S S, MAKHORIN, K E and Ilchenko, A I (1968). "On the Experimental Study of the Fluidized Bed Effective Emissivity". Heat & Mass Transfer, Vol.5, Nauka, I.Tekhn, Minsk.
- [7] ILCHENKO, A I, PIKASHOV, V S and MAKHORIN, K E (1968). "Study of Radiative Heat Transfer in a Fluidized Bed". Journal of Engineering Physics, Vol.14, No.4, pp 602-608.
- [8] MICKLEY, H S and FAIRBANKS, D F (1955). "Mechanism of Heat Transfer to Fluidized Beds". A.I.Ch.E. Journal, September, pp 374-384.

- [9] SIEGAL, R and HOWELL, J R (1972). "Thermal Radiation Heat Transfer", McGraw-Hill Book Company
- [10] HOTTEL, H C and SAROFIM, A F (1967). "Radiative Transfer", McGraw-Hill Book Company.
- [11] LOVE, T J, STOCKHAM, L W, LEE, F C, MUNTER, W A and TSAI, Y W (1967). "Radiative Heat Transfer in Absorbing, Emitting and Scattering Media, Oklahoma University (ARL-67-0210, DDC No.AD-666427), December.
- [12] CHANDRESEKHAR, S (1960). "Radiative Transfer". Dover Publications Inc, New York, NY
- [13] KOURGANOFF, V (1963). "Basic Methods in Transfer Problems". Dover Publications Inc, New York, NY
- [14] GUMPRECT, R O et al (1952). "Angular Distribution of Light Scattered by Large Droplet of Water". Journal of the Optical Society of America, Vol.42, No.4, April, pp 226-231
- [15] CHU, C M and CHURCHILL, S W (1955). "Numerical Solution of Problems in Multiple Scattering of Electromagnetic Radiation". Journal of Physical Chemistry, Vol.59, September, pp 855-863.
- [16] DAVISON, B (1957). Neutron Transport Theory, Oxford Univ. Press, London
- [17] VISKANTA, R (1960). "Heat Transfer in Thermal Radiation, Absorbing and Scattering Media". Argonne National Lab. Chicago, Illinois, ANL-6170, May.
- [18] EDWARDS, R H and BOBCO, R P (1965). "Radiant Heat Transfer from Isothermal Dispersions with Isotropic Scattering". Aerospace Technology Laboratory Research Report.

Hughes Aircraft Company, No SSD 50134R, December.

- [19] SCHUSTER, A (1905). "The Influence of Radiation on the Transmission of Heat". *Phil.Mag.Ser.6* Vol.5, Pl.II.
- [20] HAMAKER, H C "Radiation and Heat Conduction in Light Scattering Material". Philips Research Report 2, Parts I, II, III and IV 1947, pp 55-67, 103-111, 112-125, 420-425.
- [21] MORIZUMI, S J and CARPENTER, H J (1964). "Thermal Radiation from the Exhaust Plume of an Aluminized Composite Propellant Rocket". *Journal of Spacecraft and Rockets*. Vol.1, No.5, pp 501-507.
- [22] LEUNG, A T and EDWARDS, D K (1966). "Simultaneous Radiation, Conduction and Convection in a Spectrally Selective, Emitting and Scattering Porous Bed". *Journal of Heat Transfer*, May, pp 231-238.
- [23] VISKANTA, R and PRITAM, S BATHLA (1967). "Unsteady Energy Transfer in a Layer of Gray Gas by Thermal Radiation". *Z.Angew Math.Phys.* Vol.18, No.3, pp 353-367.
- [24] K KRISHNA PRASAD and HERING, R G. "Transient Radiative Heat Transfer in a Plane Layer". *Int.J.Heat Mass Transfer*, Vol.12, pp 1331 -1337.
- [25] DEISSLER, R G (1964). "Diffusion Approximation for Thermal Radiation in Gases with Jump Boundary Conditions". *J.Heat Transfer*, C 86, pp 240-246.
- [26] SPARROW, E M and CESS, R D (1966). "Radiation Heat Transfer" Brooks/Cole Publishing Company, California, USA.
- [27] HOWELL, J R and PERLMUTTER, M (1964). "Monte Carlo Solution

of Radiant Heat Transfer in a Non-grey, Non-isothermal Gas with Temperature Dependent Properties". Am.Inst. Chem.Engr.J., 10, pp 562-567.

- [28] HSIA, H M (1965). "Radiative Transfer in an Absorbing, Emitting Anisotropic Scattering and Non-isothermal Medium between Parallel Plates". PhD Thesis, University of Oklahoma, Norman Okla, June.
- [29] HSIA, H M and LOVE, T J (1967). "Radiative Heat Transfer between Parallel Plates Separated by a Non-isothermal Medium with Anisotropic Scattering". Journal of Heat Transfer. Trans. ASME Series C, Vol.89, No.3, August, pp 197-204.
- [30] WESTON, K C and HAUTH, J L (1973). "Unsteady, Combined Radiation and Conduction in an Absorbing, Scattering and Emitting Medium". Journal of Heat Transfer, Trans. ASME, August, pp 357-364.
- [31] DAVIDSON, J F and HARRISON, D (1971). "Fluidization", London Academic Press Limited.
- [32] ERGUN, S (1952). Chem.Eng.Progr., 48, pp 89.
- [33] RITTENHOUSE, G. "A Visual Method of Estimating Two-dimensional Sphericity". Journal of Sedimentary Petrology, Vol.13, No.2, pp 79-81.
- [34] BROUGHTON, J (1974). "The Influence of Bed Temperature and Particle Size Distribution on Incipient Fluidization Behaviour". Trans.Instn.Chem.Engrs. Vol.52.
- [35] DAVIDSON, J F and HARRISON, D (1963). "Fluidized Particles". London:Cambridge University Press.

- [36] KUNII, D and LEVENSPIEL, O (1969). "Fluidization Engineering"
New York, John Wiley & Sons Inc.
- [37] MII, T, YOSHIDA, K and KUNII, D (1973). "Temperature Effects
on the Characteristics of Fluidized Beds". Journal of
Chemical Engineering of Japan, 6, No.1, pp 100-102.
- [38] MELAMED, N T (1963). "Optical Properties of Powders",
Part I and Part II. Journal of Applied Physics,
Volume 34, No.3, March, pp 560-570.
- [39] YOKOBORI, S (1961). "On the Emissivity of a Gas which
Contains Particles". Bulletin of J.S.M.E. Vol.4, No.13.
- [40] WILLIAMS, J R, SHENOY, A S and CLEMENT, J D. "Theoretical
Calculations of Radiant Heat Transfer Properties of
Particle-Seeded Gases".
- [41] BROWN, G G et al (1950). "Unit Operations". John Wiley &
Sons, New York.
- [42] McADAMS, W H (1964). "Heat Transmission", McGraw-Hill,
New York.
- [43] Thermophysical Properties of Matter, TPRC Data Series Vol.2,
4th Symp, Thermophysical Properties Symposium of Thermal
Radiation of Solids.
- [44] JUVELAND, A C, DEINKEN, H P and DOUGHERTY, J E (1964).
"Particle-to-Gas Heat Transfer in Fluidized Beds".
I and E C Fundamentals, Vol.3, No.4, November pp 329-333.
- [45] HIBY, J W (1967). "Periodic Phenomena Connected with Gas-
Solid Fluidization". Proc.Int.Symp.on Fluidization,
Netherlands University Press, Amsterdam, pp 99-110.
- [46] VERLOOP, J and HEERTJES, P M (1974). "Periodic Pressure

Fluctuations in Fluidized Beds". Chem.Eng.Science,
Vol.29, pp 1035 - 1042.

- [47] SMITH, R A, JONES, F E and CHASMAR, R P. (1968). "The Detection and Measurement of Infra Red Radiation". Oxford Clarendon Press.
- [48] SADILOV, P V and BASKAKOV, A P (1973). "Temperature Fluctuations at the Surface of a Fluidized Bed with Gas Combustion Occurring therein", Int.Chem.Engrg. Vol.13, July, pp 449-451.
- [49] HILL, F B and WILHELM, R H (1959). "Radiative and Conductive Heat Transfer in a Quiescent Gas-Solid Bed of Particles Theory and Experiment." A.I.Ch.E. Journal, December, pp 486-496.
- [50] BOBCO, R P (1967). "Directional Emissivities from a Two-Dimensional, Absorbing, Scattering Medium: The Semi-Infinite Slab". J.Heat Transfer, Vol.89, No.4, pp 313-320.
- [51] CHEUNG, L, NIENOW, A W and ROWE, P N (1974). "The Minimum Velocity of a Binary Mixture of different Sized Particles". Chemical Engineering Science, Vol.29, pp 1301-1303.
- [52] GIBILARO, L G and ROWE, P N (1974). "A Model for a Segregating Gas Fluidized Bed". Chemical Engineering Science, Vol.29, pp 1403-1412.
- [53] CHANDRASEKHAR, S et al (1952). "The X- and Y- Functions for Isotropic Scattering, Parts I and II". Astrophysical Journal, Vol.115, pp 244-278.
- [54] CHANDRASEKHAR, S (1948). "On the Radiative Equilibrium of

a Stellar Atmosphere". XXIV Astrophysical Journal, Vol.107, pp 92-111.

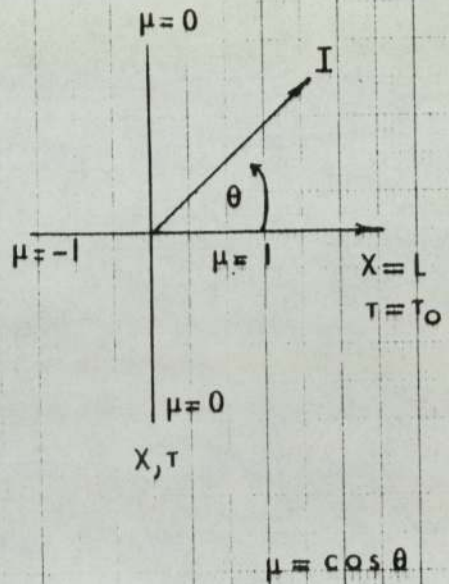
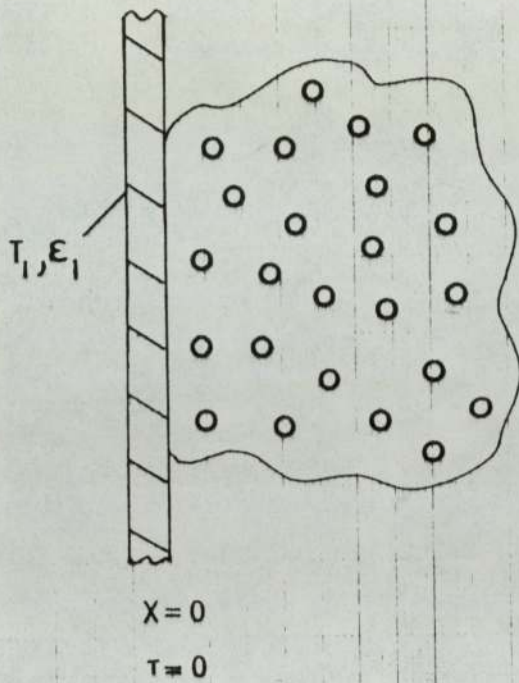
- [55] ZENZ, F A and WEIL, N A (1958). "Theoretical-Empirical Approach to Mechanism of Particle Entrainment from Fluidized Beds". Am.Inst.Chem.Engrs.J. 4, pp 472.
- [56] DO, H T, GRACE, J R and CLIFT, R (1972). "Particle Ejection and Entrainment from Fluidized Beds". Powder Technology, 6, pp 195-200.
- [57] BOTTERILL, J S M, GEORGE, J S and BESFORD, H (1966). "Bubble Chains in Gas Fluidized Beds". Chem.Eng.Prog. Symp.Ser.62 (62), p 7.
- [58] BASOV, V A, MARKHEVKA, V I and KELIK-AKHNAZAROV, T K (1969). "Investigation of the Structure of a Non-uniform Fluidized Bed". Intern.Chem.Eng. 9, p 263.
- [59] KEHOE, P W K (1969). "The Effect of Particle Size on Slugging Fluidized Beds". PhD Thesis, Cambridge.
- [60] ROWE, P N and EVERETT, D J (1972). Trans.Inst.Chem.Engrs. 50, p 42.
- [61] ROWE, P N and EVERETT, D J (1972). Trans.Inst.Chem.Engrs. 50, p 49.
- [62] ROWE, P N and EVERETT, D J (1972). Trans.Inst.Chem.Engrs. 50, p 55.
- [63] WERTHER, J (1974). "Bubbles in Gas Fluidized Beds". Part I and II. Trans.Inst.Chem.Engrs. Vol.52, pp 149-169.
- [64] KASSIM, W M S (1972). PhD Thesis, University of Aston in Birmingham, Department of Chemical Engineering.
- [65] McGRATH, L and STREATFIELD, R E (1971). "Bubbling in Shallow

- [66] NEMCHINOV, I V (1960). Zhur.Prikl.Mekhan.i Tekhn. Fiz, No.1, p 37.
- [67] ONUFRIEV, A T (1961). Zhur.Prikl.Mekhan.i Tekhn. Fiz, No.2, p 31.
- [68] ADRIANKIN, E I (1960). Soviet Physics-Technical Physics 4, p 1258.
- [69] VISKANTA, R and LALL, P S (1965). "Transient Heating and Cooling of a Spherical Mass of Gray Gas by Thermal Radiation". Trans.ASME, J.Appl.Mech. 32E, p 740.
- [70] CARSLAW, H S and JAEGER, J C (1948). "Conduction of Heat in Solids". Oxford University Press.
- [71] SZEKELY, J and FISHER, R J (1969). "Bed to Wall Radiation Heat Transfer in a Gas-Solid Fluidized Bed". Chemical Engineering Science, Vol.24, pp 833-849.
- [72] SULLY, A H, BRANDES, E A and WATERHOUSE, R B (1952). Brit.J.Appl.Phys. 3, 97.
- [73] PATTISON, J R (1955). "The Total Emissivity of Some Refractory Materials above 900°C". Trans.Brit.Ceramic Soc. Vol.54, 11, November.
- [74] PIRANI, M (1939). J.Sci.Instrum. 16, 372.
- [75] MICHAND, M (1952). "Emissivities of Metallic and Refractory Oxides at High Temperatures". Thesis, Paris.
- [76] LEVA, M et al (1948). "Fluidization of Solid Non-Vesicular Particles". Chem.Engrg.Prog. 44(8), 619-626.
- [77] LICK, W (1965). "Transient Energy Transfer by Radiation and Conduction". Int.Journal Heat & Mass Transfer, Vol.8, pp 119-127.

- [78] HEINISCH, R P and VISKANTA, R (1968). "Transient Combined Conduction-Radiation in an Optically Thick Semi-infinite Medium". AIAA Journal, Vol.6, No.7, pp 1409-1411.
- [79] HAZZAH, A S and BECK, J V (1970). "Unsteady Combined Conduction and Radiation Energy Transfer Using a Rigorous Differential Method". Int.J.Heat Mass Transfer, Vol.13, pp 517-522.
- [80] DOORNINK, D G and HERING, R G (1972). "Transient Combined Conductive and Radiative Heat Transfer". ASME Journal of Heat Transfer, November, pp 473-478.
- [81] WICKE, E and FETTING, F (1954). Chem.Ing.Tech. 26(6), pp 301-309.
- [82] KUBIE, J and BROUGHTON, J (1975). "A Model of Heat Transfer in Gas Fluidized Beds". Int.J.Heat Mass Transfer, Vol.18, pp 289-299.
- [83] BASKAKOV, A P and GOLDOBIN Y U M (1970). "Radiant Heat Transfer in a Gas Fluidized Boiling Bed". Heat Transfer-Soviet Research, Vol.2, No.6, November.
- [84] KARCHENKO, N V and MAKHORIN, K E (1964). "The Rate of Heat Transfer between a Fluidized Bed and an Immersed Body of High Temperatures". Int.Chem.Engrg. Vol.4, No.4. October.
- [85] BASKAKOV, A P et al (1973). "Heat Transfer to Objects Immersed in Fluidized Beds". Powder Technology 8, pp 273-282.
- [86] KUNII, D and SMITH, J M (1960). "Heat Transfer Characteristics of Porous Rocks". A.I.Chem.Eng.Journal, Vol.6, pp 71-78.
- [87] DONSI, G et al (1972). "Solid Flow Pattern at the Wall of a Fluidization Column Induced by Single Bubbles". Powder

Technology, Vol.6, pp 217-224.

PHYSICAL SYSTEM OF PACKET MODEL
 FOR RADIATIVE TRANSFER TO A
 PLANE BOUNDARY



:FIG 1.1

COMPARISON OF APPROXIMATE SOLUTIONS
OF RADIATIVE TRANSFER EQUATION

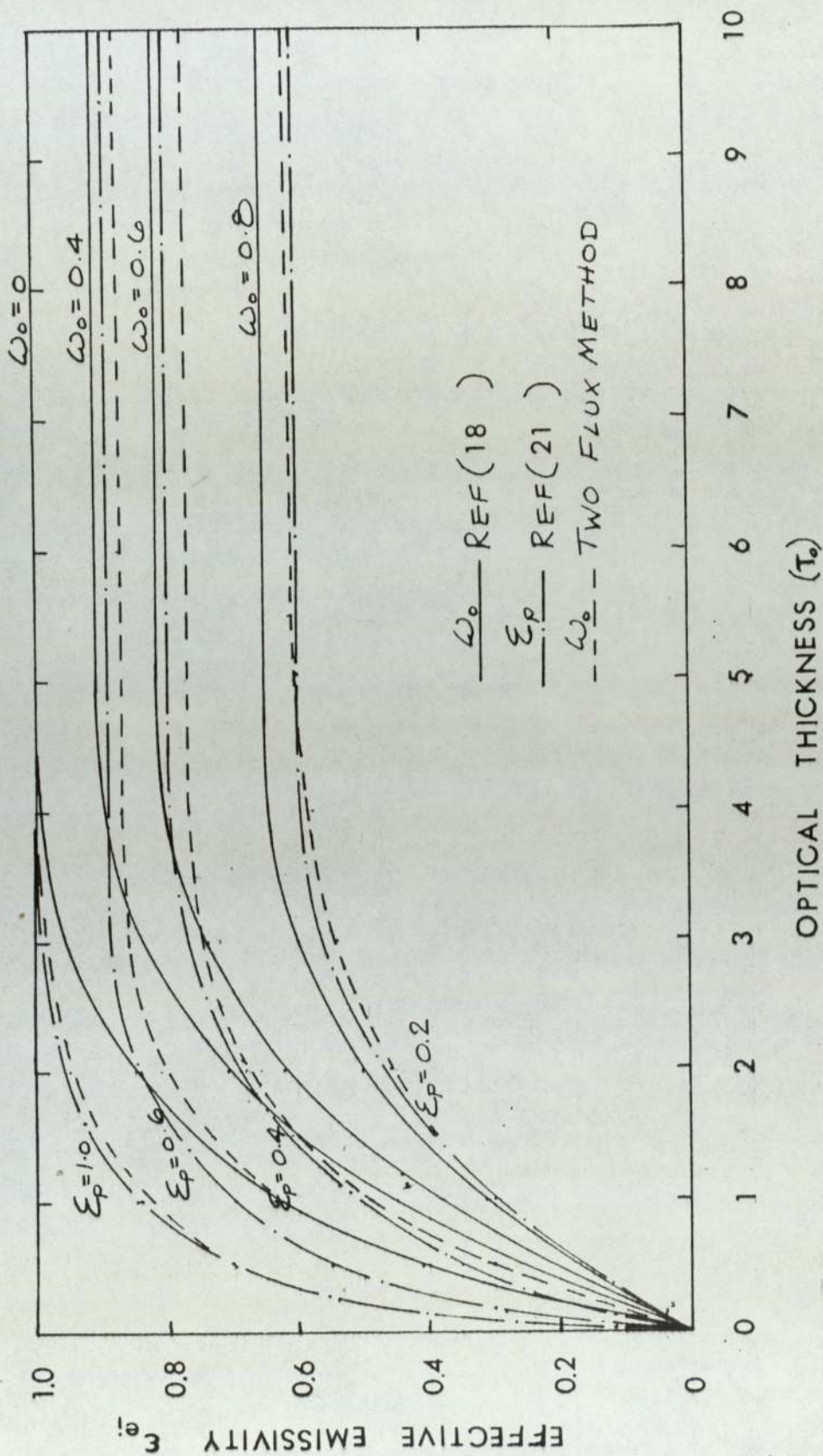
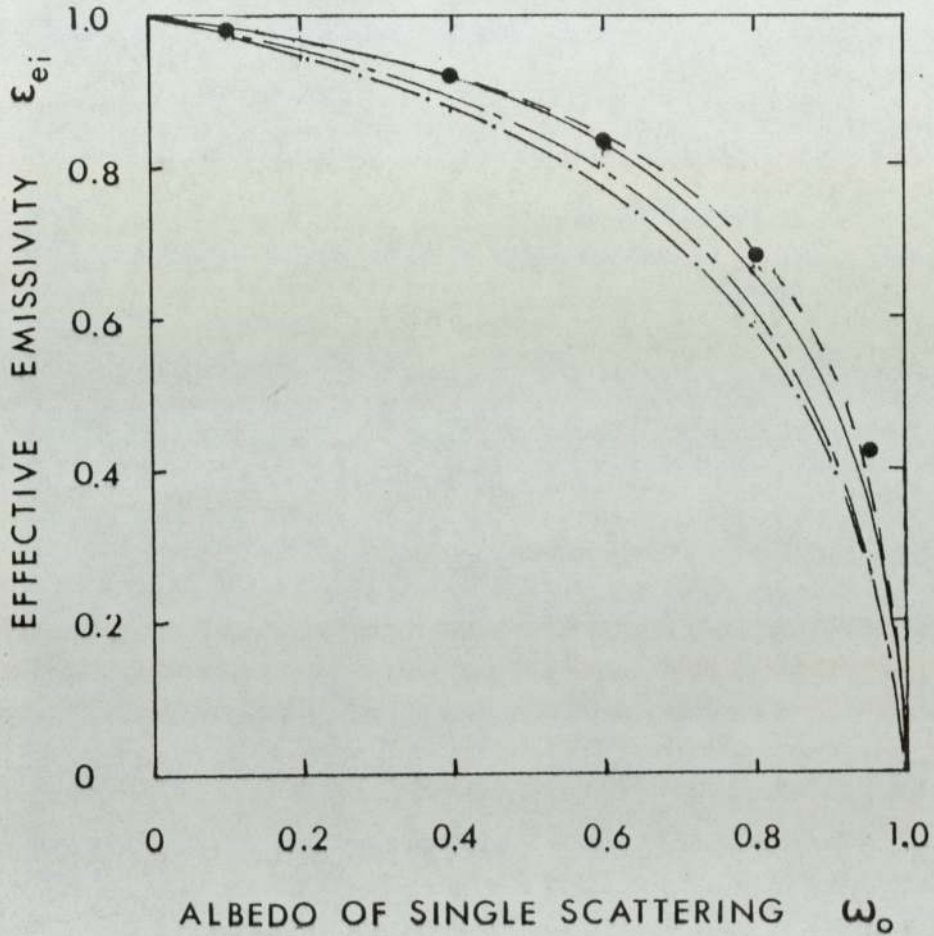


FIG 2.1

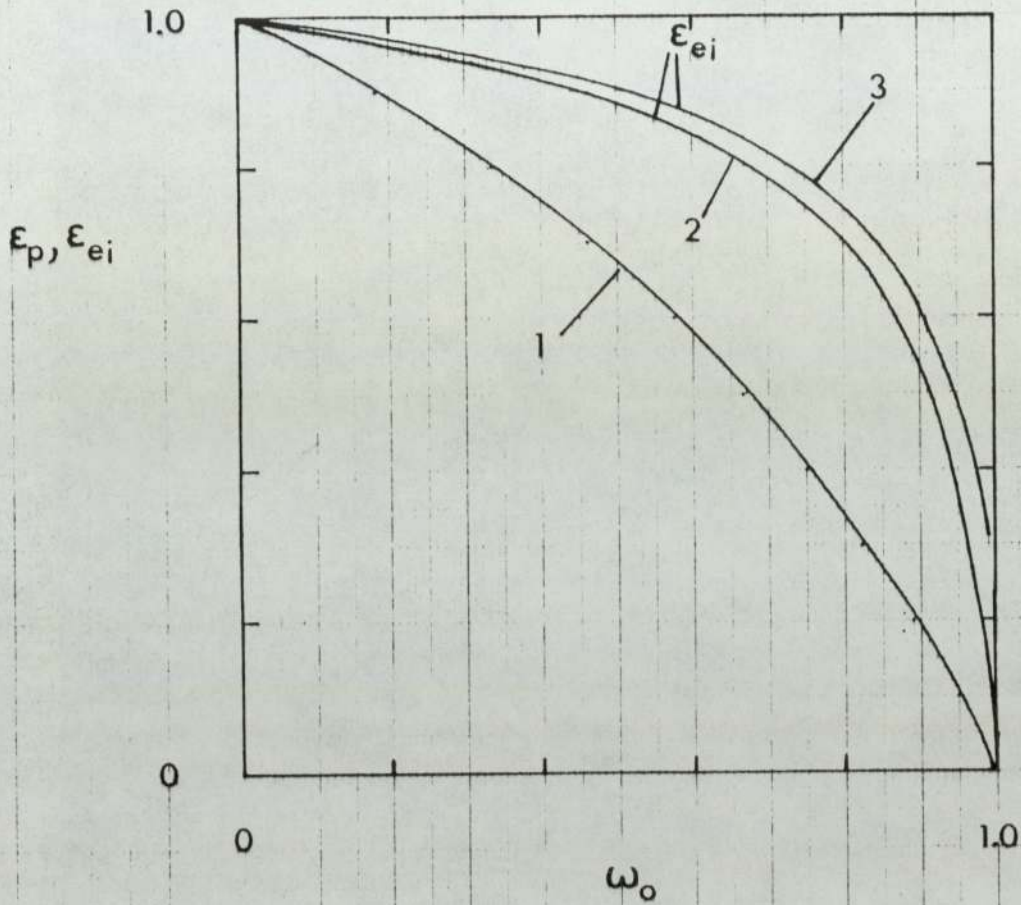
COMPARISON OF APPROXIMATE SOLUTIONS
OF RADIATIVE TRANSFER EQUATION



- | | | |
|-----------|-----------------|-------------------|
| ----- | PRESENT WORK | $\tau_0 = 10.0$ |
| ———— | REF (18) | $\tau_0 = \infty$ |
| - · - · - | REF (21) | $\tau_0 = 10.0$ |
| · · · · | TWO FLUX METHOD | $\tau_0 = 10.0$ |
| ● | REF (12) | $\tau_0 = \infty$ |

FIG. 2.2

EFFECT OF ALBEDO ON PARTICLE
AND EFFECTIVE EMISSIVITY



1,
$$\omega_o = \frac{1}{1 + \frac{\epsilon_p}{2(1 - \epsilon_p)}}$$

2, PRESENT WORK

3, DIFFUSE CONICAL GROOVE [26]

FIG 2.3

EXPERIMENTAL CONFIGURATION FOR U_{mf} DETERMINATION

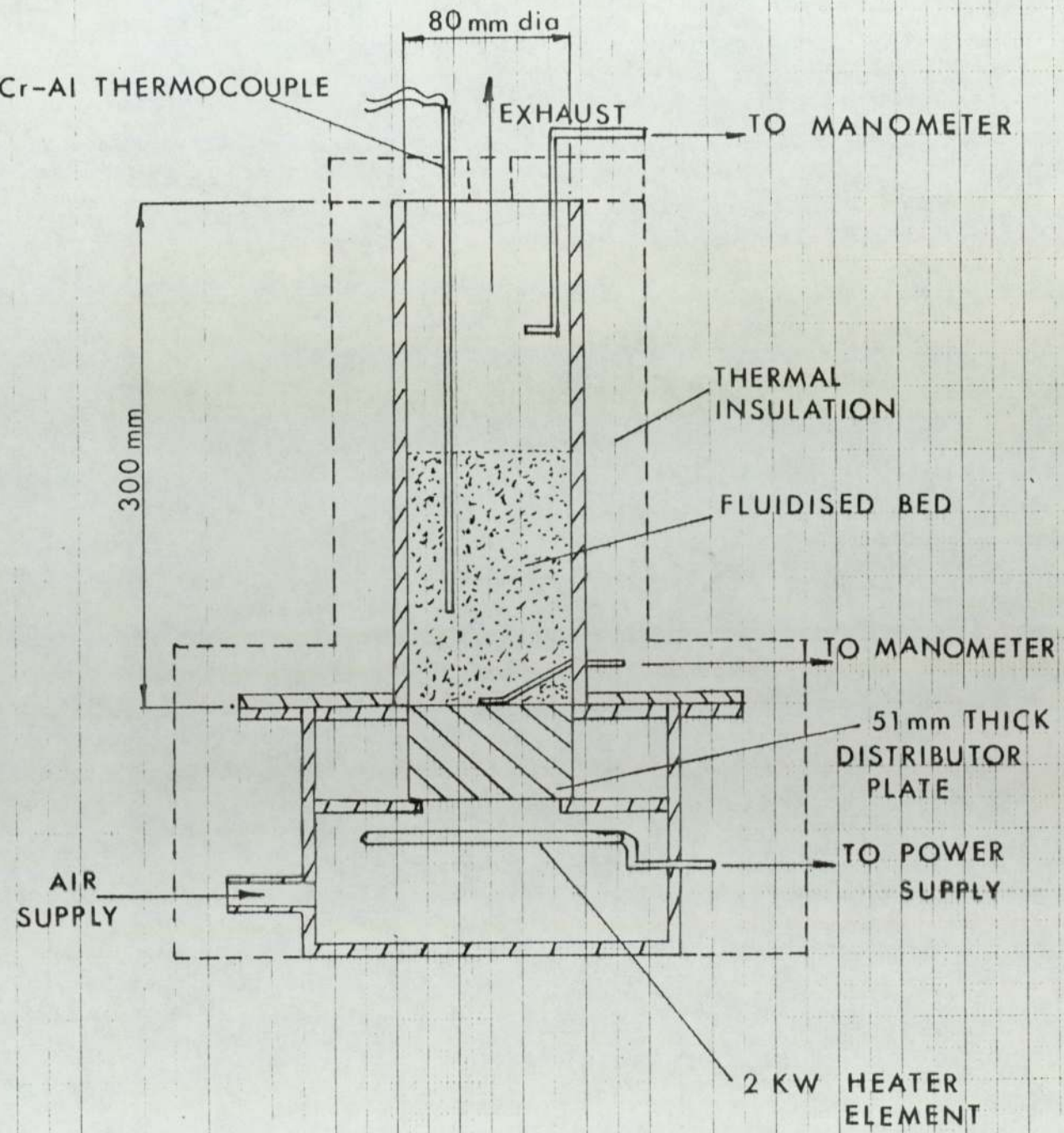


FIG 3.1

EFFECT OF GAS VELOCITY ON BED PRESSURE DROP

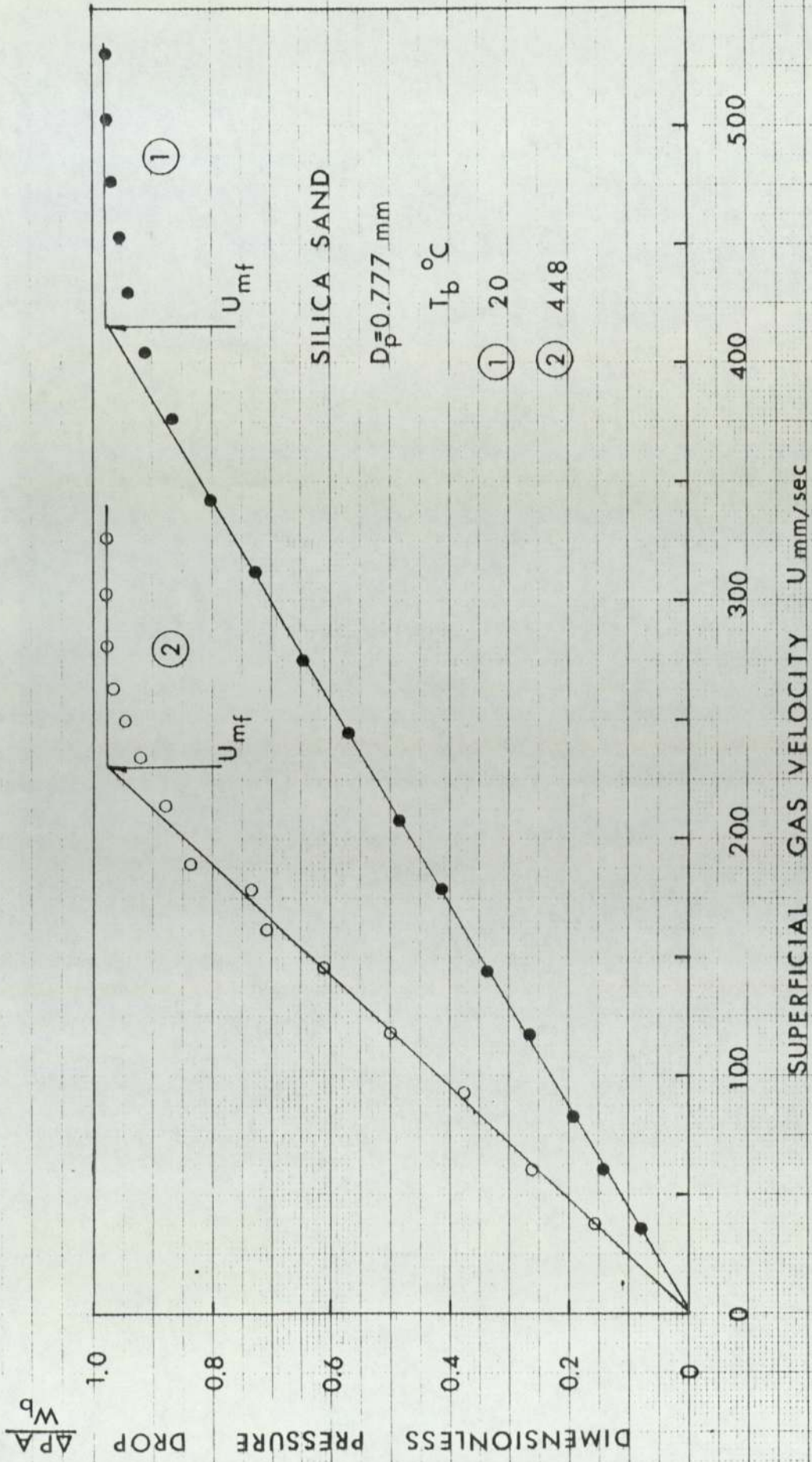


FIG 3.2

TEMPERATURE EFFECT ON MINIMUM FLUIDISING VELOCITY

D_p mm 0.354

MAT^L

● SILICA SAND

○ SILICON CARBIDE

■ ALUMINA

□ MAGNESIA

--- EQN 3.1

— EQN 3.5

MINIMUM FLUIDISING VELOCITY mm/sec

300

200

100

0

100

200

300

400

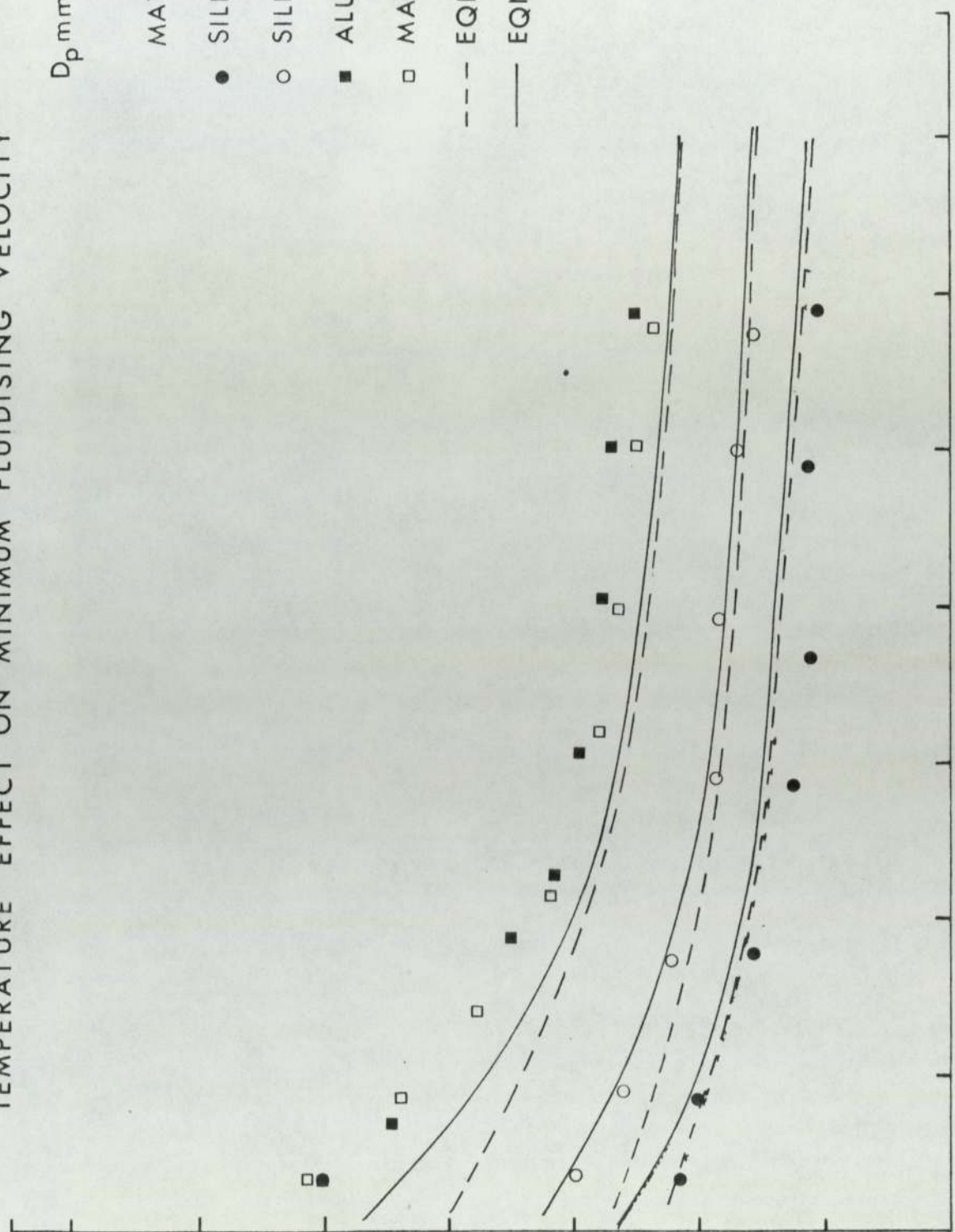
500

600

700

BED TEMPERATURE °C

FIG 3.3a



TEMPERATURE EFFECT ON MINIMUM FLUIDISING VELOCITY

D_p mm 0.55

MATL

● SILICA SAND

○ SILICON CARBIDE

■ ALUMINA

□ MAGNESIA

--- EQN 3.1

— EQN 3.5

MINIMUM FLUIDISING VELOCITY mm/sec

BED TEMPERATURE °C

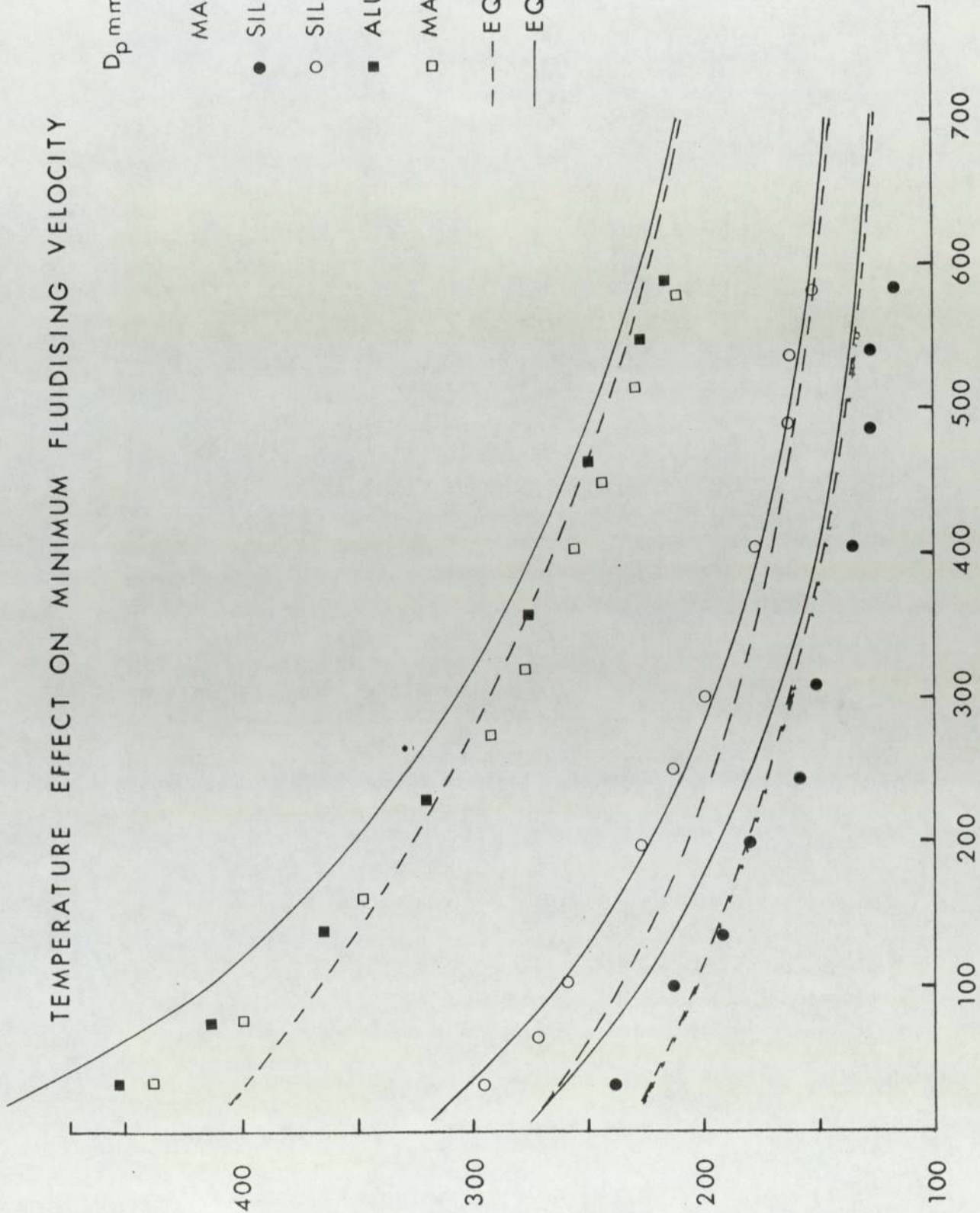


FIG 3.3b

TEMPERATURE EFFECT ON MINIMUM FLUIDISING VELOCITY

D_p mm 0.777

MAT'L

- SILICA SAND
- SILICON CARBIDE
- ALUMINA
- MAGNESIA

- EQN 3.1
- EQN 3.5

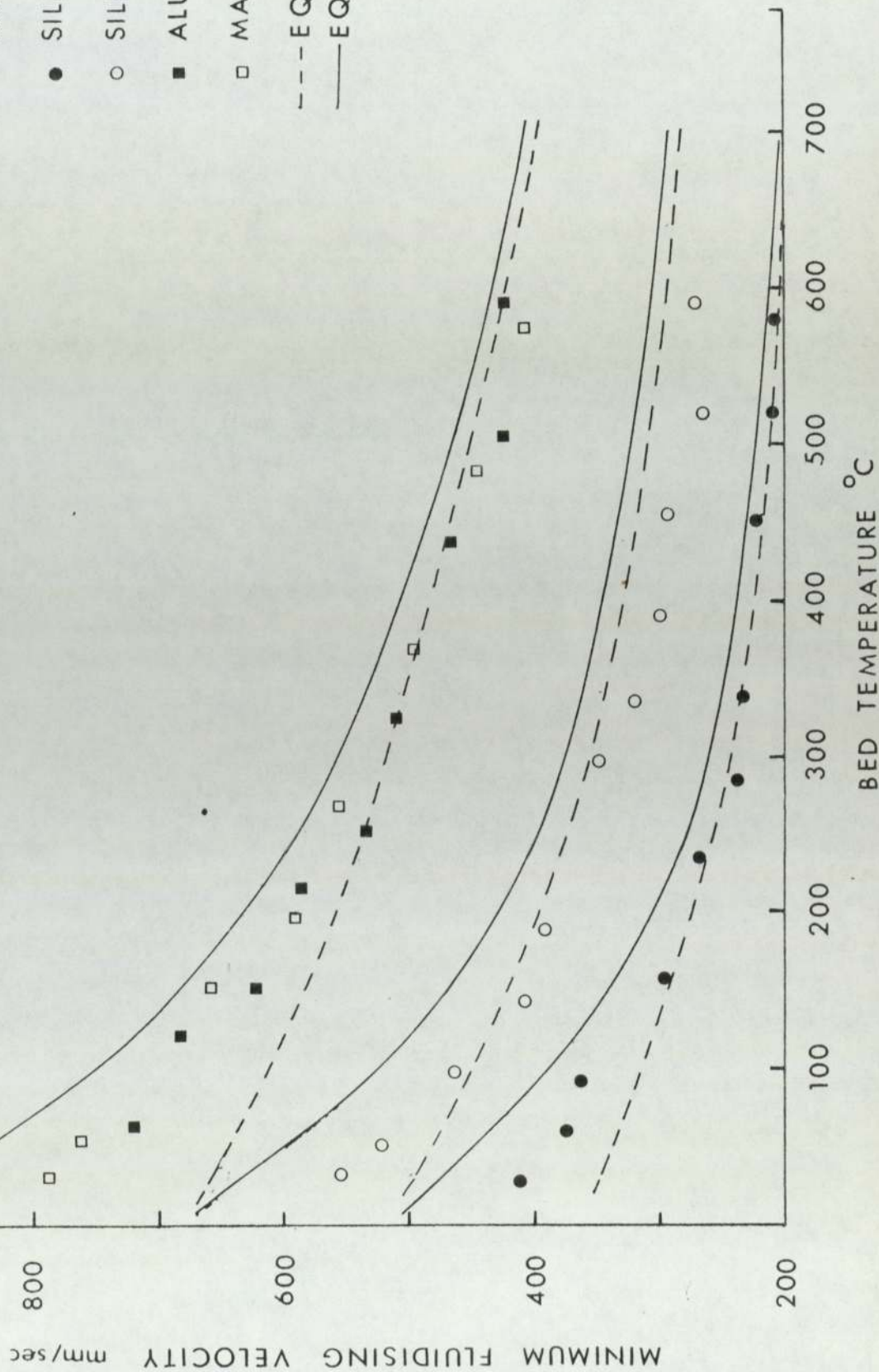
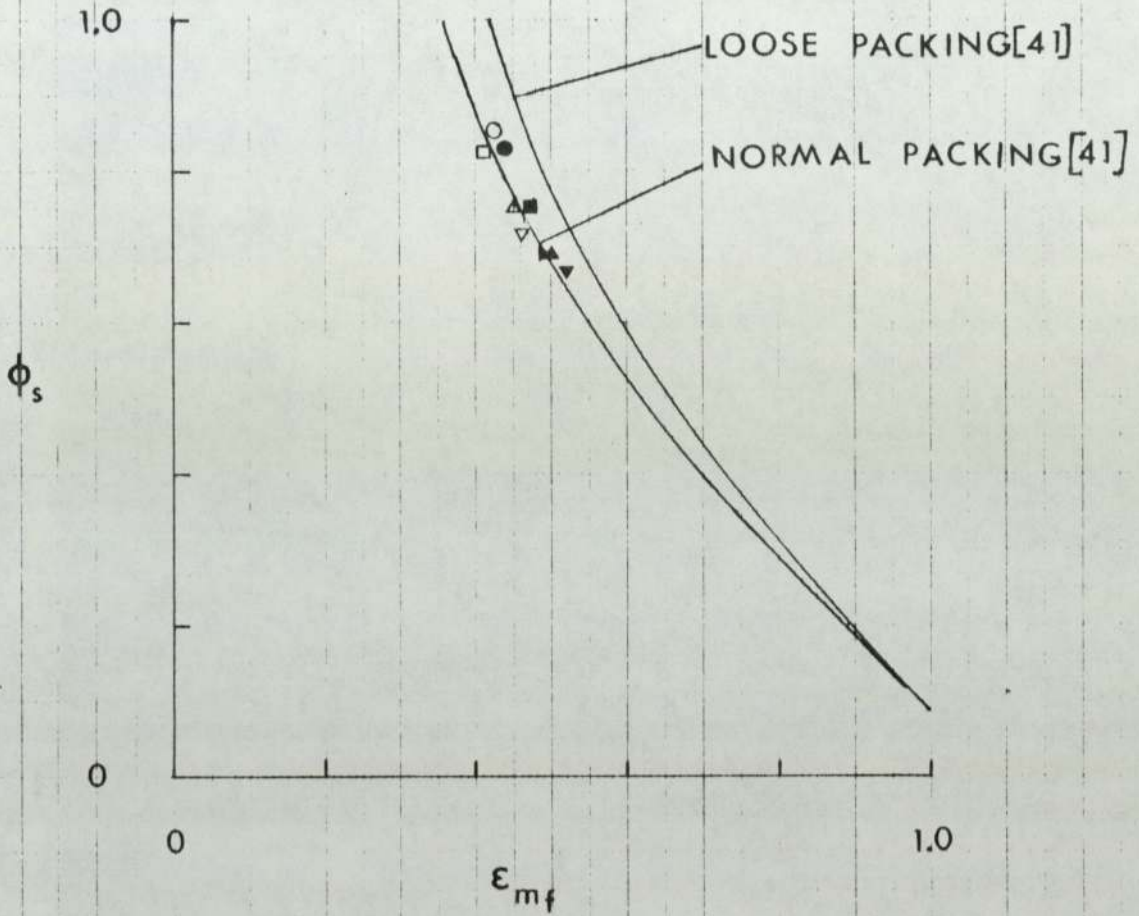


FIG 3.3c

PARTICLE SPHERICITY Vs MINIMUM VOIDAGE

FROM [41]



Symbol	MAT ^L	D_p mm
●	SAND	0.354
○		0.55
□		0.777
▼	ALUMINA	0.354
▲		0.55
▶		0.777
■	SILICON CARBIDE	0.354
▽		0.55
△		0.777

FIG 3.4

CONFIGURATION FOR PARTICLE
EMISSIVITY MEASUREMENT

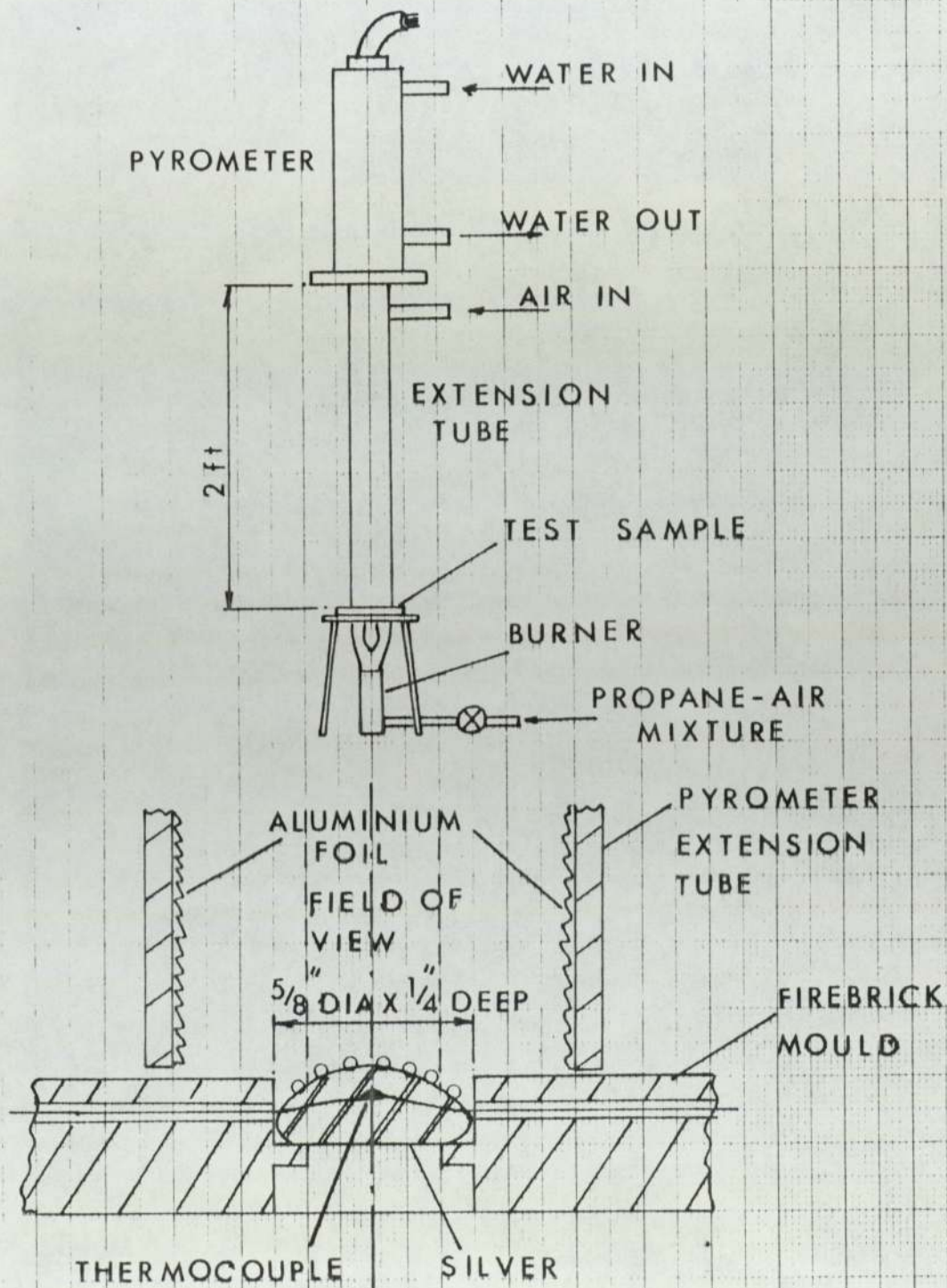


FIG 3.5

DETAIL OF TEST SAMPLE

VARIATION OF SAMPLE EMISSIVITY WITH TEMPERATURE

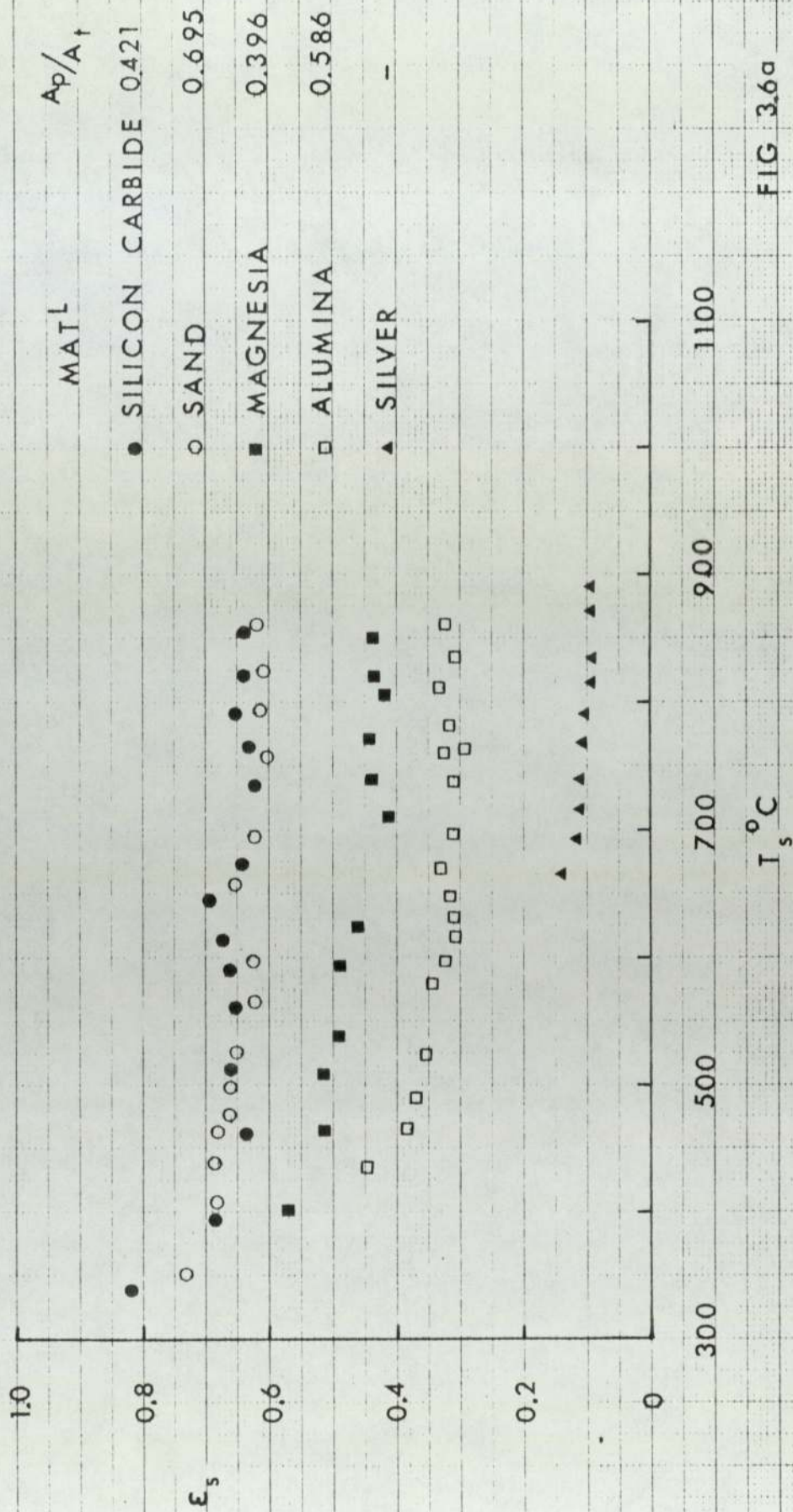
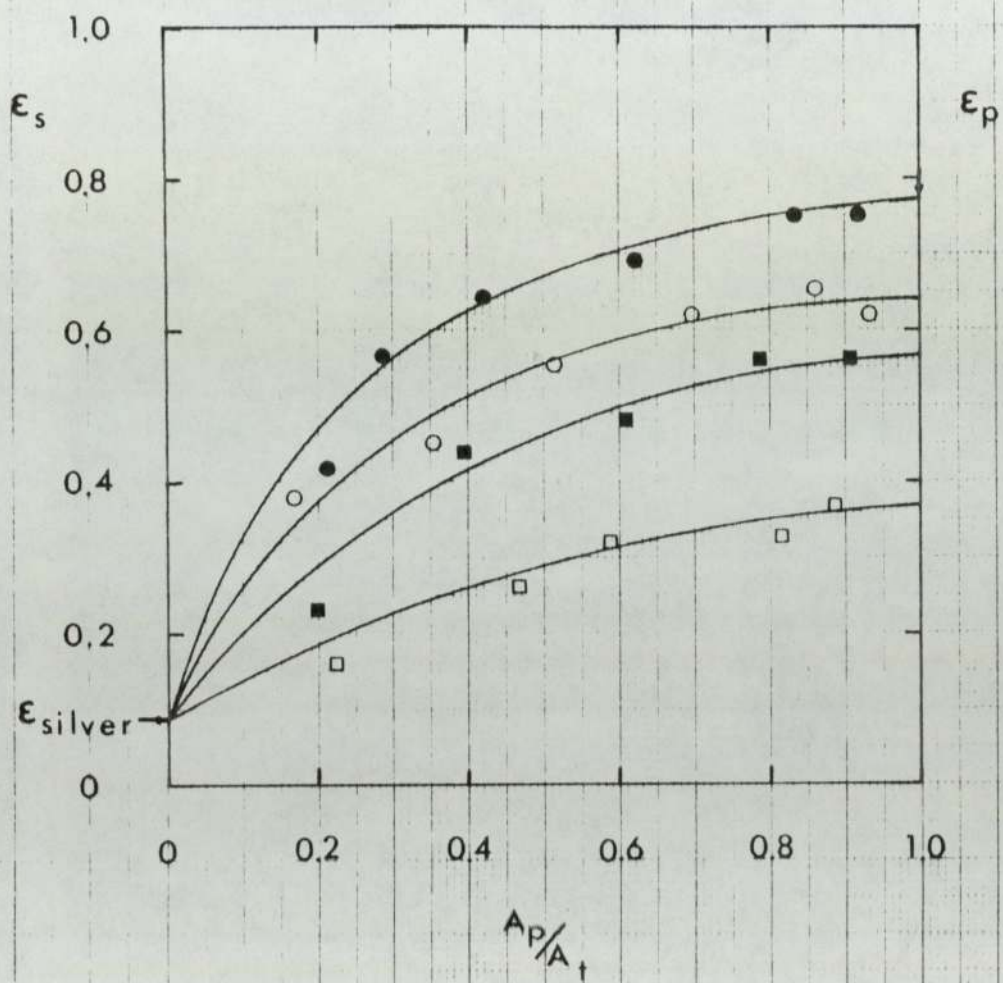


FIG 3.6a

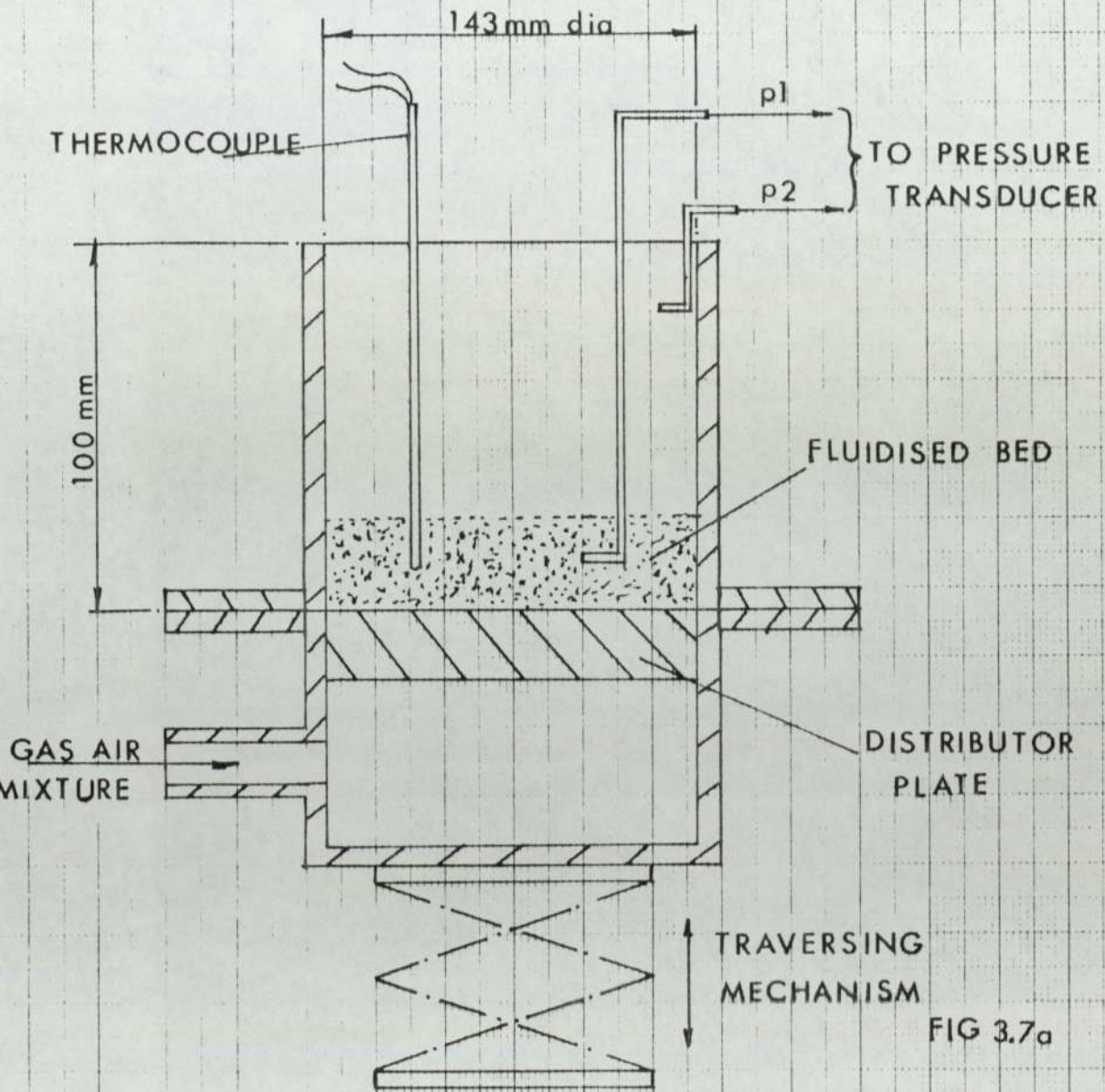
VARIATION OF SAMPLE EMISSIVITY
WITH PARTICLE AREA FRACTION



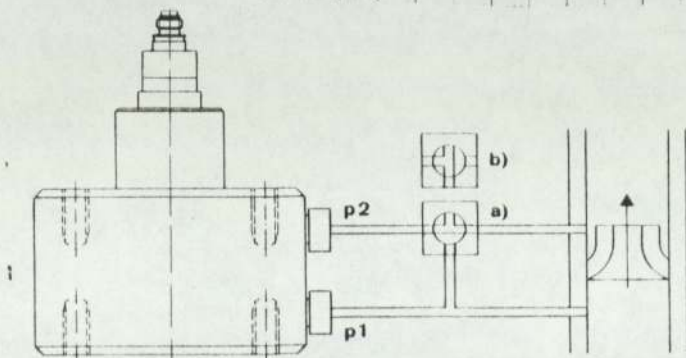
	MAT ^L	T _s °C
○	SILICA SAND	860
●	SILICON CARBIDE	855
■	MAGNESIA	853
□	ALUMINA	863

FIG 3.6b

CONFIGURATION FOR MEASUREMENT OF BED
PRESSURE DROP DISTRIBUTION



DIFFERENTIAL PRESSURE TRANSDUCER



U-V-R TRACE OF TRANSDUCER OUTPUT AT
DIFFERENT PROBE POSITIONS IN A FLUIDISED BED

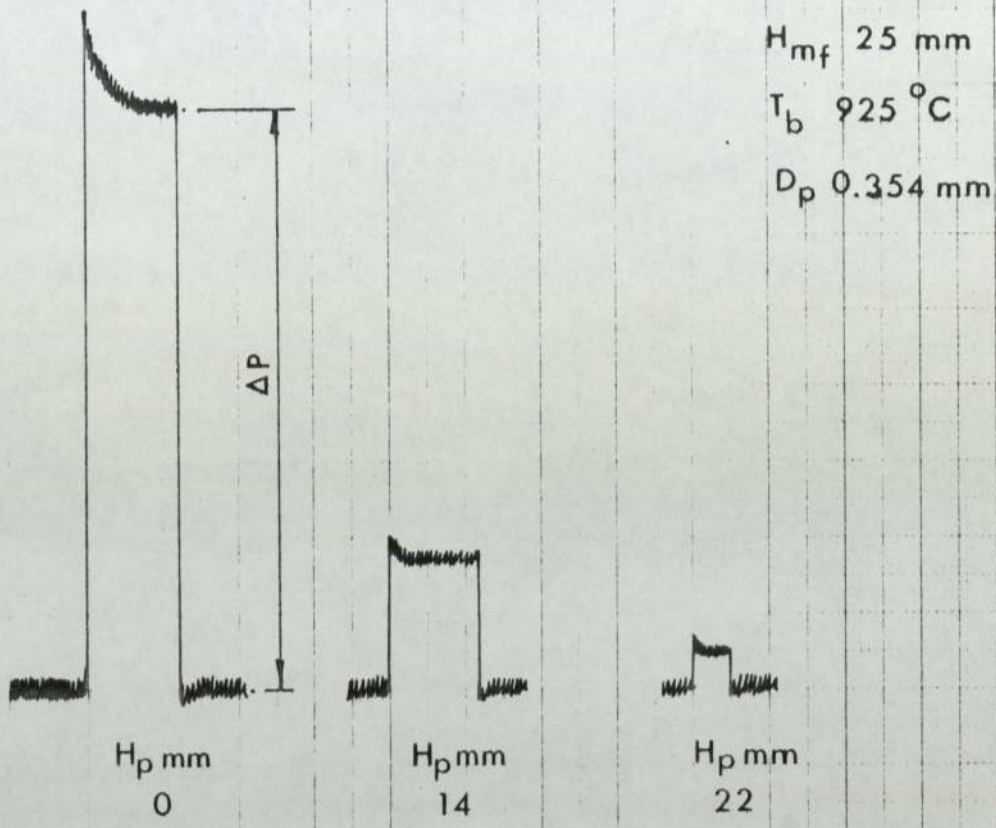


FIG 3.8

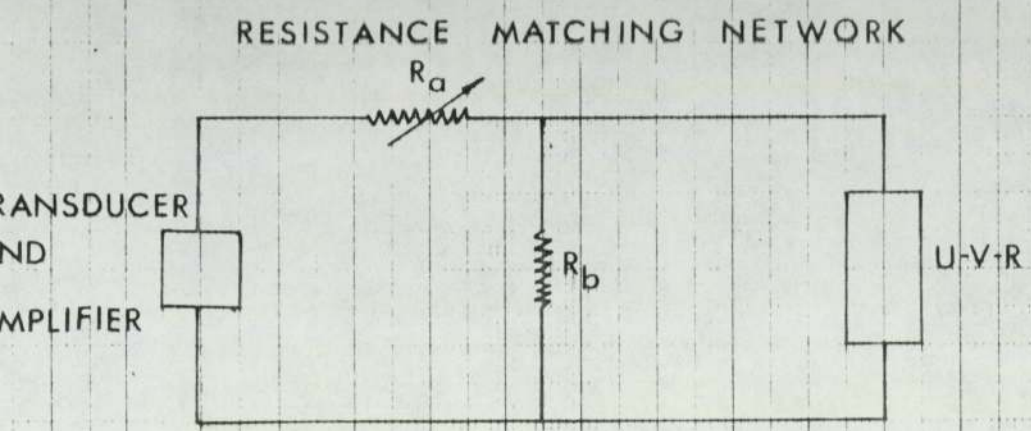
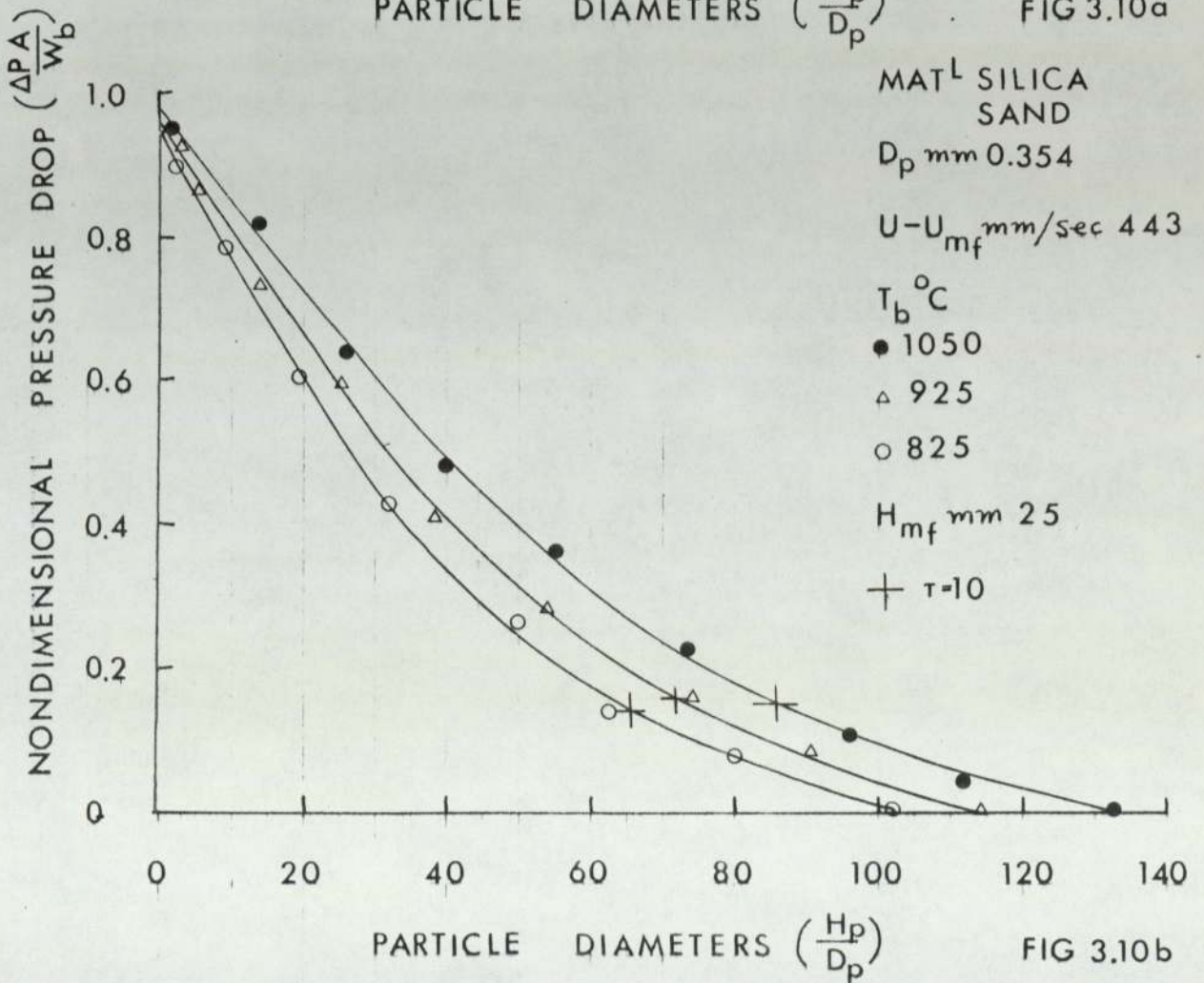
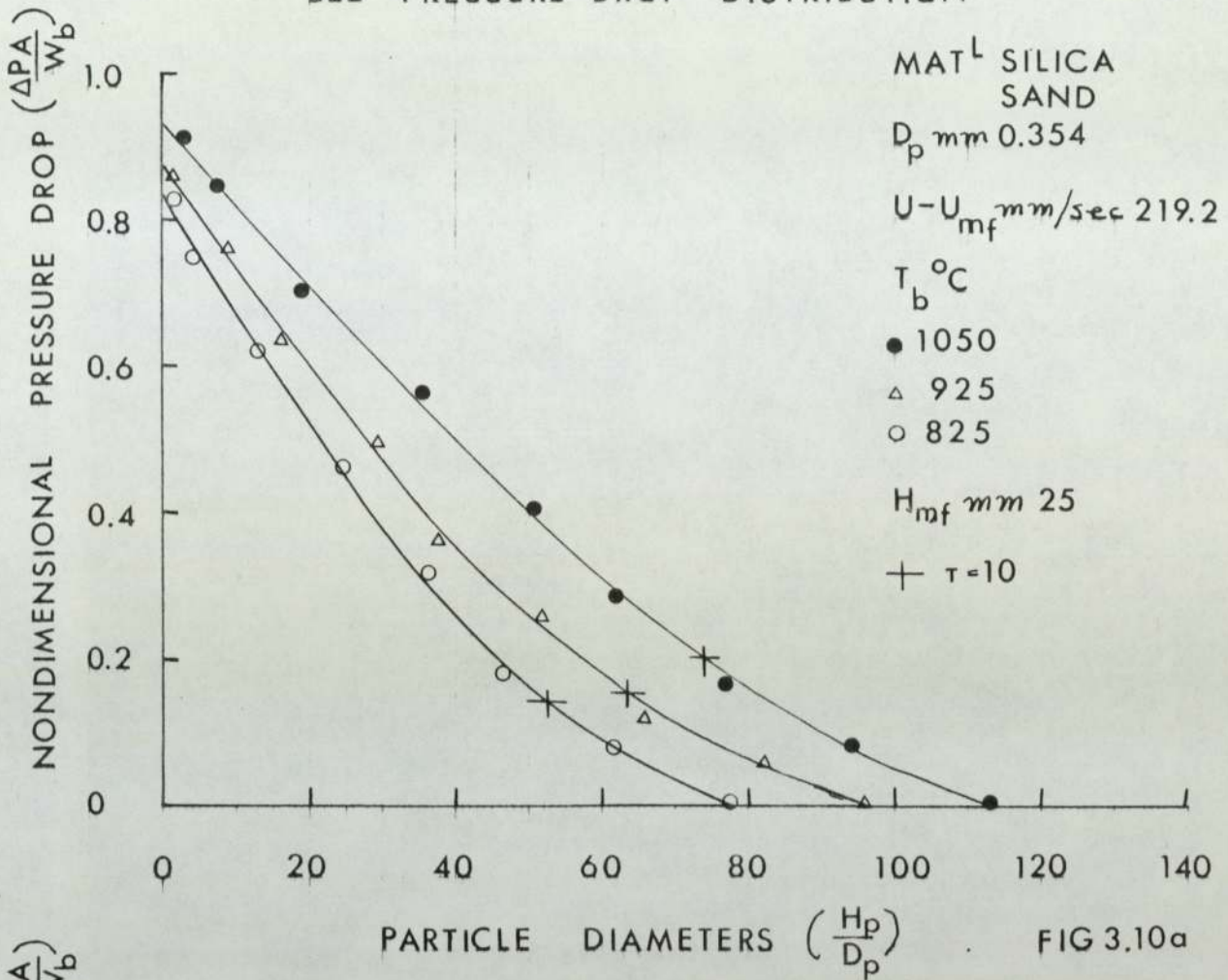
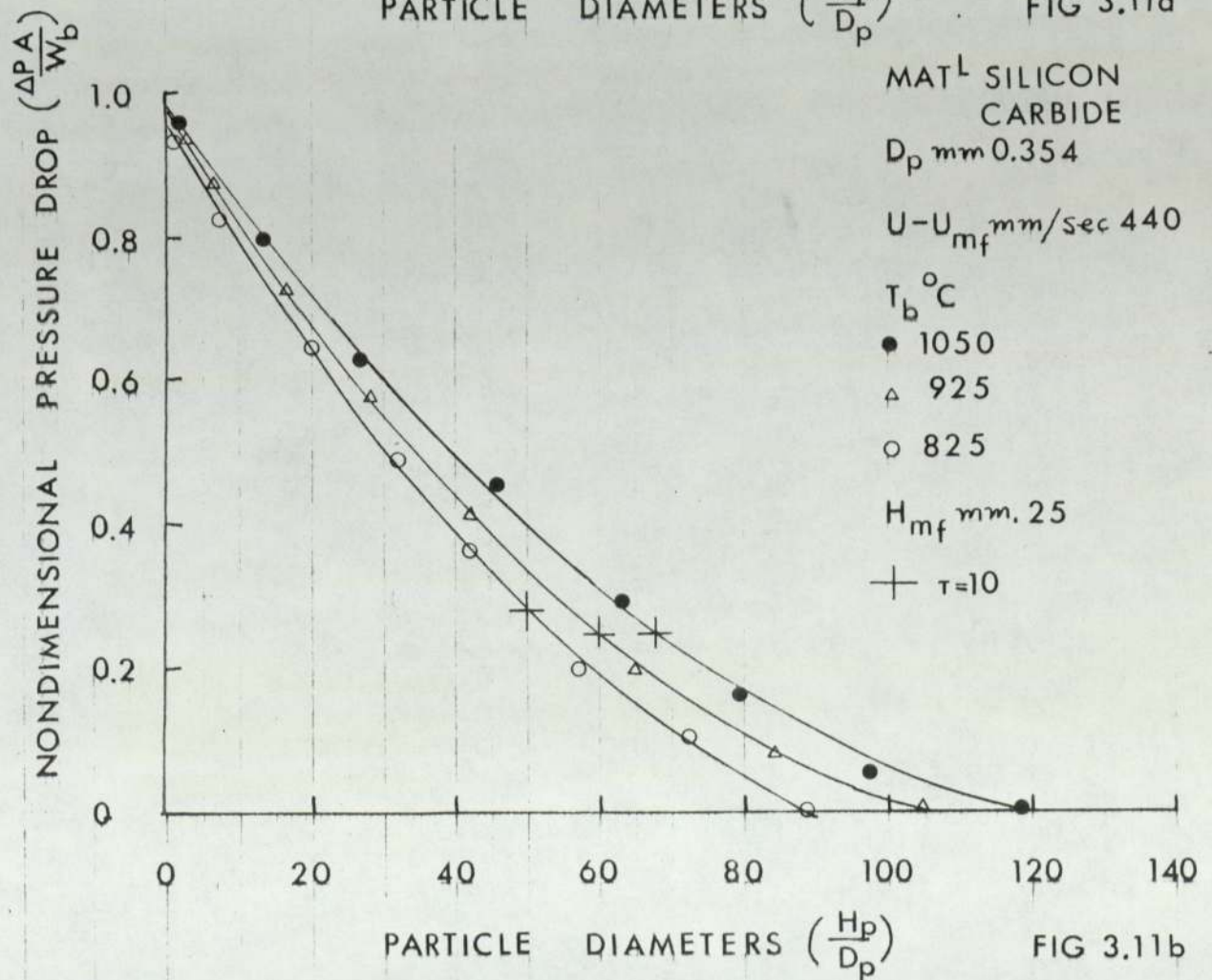
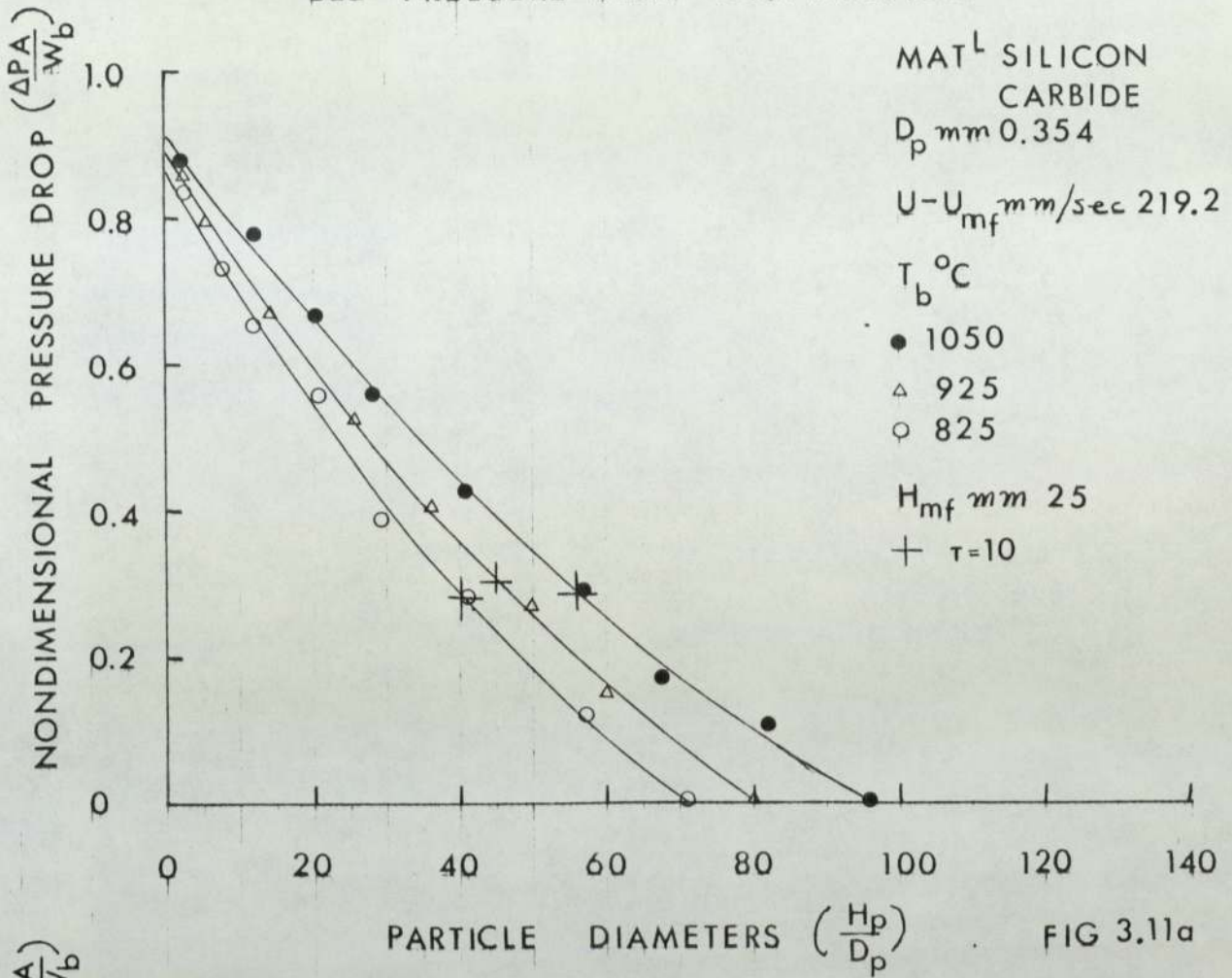


FIG 3.9

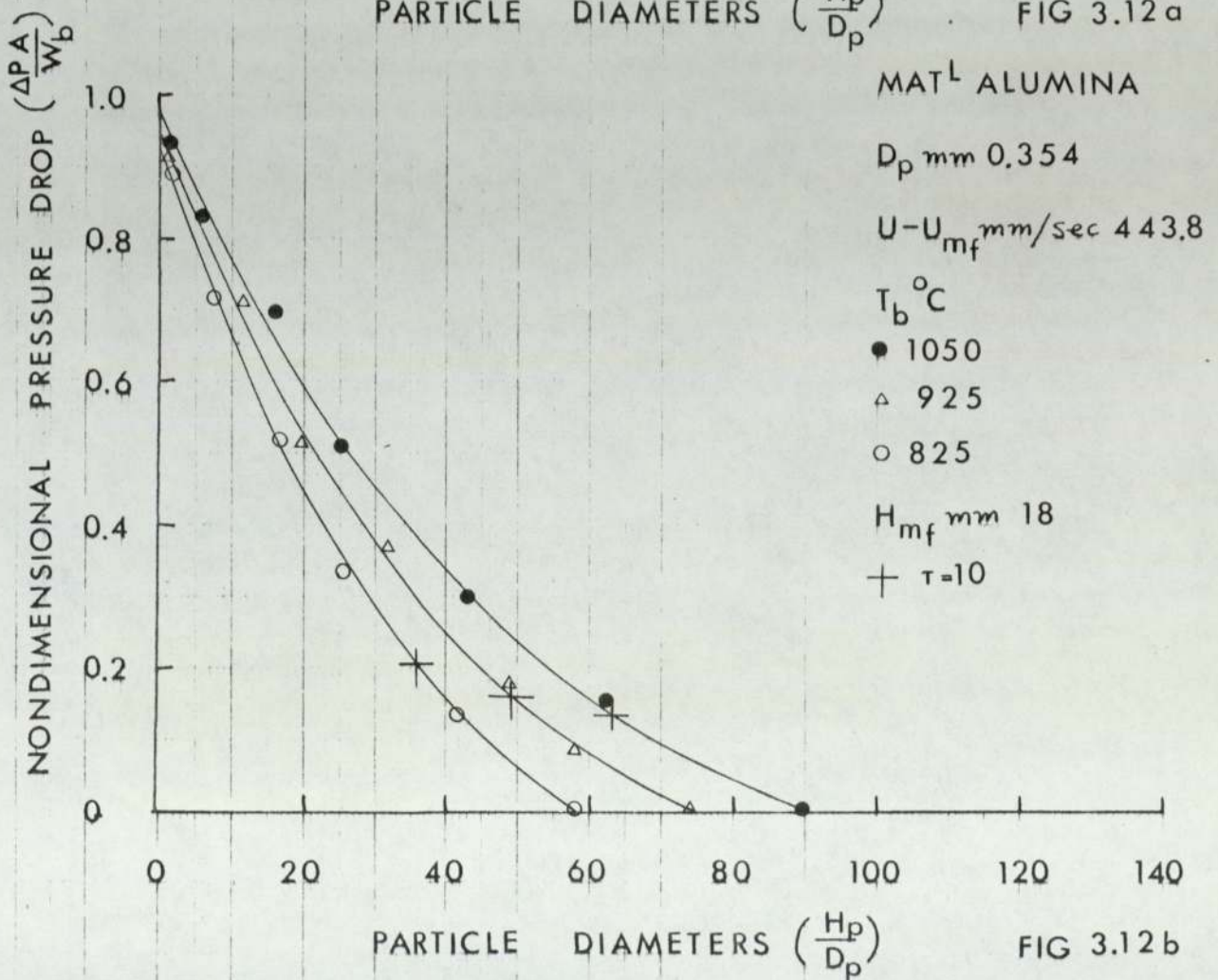
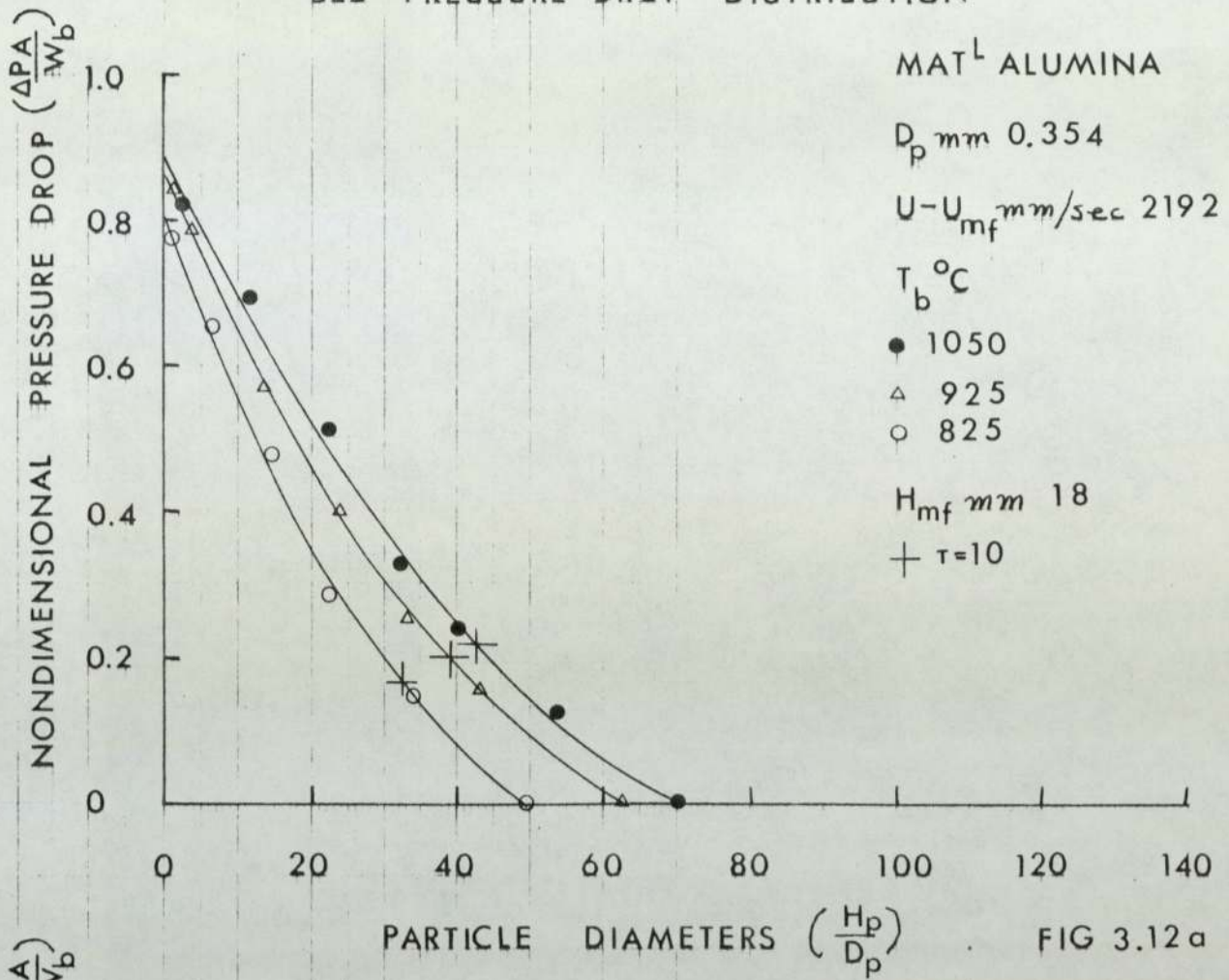
BED PRESSURE DROP DISTRIBUTION



BED PRESSURE DROP DISTRIBUTION



BED PRESSURE DROP DISTRIBUTION



EFFECT OF EXCESS GAS VELOCITY AND BED TEMPERATURE

ON EXTINCTION COEFFICIENT

MAT^L SILICA SAND
 D_p 0.354 mm
 H_{mf} 25 mm
 T_b °C ϵ_p
 ● 825 0.64
 ○ 925
 ▼ 1050

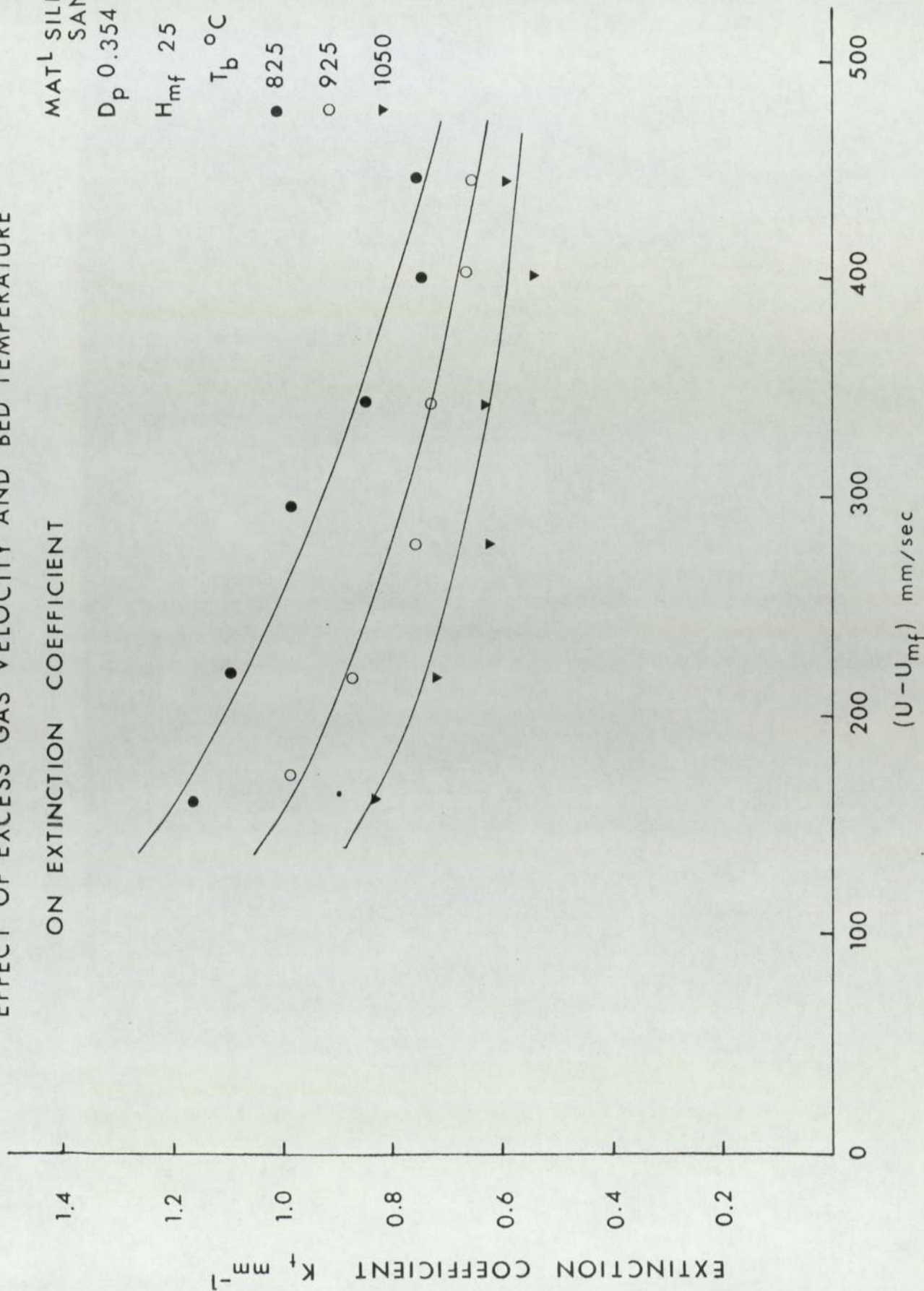


FIG 3.13

EFFECT OF EXCESS GAS VELOCITY AND BED TEMPERATURE

ON EXTINCTION COEFFICIENT

MAT^L SILICON
CARBIDE

D_p 0.354 mm

H_{mf} 25 mm

T_b °C ϵ_p

● 825 0.77

○ 925

▼ 1050

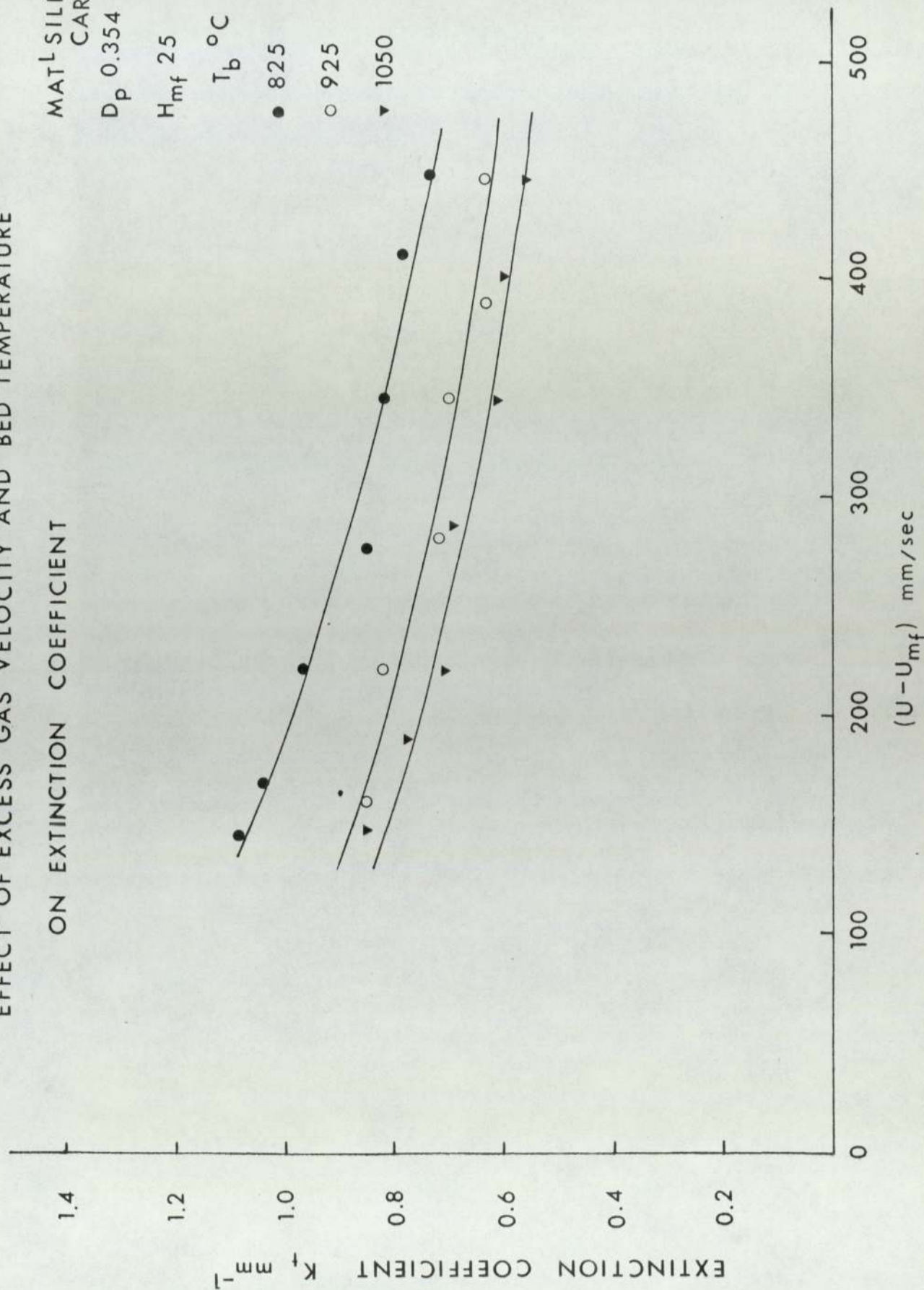


FIG 3.14

EFFECT OF EXCESS GAS VELOCITY AND BED TEMPERATURE

ON EXTINCTION COEFFICIENT

MAT^L ALUMINA

D_p 0.354 mm

H_{mf} 18 mm

T_b °C ϵ_p

● 825 0.37

○ 925

▼ 1050

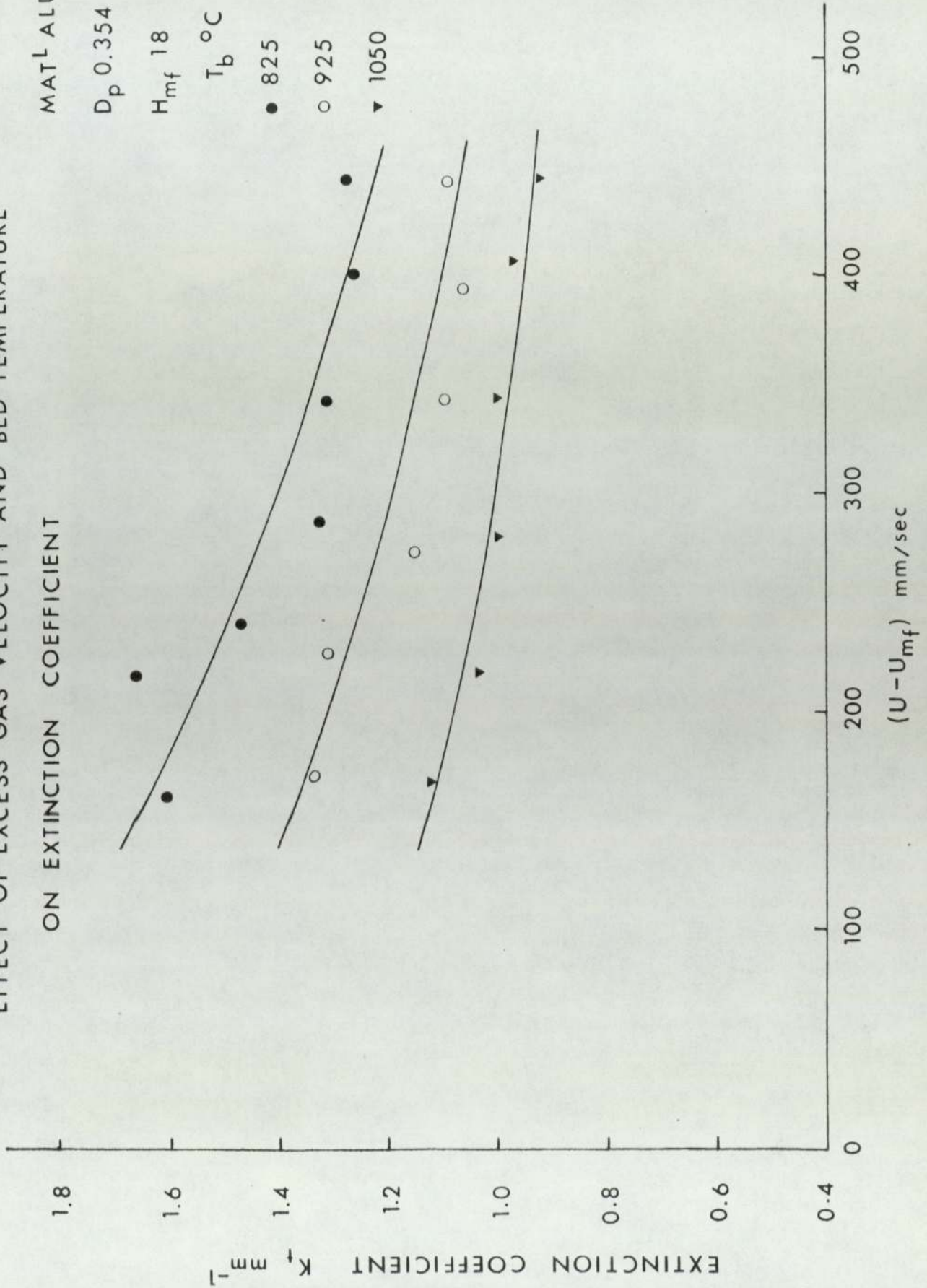


FIG 3.15

EFFECT OF EXCESS GAS VELOCITY AND BED TEMPERATURE
ON EXTINCTION COEFFICIENT

MAT^L SILICA SAND

D_p 0.55 mm

H_{mf} 25 mm

T_b °C ϵ_p
 ● 825 0.64
 ○ 925
 ▼ 1050

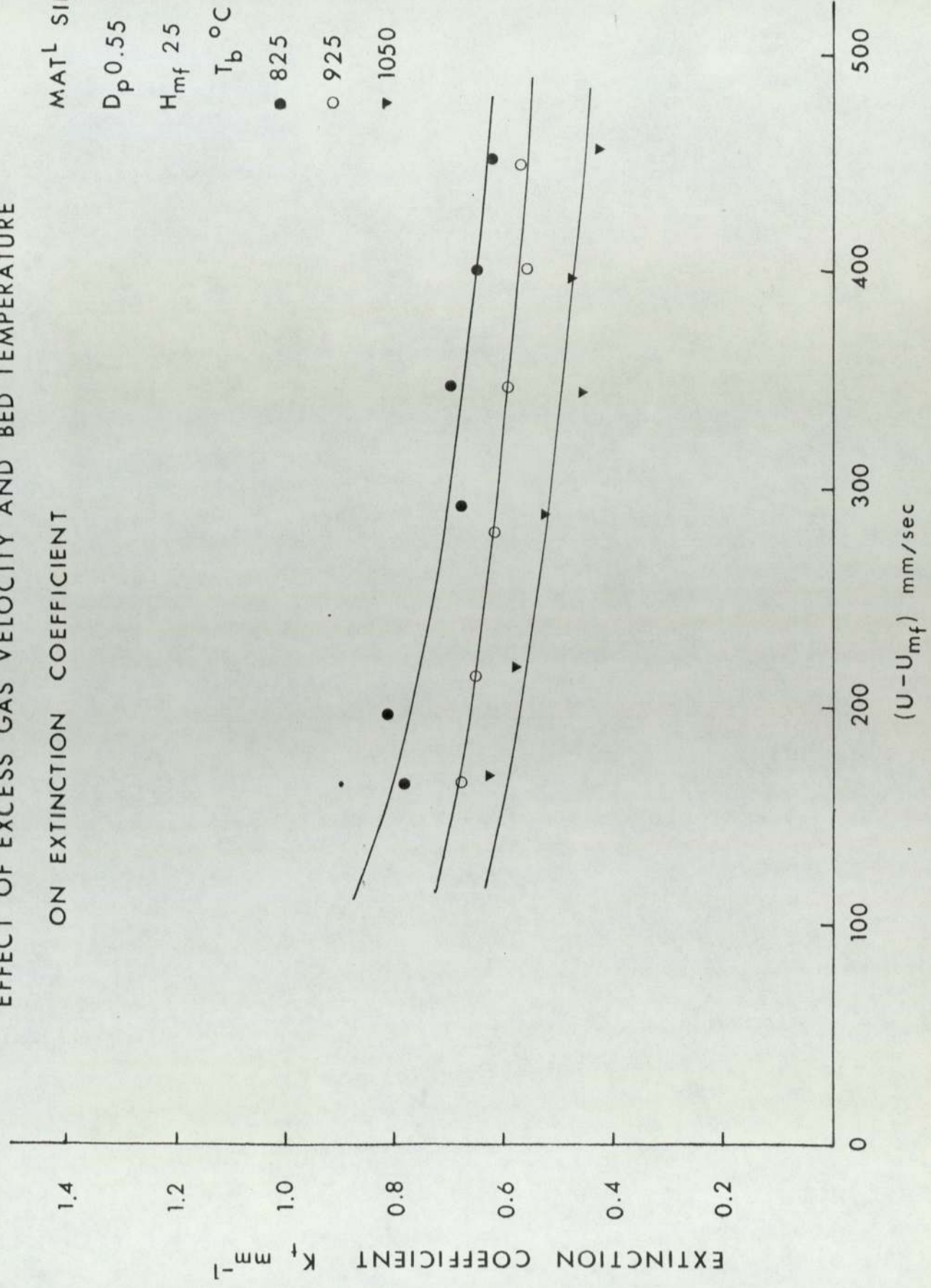


FIG 3.16

EFFECT OF EXCESS GAS VELOCITY AND BED TEMPERATURE

ON EXTINCTION COEFFICIENT

MAT^L SILICON
CARBIDE
 D_p 0.55 mm
 H_{mf} 25 mm
 T_b °C ϵ_p
 ● 825 0.77
 ○ 925
 ▼ 1050

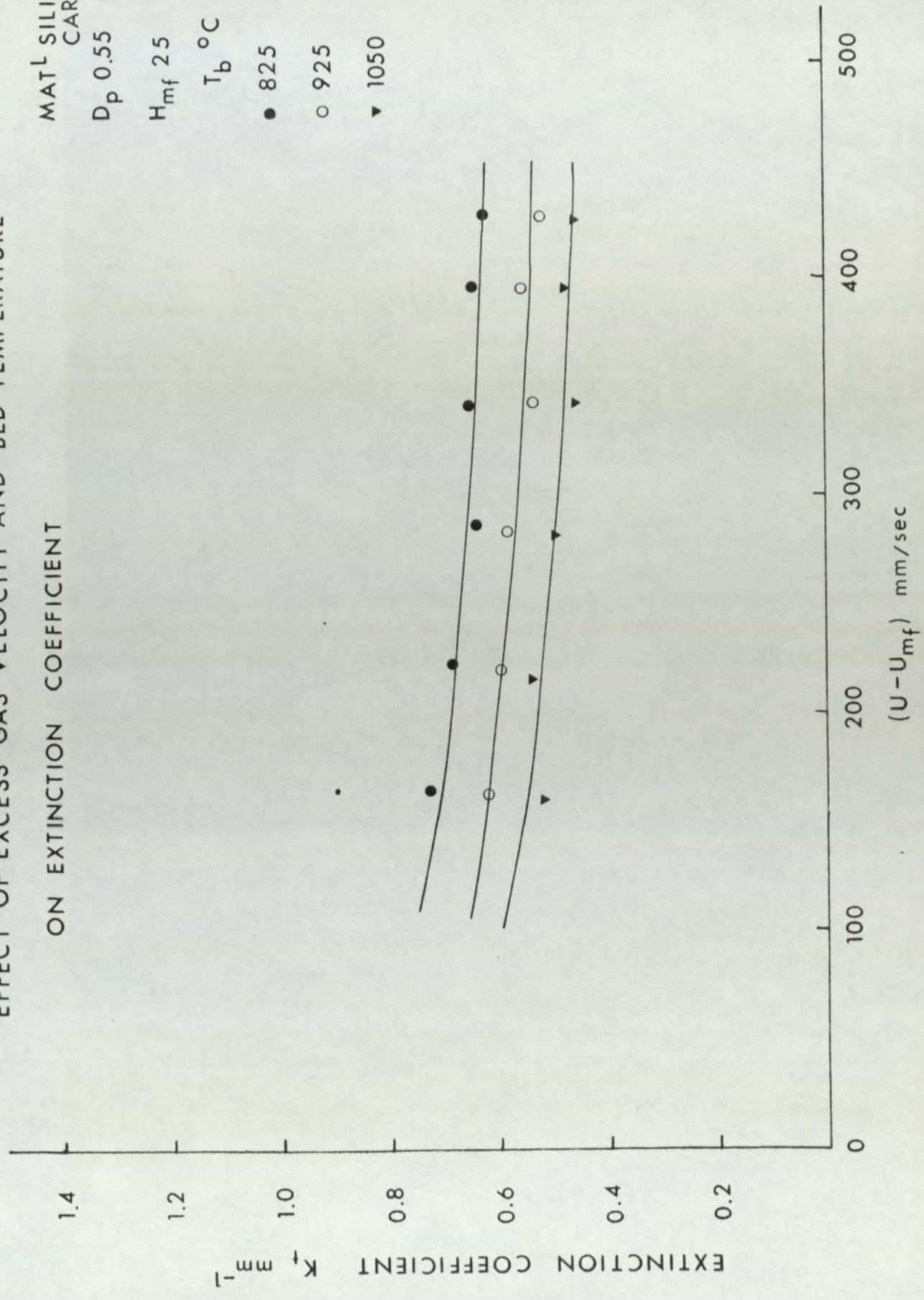


FIG 3.17

EFFECT OF EXCESS GAS VELOCITY AND BED TEMPERATURE
ON EXTINCTION COEFFICIENT

MAT^L ALUMINA
 D_p 0.55 mm
 H_{mf} 18 mm
 T_b °C ϵ_p
 ● 825 0.37
 ○ 925
 ▼ 1050

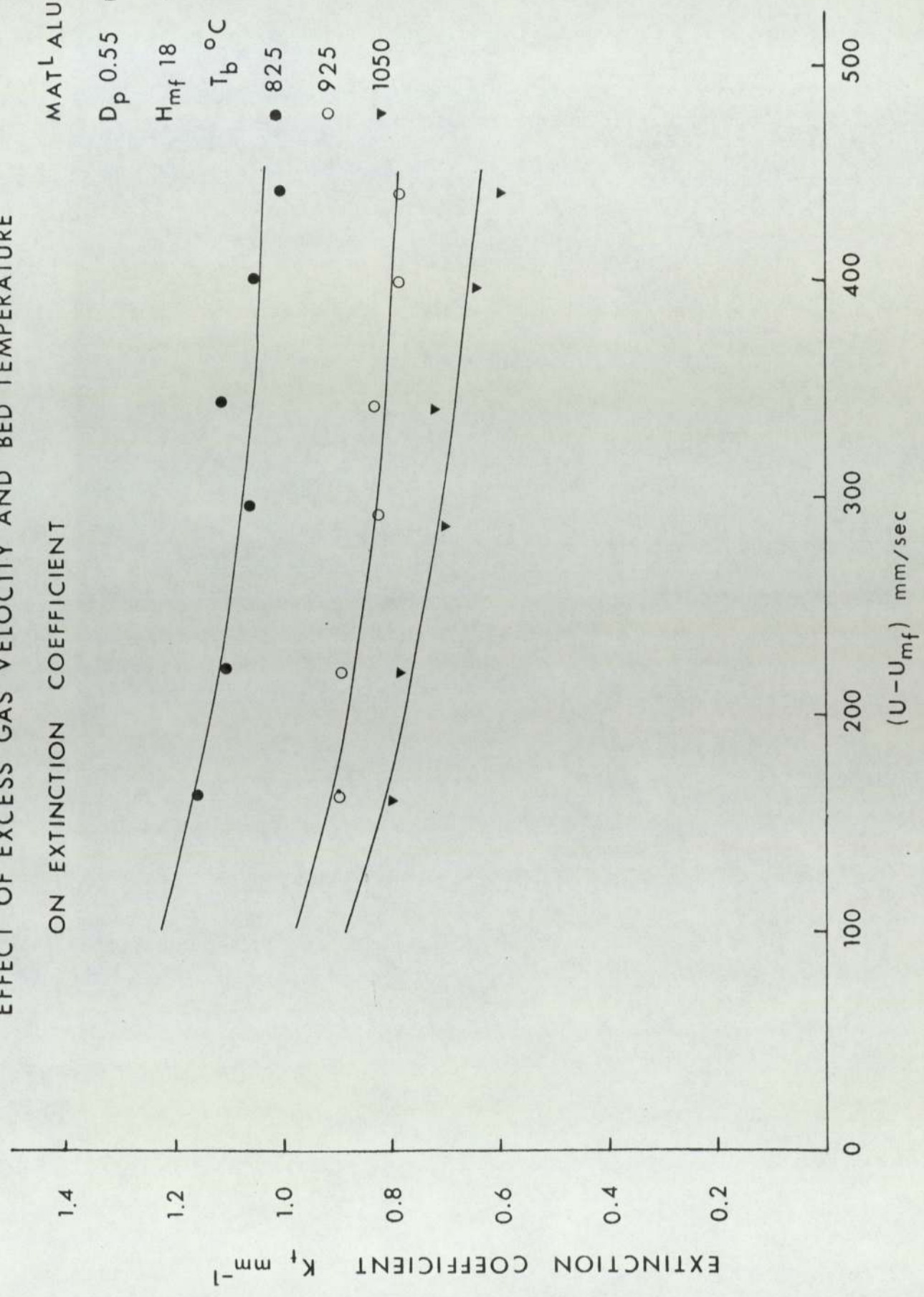


FIG 3.18

EFFECT OF EXCESS GAS VELOCITY AND BED TEMPERATURE
ON EXTINCTION COEFFICIENT

MAT^L SILICA
SAND

D_p 0.777 mm

H_{mf} 25 mm

T_b °C ϵ_p

● 825 0.64

○ 925

▼ 1050

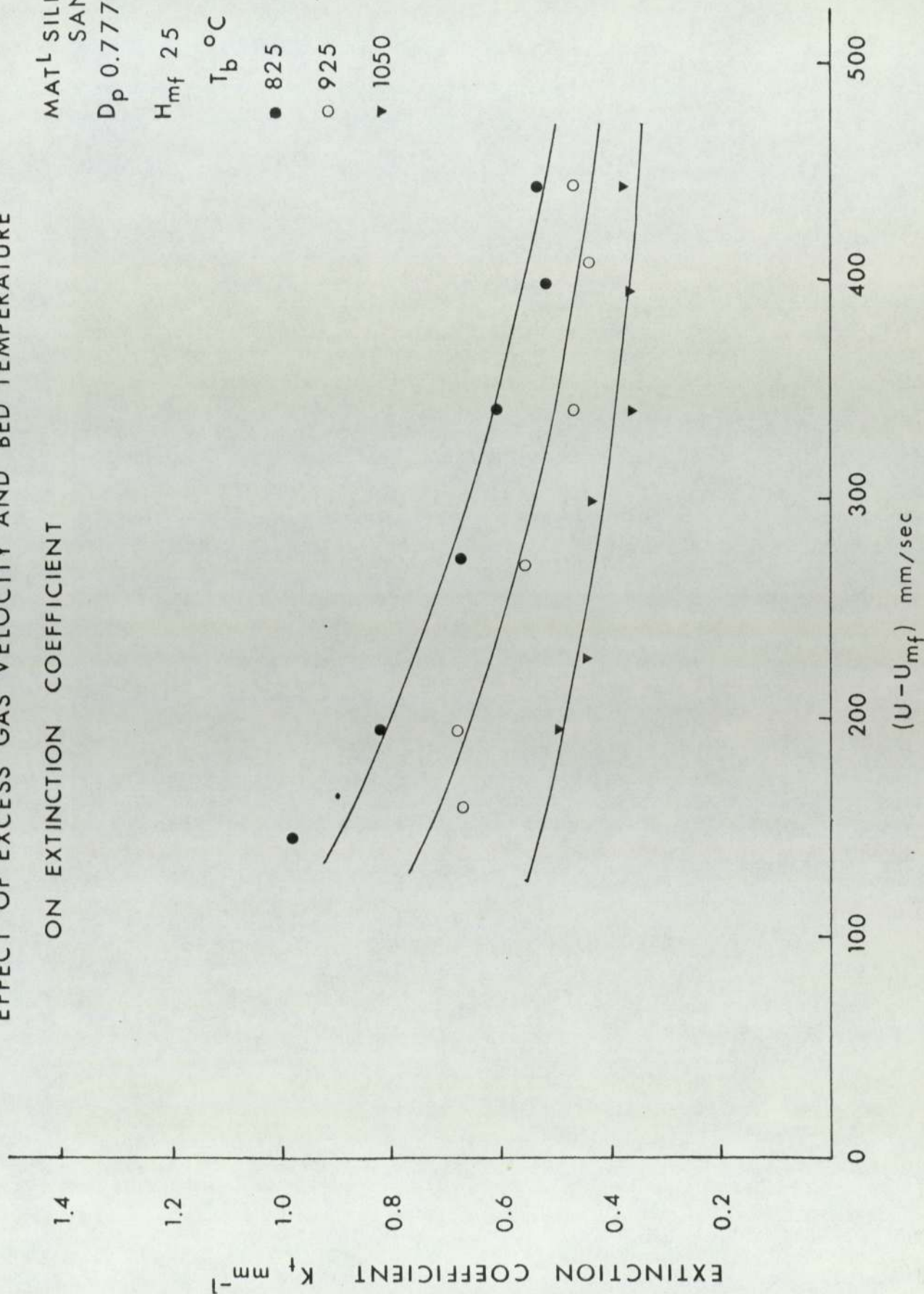


FIG 3.19

EFFECT OF EXCESS GAS VELOCITY AND BED TEMPERATURE
ON EXTINCTION COEFFICIENT

MAT^L SILICON
CARBIDE
 D_p 0.777 mm

H_{mf} 25 mm

T_b °C ϵ_p
● 825 ○ 0.77
○ 925
▼ 1050

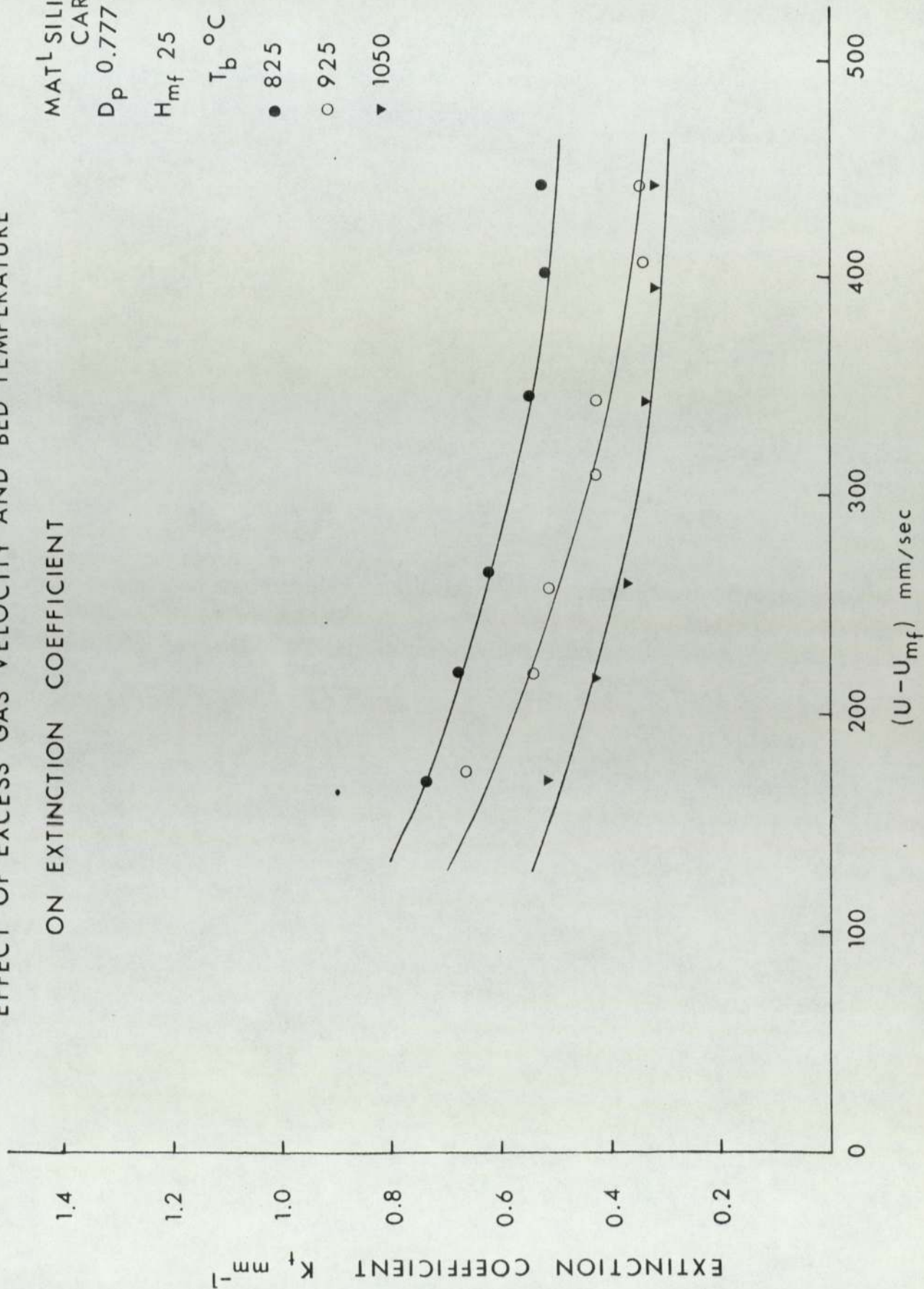


FIG 3.20

EFFECT OF EXCESS GAS VELOCITY AND BED TEMPERATURE
ON EXTINCTION COEFFICIENT

MAT^L ALUMINA

D_p 0.777 mm

H_{mf} 18 mm

T_b °C ϵ_p

● 825 0.37

○ 925

▼ 1050

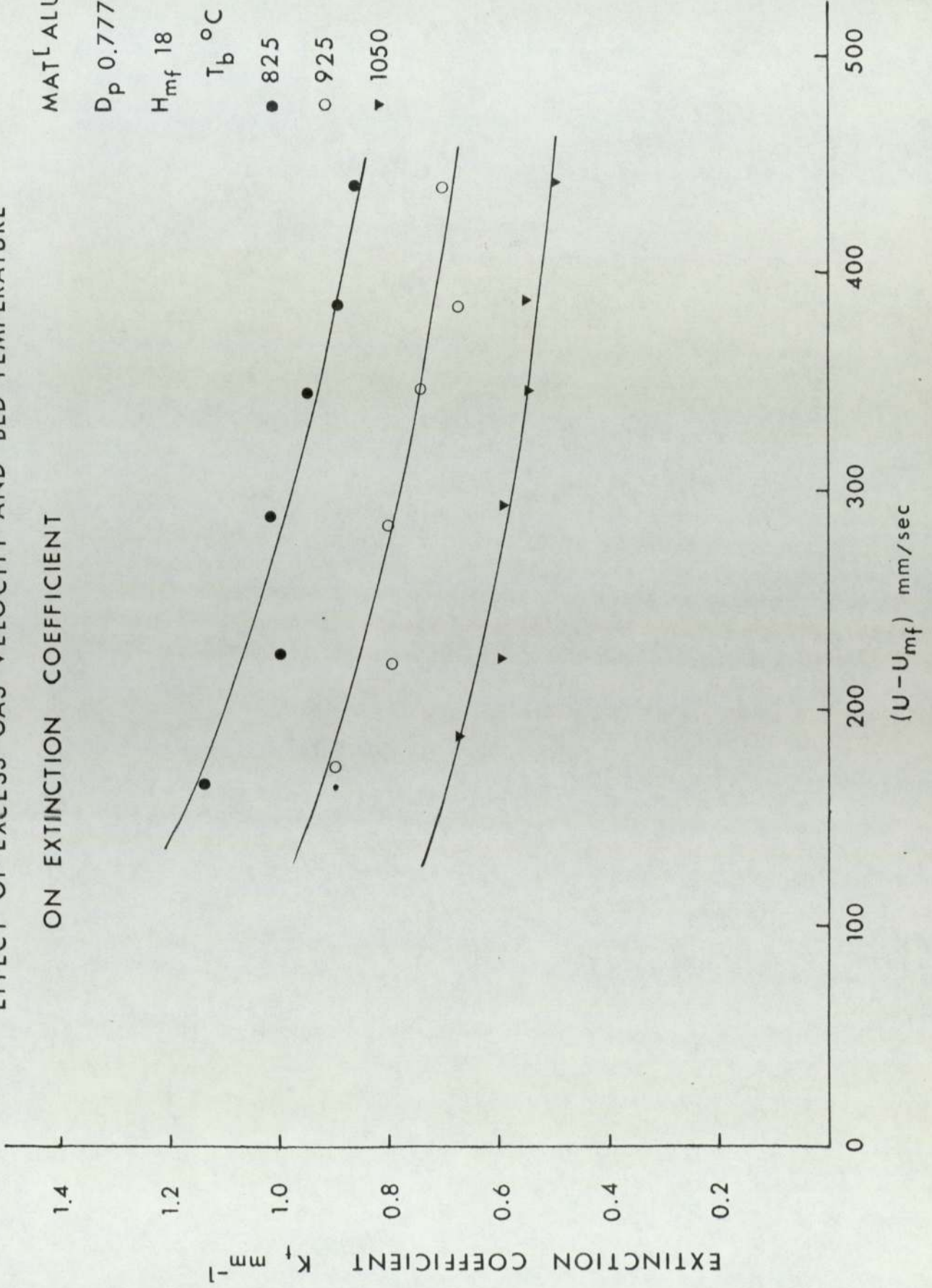


FIG 3.21

MEASUREMENT OF BED SURFACE TEMPERATURE GRADIENT

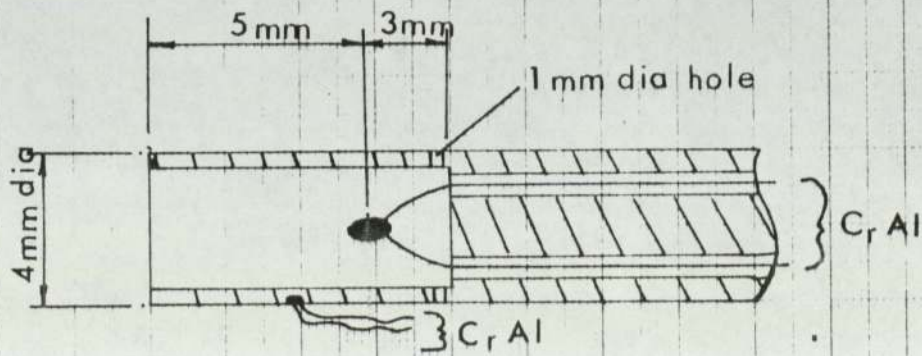
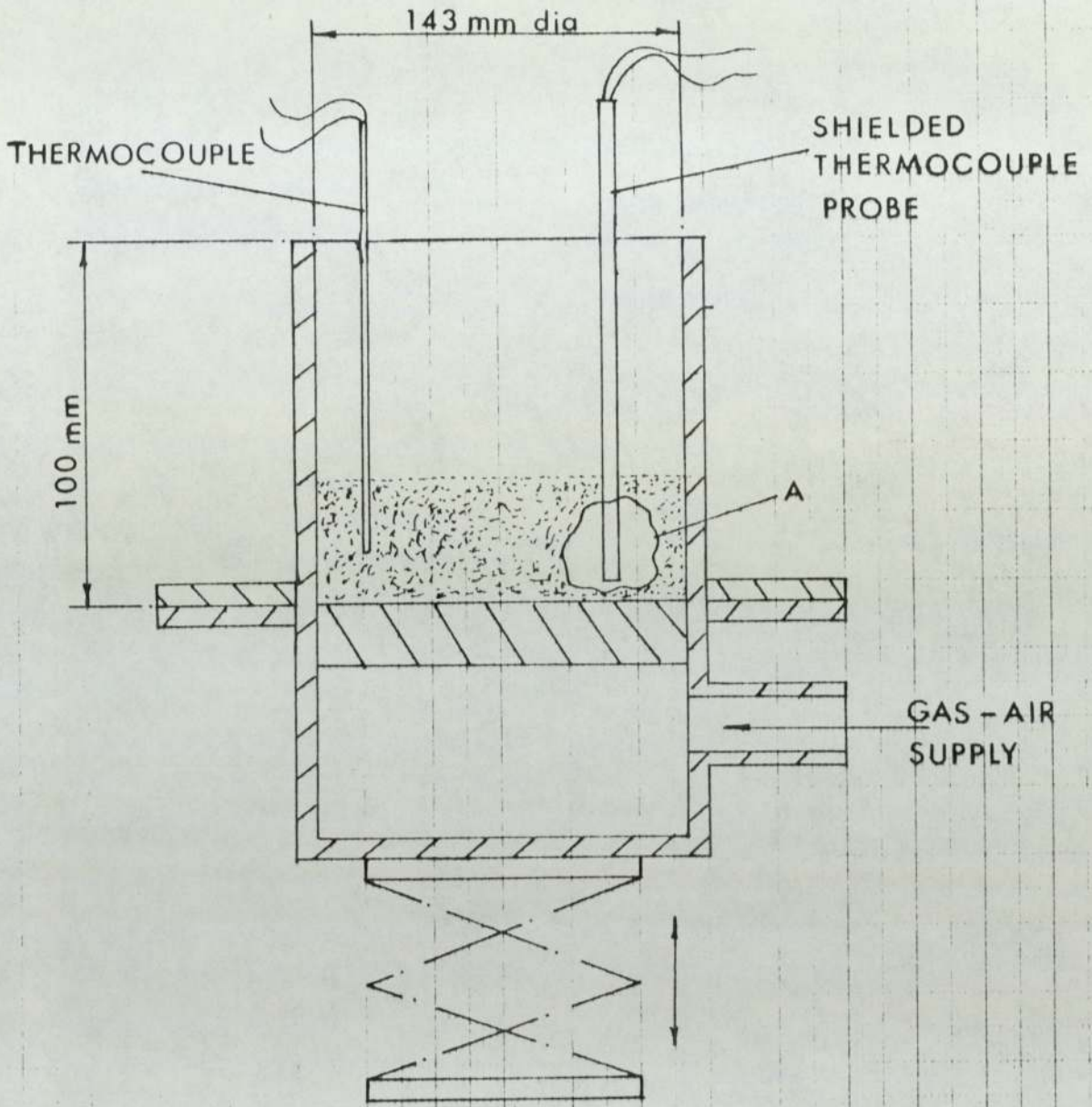
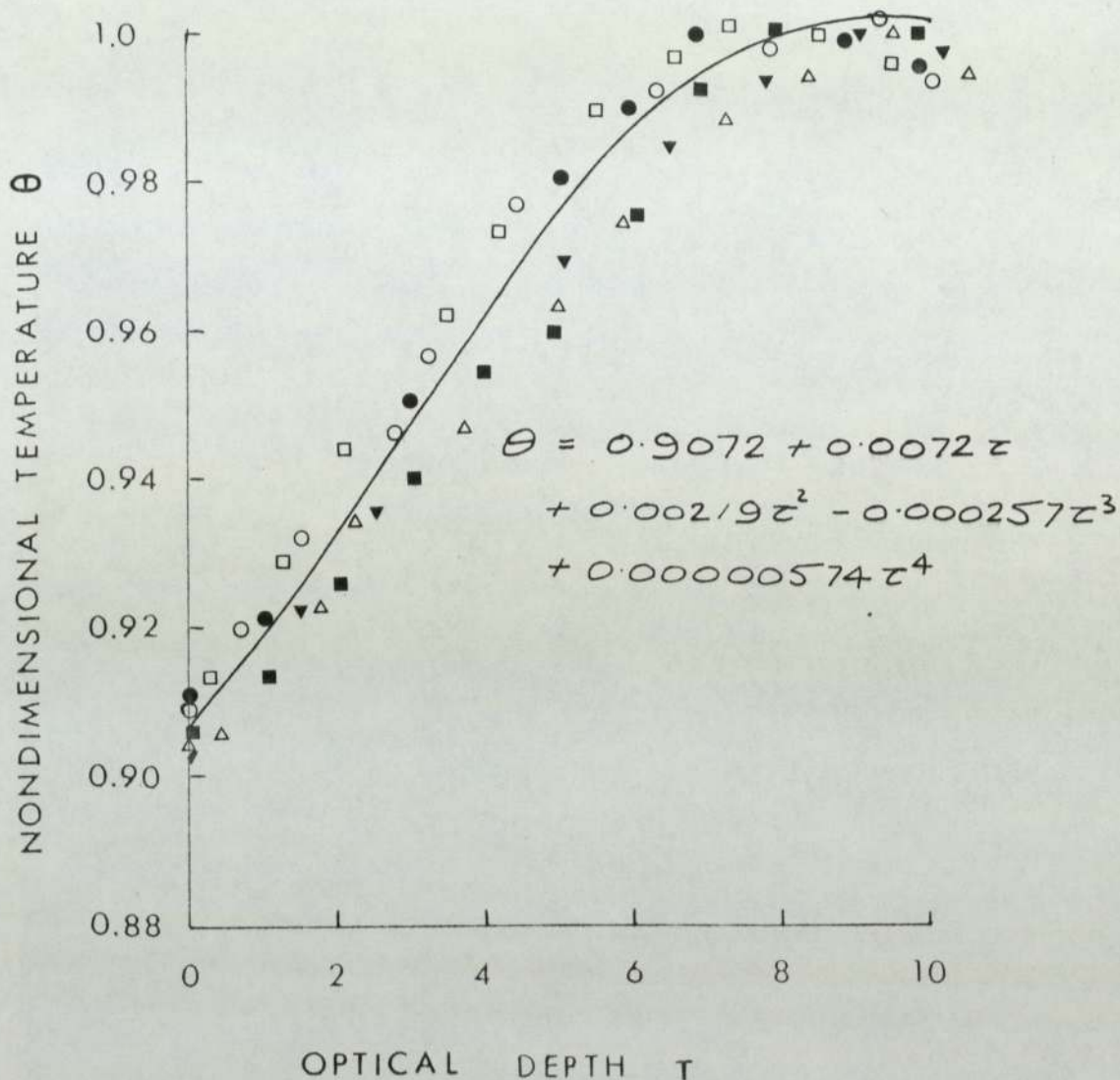
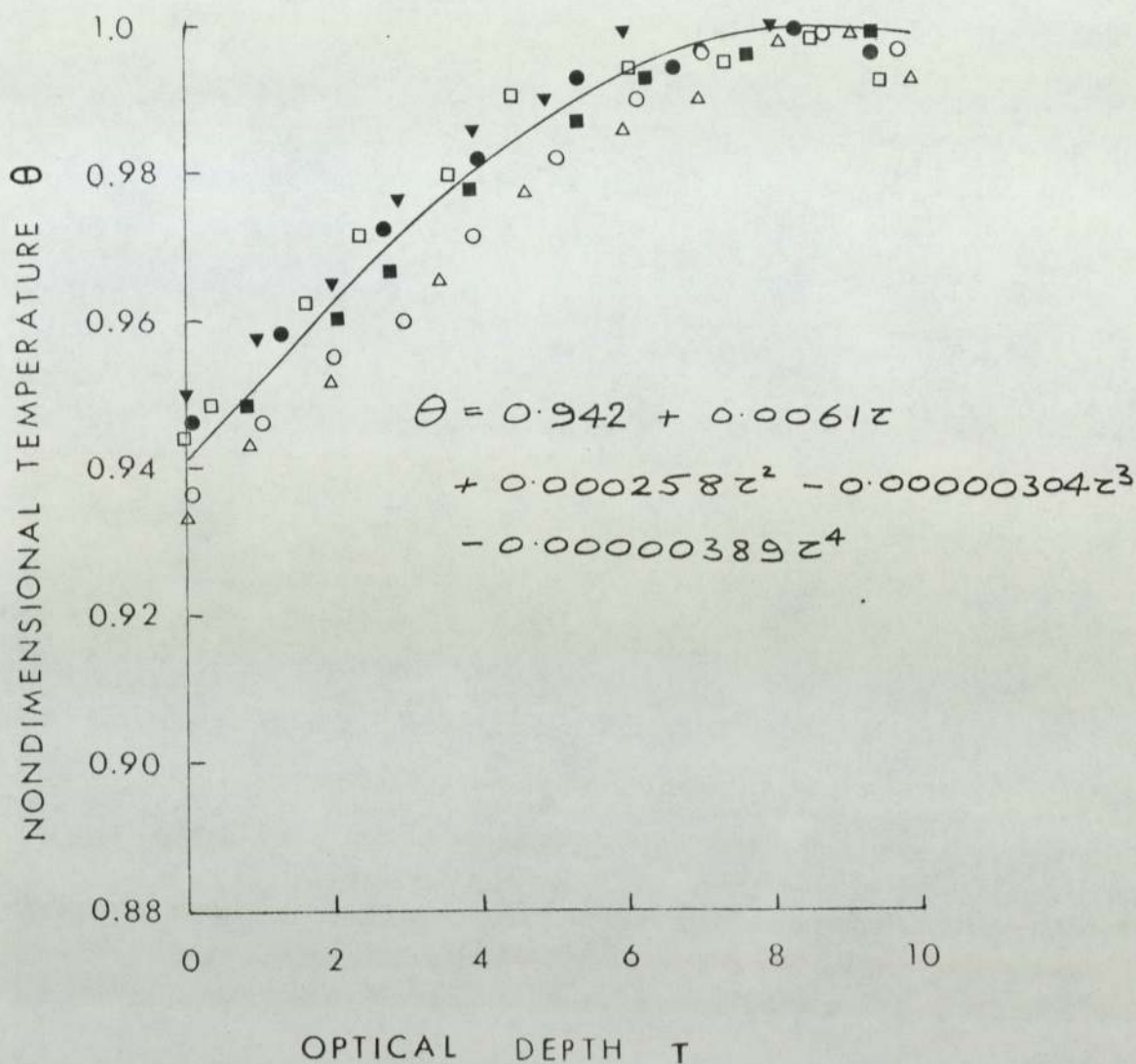


FIG. 3.22



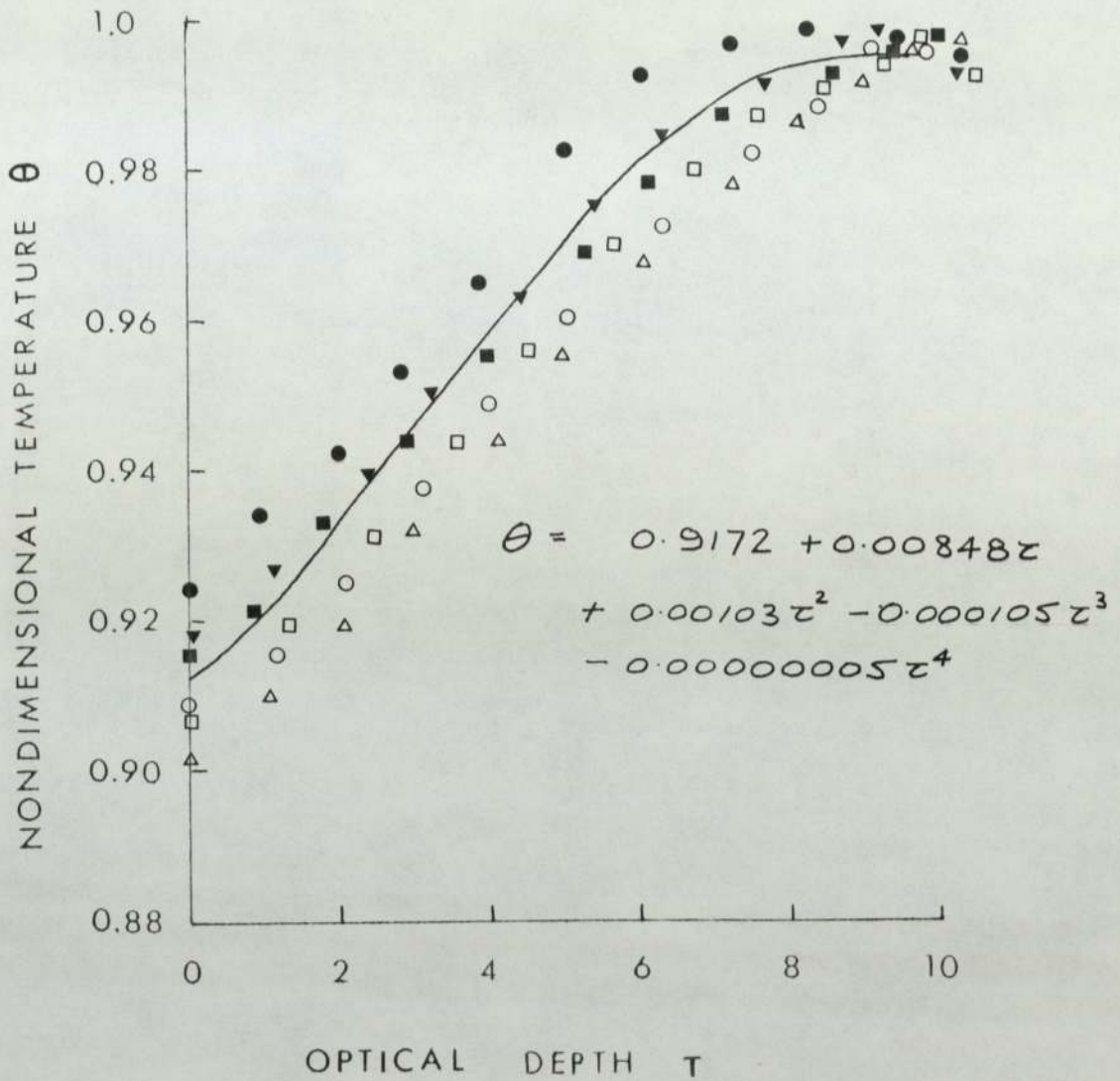
$U - U_{mf}$ mm/sec	K_t mm^{-1}	$T_{bed} \pm 10$ $^{\circ}\text{C}$	D_p mm	MAT ^L SILICON CARBIDE	H_{mf} mm
● 439.0	0.479	1048	0.55	SILICON CARBIDE	25
■ 220.0	0.535	1053	0.777		
○ 440.0	0.612	868	0.354		
▼ 221.0	0.654	874	0.55		
△ 219.0	0.81	925	0.354		
□ 443.0	0.372	928	0.777		

FIG 3.23



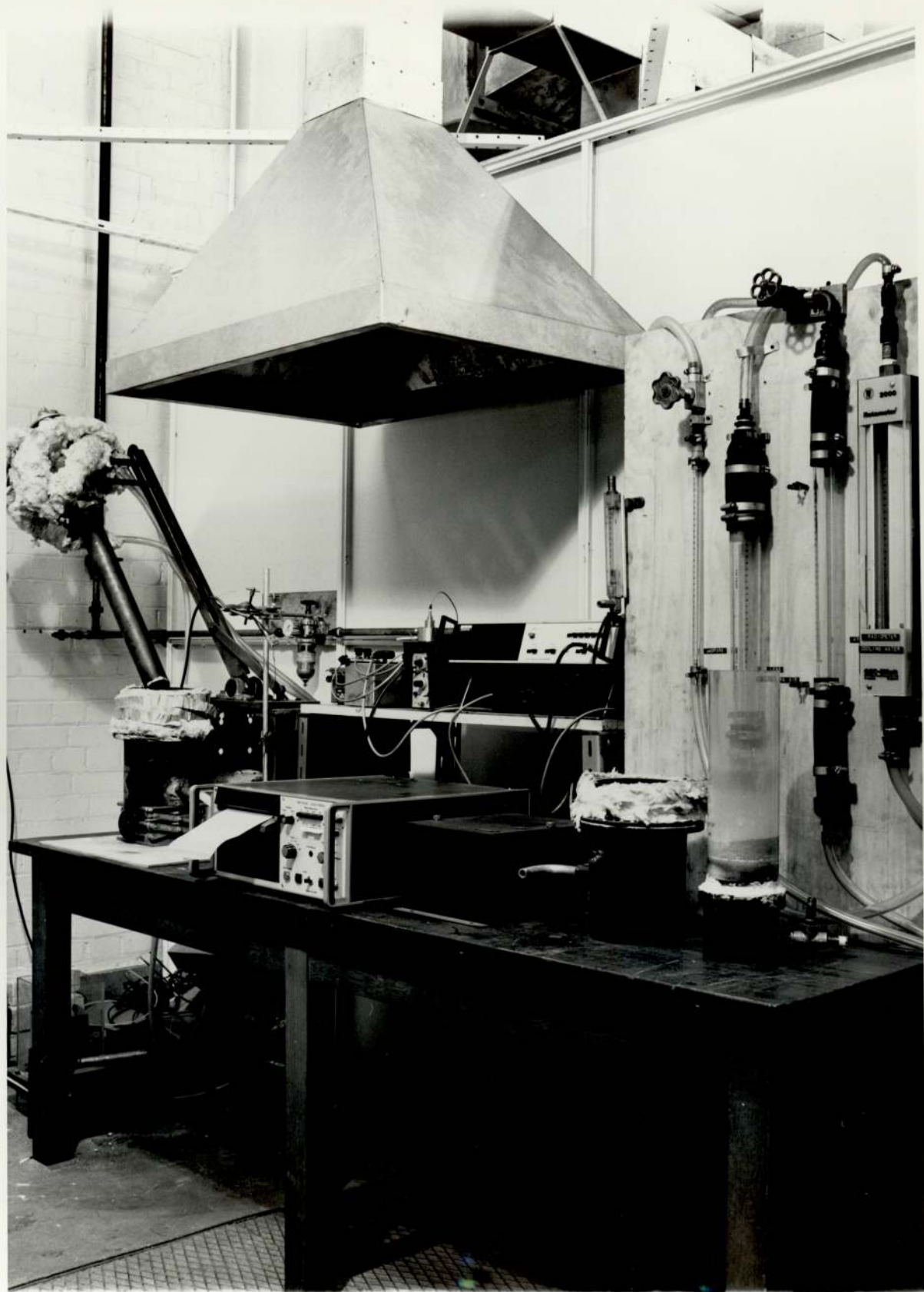
$U - U_{mf}$ mm/sec	K_t mm^{-1}	$T_{bed} \pm 10$ $^{\circ}C$	D_p mm	MAT ^L	H_{mf} mm
● 440.0	0.5	1045	0.777	ALUMINA	25
■ 225.0	0.625	1053	0.55		
○ 442.0	0.81	865	0.354		
▼ 219.0	0.97	876	0.777		
△ 442.0	0.82	934	0.55		
□ 220.0	1.32	924	0.354		

FIG 3.24



$U - U_{mf}$ mm/sec	K_t mm^{-1}	$T_{bed} \pm 10$ $^{\circ}\text{C}$	D_p mm	MAT ^L	H_{mf} mm
● 441.0	0.371	1052	0.777	SILICA SAND	25
■ 221.0	0.748	1050	0.354		
○ 440.0	0.643	875	0.55		
▼ 219.0	0.672	872	0.777		
△ 442.0	0.710	923	0.354		
□ 214.0	0.681	927	0.55		

FIG 3.25



Photograph of the experimental arrangement

FIG 4.1a

CONFIGURATION FOR SURFACE EMITTED
FLUX DETERMINATION

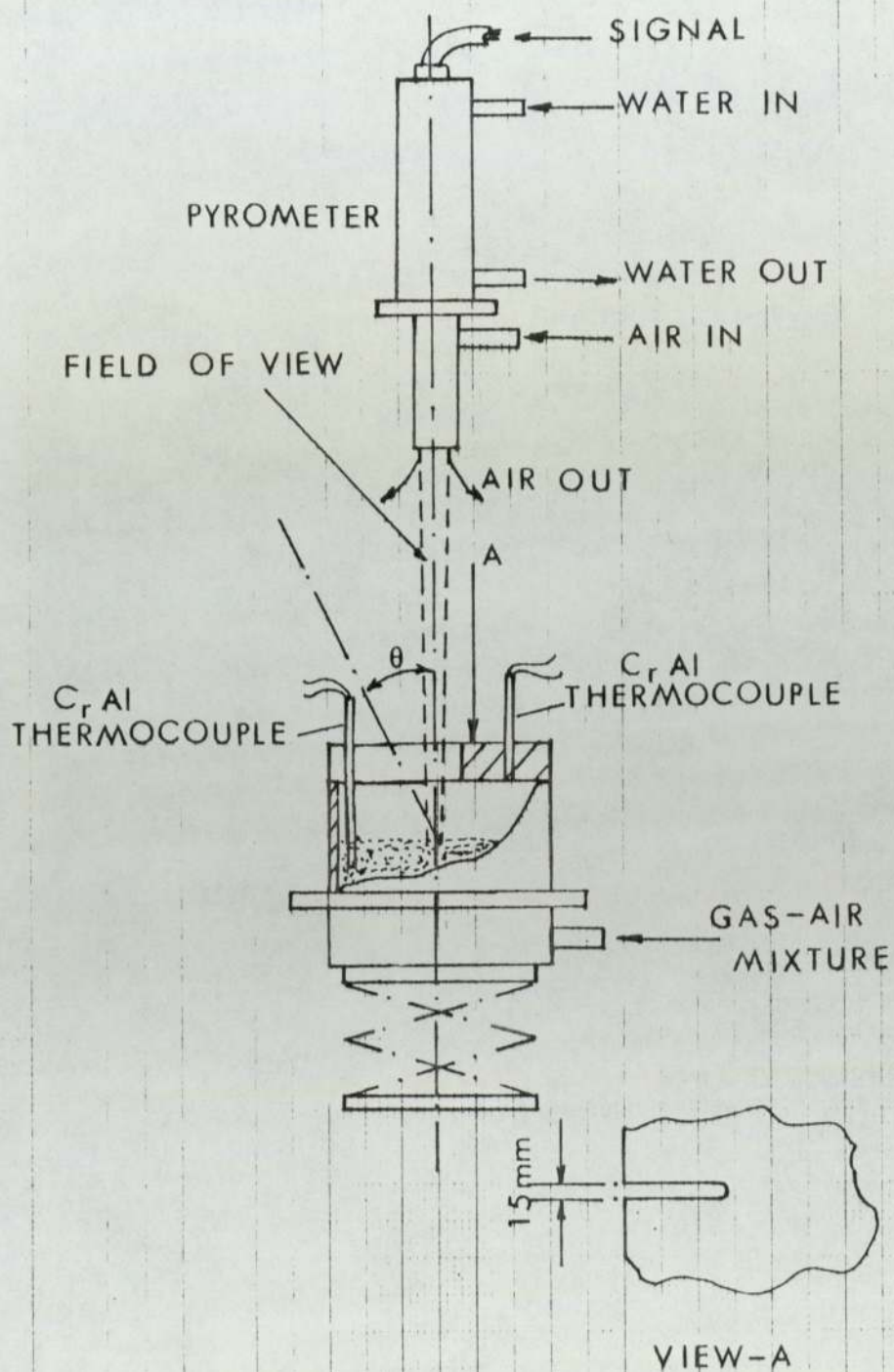
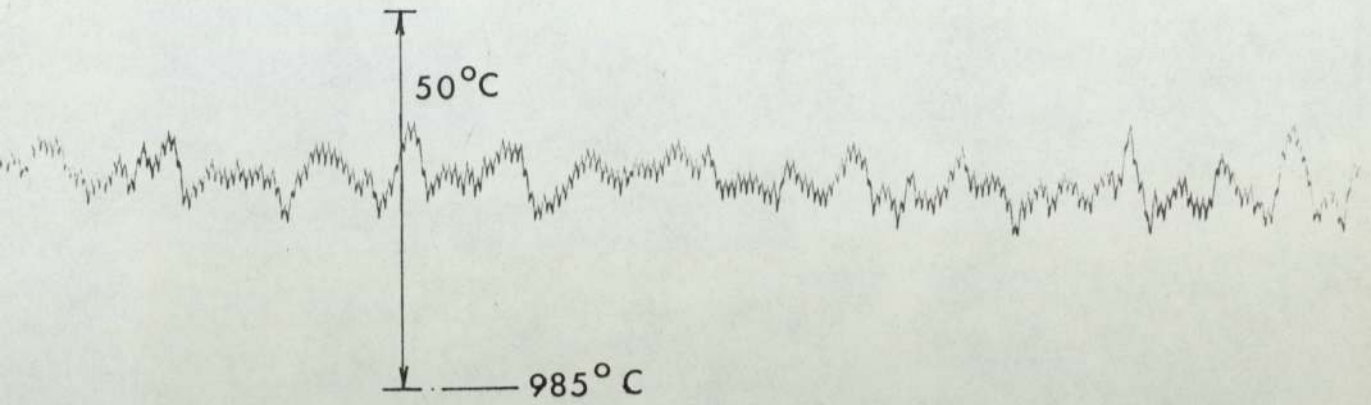


FIG 4.1b

TYPICAL PYROMETER OUTPUT TRACE FOR
AN ISOTHERMAL (A) AND NONISOTHERMAL (B) BED

(A)



	$U - U_{mf}$ mm/sec	T_b °C	D_p mm	
(A)	443	1050	0.55	SAND
(B)	437	"	"	"

(B)

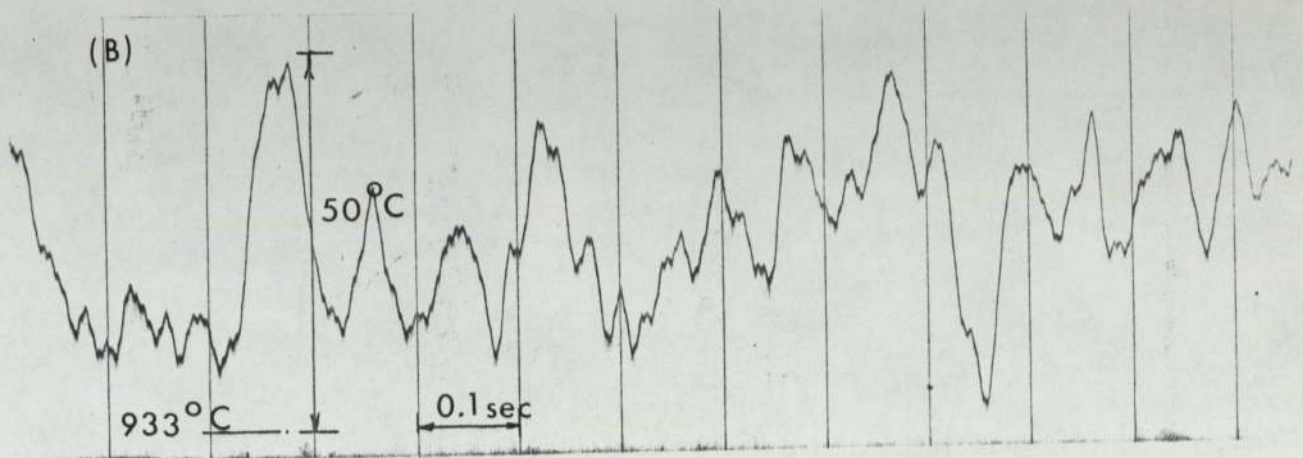
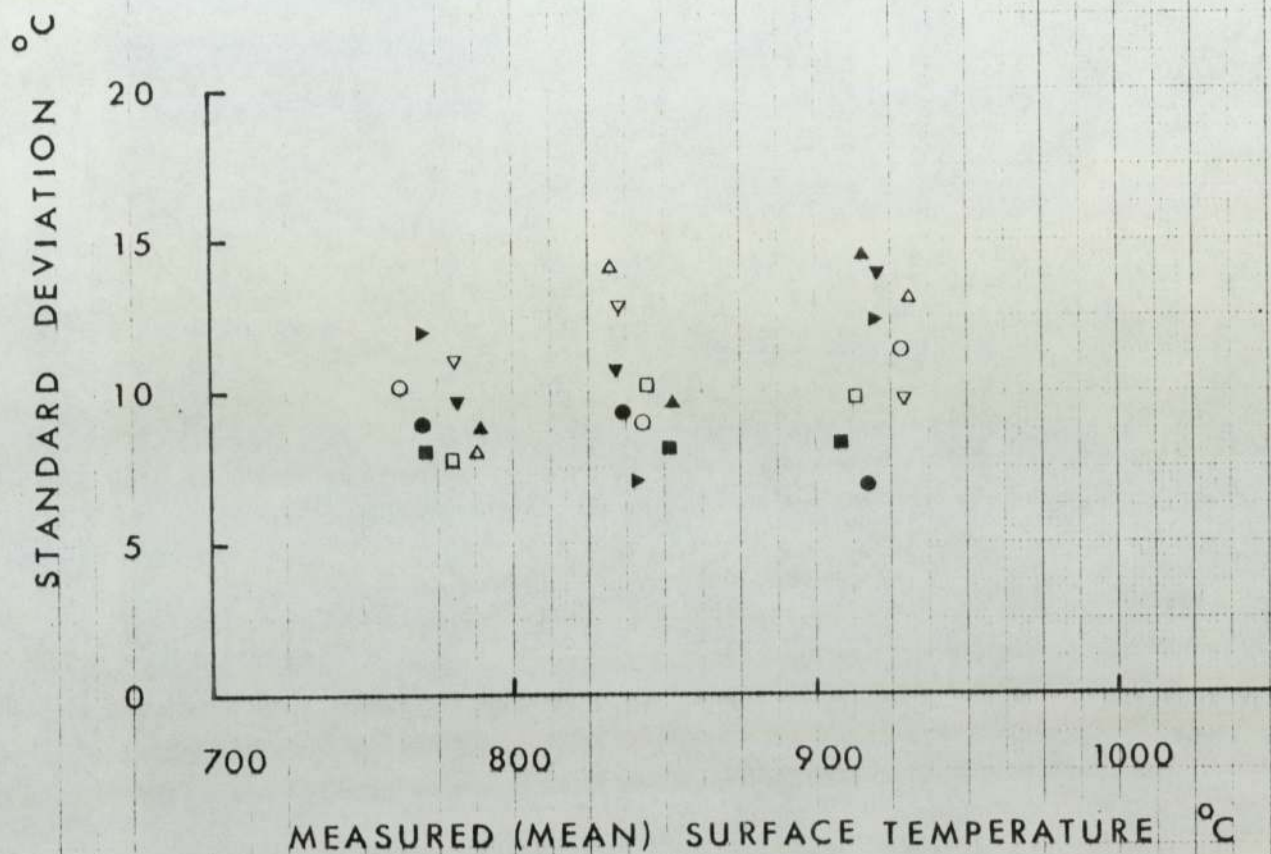


FIG 4.2

TYPICAL STANDARD DEVIATIONS
OF SURFACE TEMPERATURE FLUCTUATIONS



MAT ^L SILICA SAND	D _p mm	H _{mf} mm	U - U _{mf} mm/sec
●	0.55	15	214
○		33	--
□		50	--
■		15	338.6
▼		33	--
▽		50	--
▲		15	437.7
△		33	--
▶		50	--

FIG 4.3

EFFECT OF EXCESS GAS VELOCITY ON EFFECTIVE EMISSIVITY

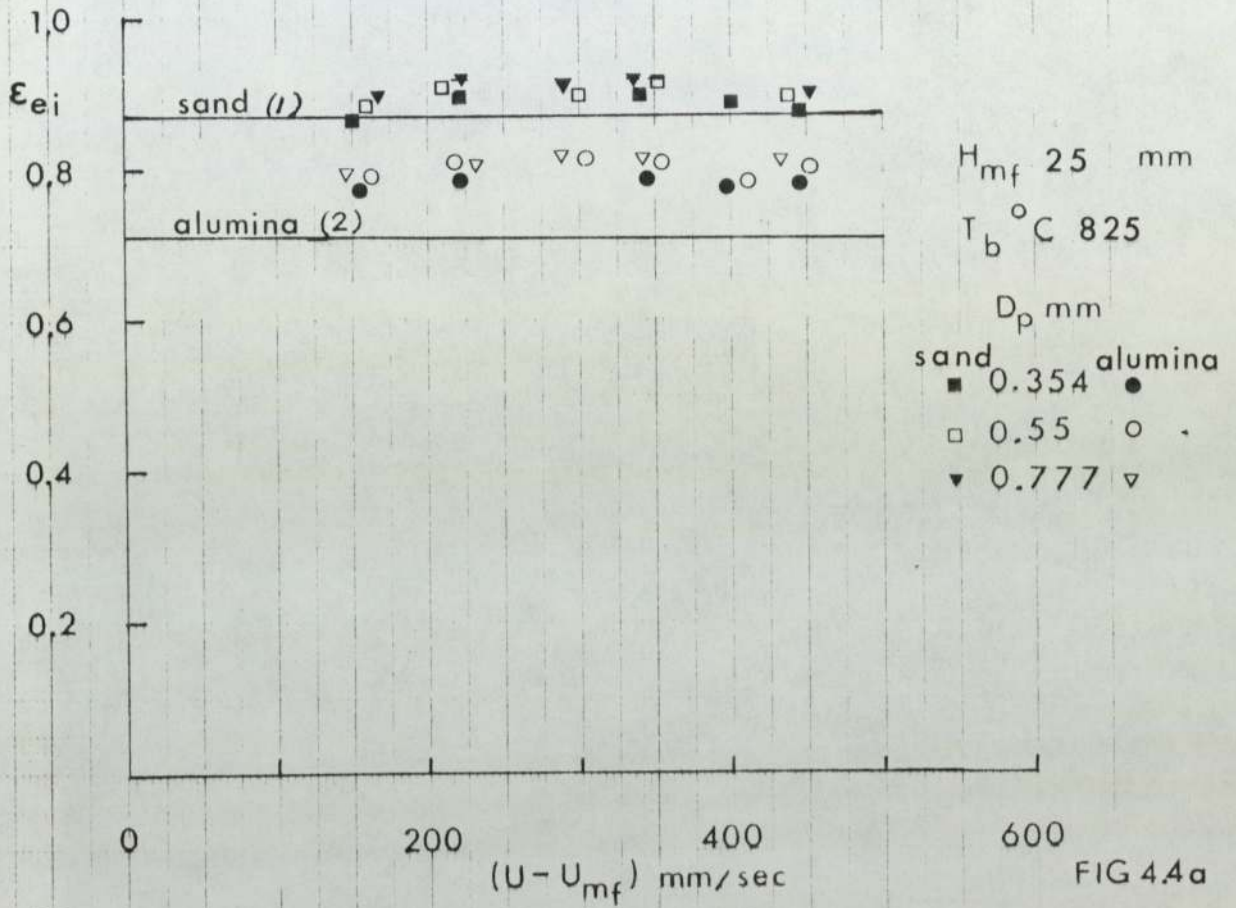


FIG 4.4a

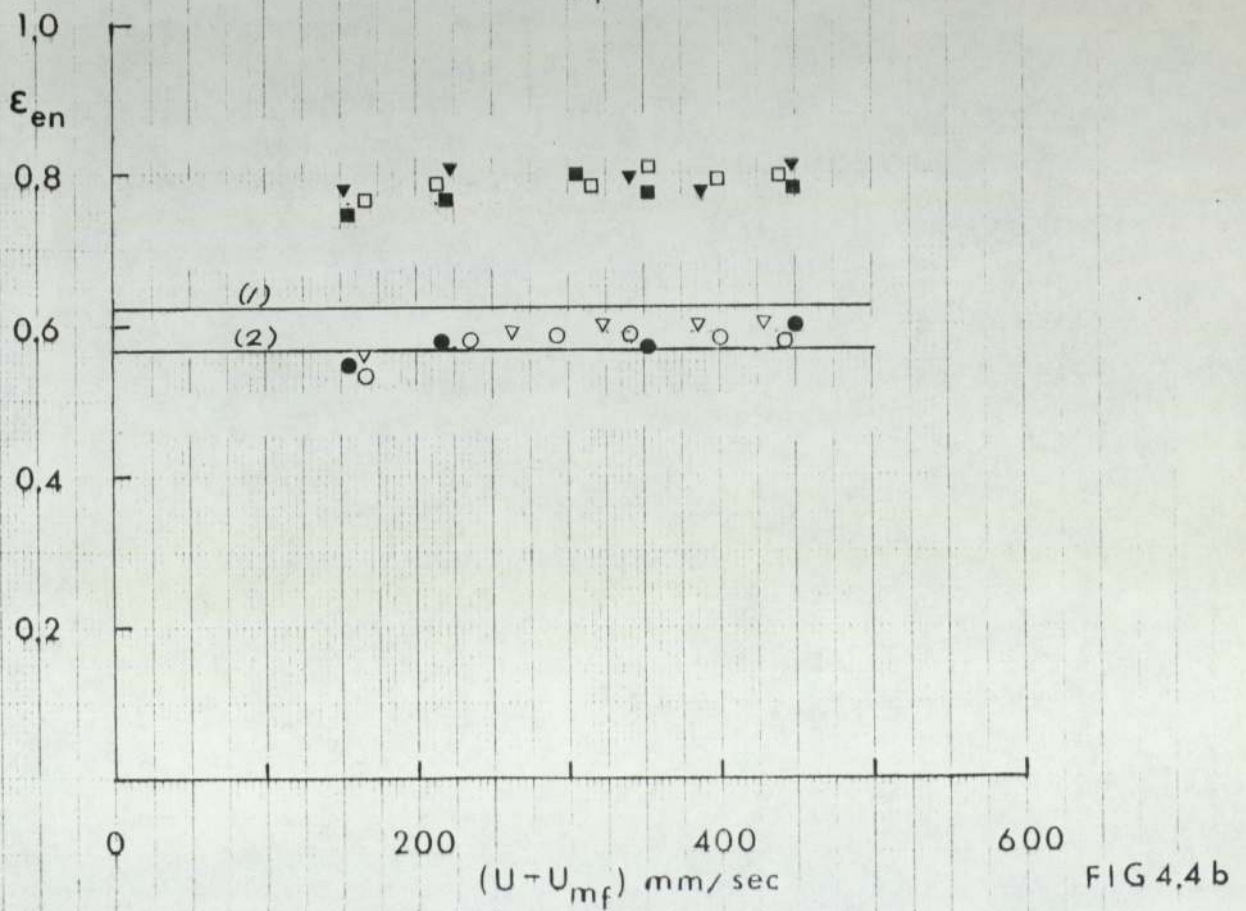


FIG 4.4b

EFFECT OF EXCESS GAS VELOCITY ON EFFECTIVE EMISSIVITY

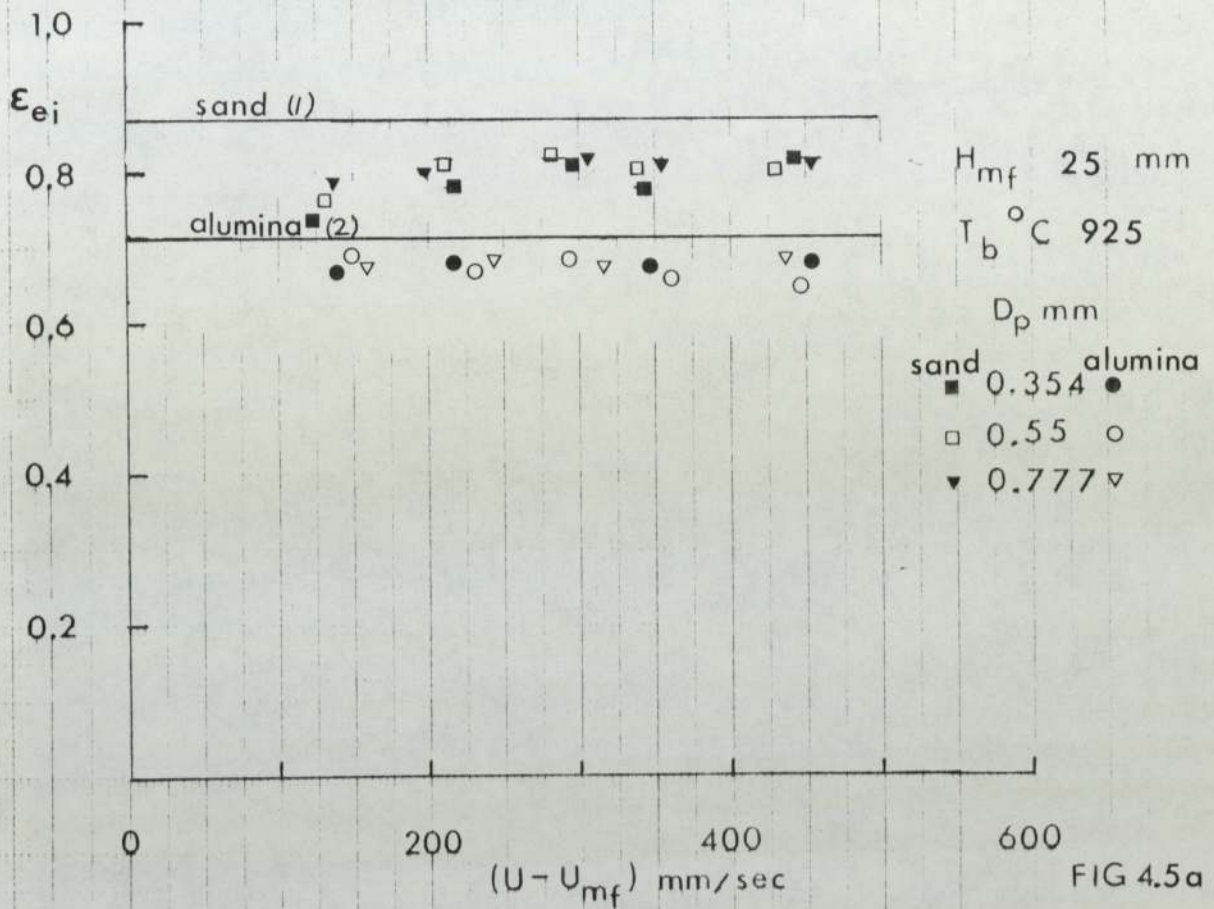


FIG 4.5a

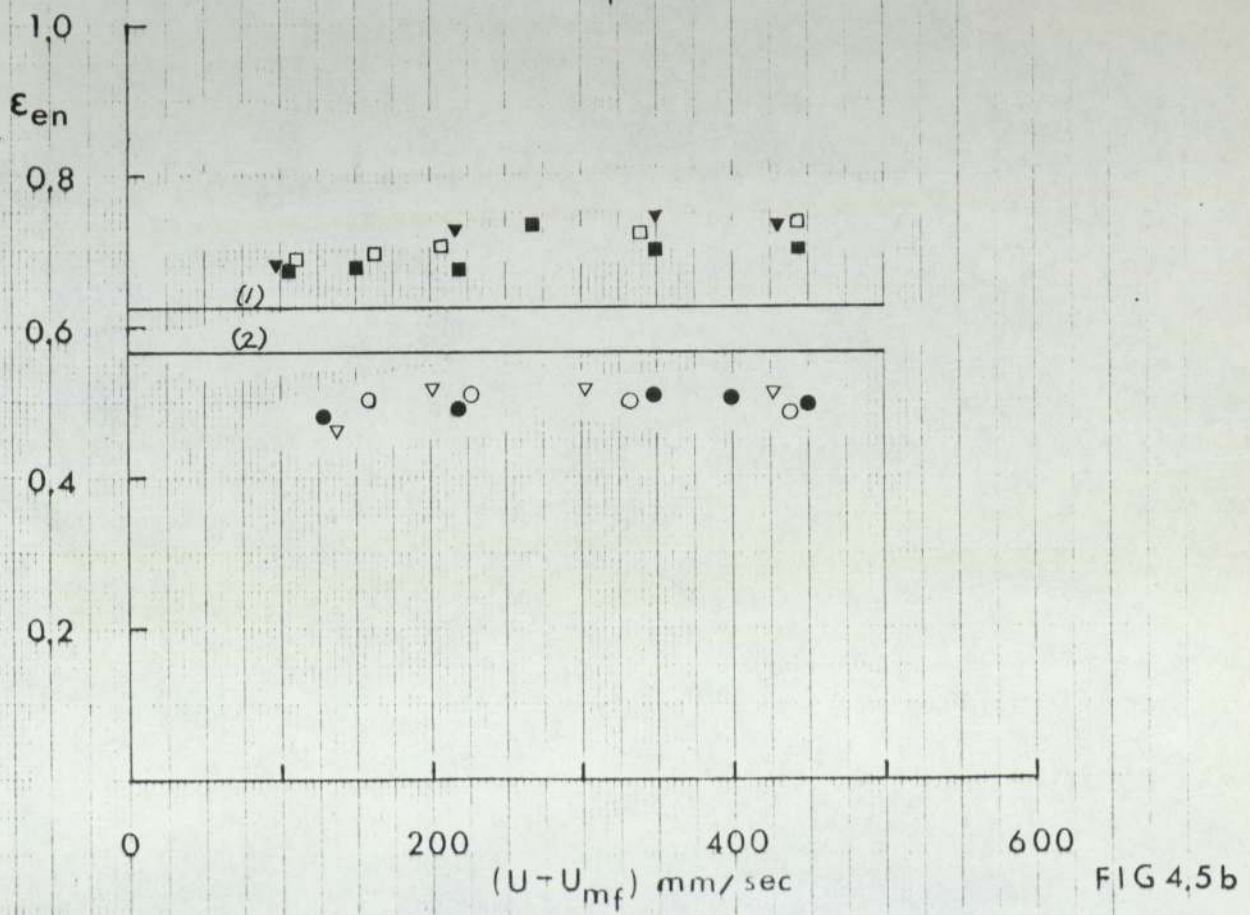
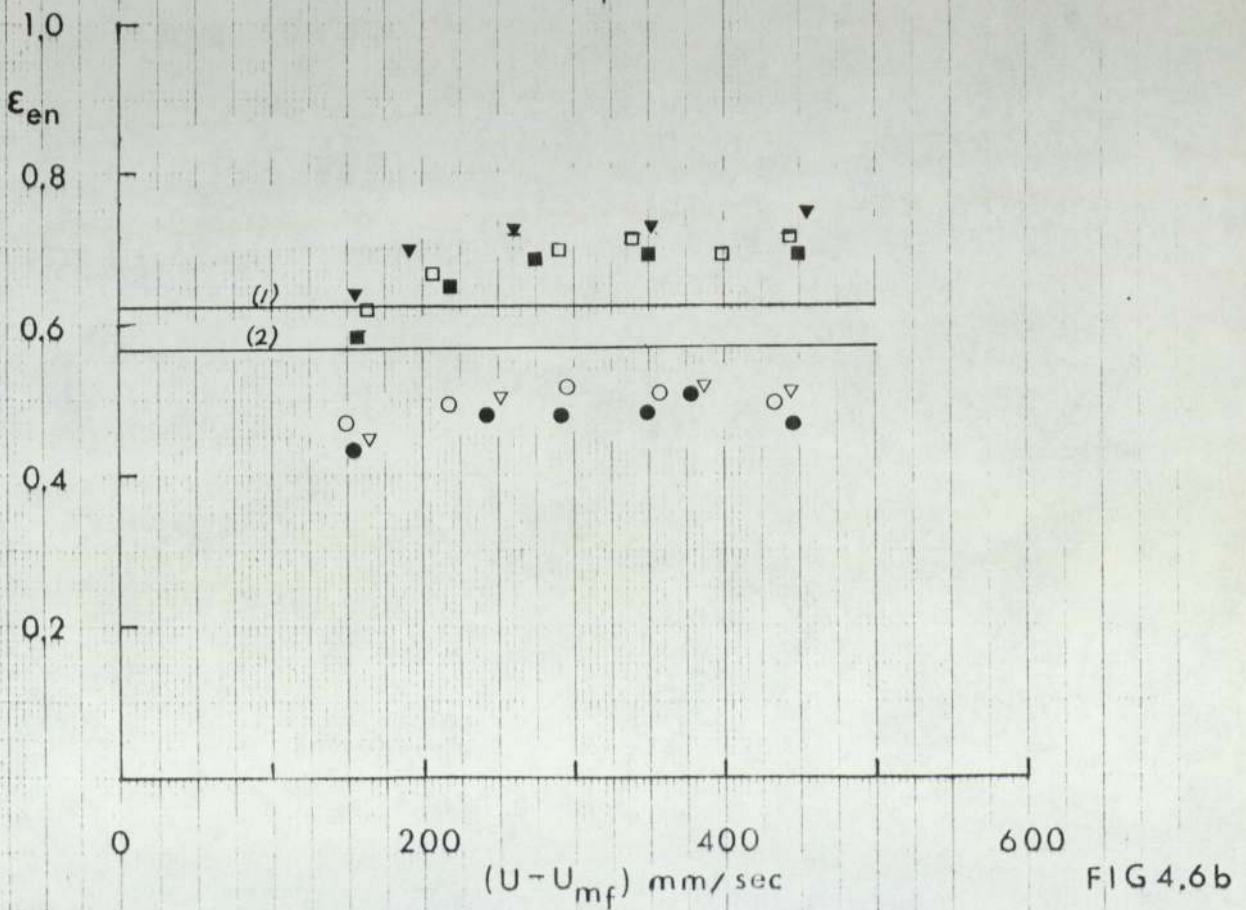
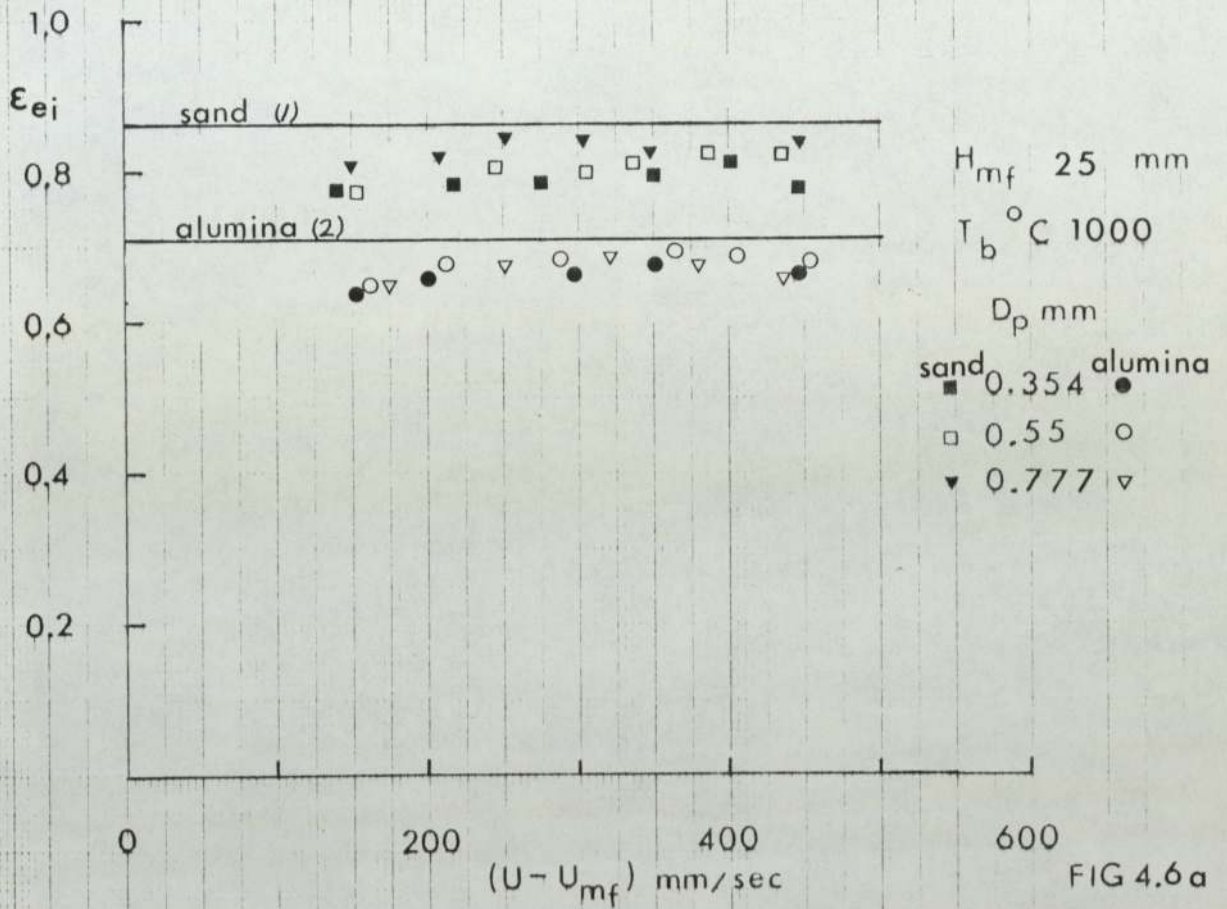
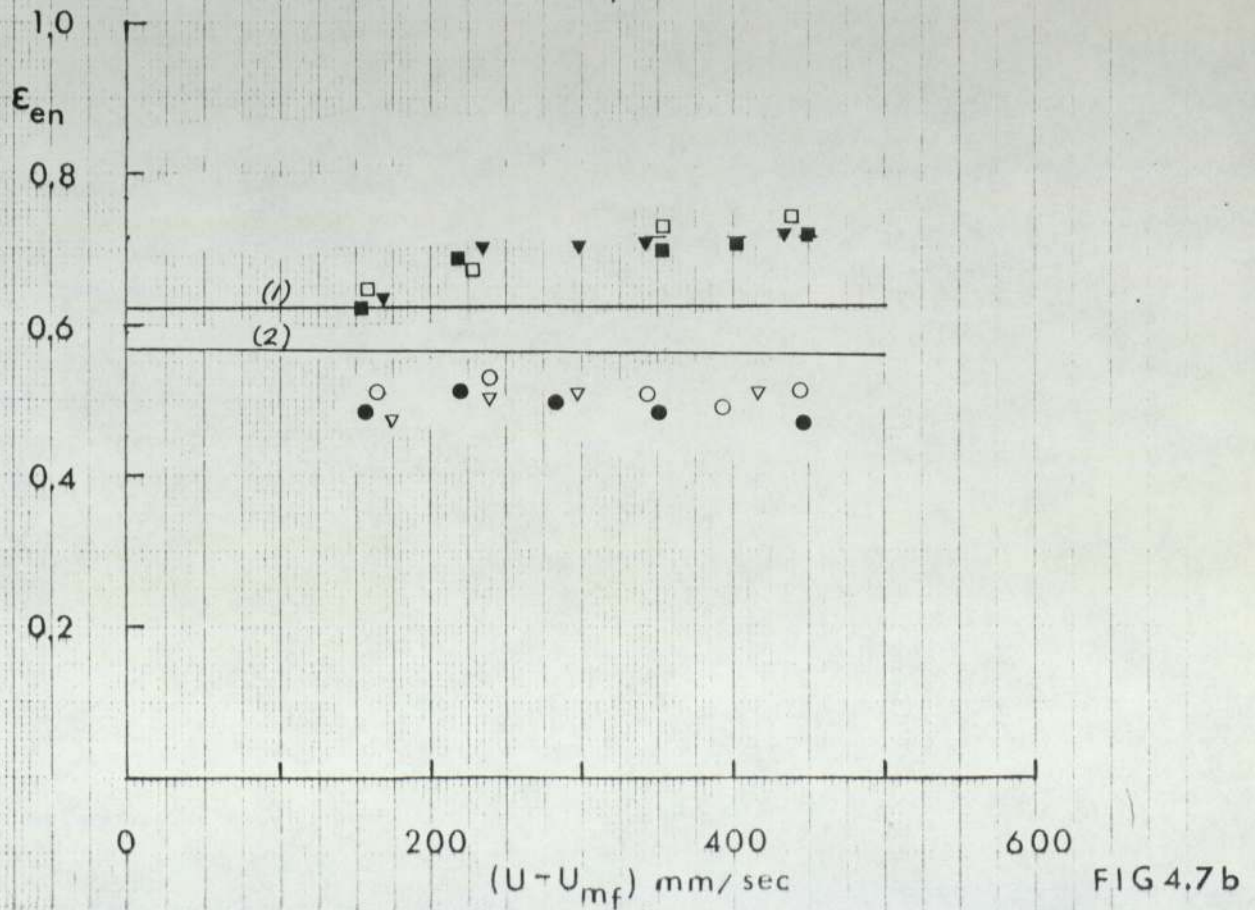
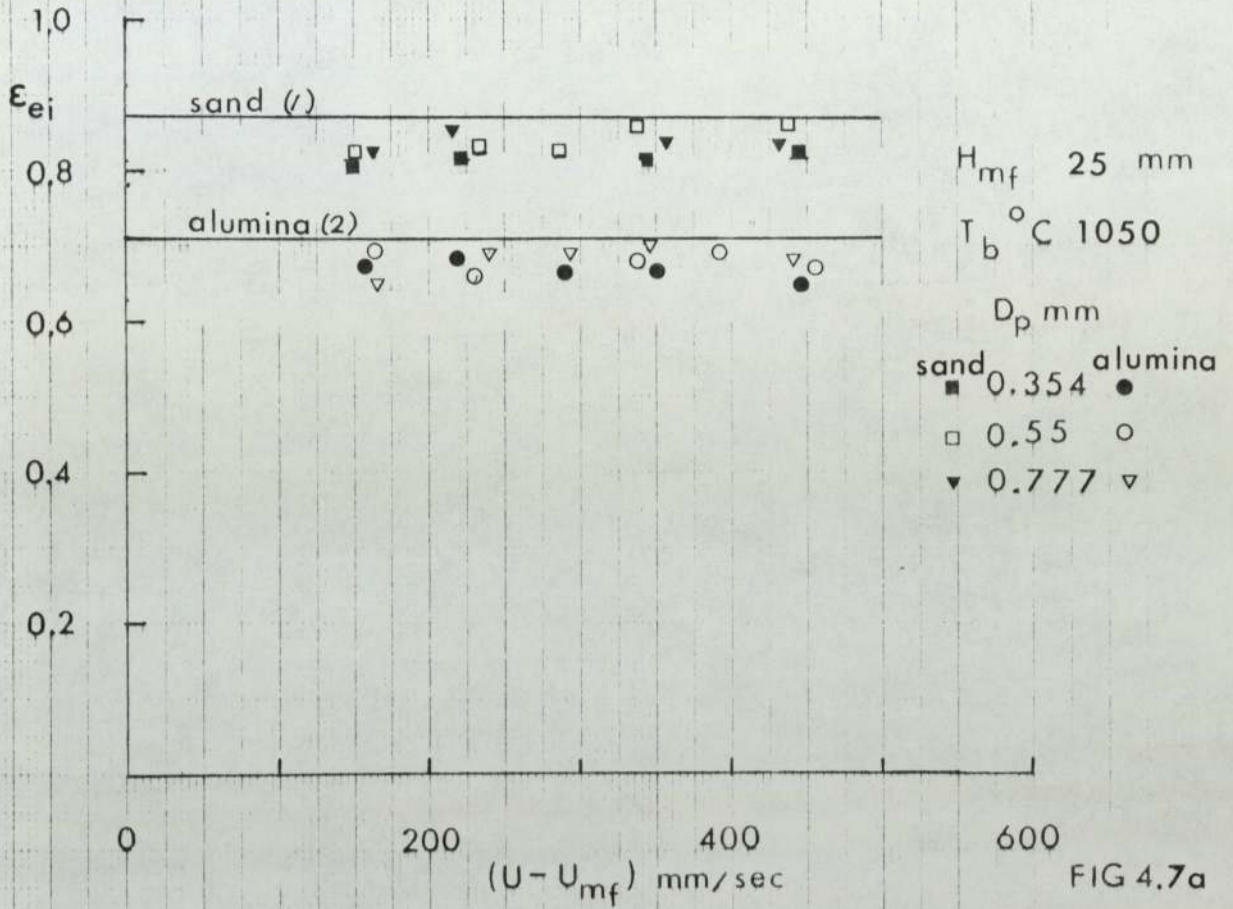


FIG 4.5b

EFFECT OF EXCESS GAS VELOCITY ON EFFECTIVE EMISSIVITY



EFFECT OF EXCESS GAS VELOCITY ON
EFFECTIVE EMISSIVITY



EFFECT OF EXCESS GAS VELOCITY ON EFFECTIVE EMISSIVITY

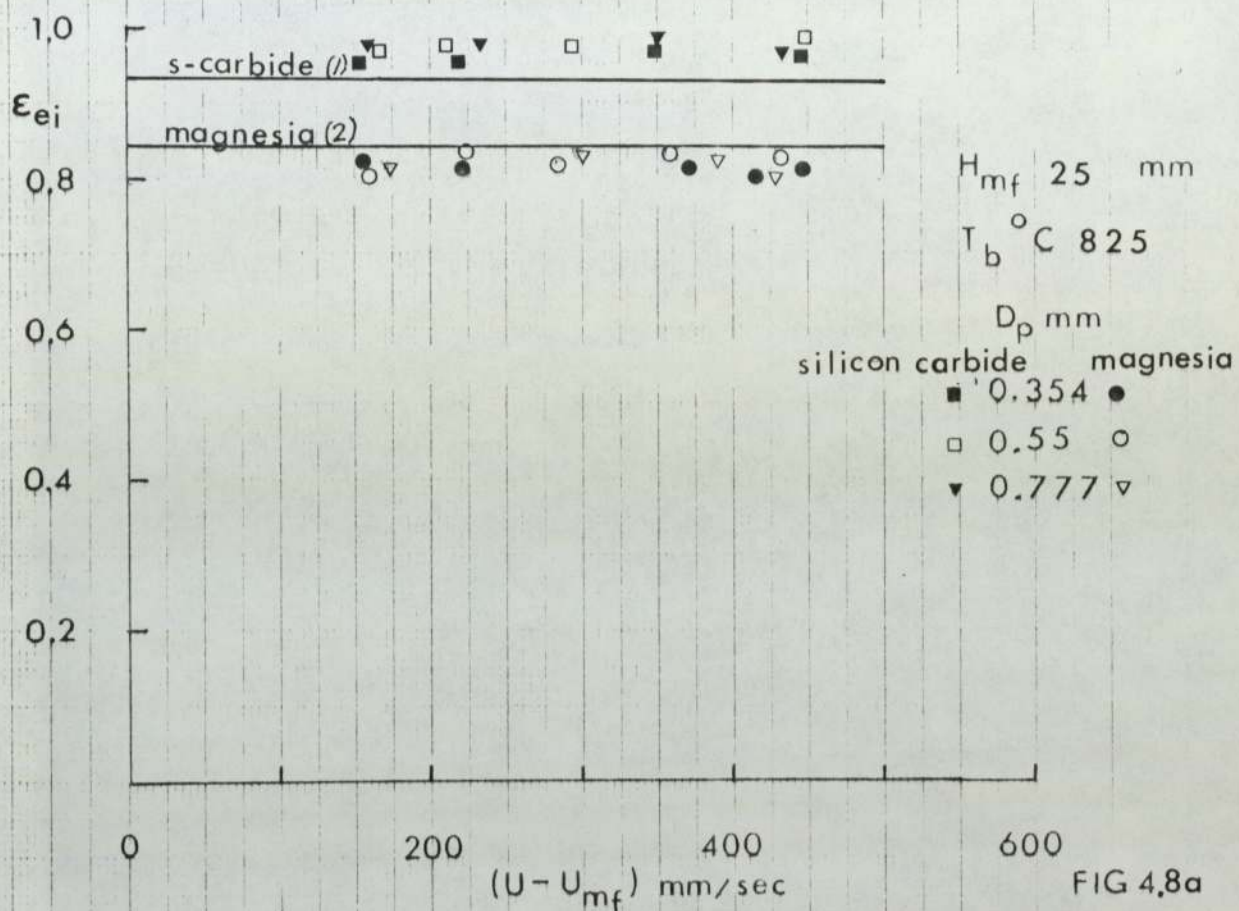


FIG 4.8a

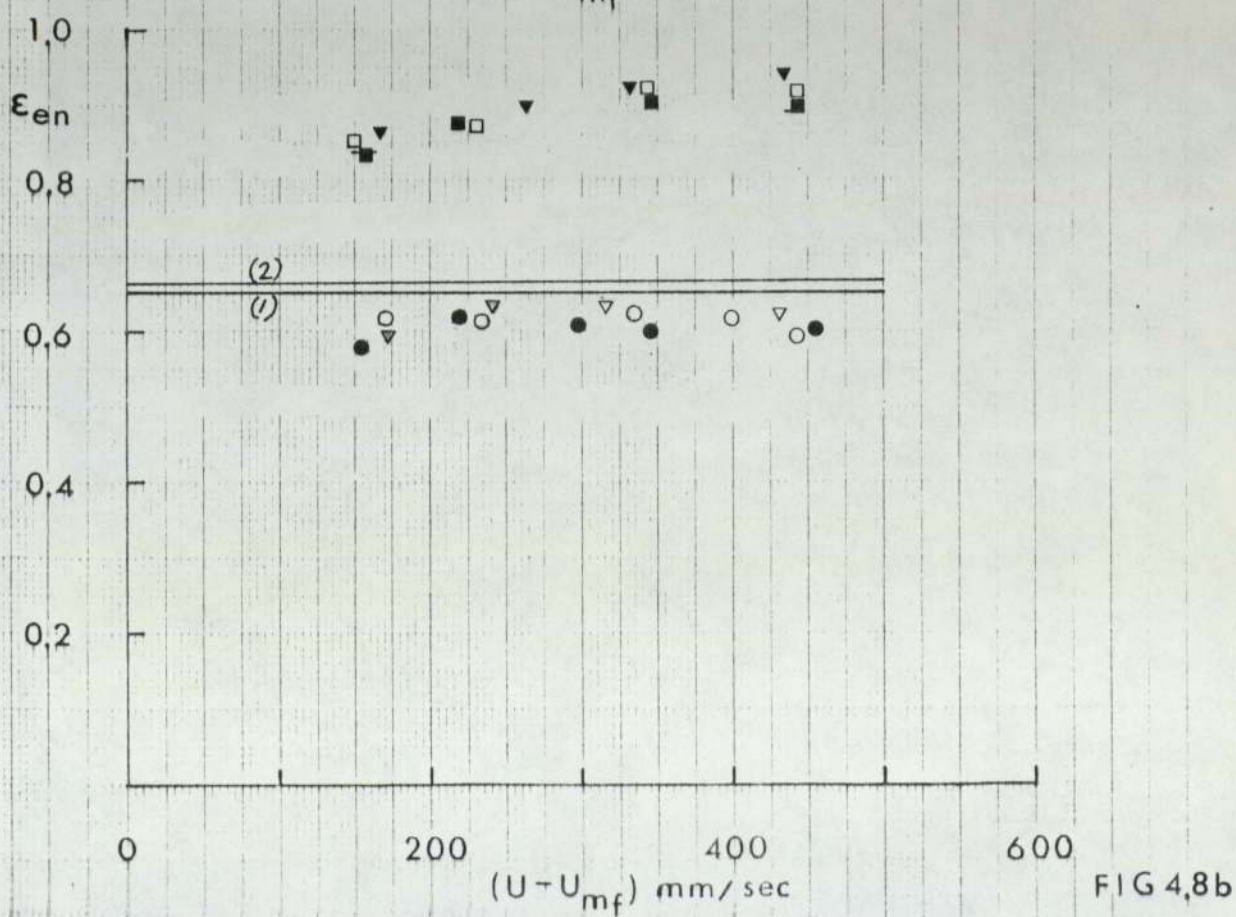
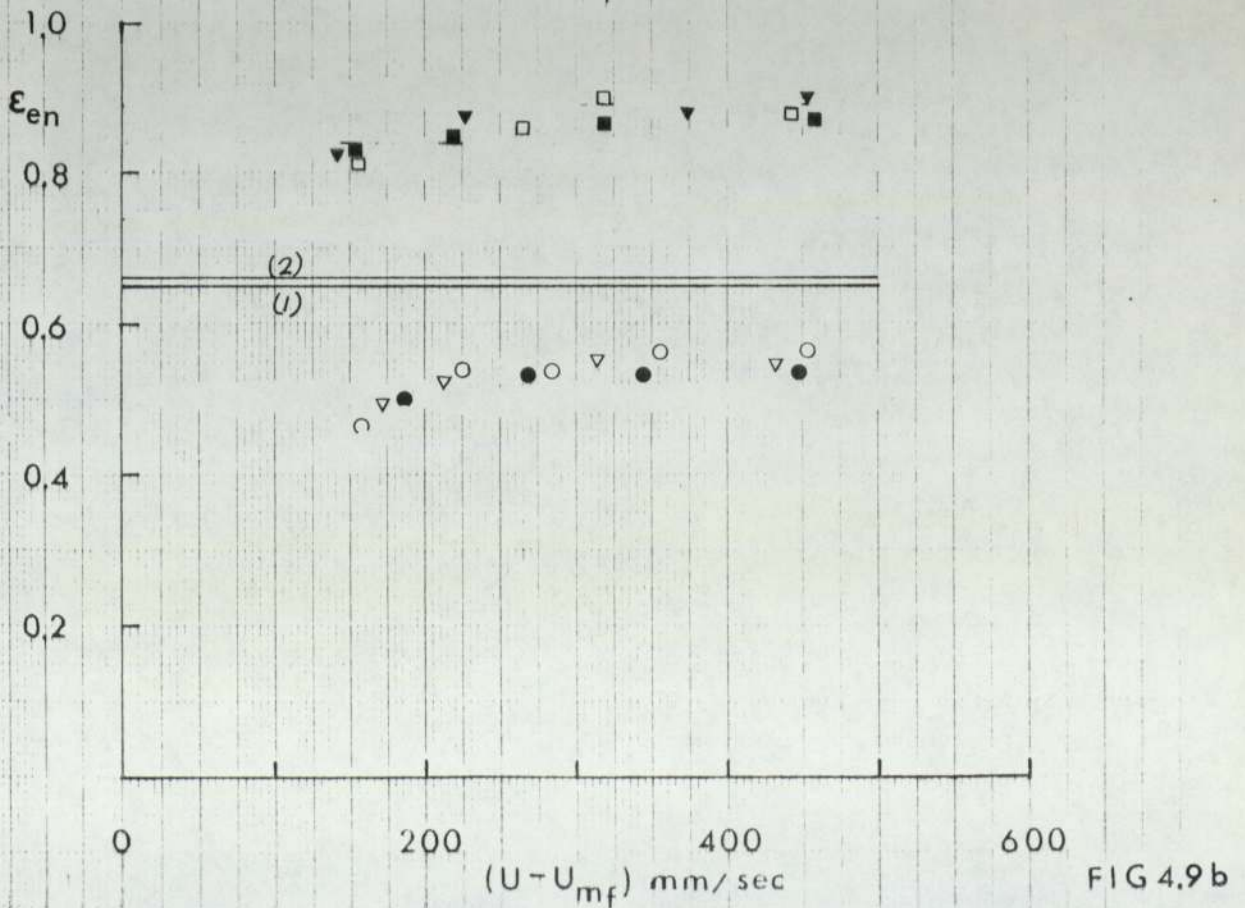
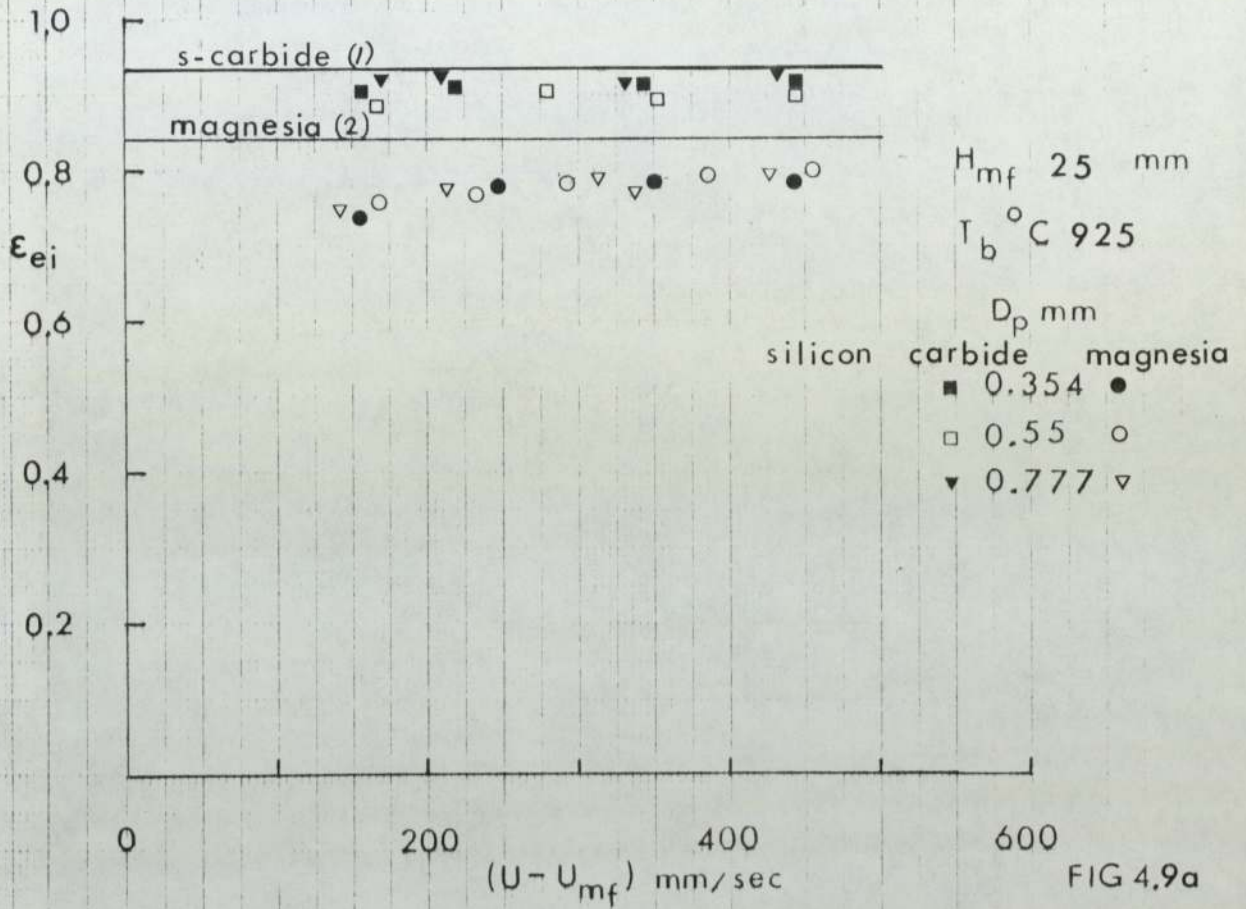
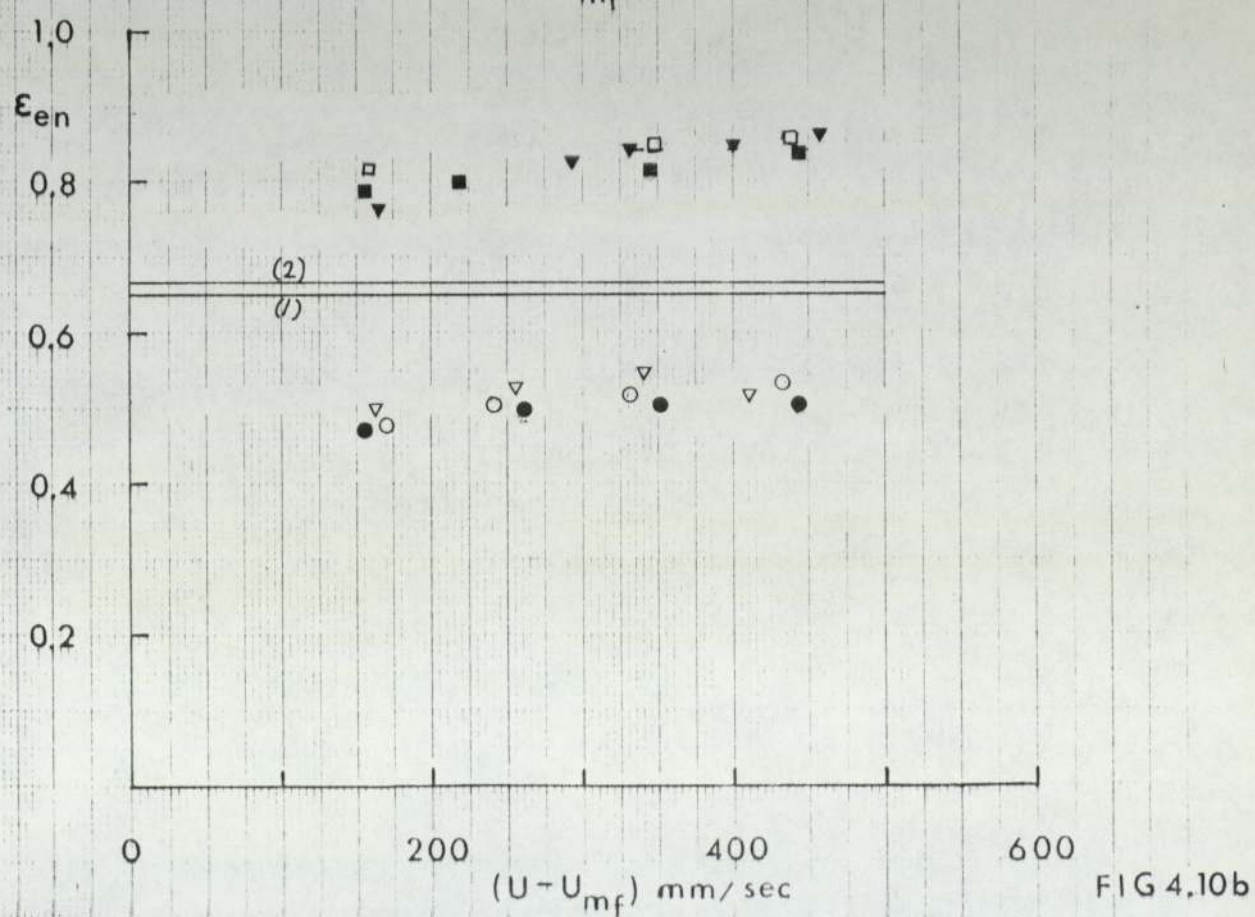
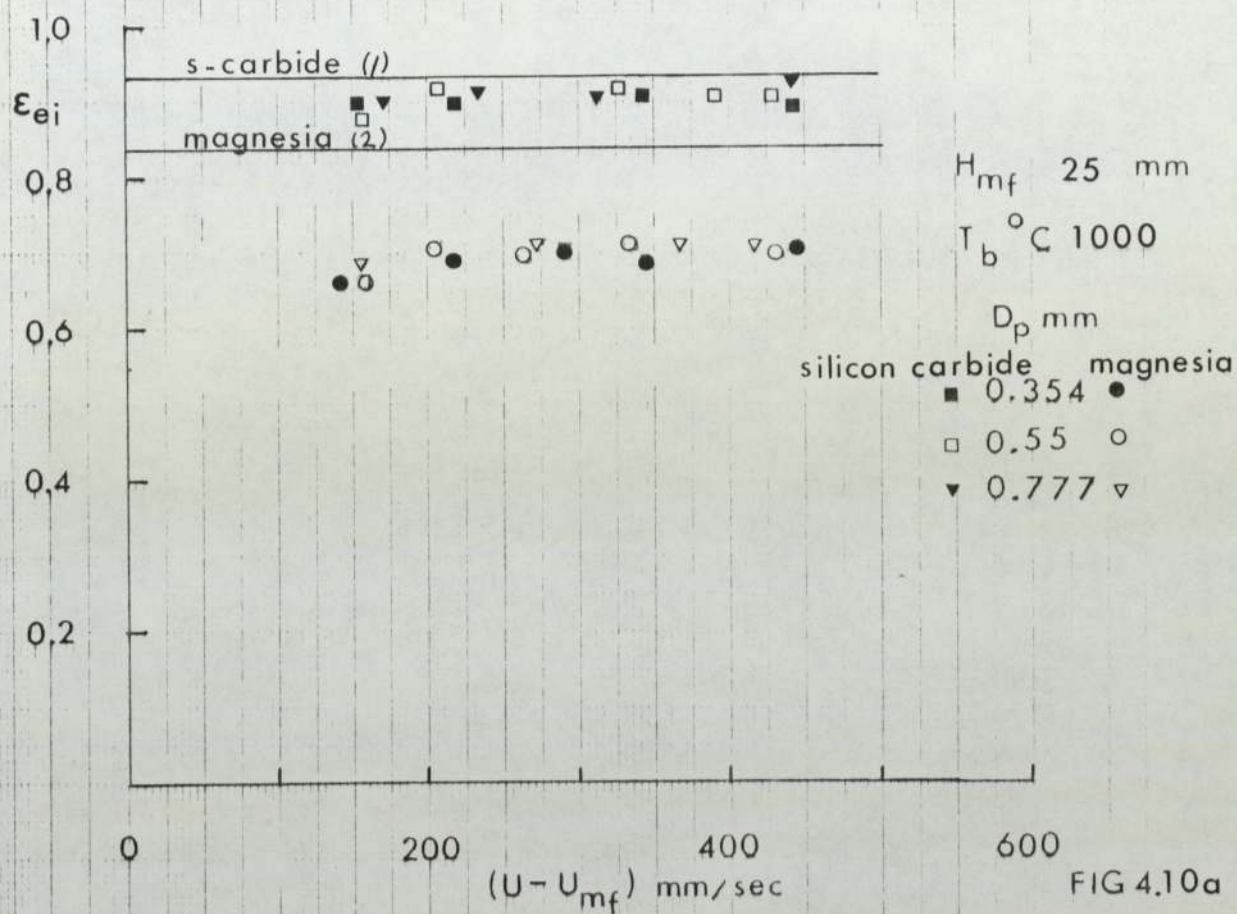


FIG 4.8b

EFFECT OF EXCESS GAS VELOCITY ON
EFFECTIVE EMISSIVITY



EFFECT OF EXCESS GAS VELOCITY ON EFFECTIVE EMISSIVITY



EFFECT OF EXCESS GAS VELOCITY ON EFFECTIVE EMISSIVITY

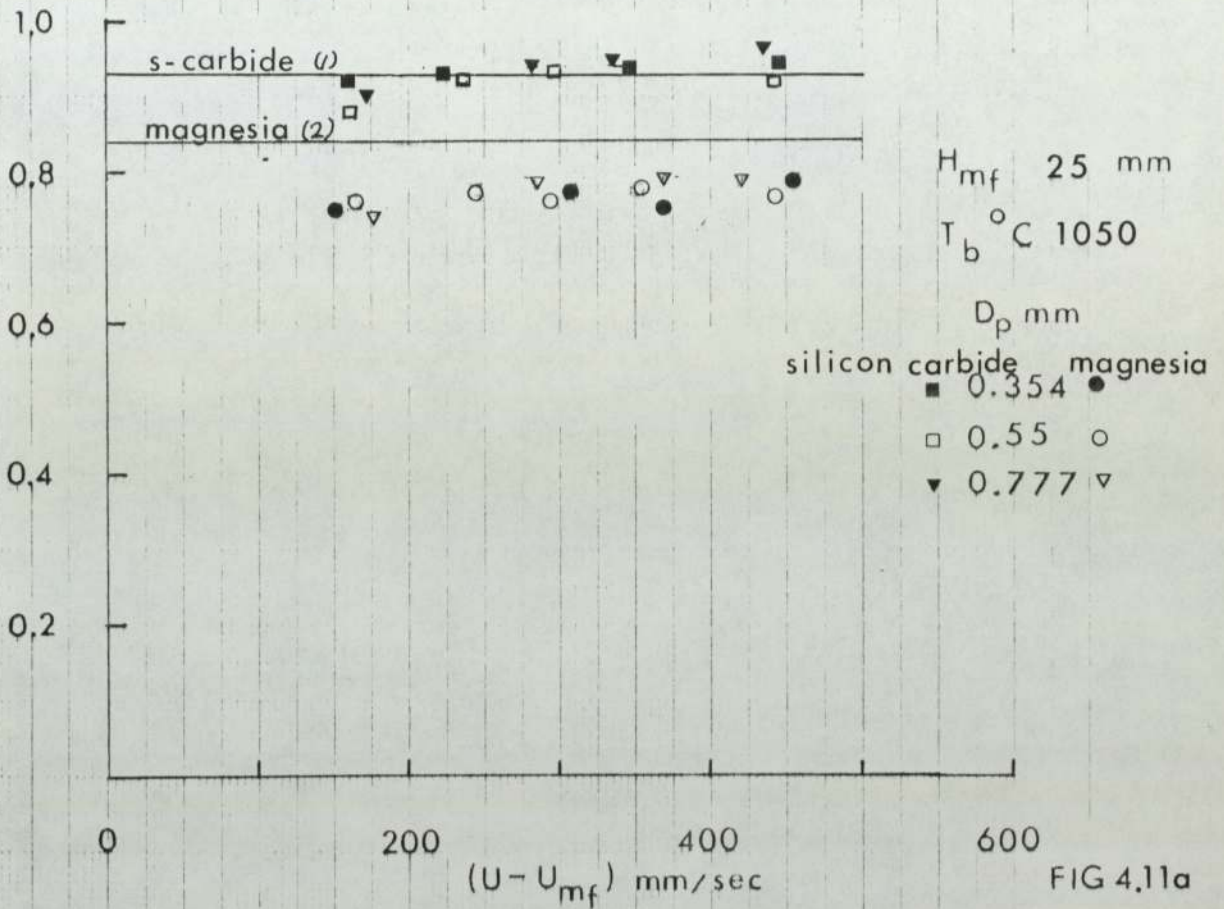


FIG 4.11a

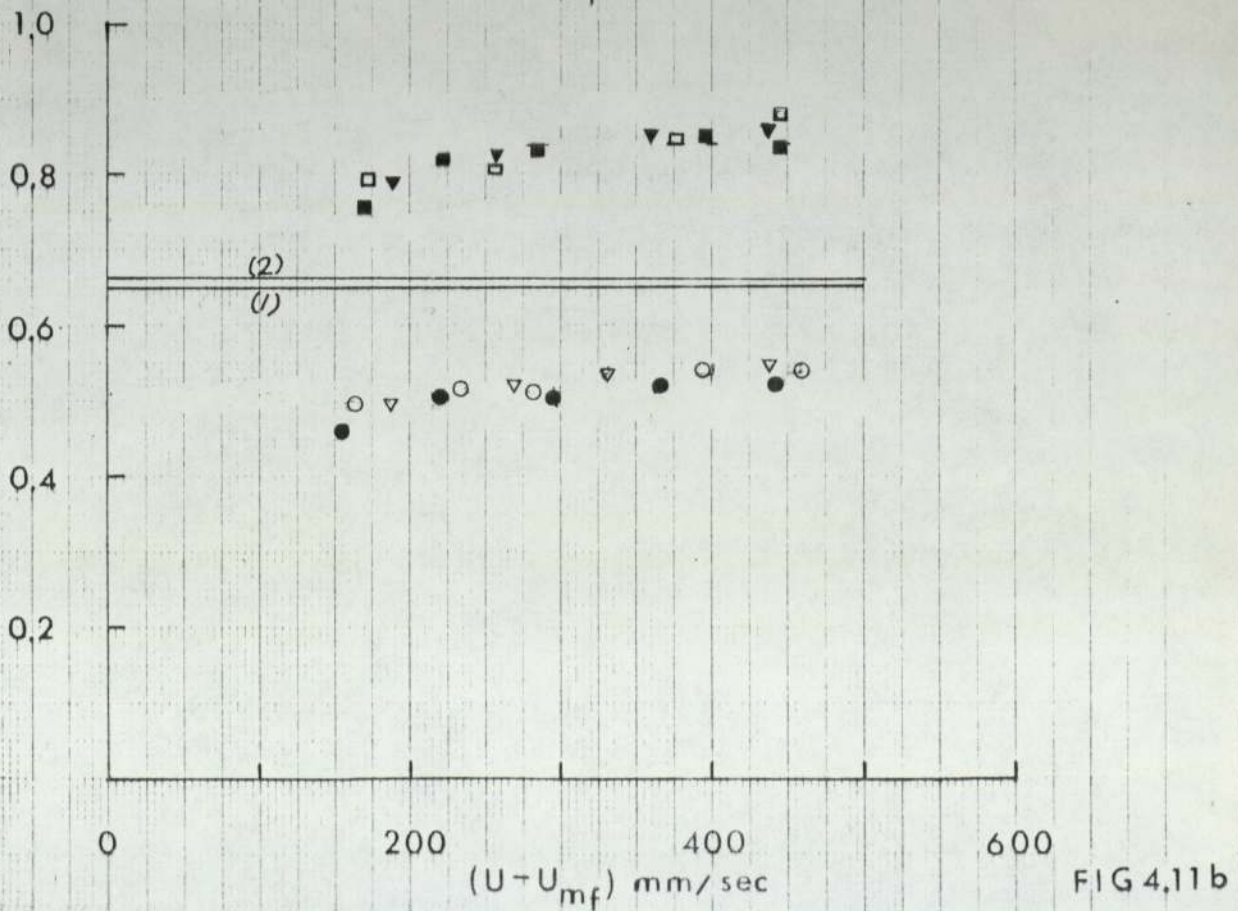
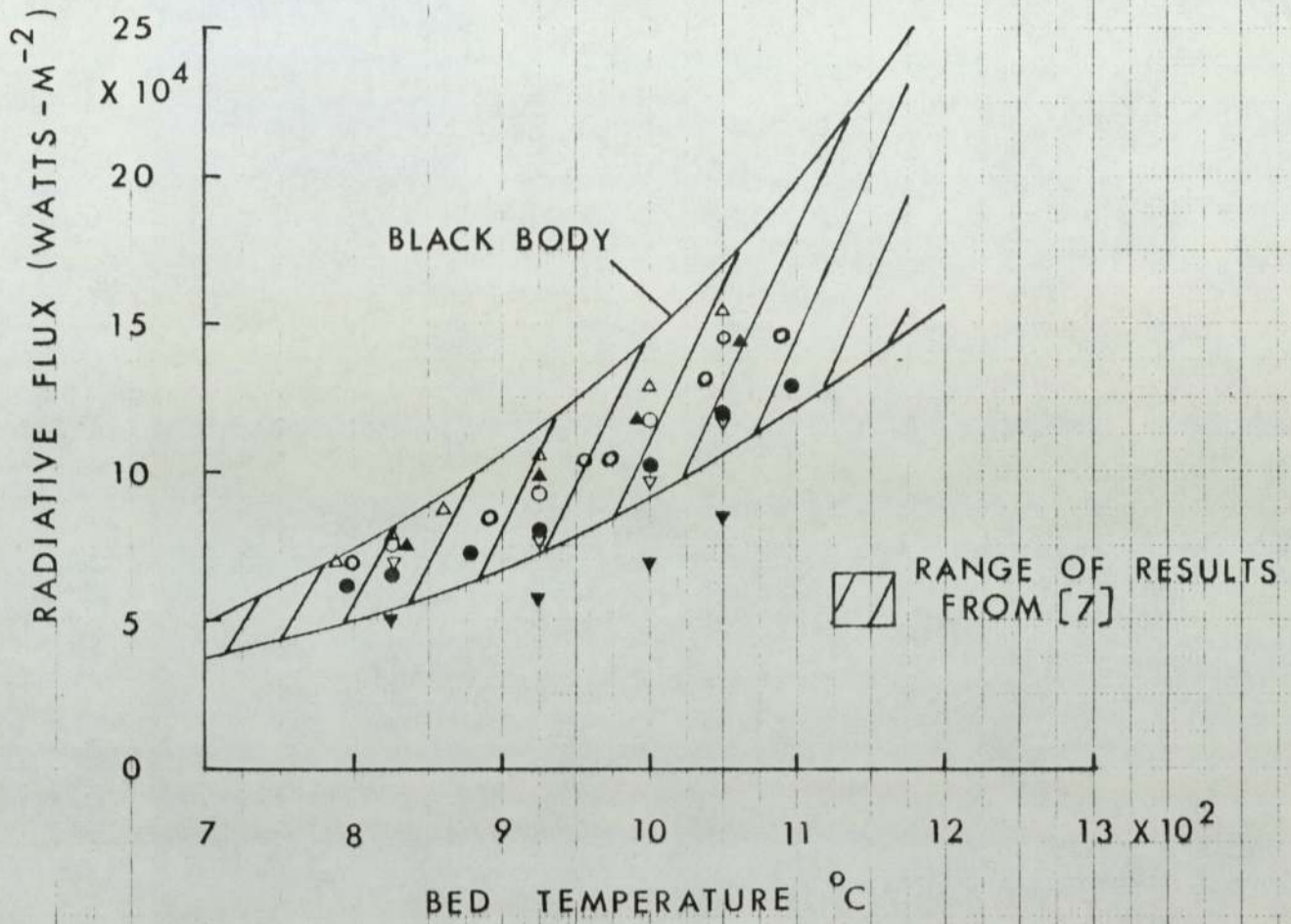


FIG 4.11b

EFFECT OF BED TEMPERATURE ON
SURFACE EMITTED RADIATIVE FLUX



	MAT ^L	D _p mm	(U - U _{mf}) mm/sec
a	□ SAND	0.55	340
b	● —//—	—//—	—//—
a	▽ ALUMINA	0.354	344
b	▼ —//—	—//—	—//—
a	△ SILICON CARBIDE	0.777	334
b	▲ —//—	—//—	—//—

a ISOTHERMAL BED
b NONISOTHERMAL BED

FIG 4.12

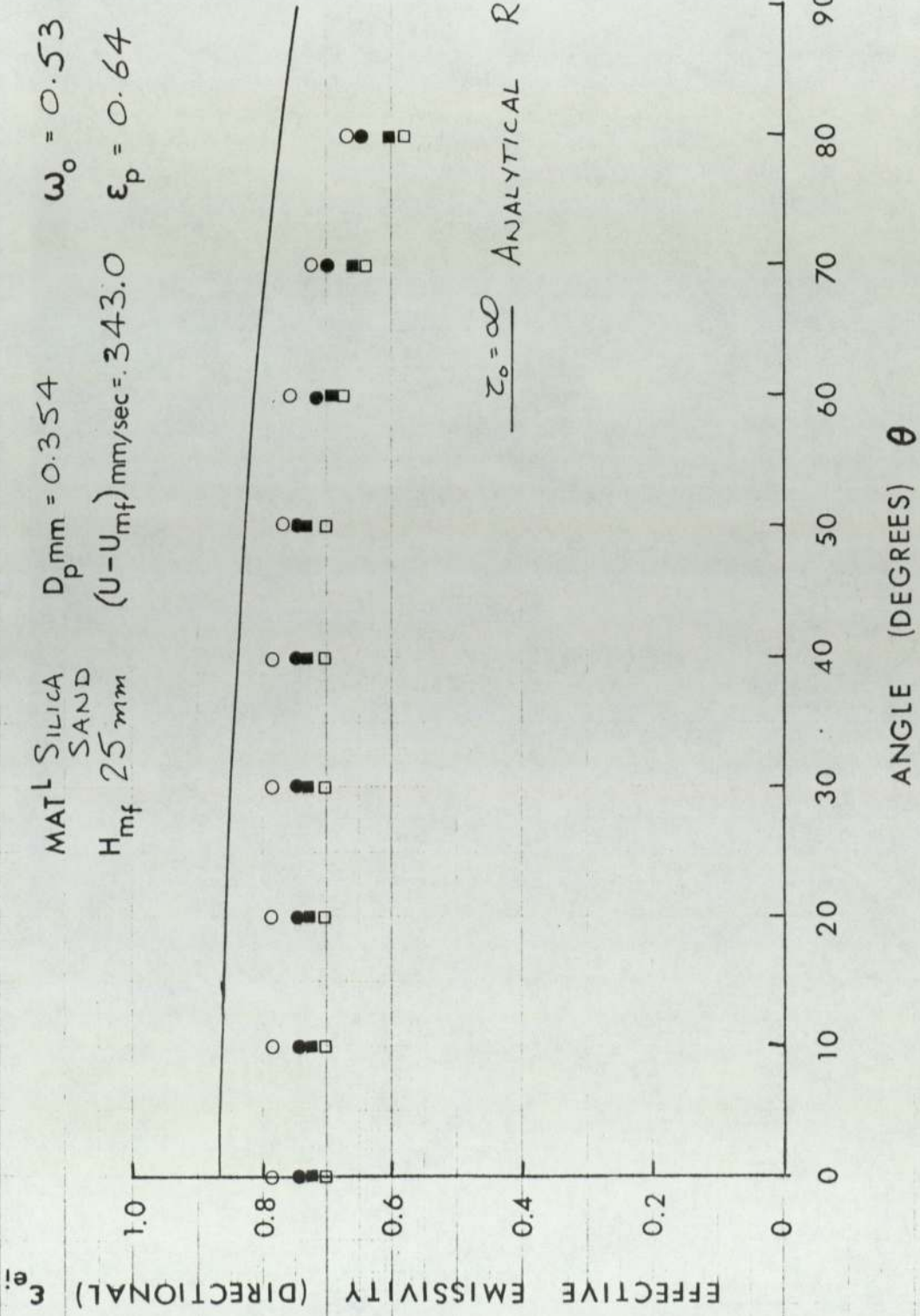


FIG 4.13

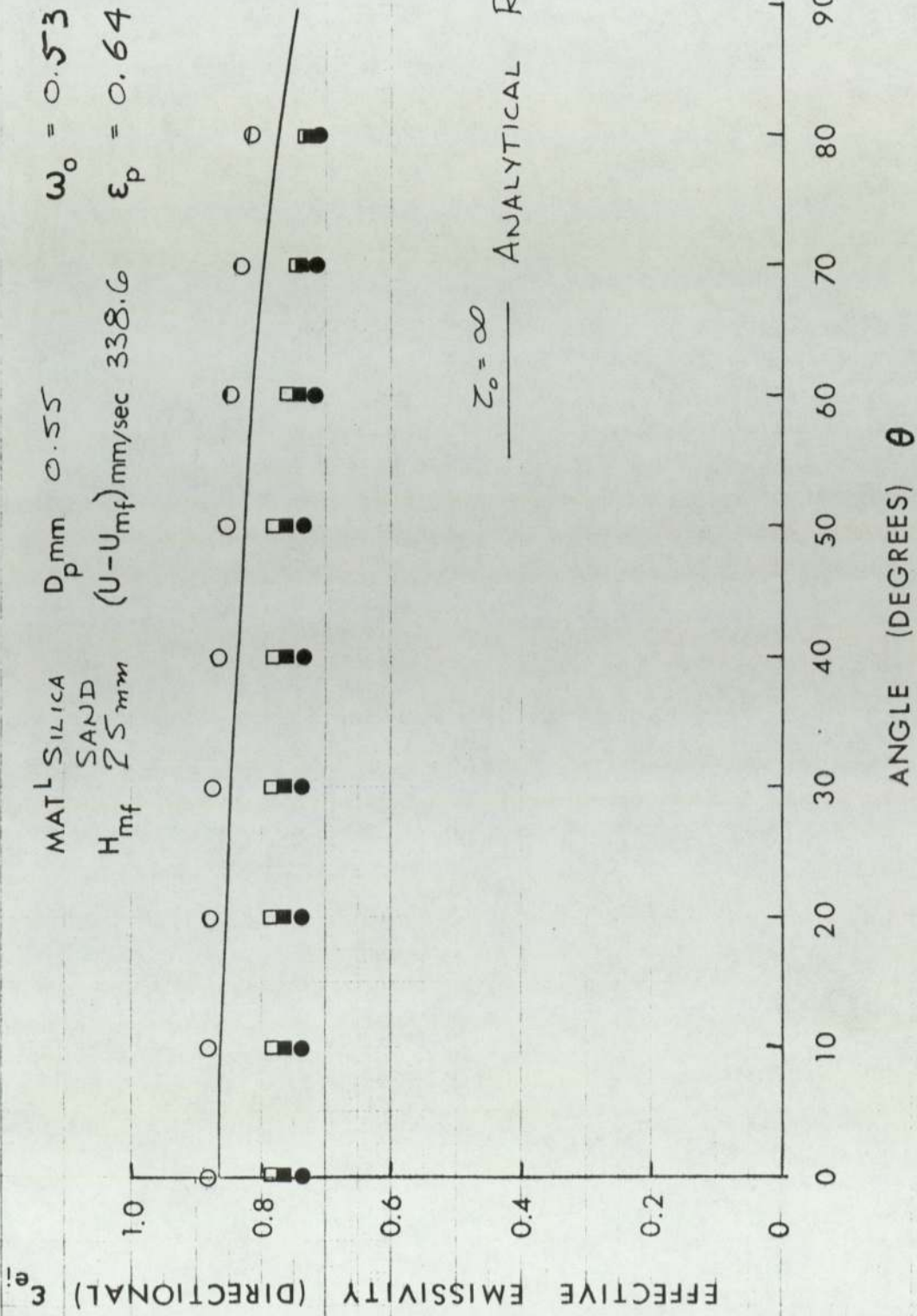


FIG 4.14

MAT^L SILICA SAND 25 mm
 D_p mm 0.77
 H_{mf} (U-U_{mf}) mm/sec 347.9
 $\omega_0 = 0.53$
 $\epsilon_p = 0.64$

T_b °C	T_s °C
● 1050	701
□ 1000	660
■ 925	611
○ 825	595

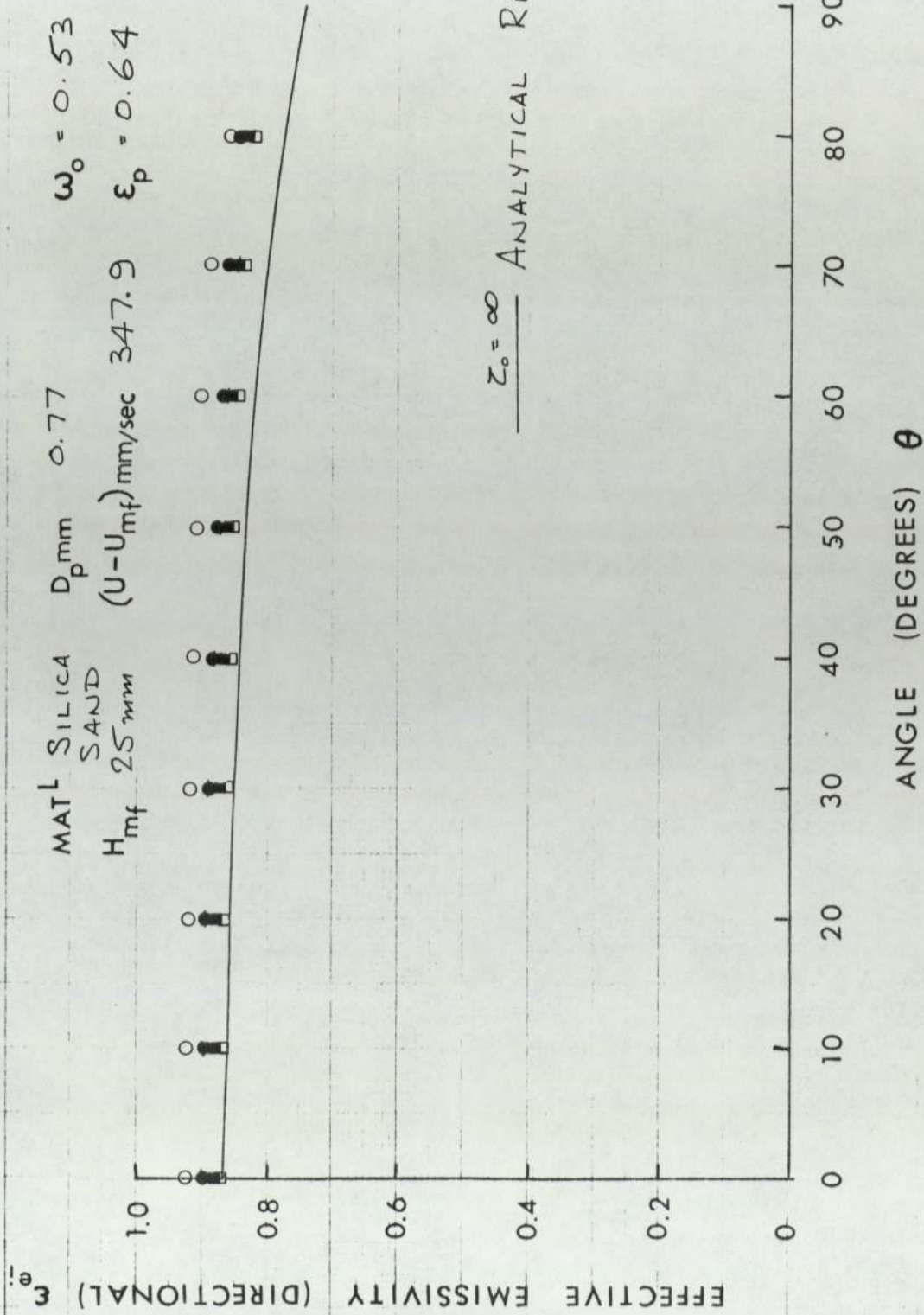


FIG 4.15

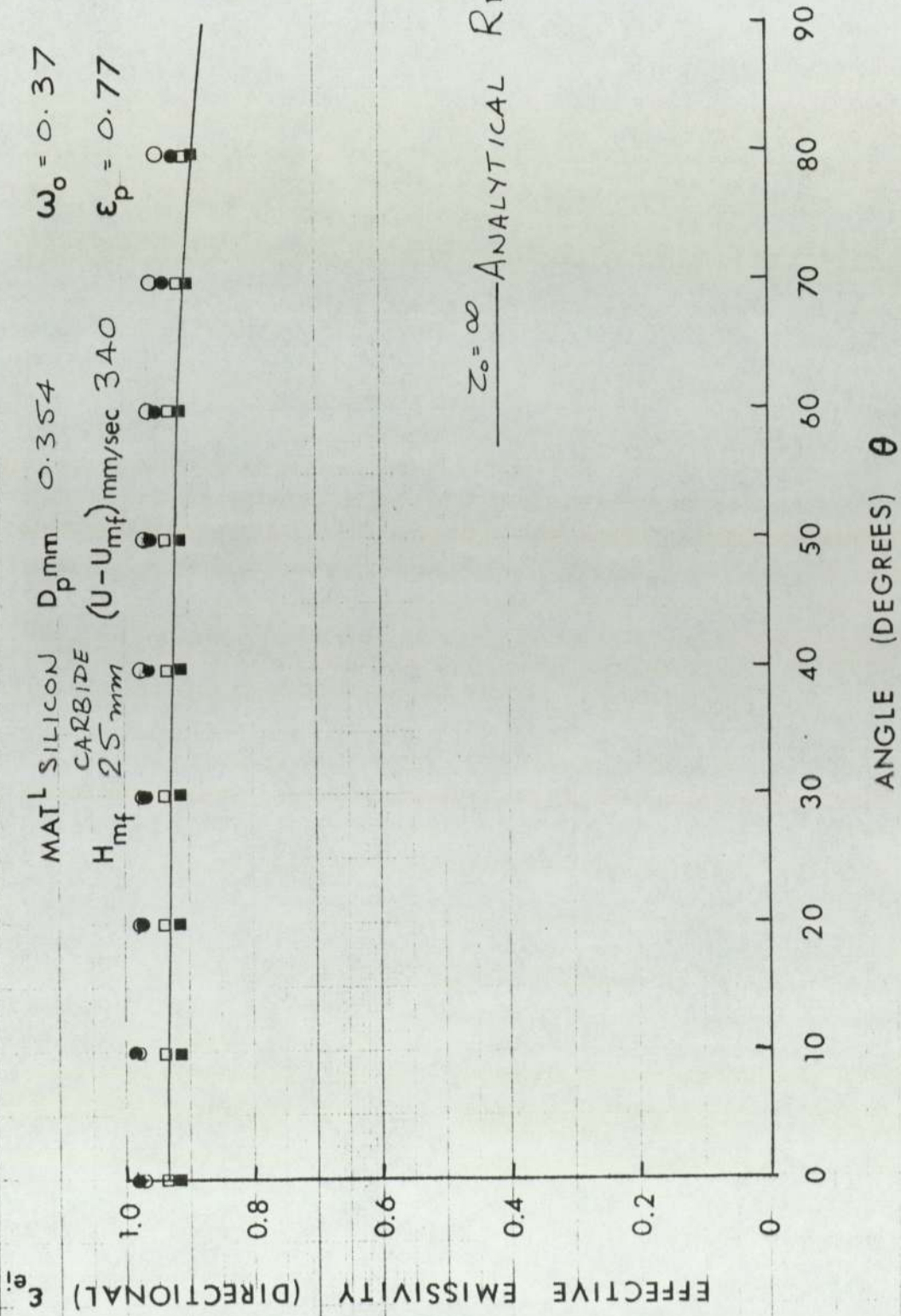


FIG 4.16

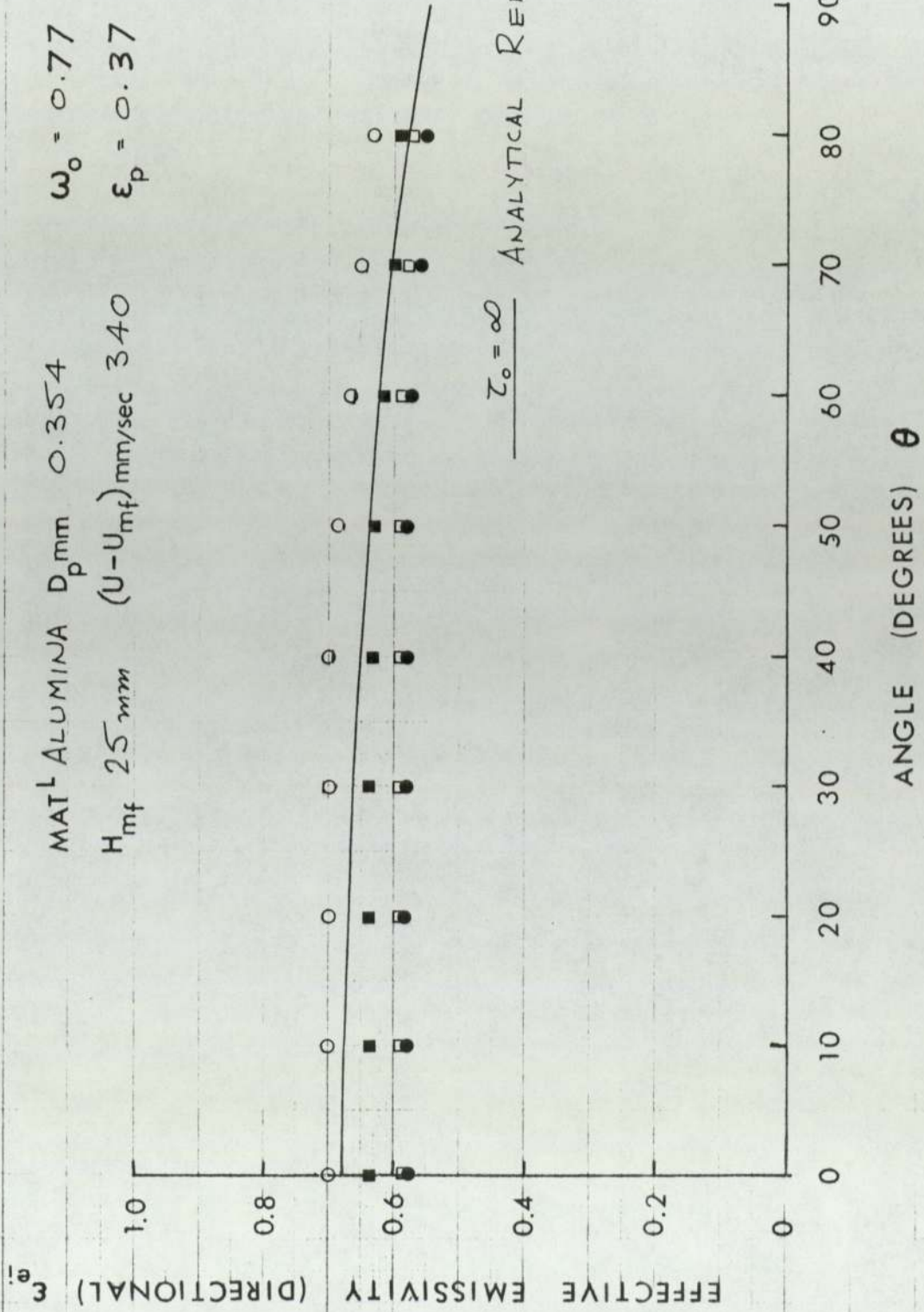
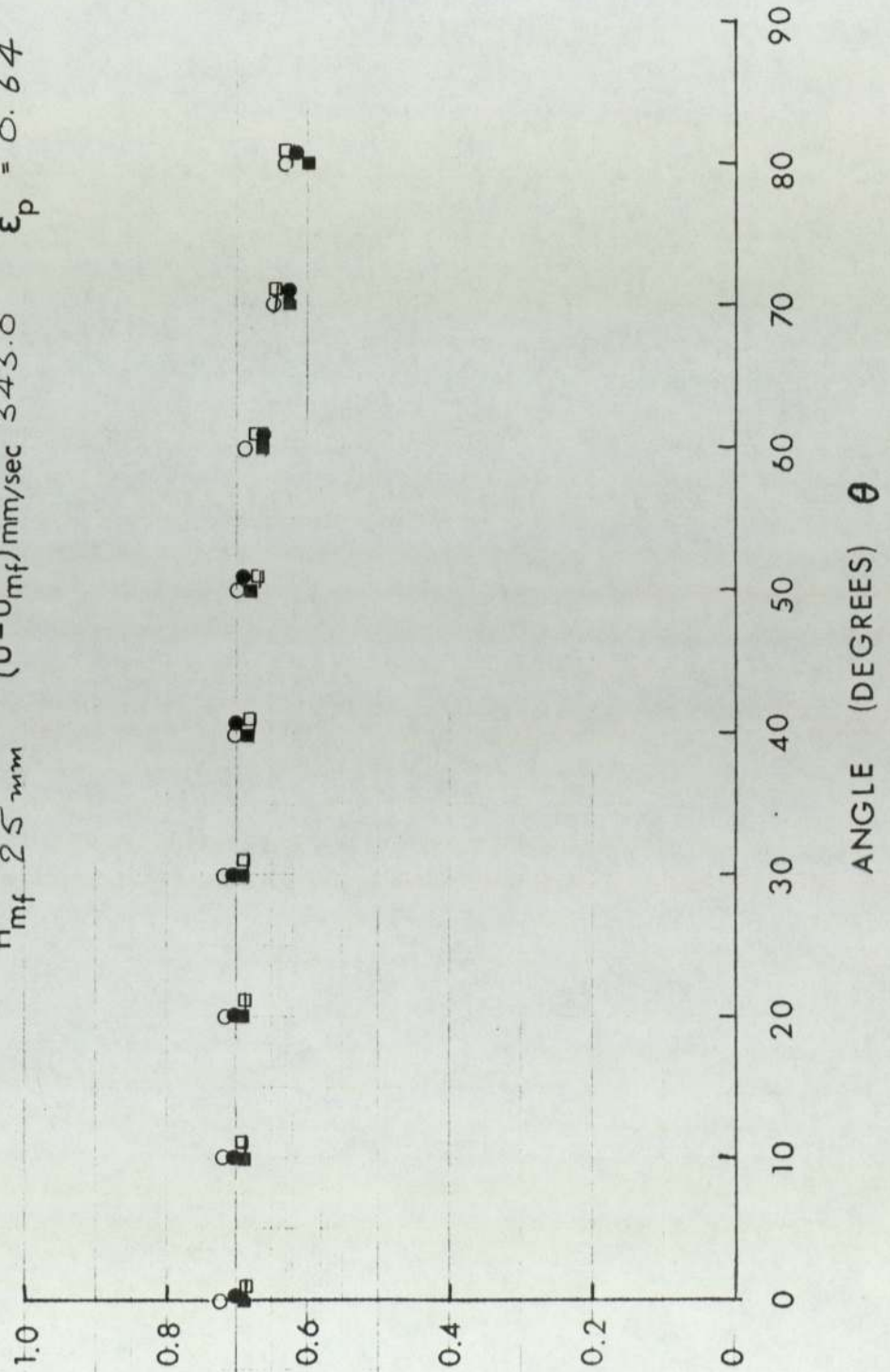


FIG 4.17

EFFECTIVE EMISSIVITY (DIRECTIONAL) ϵ_{en}

MAT'L SILICA
SAND
 $H_{mf} = 25 \text{ mm}$
 $D_p = 0.354 \text{ mm}$
 $(U - U_{mf}) = 343.0 \text{ mm/sec}$
 $\omega_o = 0.53$
 $\epsilon_p = 0.64$

T_b °C T_s °C
 ● 1050 —
 □ 1000 —
 ■ 925 —
 ○ 825 —



ANGLE (DEGREES) θ

FIG 4.18

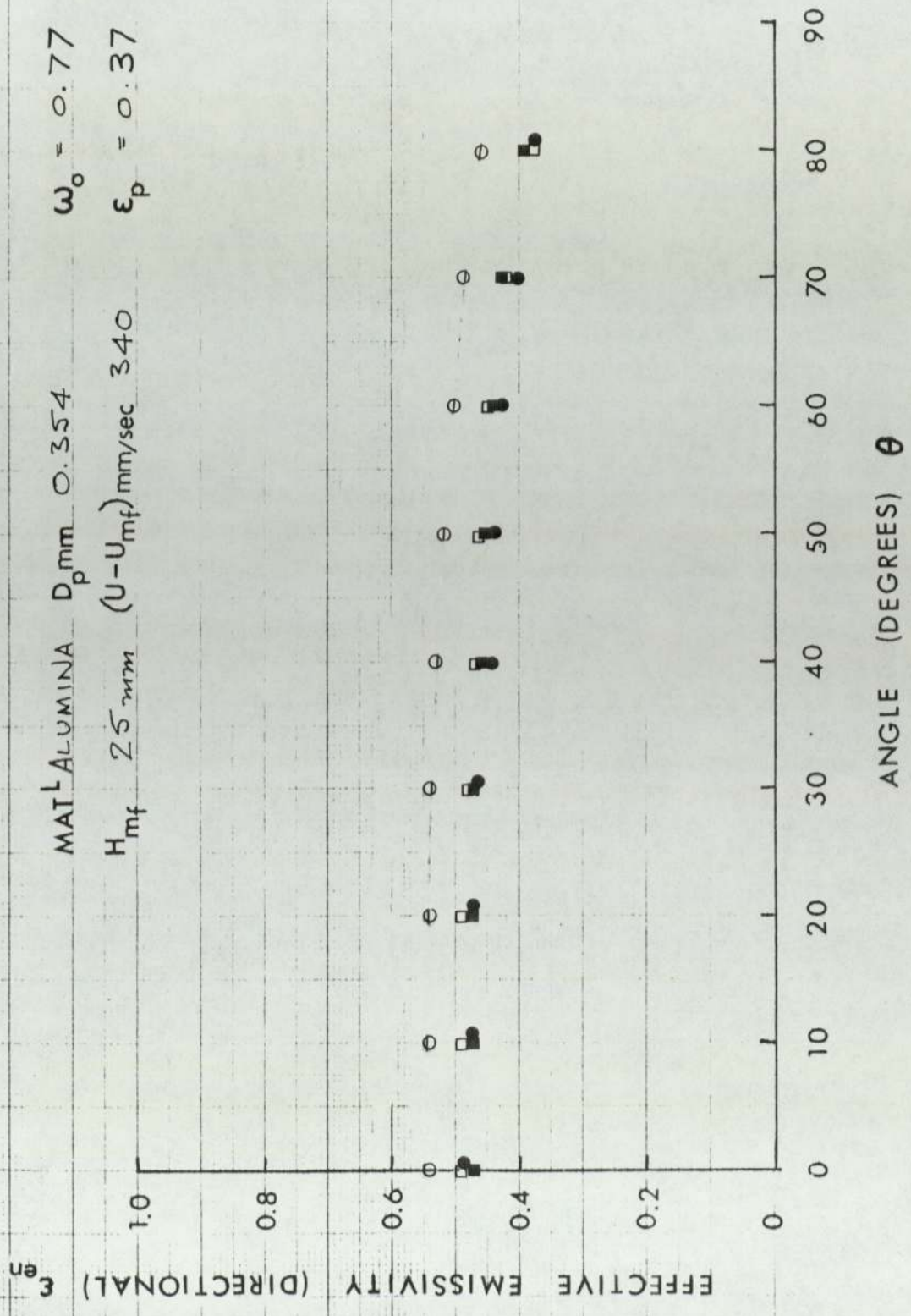


FIG 4.19

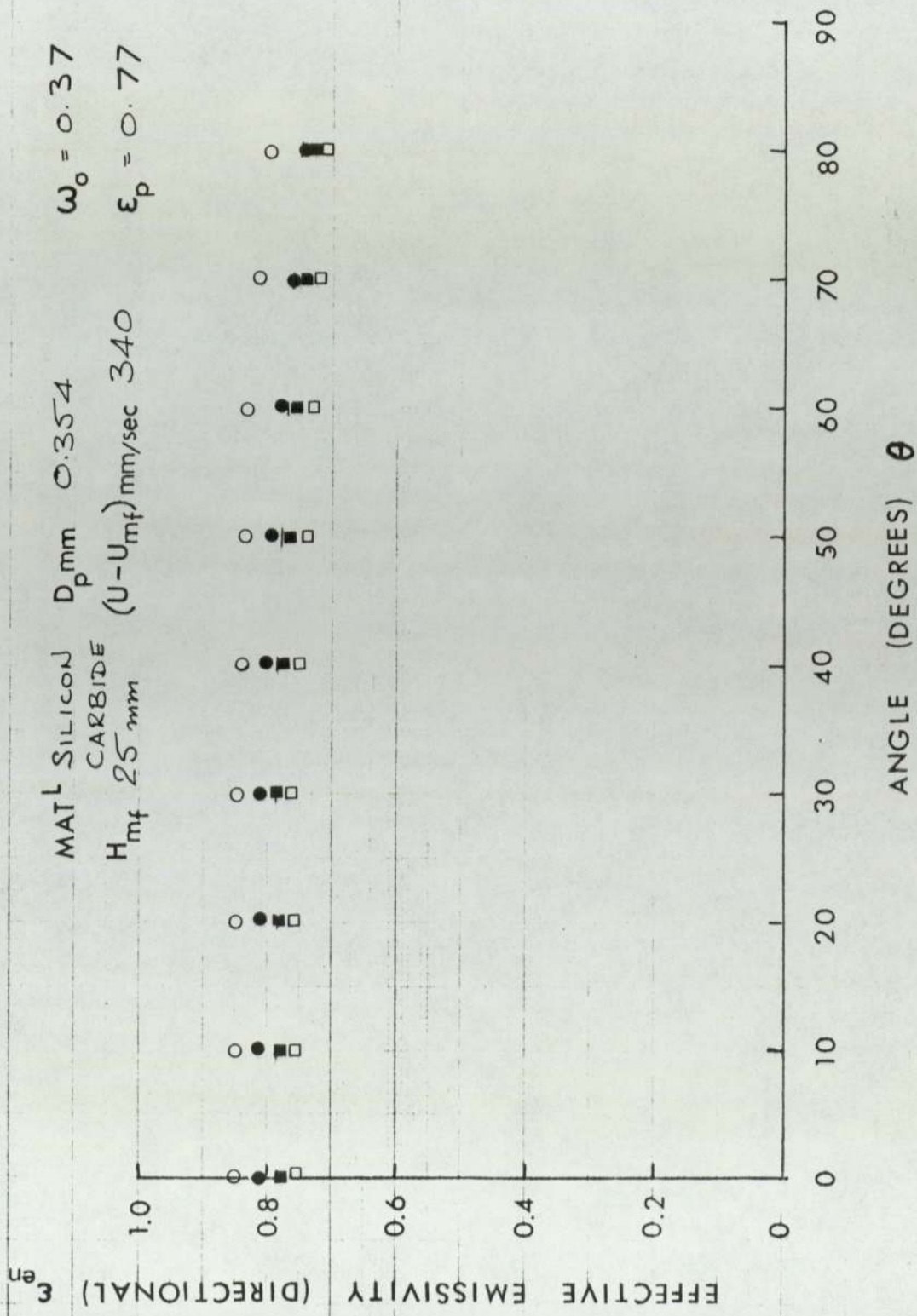


FIG 4.20

EFFECT OF EXCESS GAS VELOCITY ON
EFFECTIVE EMISSIVITY OF A BINARY

MIXTURE

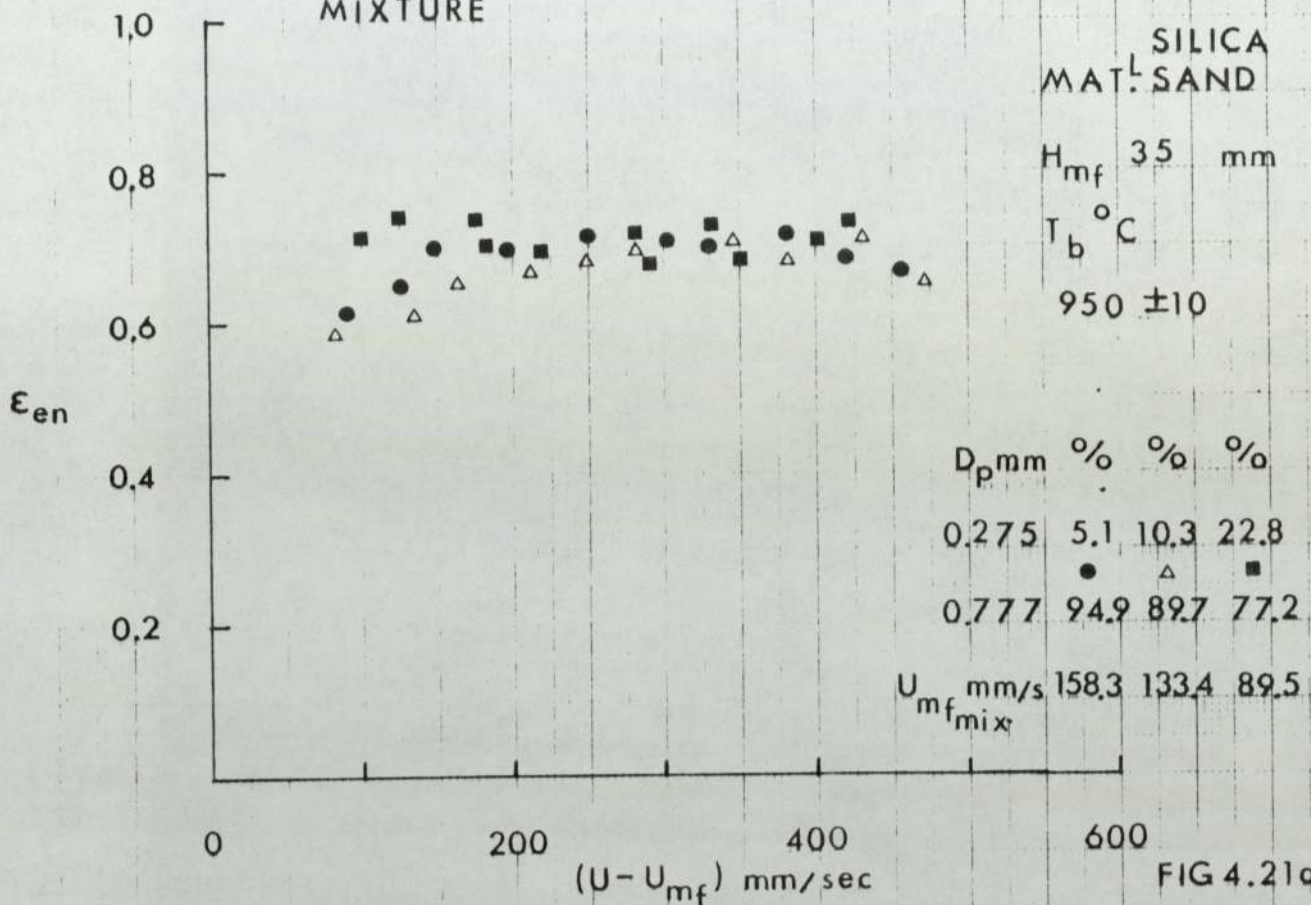


FIG 4.21a

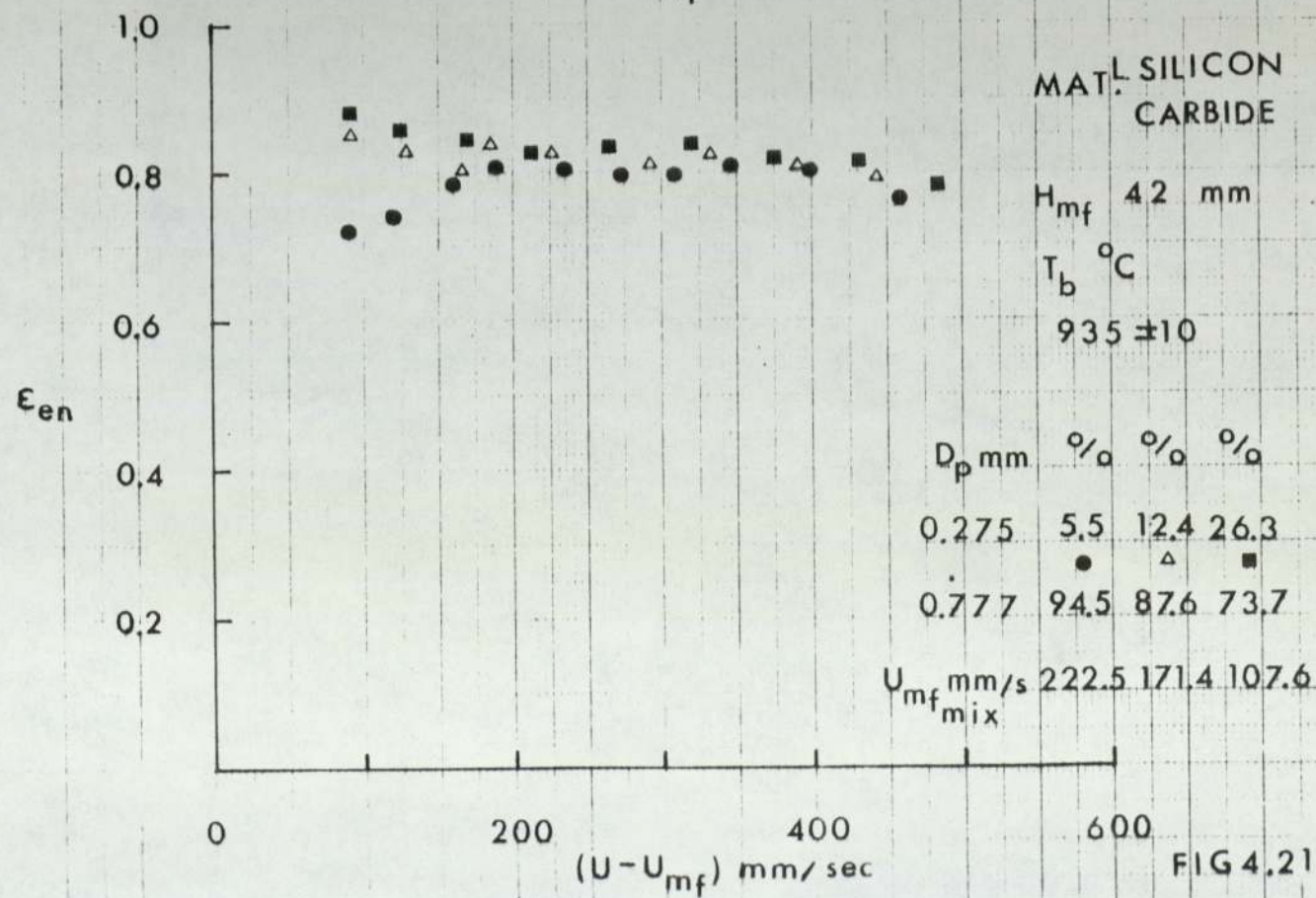


FIG 4.21b

EXPERIMENTAL CONFIGURATION FOR
A STUDY OF '2-D' BUBBLES

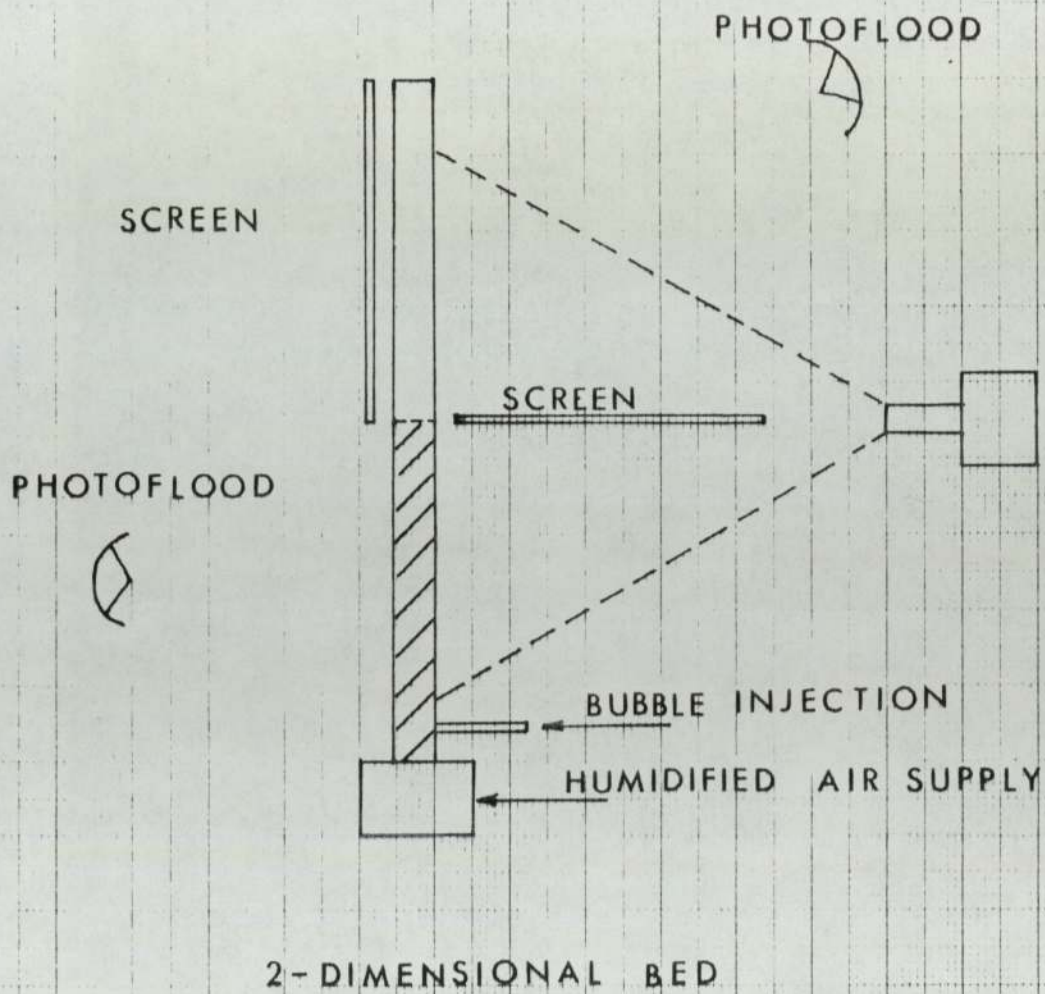
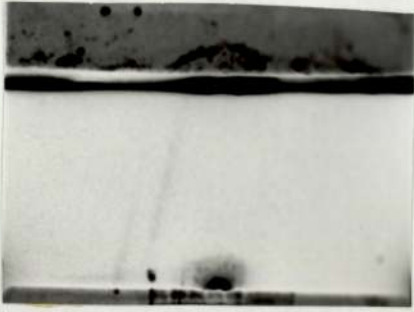


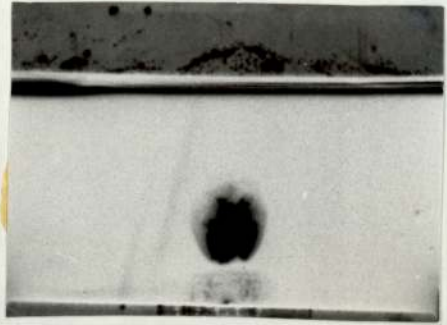
FIG 5.1

Sequence of single bubble rise and particle ejection
in a two dimensional bed

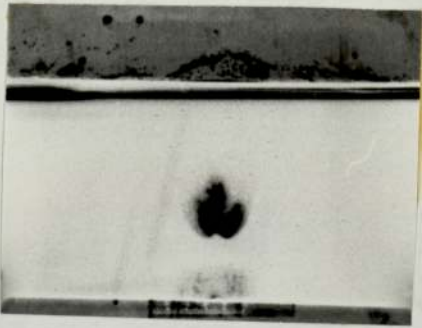
FIG 5.2



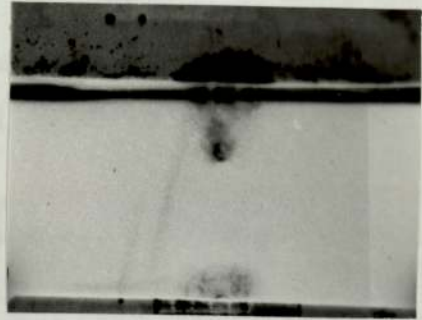
a) 0.05 sec



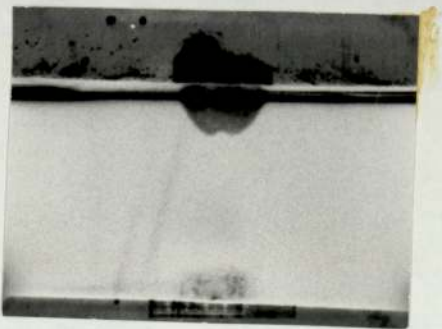
b) 0.15 sec



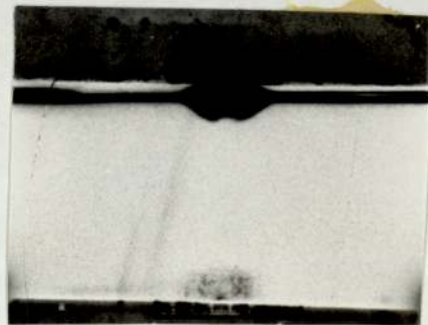
c) 0.2 sec



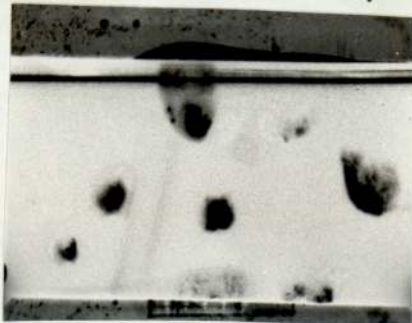
d) 0.3 sec



e) 0.35 sec



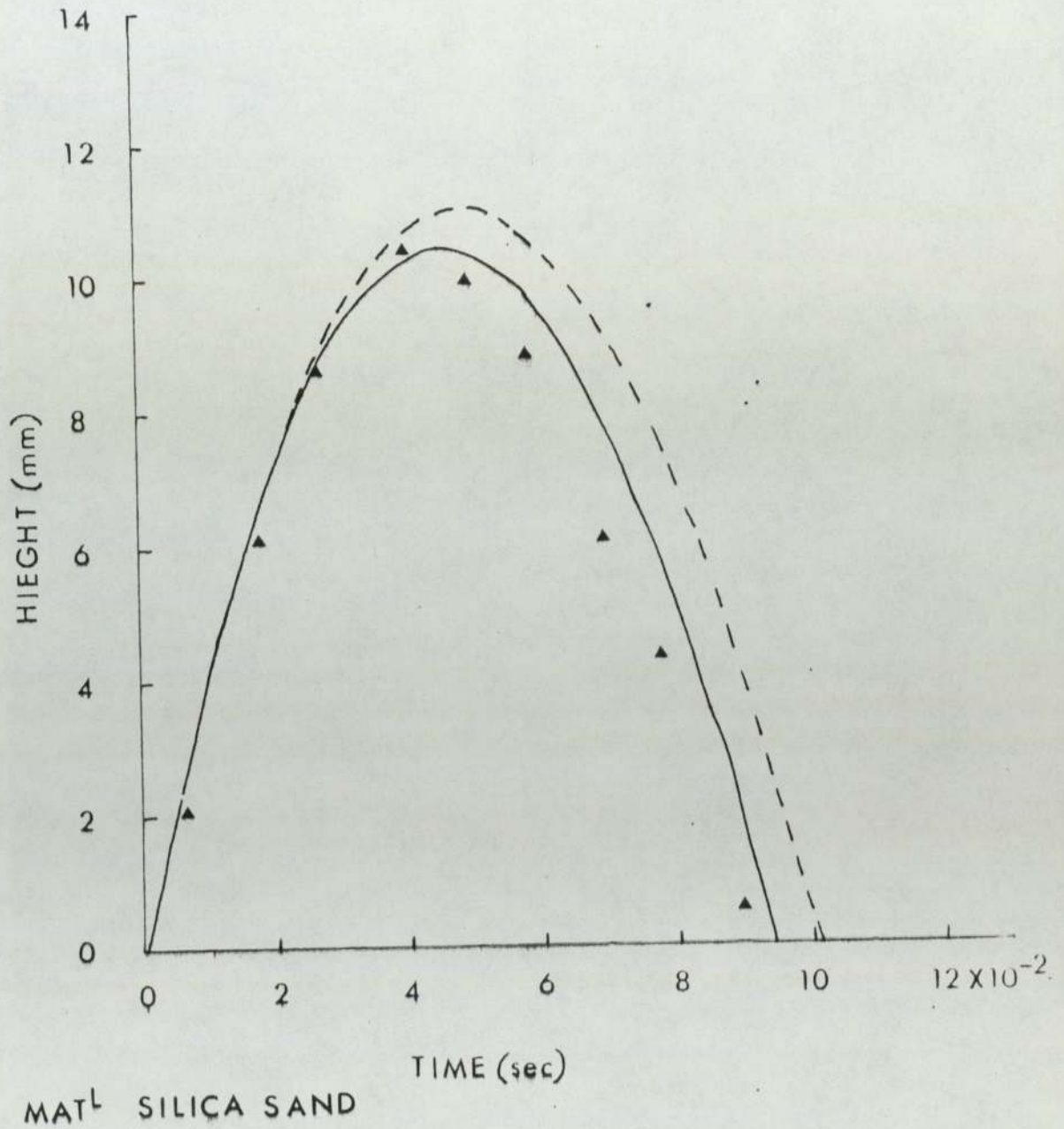
f) 0.39 sec



Freely bubbling bed

FIG 5.3

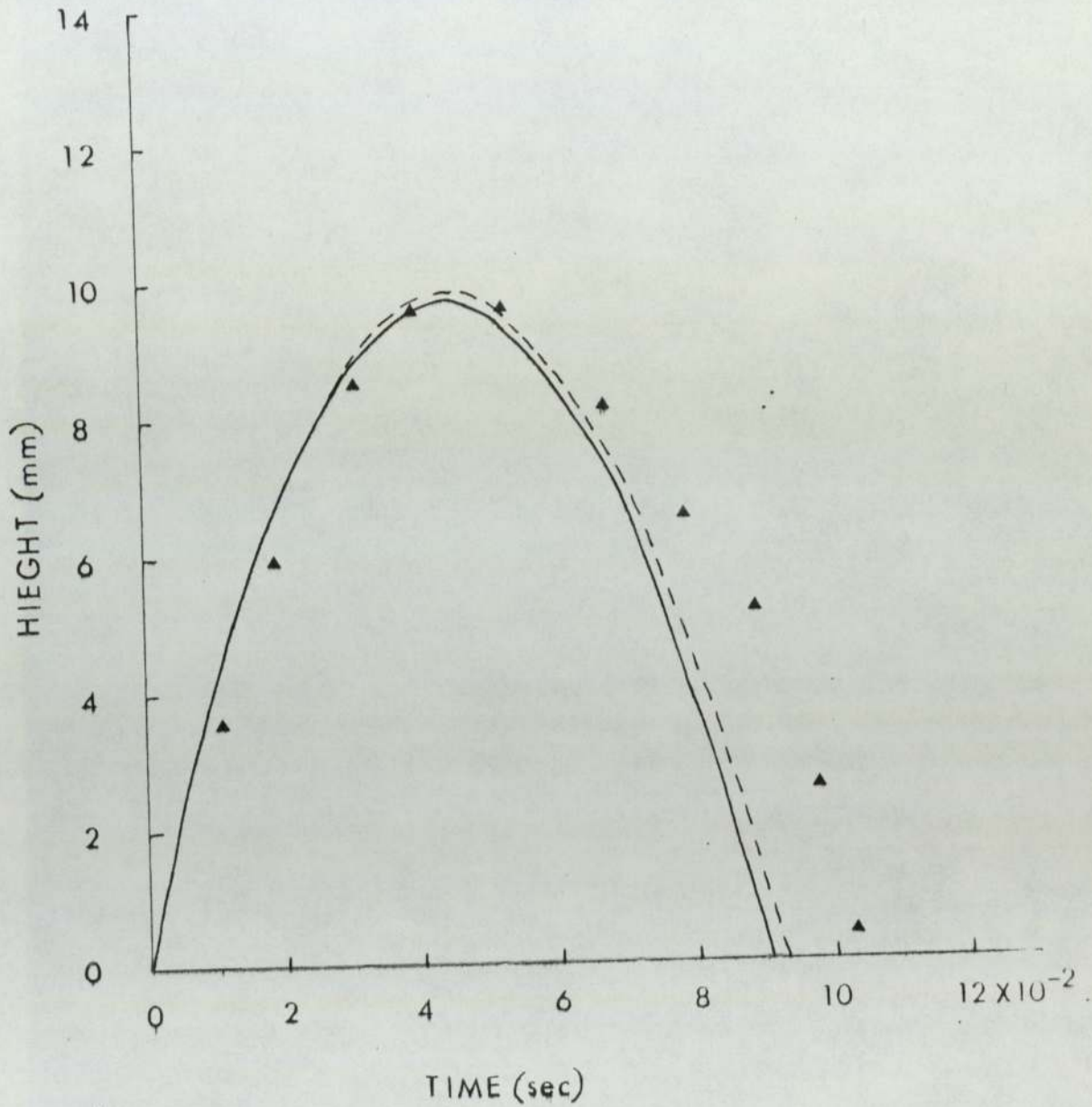
PREDICTED AND OBSERVED
PARTICLE CLOUD TRAJECTORIES



	U_b mm/sec	T_b °C	D_p mm
—▲—	355	20	0.354
- - -	-//-	1000	-//-

FIG 5.4

PREDICTED AND OBSERVED
PARTICLE CLOUD TRAJECTORIES

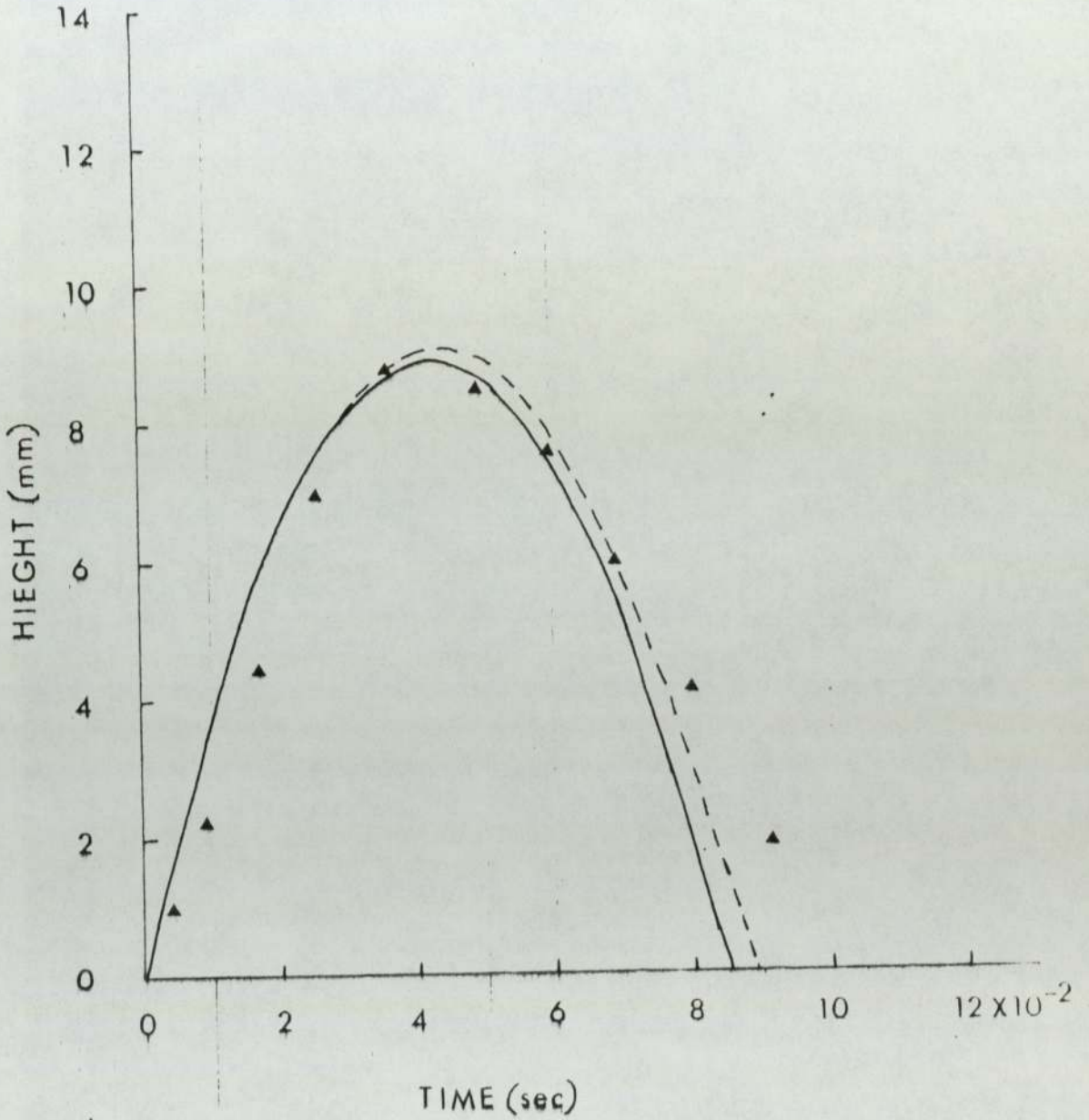


MAT^L SILICA SAND

	U_b mm/sec	T_b °C	D_p mm
—▲—	336.9	20	0.777
---	---	1000	---

FIG 5.5

PREDICTED AND OBSERVED
PARTICLE CLOUD TRAJECTORIES



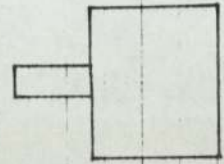
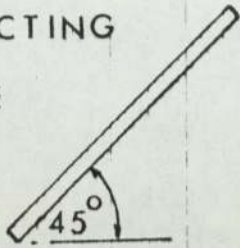
MAT^L SILICA SAND

	U_b mm/sec	T_b °C	D_p mm
—▲—	323	20	0.55
-//-	-//-	1000	-//-

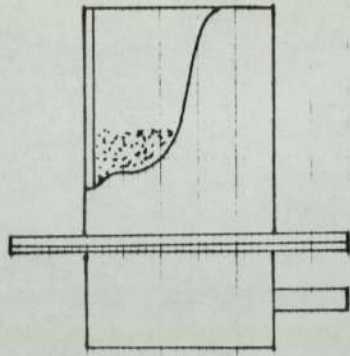
FIG 5.6

PHOTOGRAPHIC STUDY OF BED SURFACE

REFLECTING PLATE



CAMERA

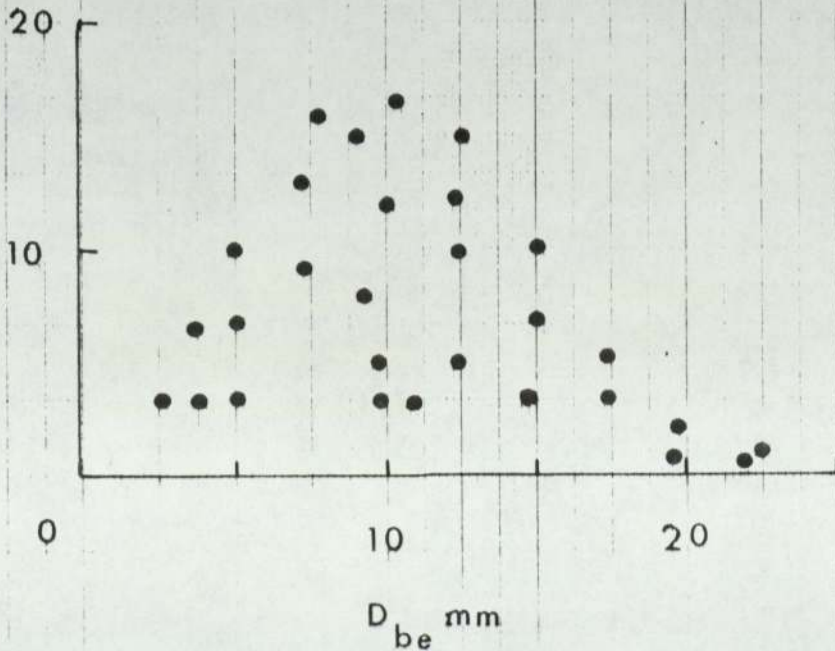


AIR SUPPLY

FLUIDISED BED

FIG 5.7

NUMBER OF BUBBLES/FRAME



$U - U_{mf}$
40.76 mm/sec

T_b °C
20

FIG 5.8

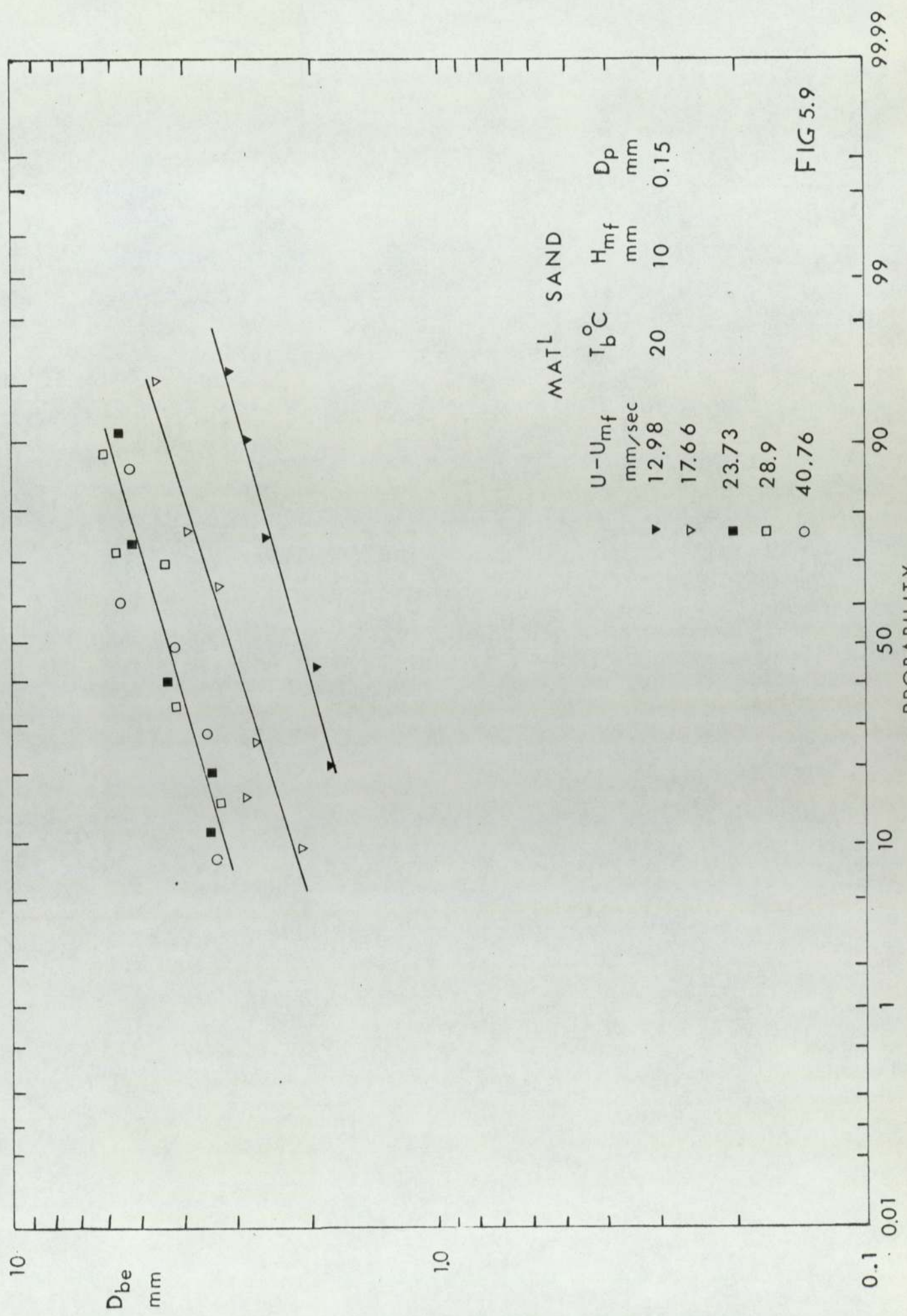


FIG 5.9

10
1.0
0.1

PROBABILITY

1 10 50 90 99 99.99

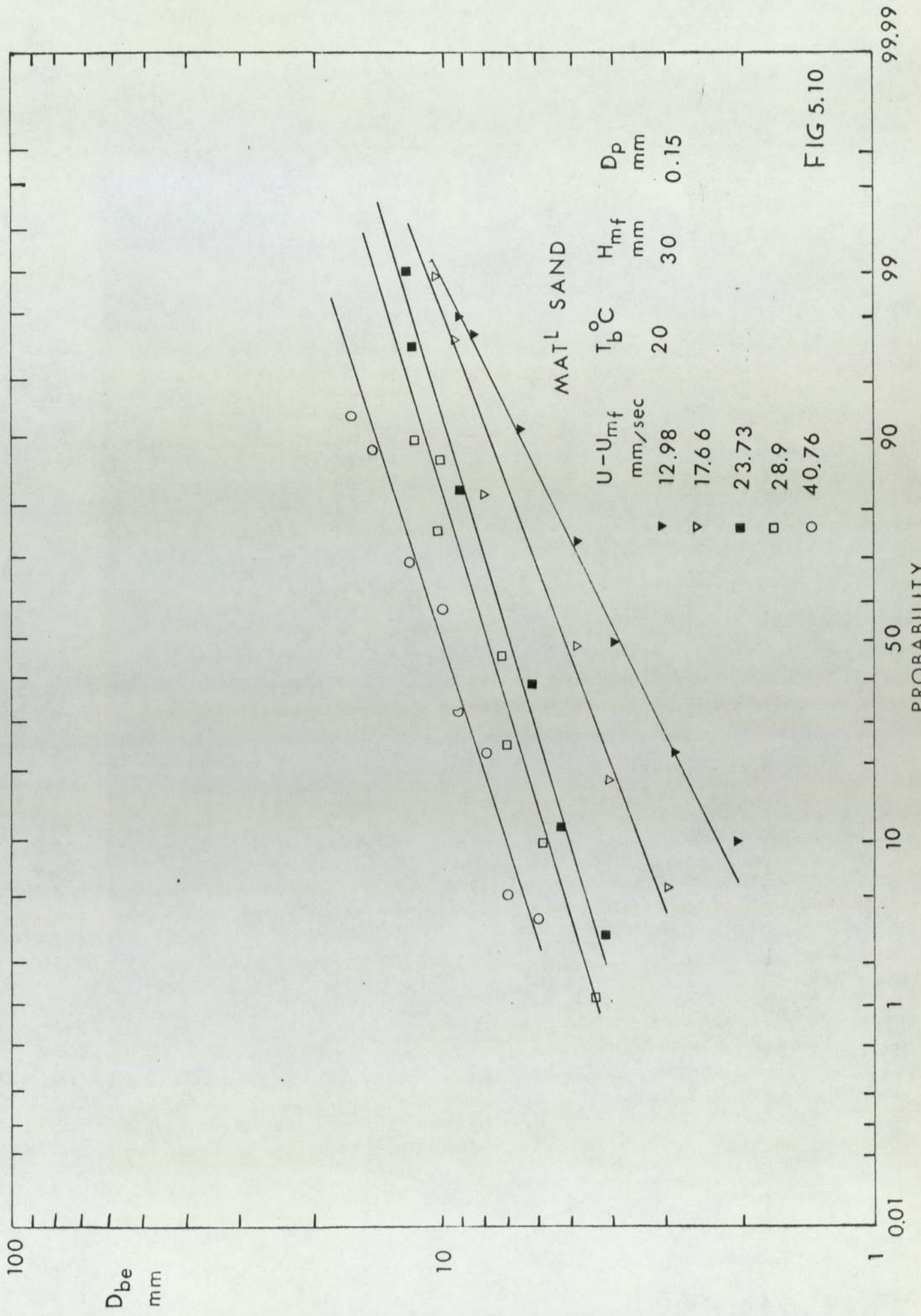


FIG 5.10

D_{be}
mm

10

100

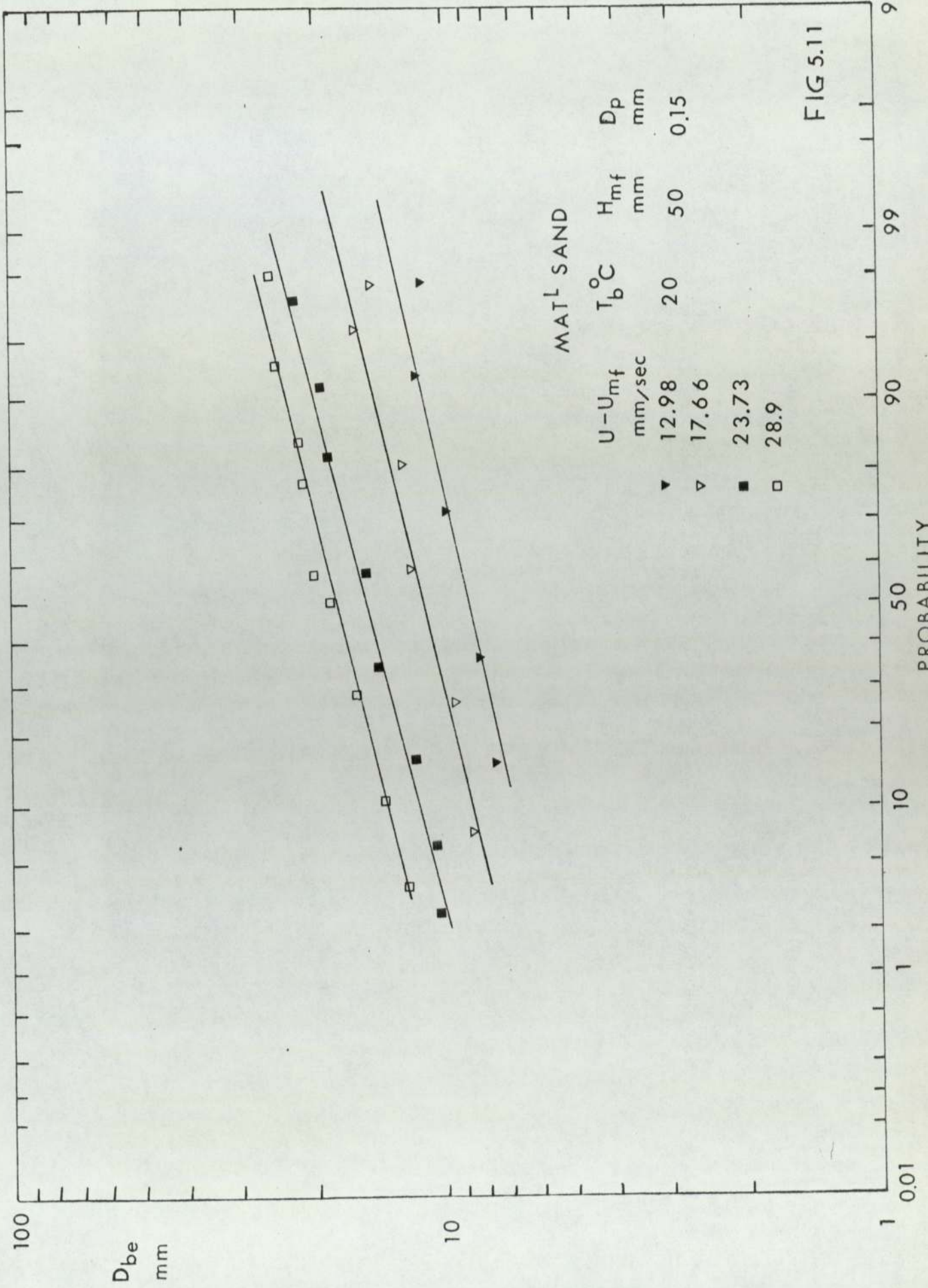


FIG 5.11

PROBABILITY

D_{be}
mm

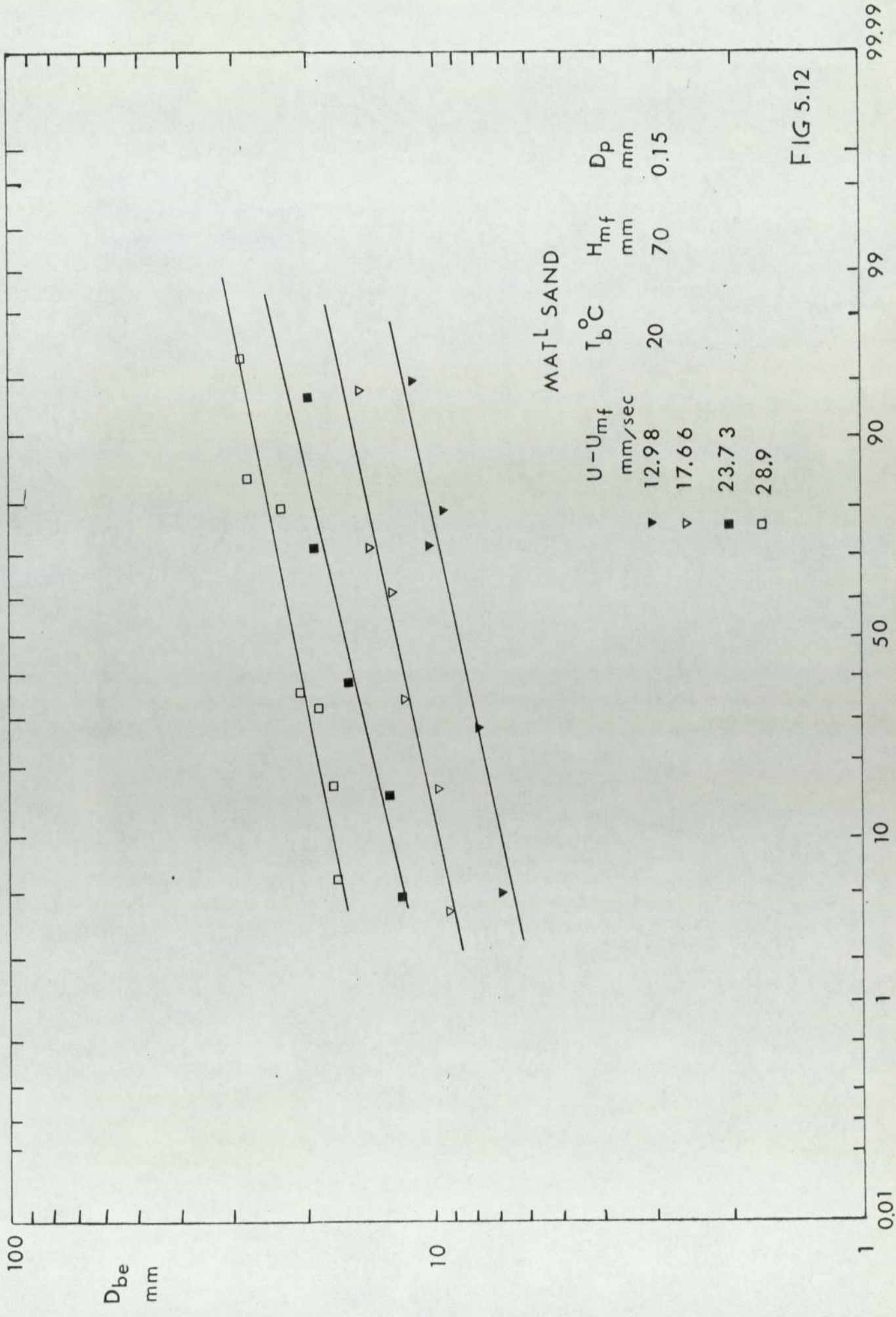


FIG 5.12

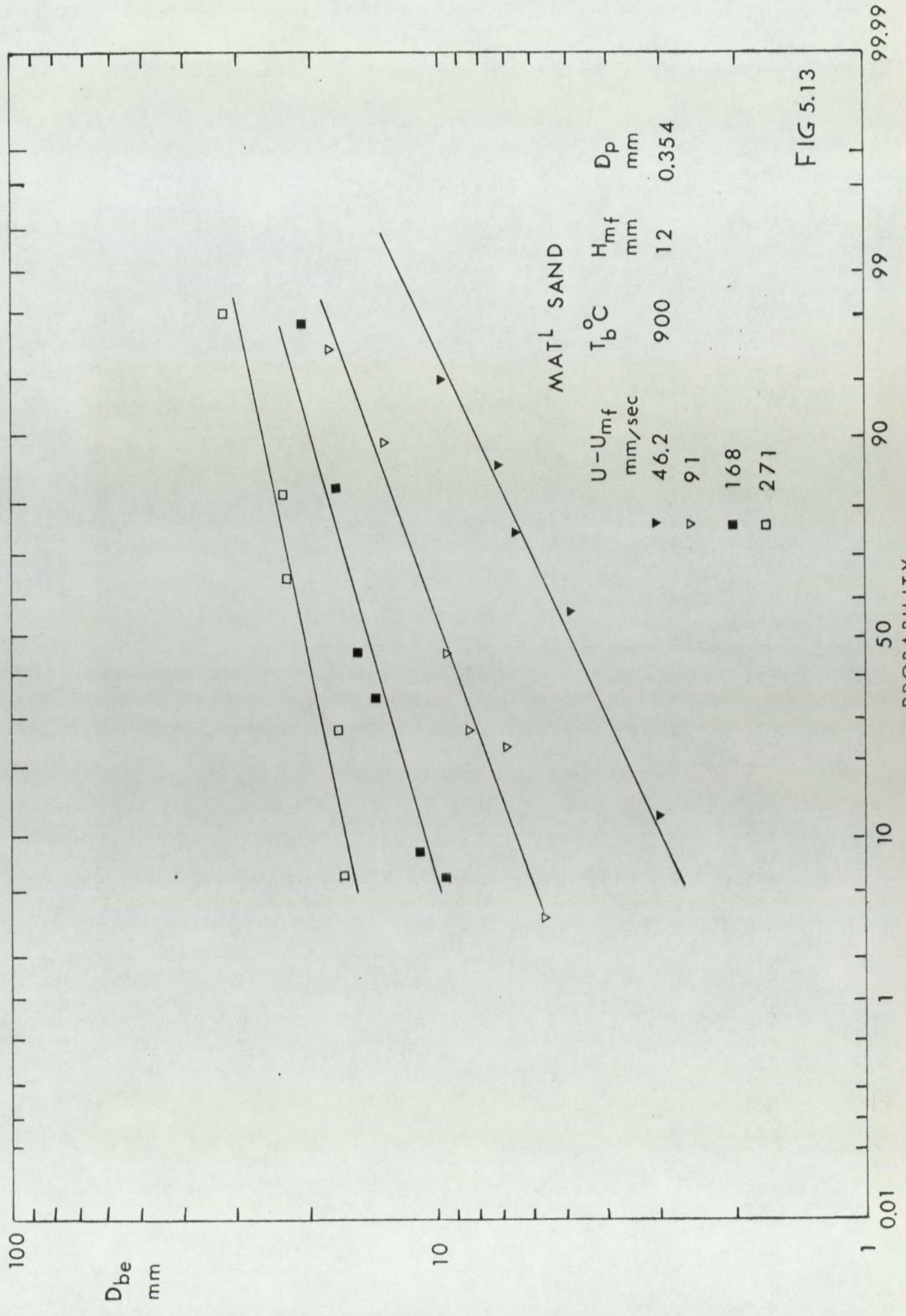
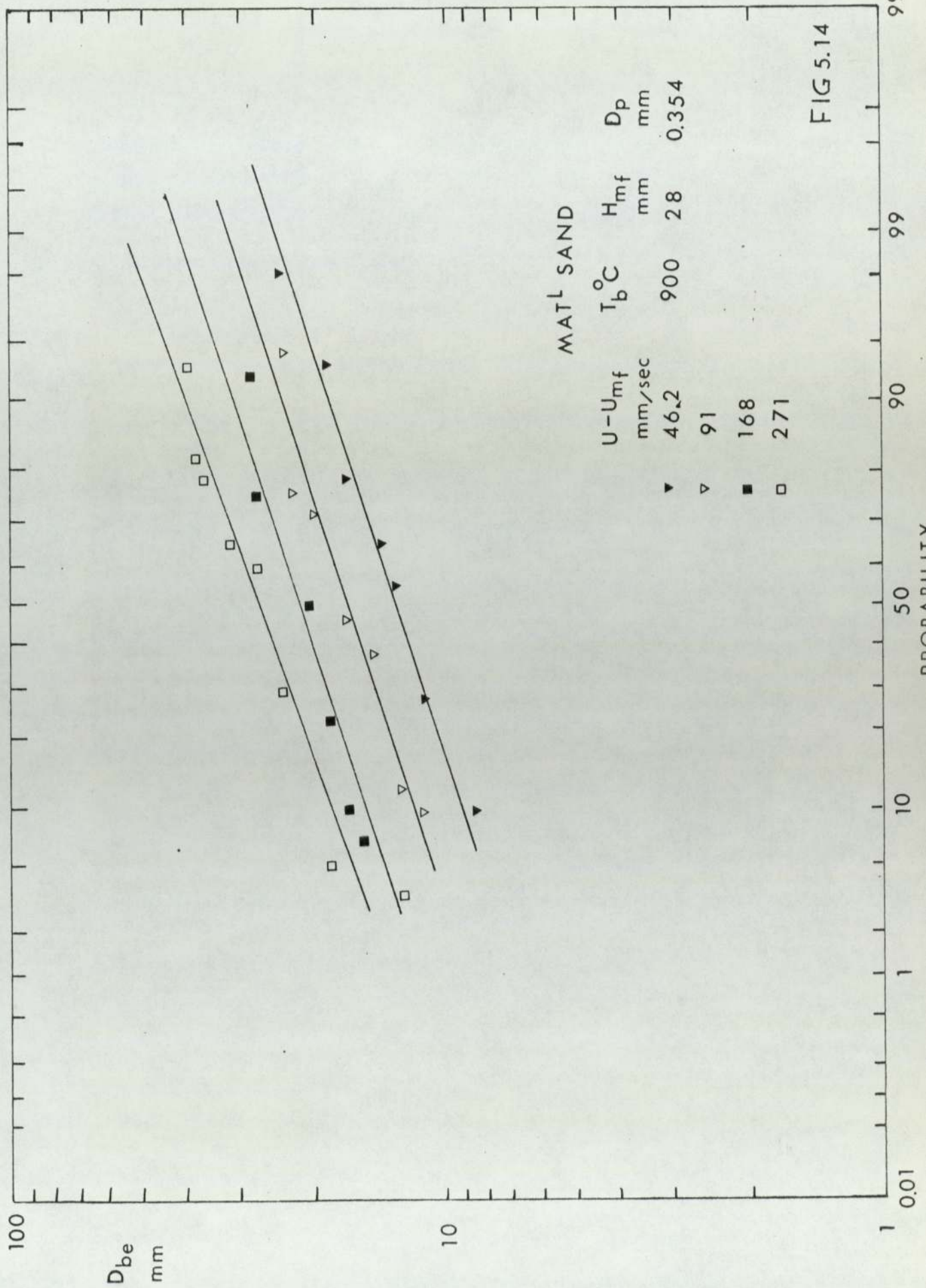


FIG 5.13



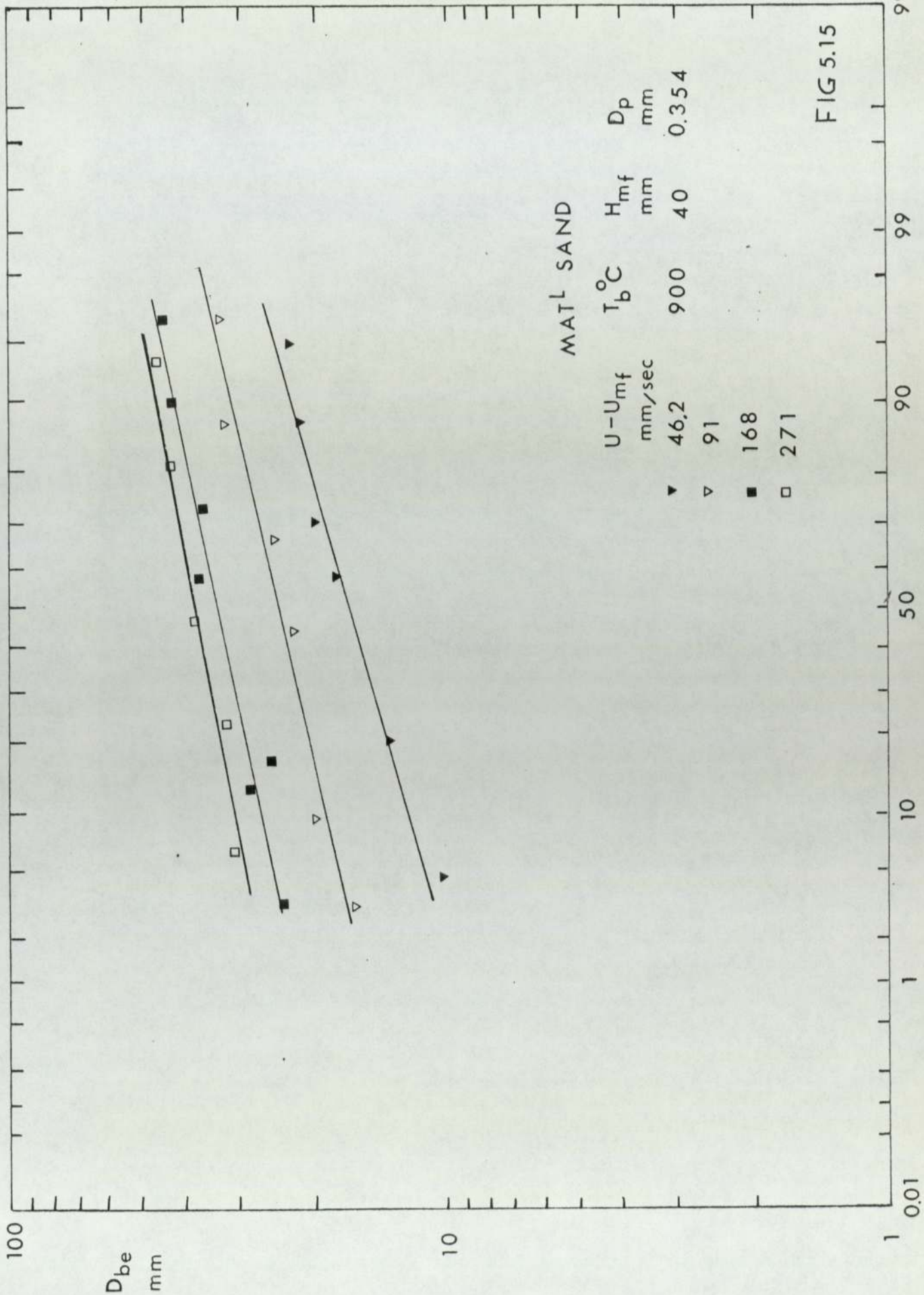


FIG 5.15

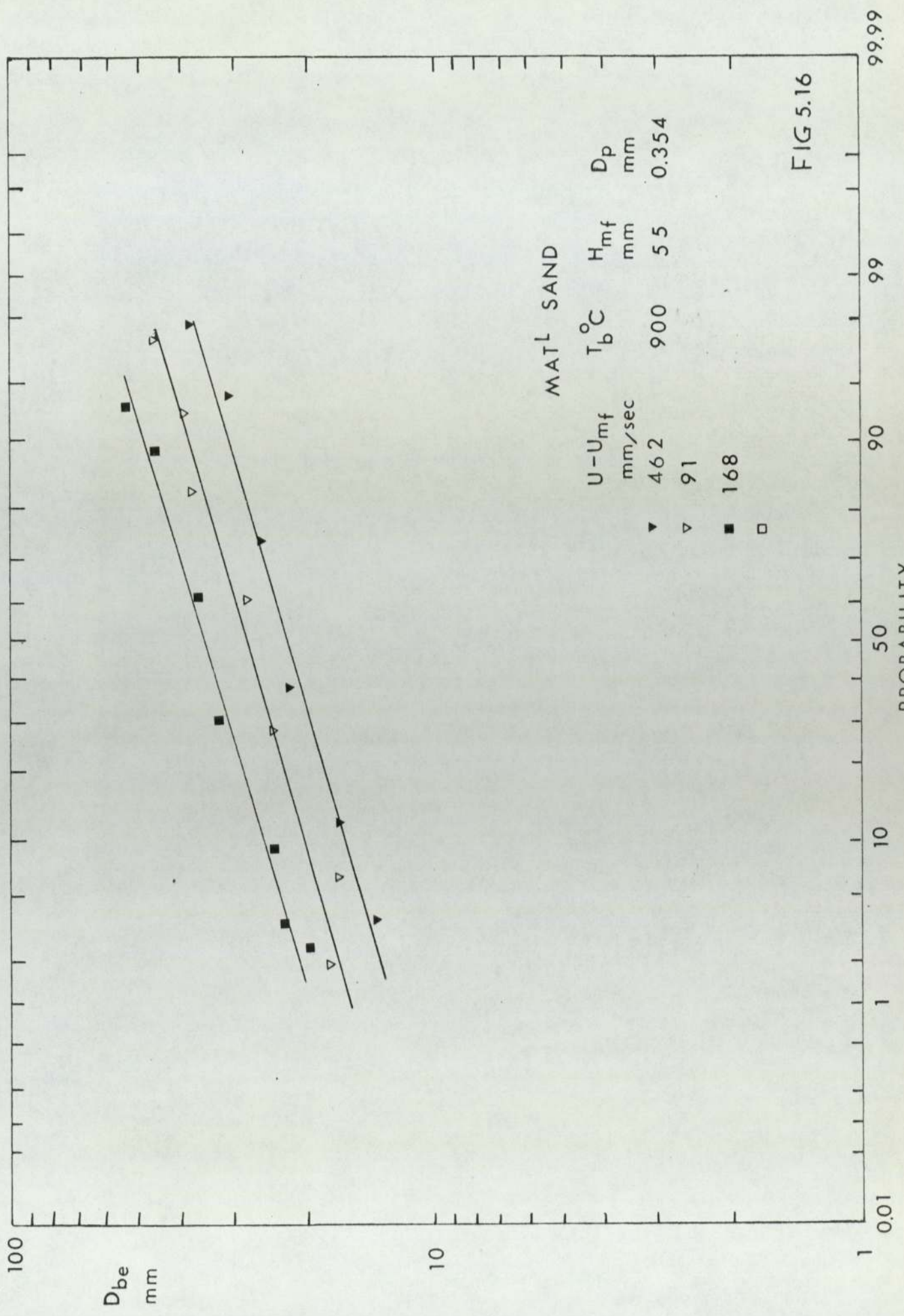


FIG 5.16

A CORRELATION OF D_b , $H_{mf}(U-U_{mf})$ AT AMBIENT AND ELEVATED
BED TEMPERATURES

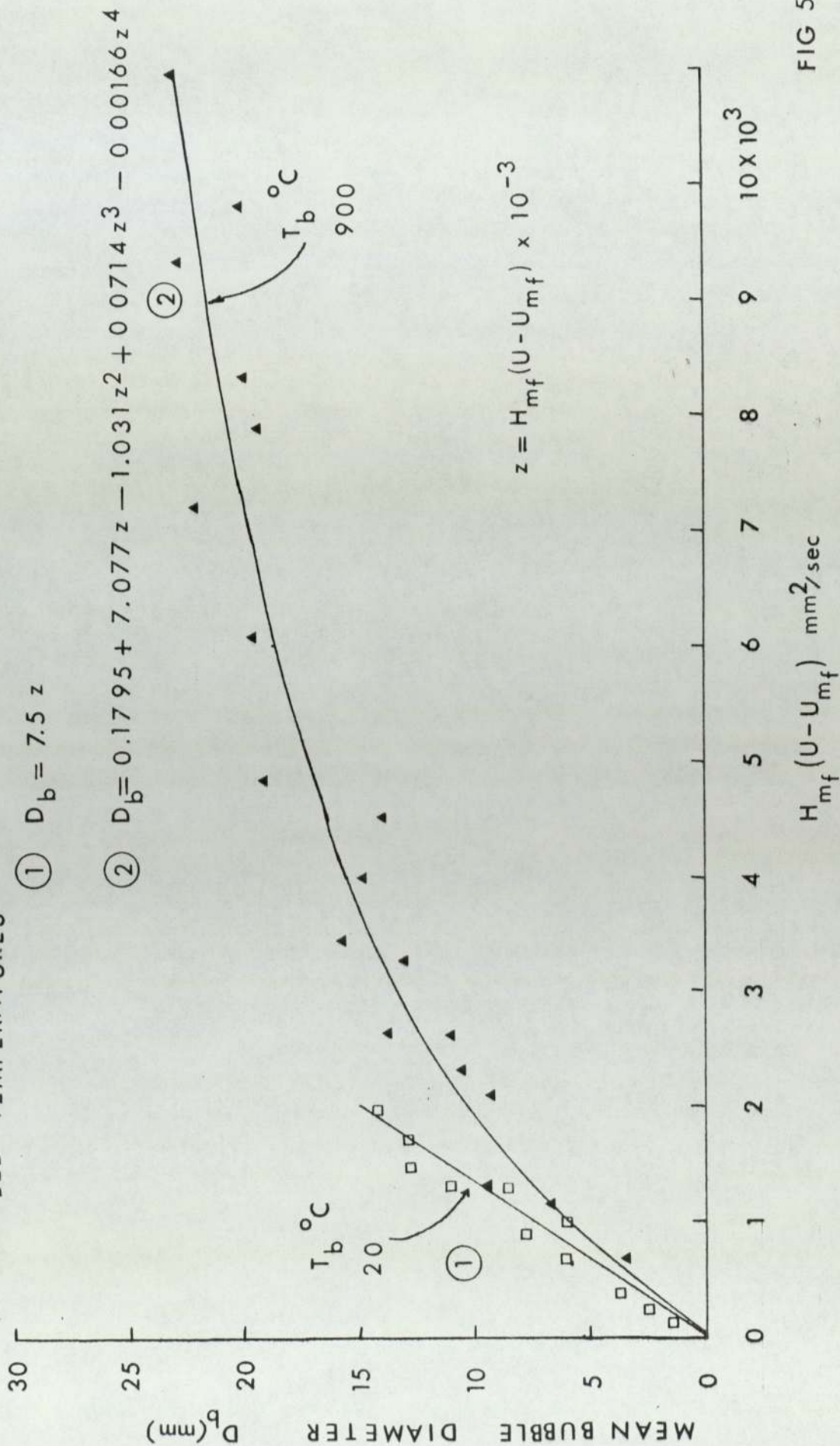
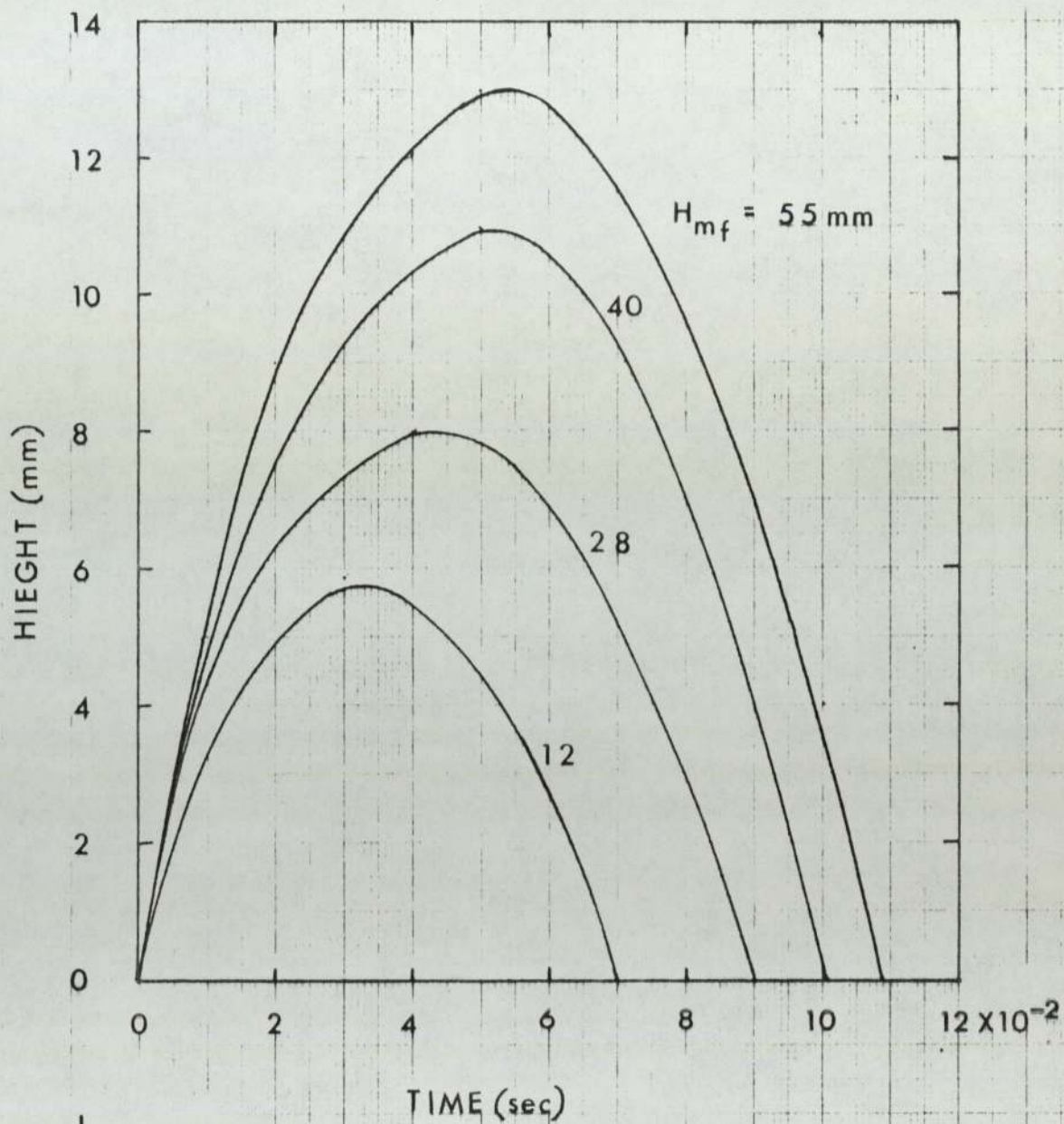


FIG 5.17

PREDICTED PARTICLE CLOUD TRAJECTORIES



MAT^L SAND

$U - U_{mf}$ mm/sec

100

T_b °C

1000

D_p mm

0.354

FIG 5.18

PREDICTED PARTICLE CLOUD RESIDENCE TIMES

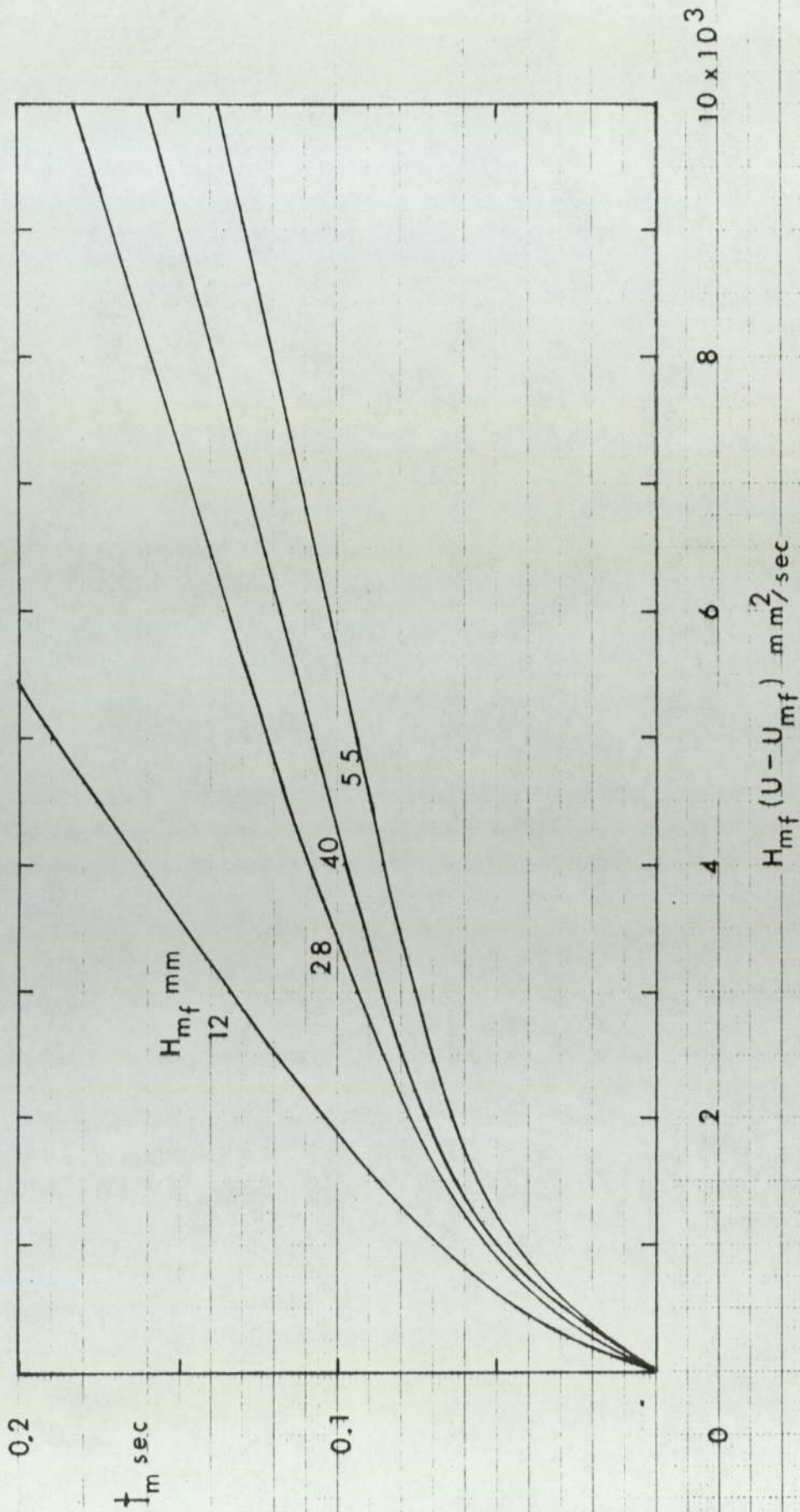


FIG 5.19

COMPARISON OF SOLUTIONS FOR
TRANSIENT RADIATIVE TRANSFER

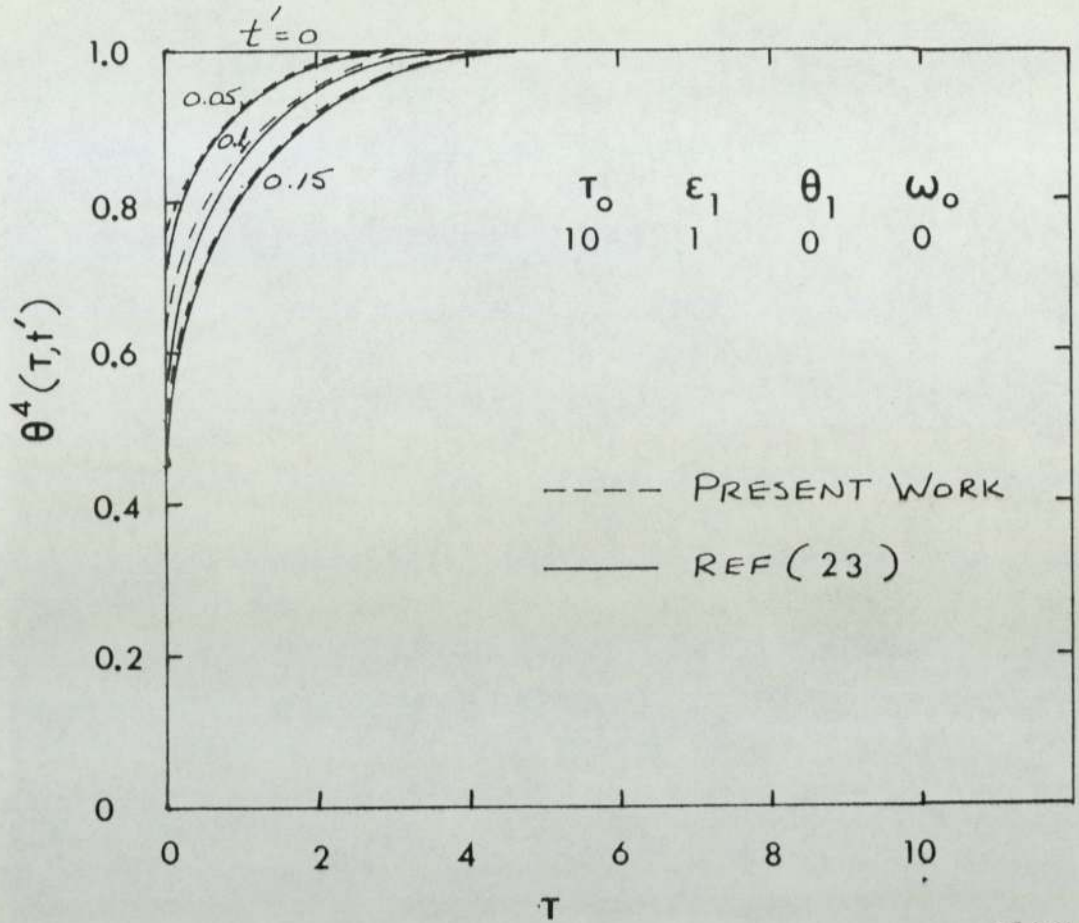


FIG. 6.1a

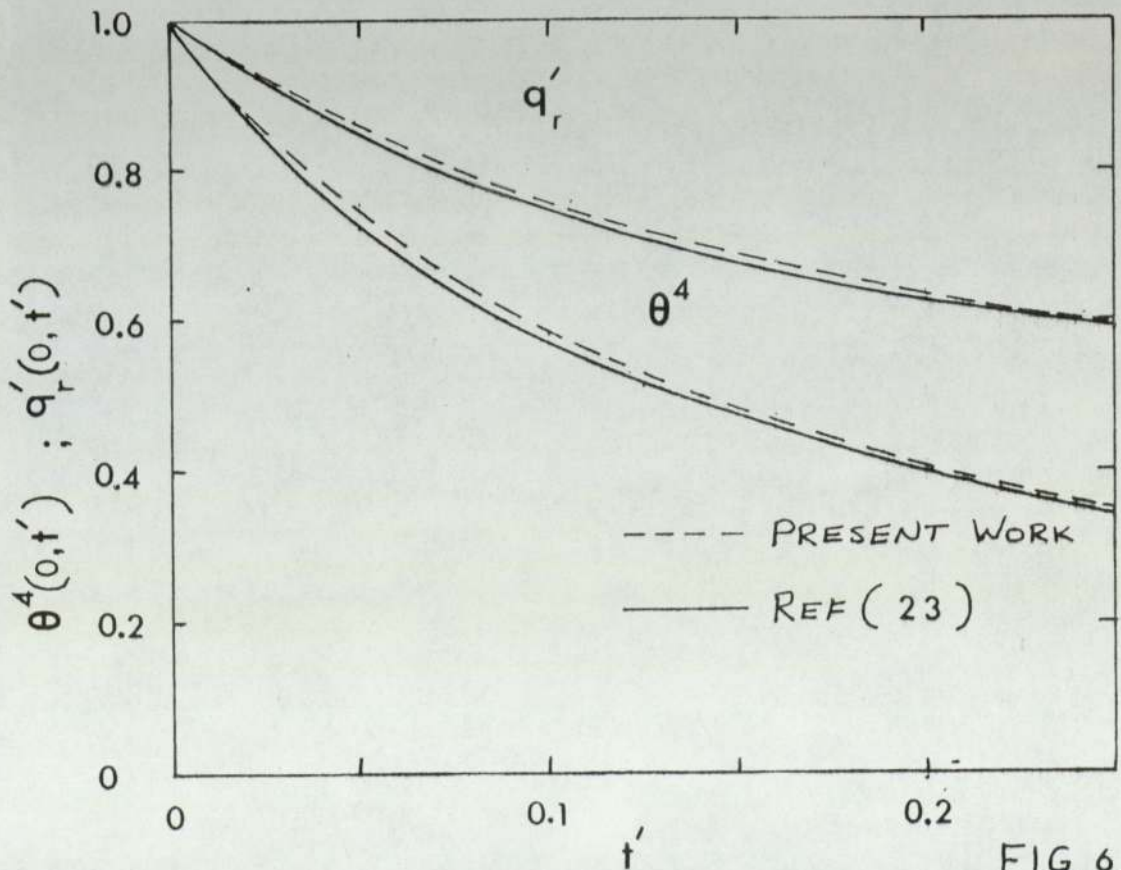


FIG. 6.1b

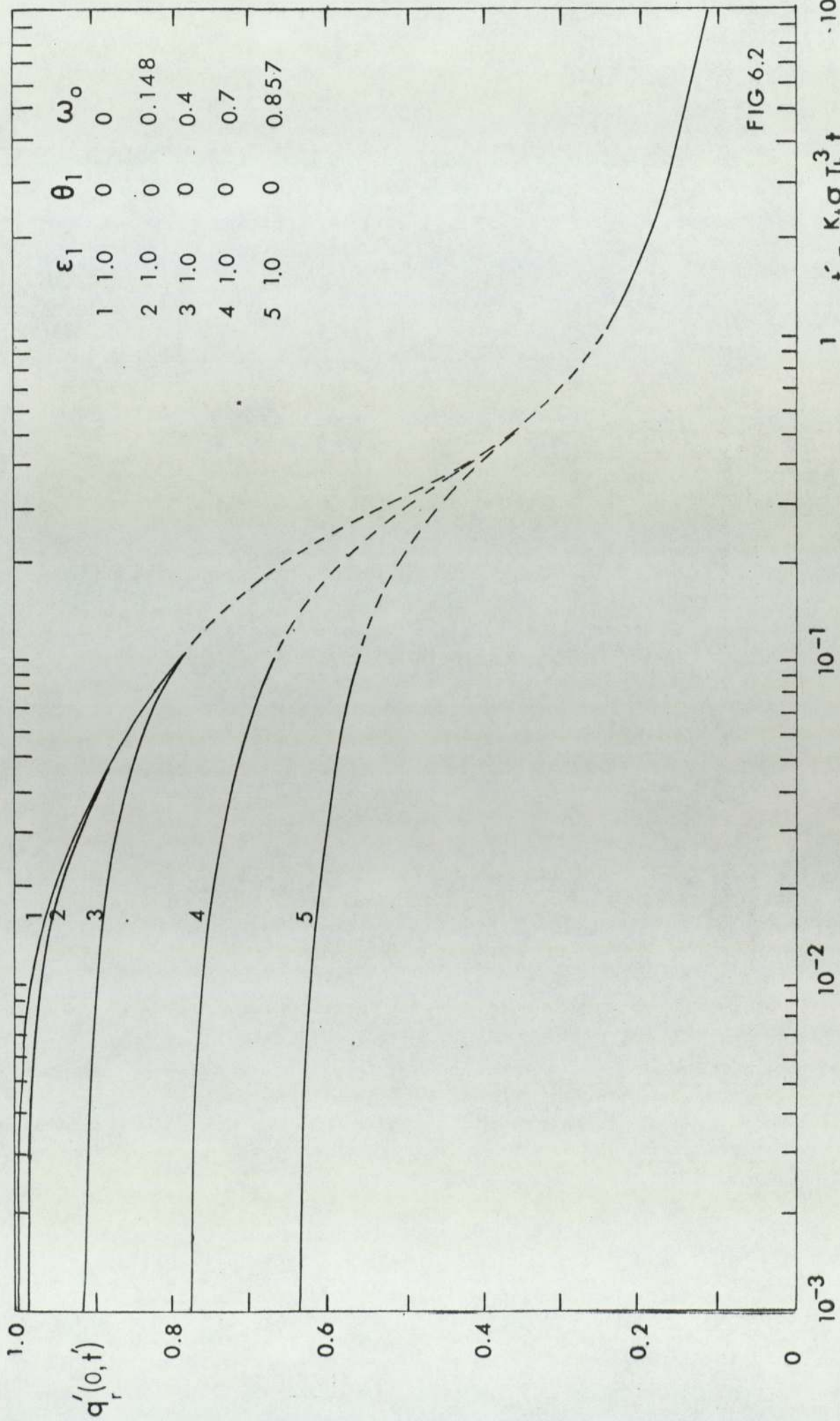


FIG 6.2

$$f' = \frac{\kappa_t \sigma T_b^3 t}{\rho_b C_p (1 - \epsilon_b)}$$

TRANSIENT
TEMPERATURE DISTRIBUTION

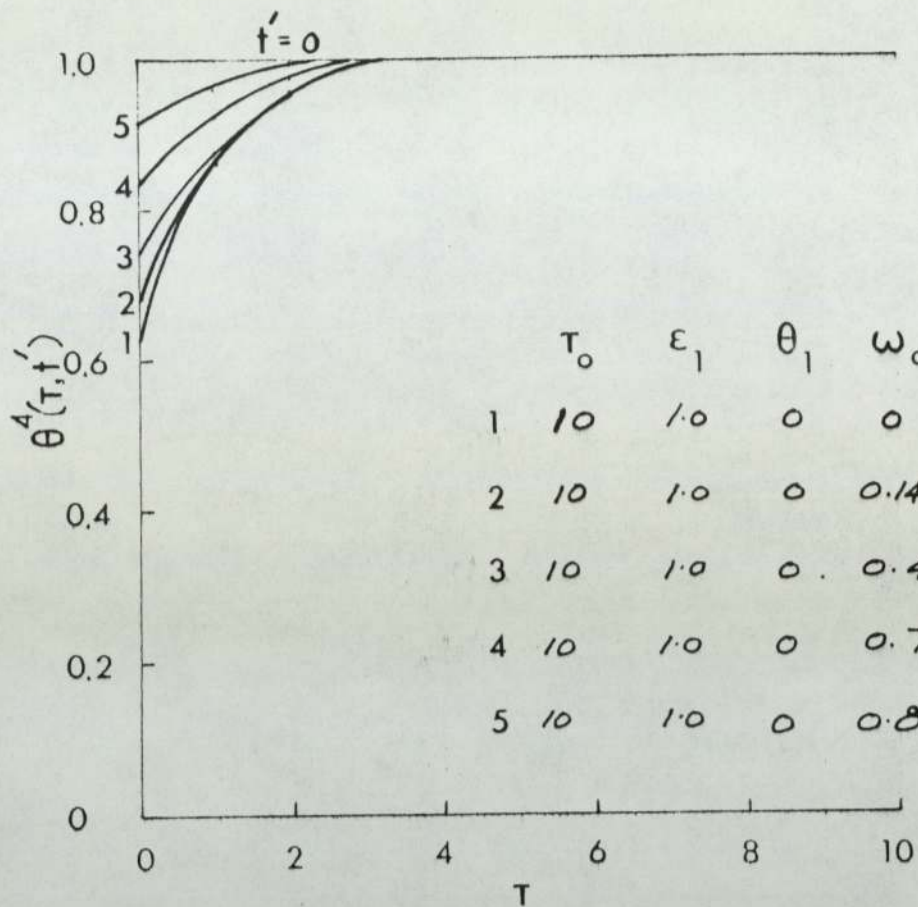


FIG. 6.3

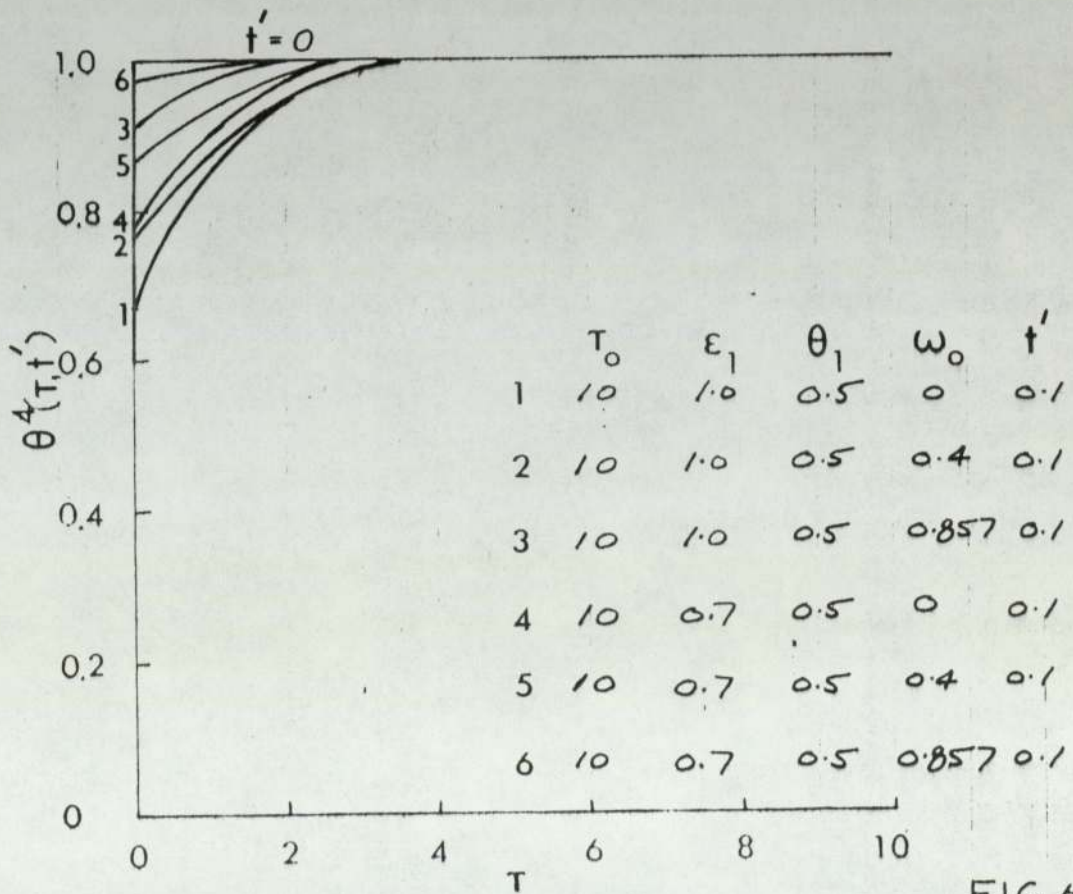
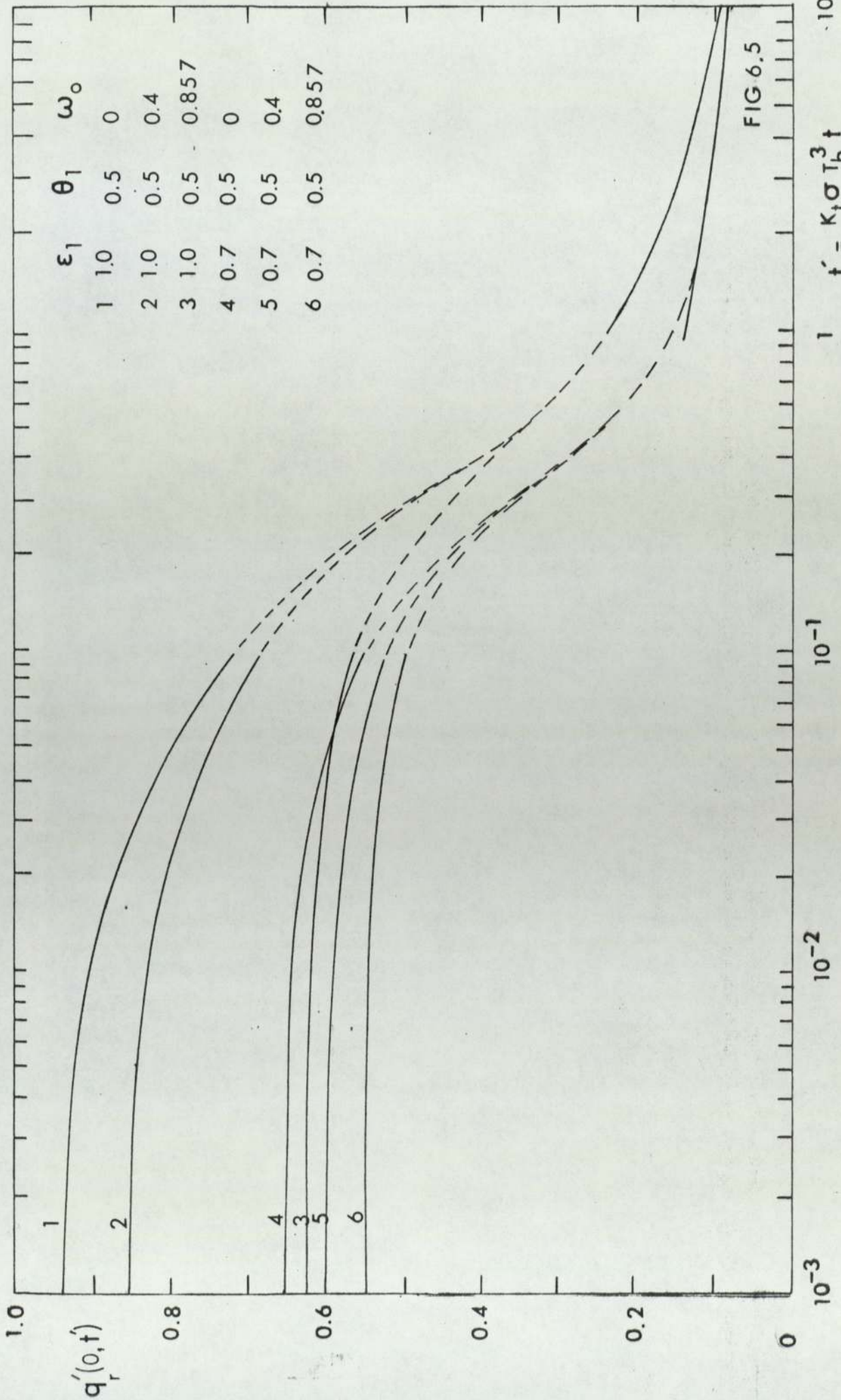


FIG. 6.4



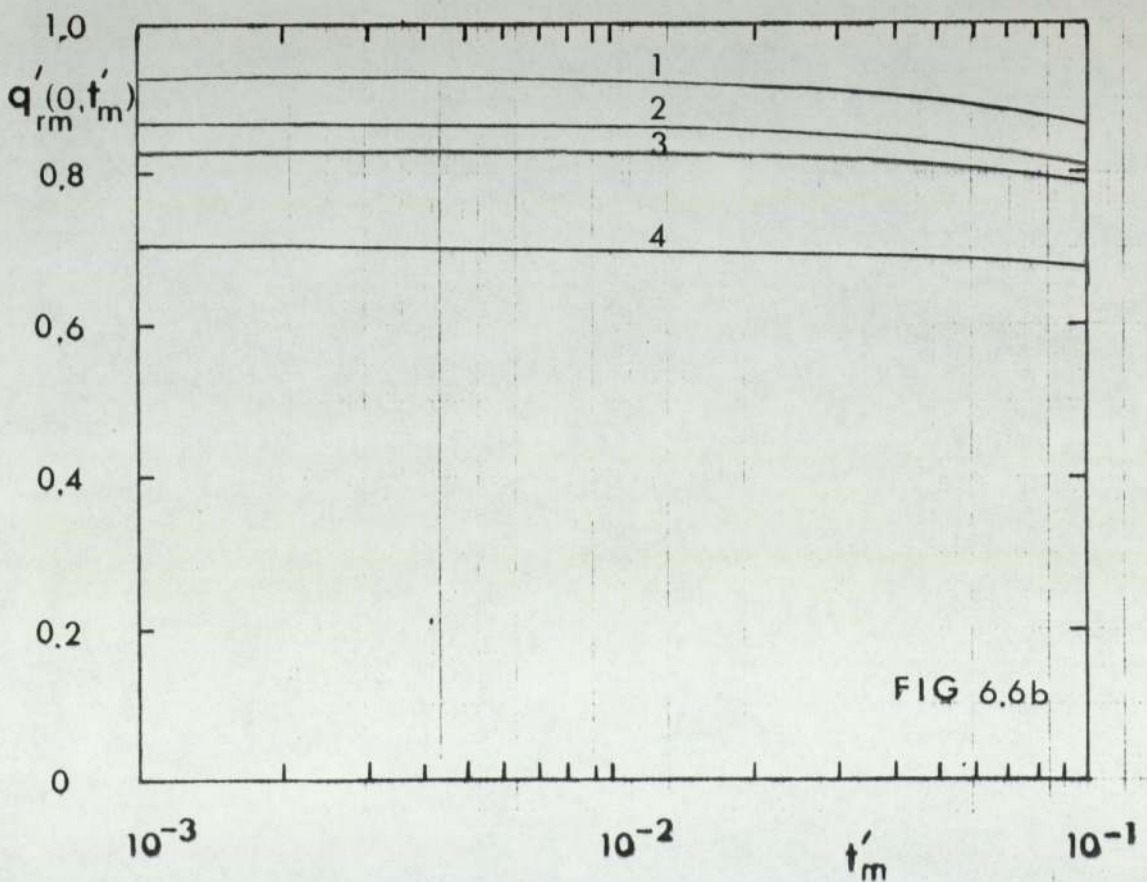
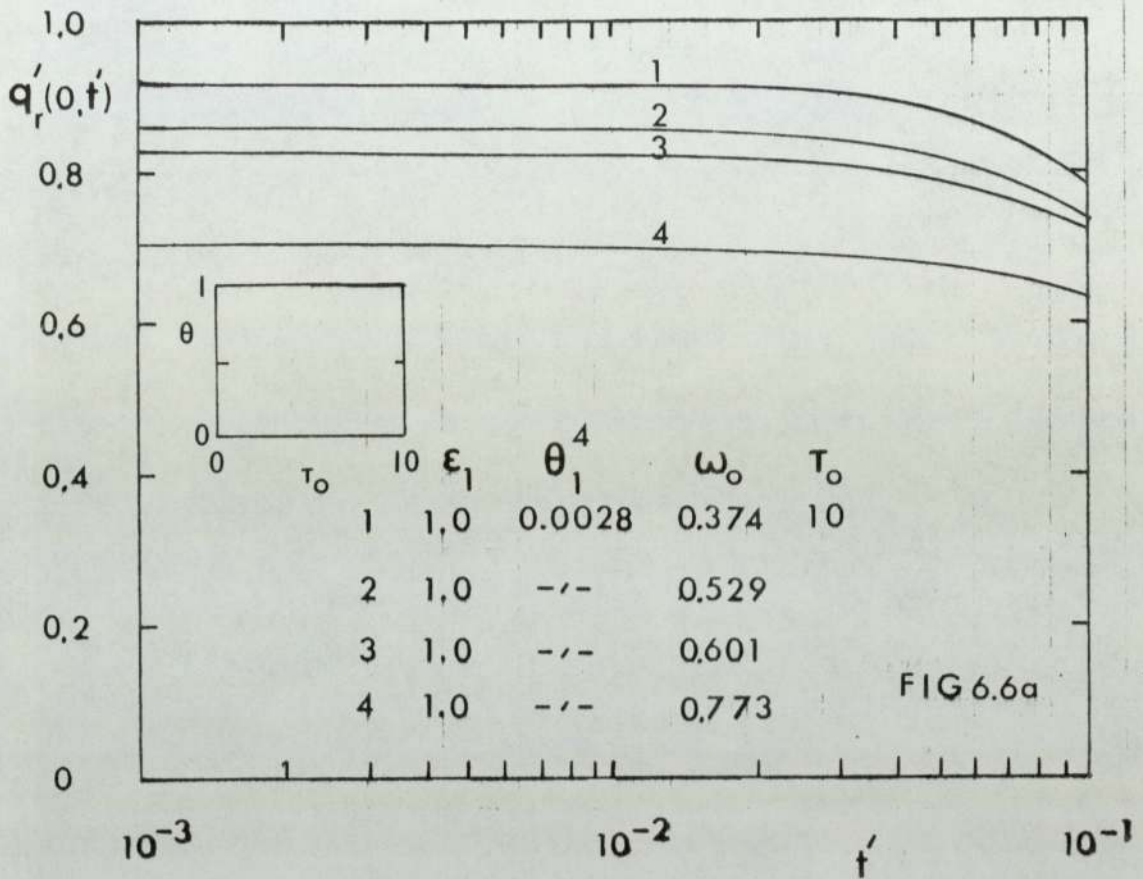
	ϵ_1	θ_1	ω_0
1	1.0	0.5	0
2	1.0	0.5	0.4
3	1.0	0.5	0.857
4	0.7	0.5	0
5	0.7	0.5	0.4
6	0.7	0.5	0.857

FIG 6.5

$$f' = \frac{\kappa_1 \sigma T_b^3 t}{\rho C_p (1 - \epsilon_b)}$$

10⁻³ 10⁻² 10⁻¹ 1 10

TIME VARIATION OF RADIATIVE FLUX
EMITTED BY AN OPTICALLY DENSE MEDIUM



EFFECT OF EXCESS GAS VELOCITY ON
TIME MEAN RADIATIVE FLUX

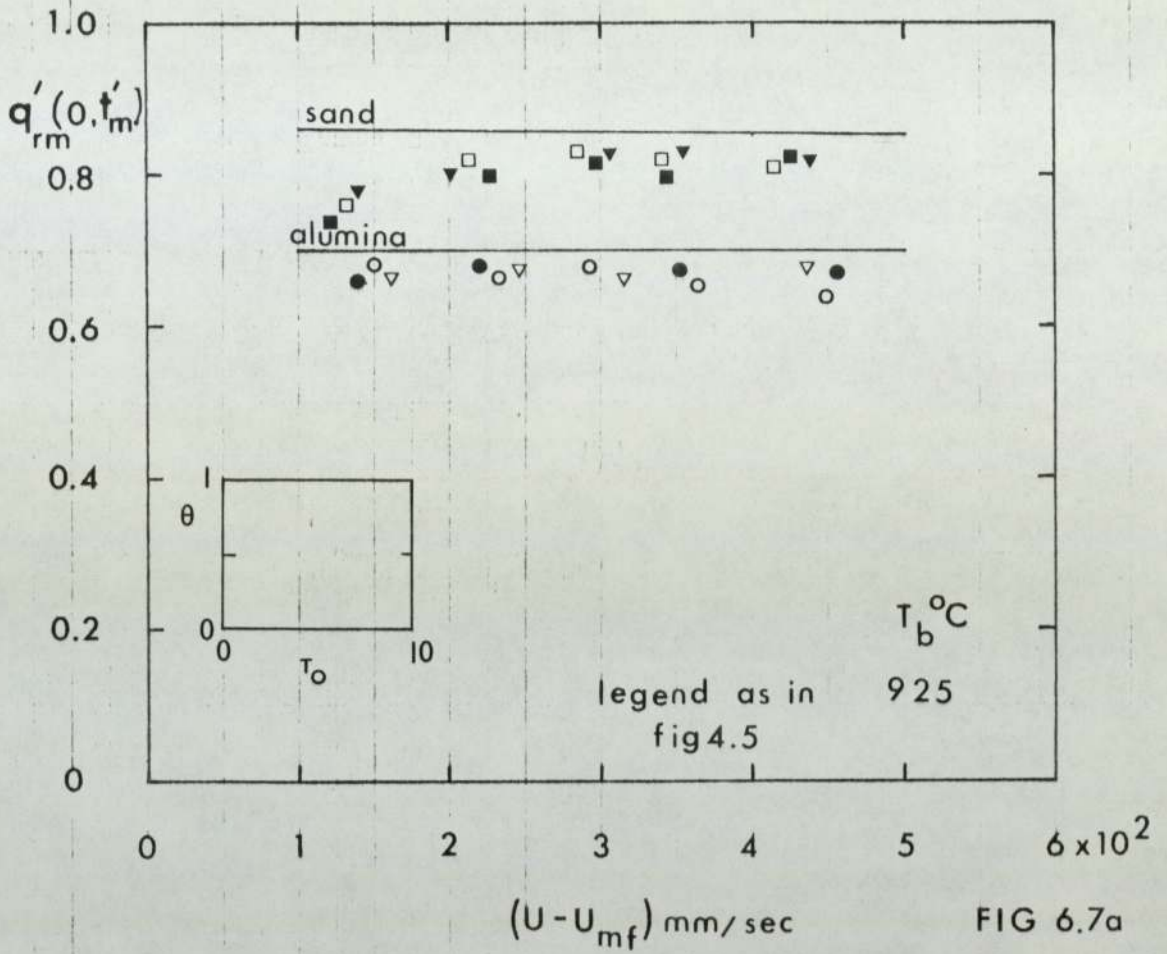


FIG 6.7a

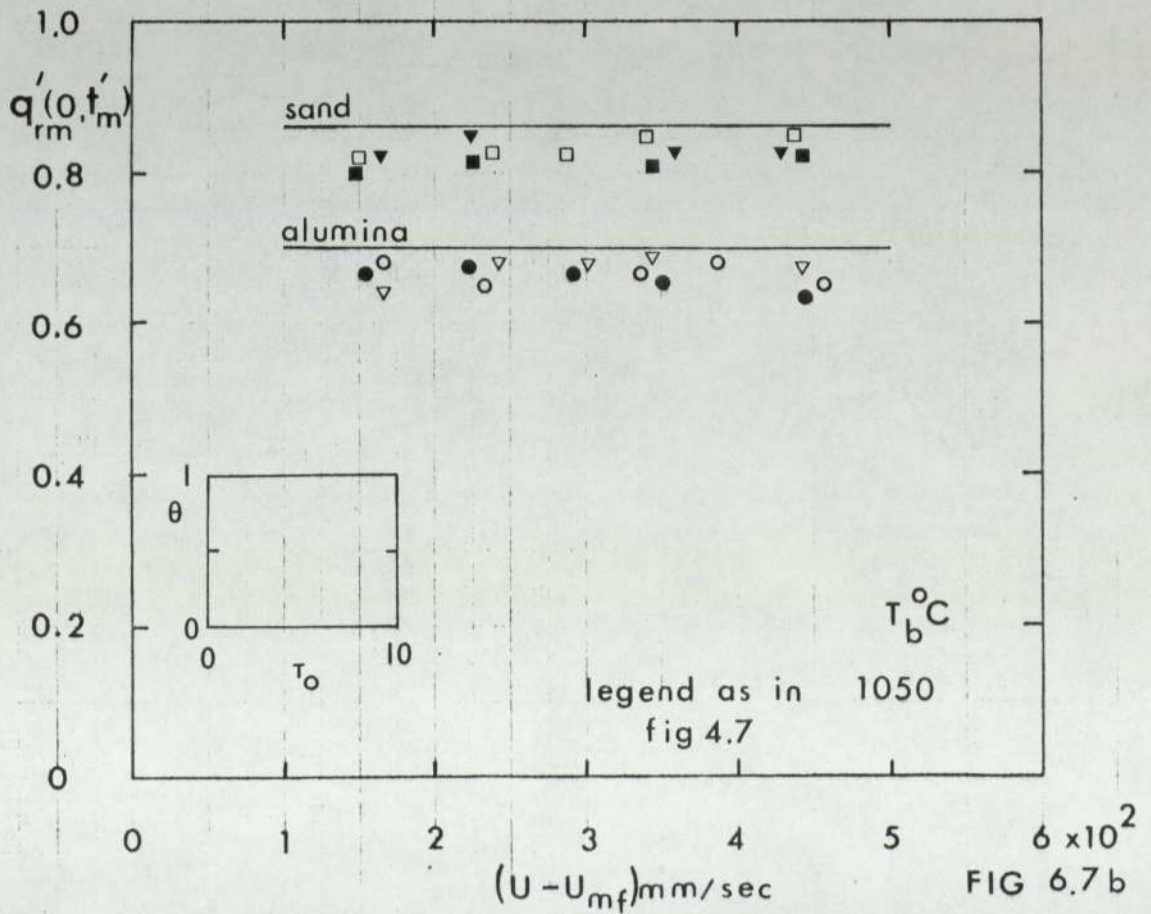


FIG 6.7b

EFFECT OF EXCESS GAS VELOCITY ON
TIME MEAN RADIATIVE FLUX

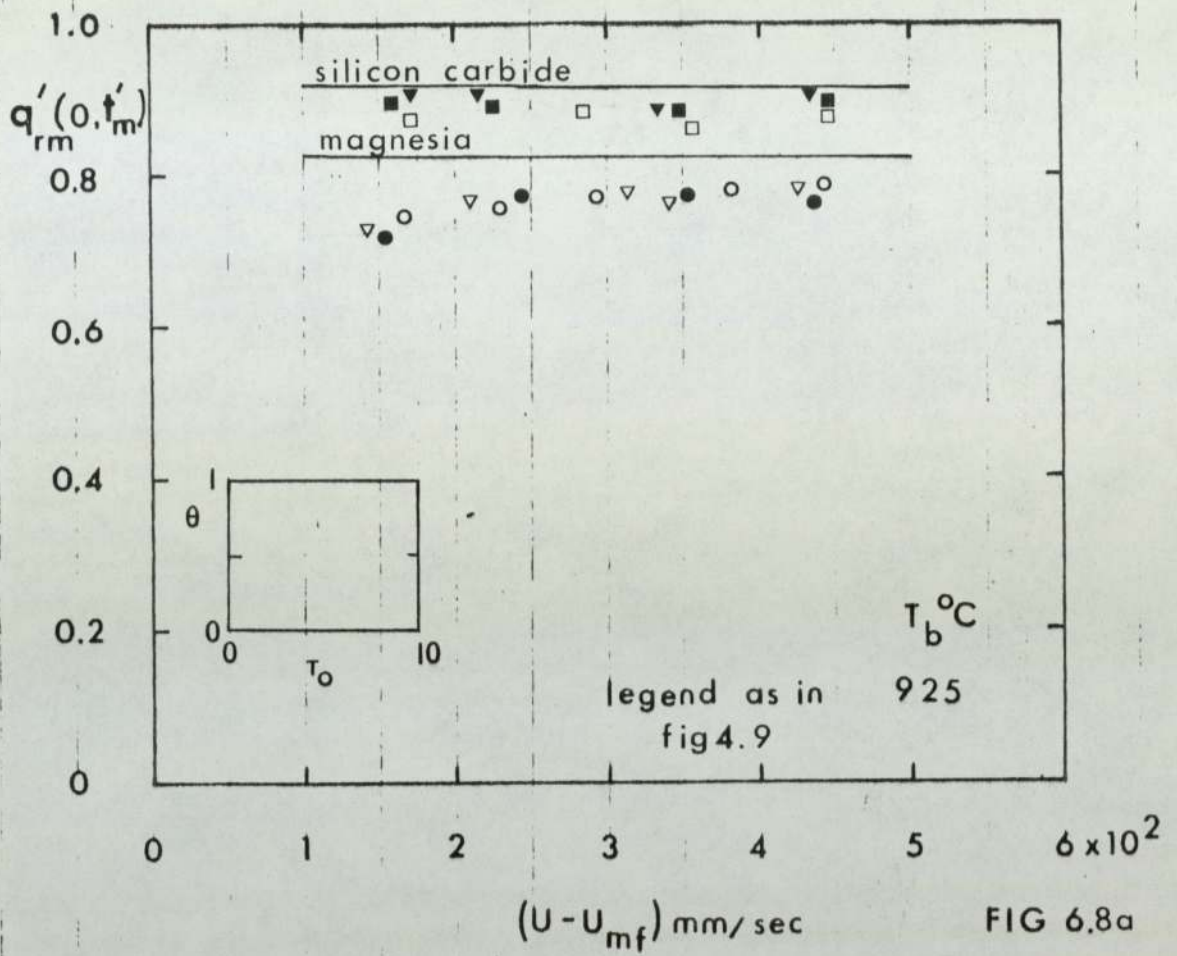


FIG 6.8a

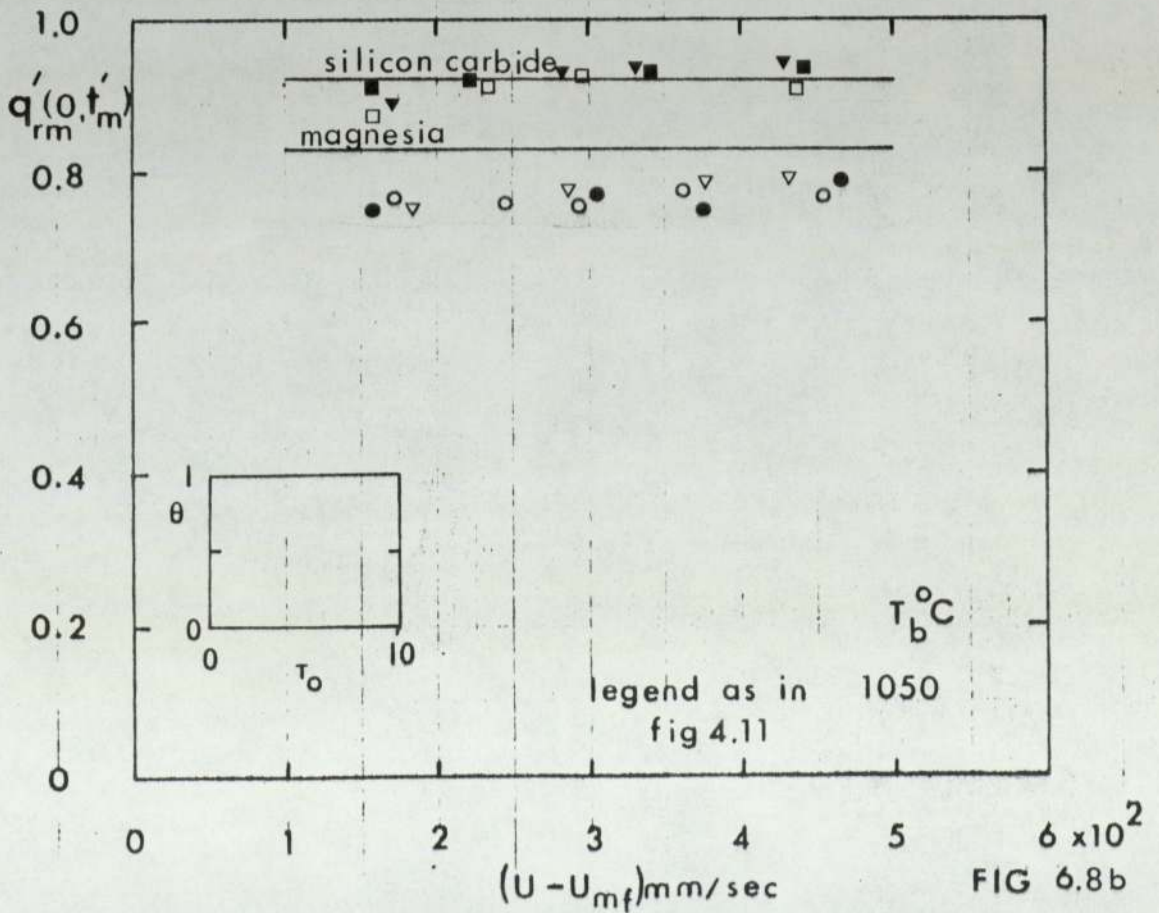
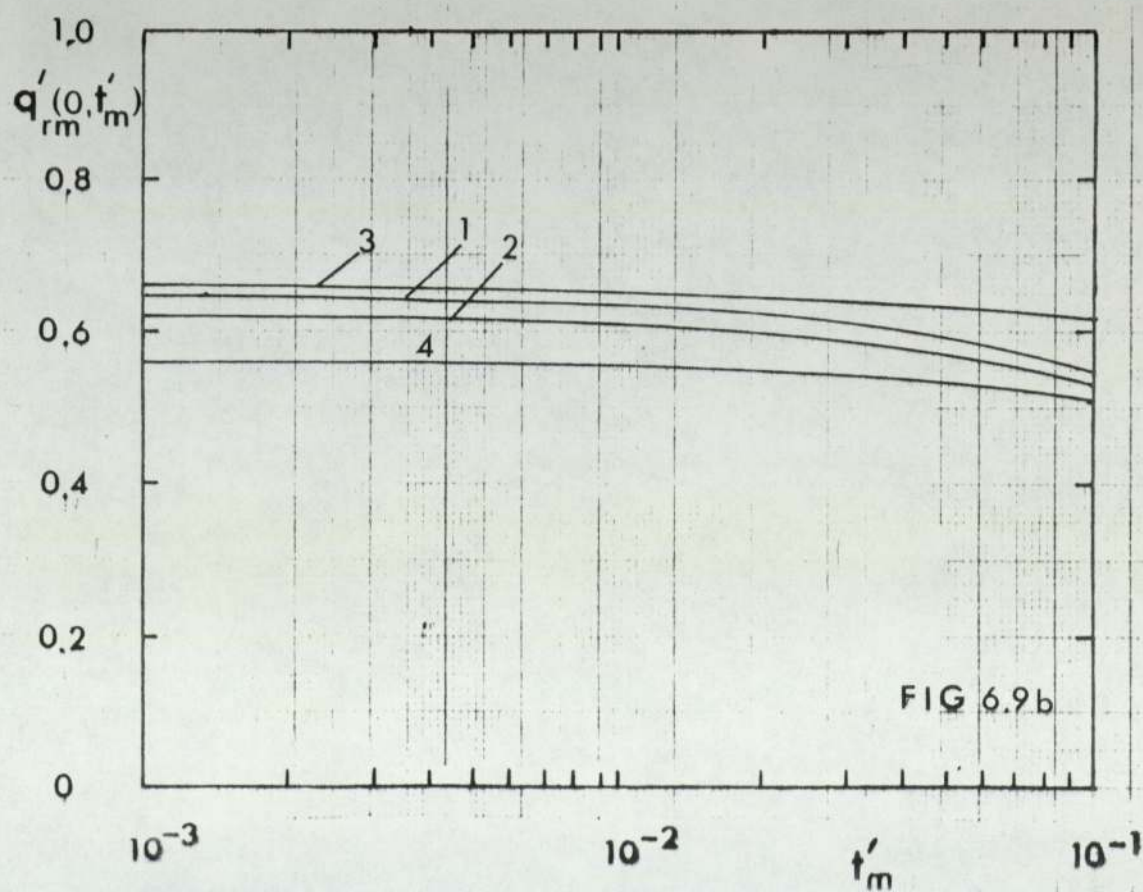
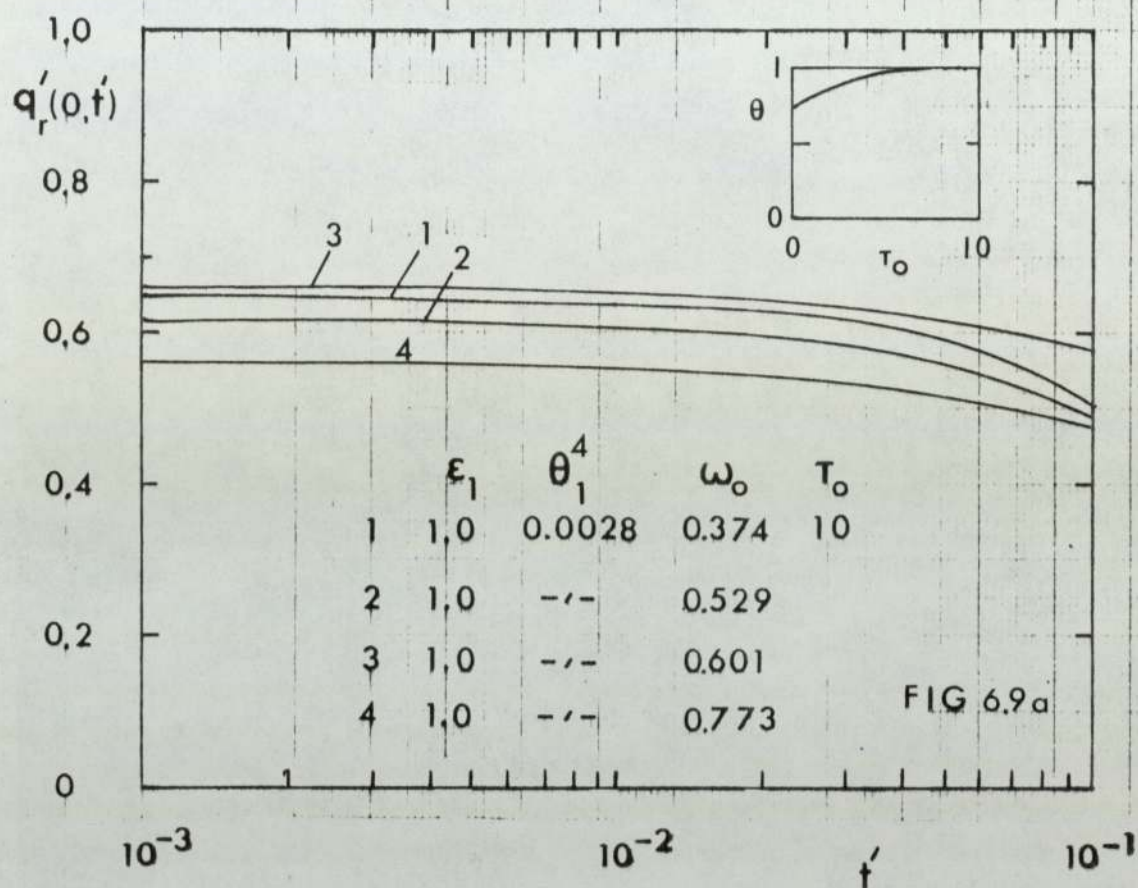


FIG 6.8b

TIME VARIATION OF RADIATIVE FLUX
EMITTED BY AN OPTICALLY DENSE MEDIUM



TRANSIENT
TEMPERATURE DISTRIBUTION

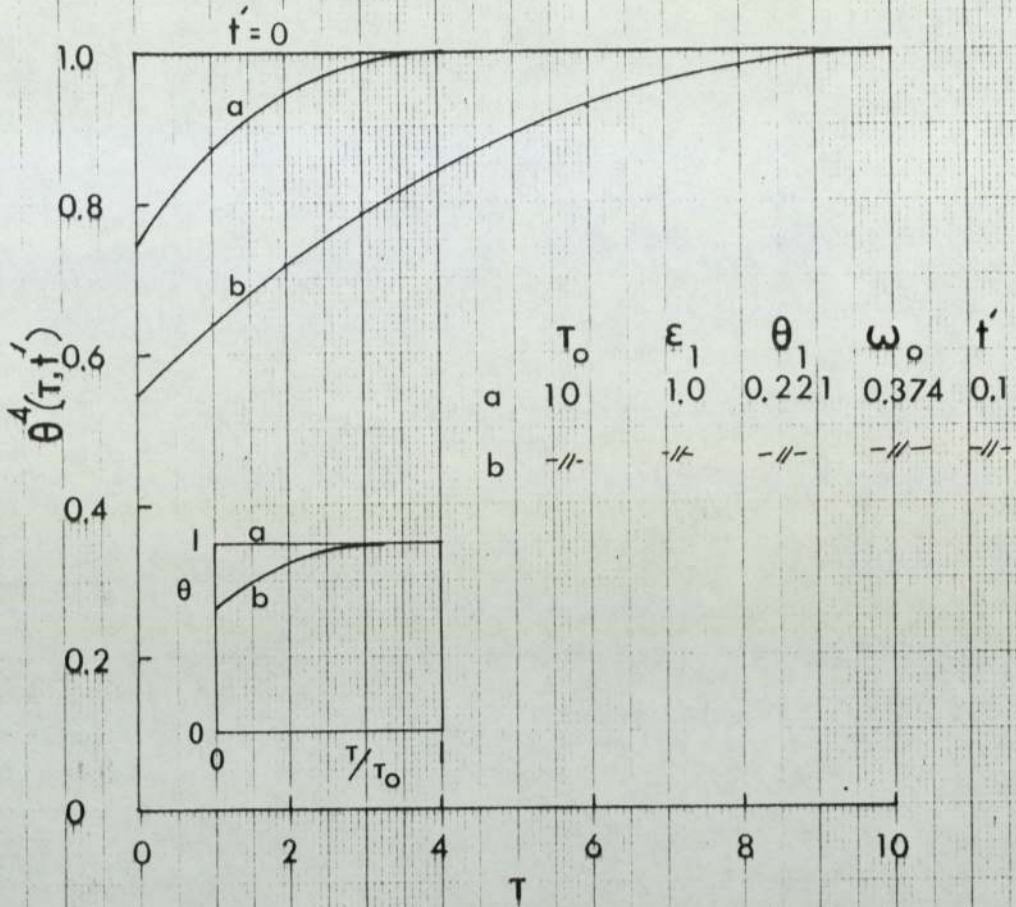


FIG. 6.10

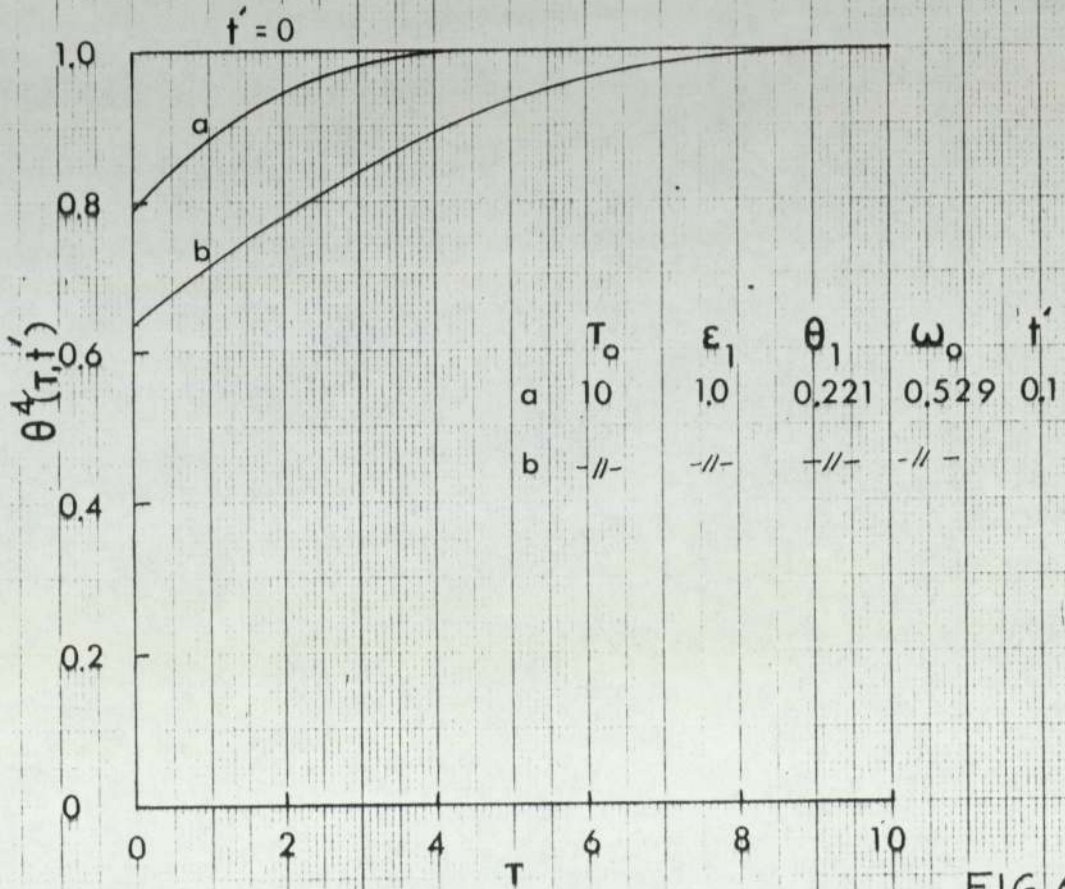


FIG. 6.11

PREDICTED INSTANTANEOUS NUSSELT - FOURIER NUMBER RELATIONSHIP

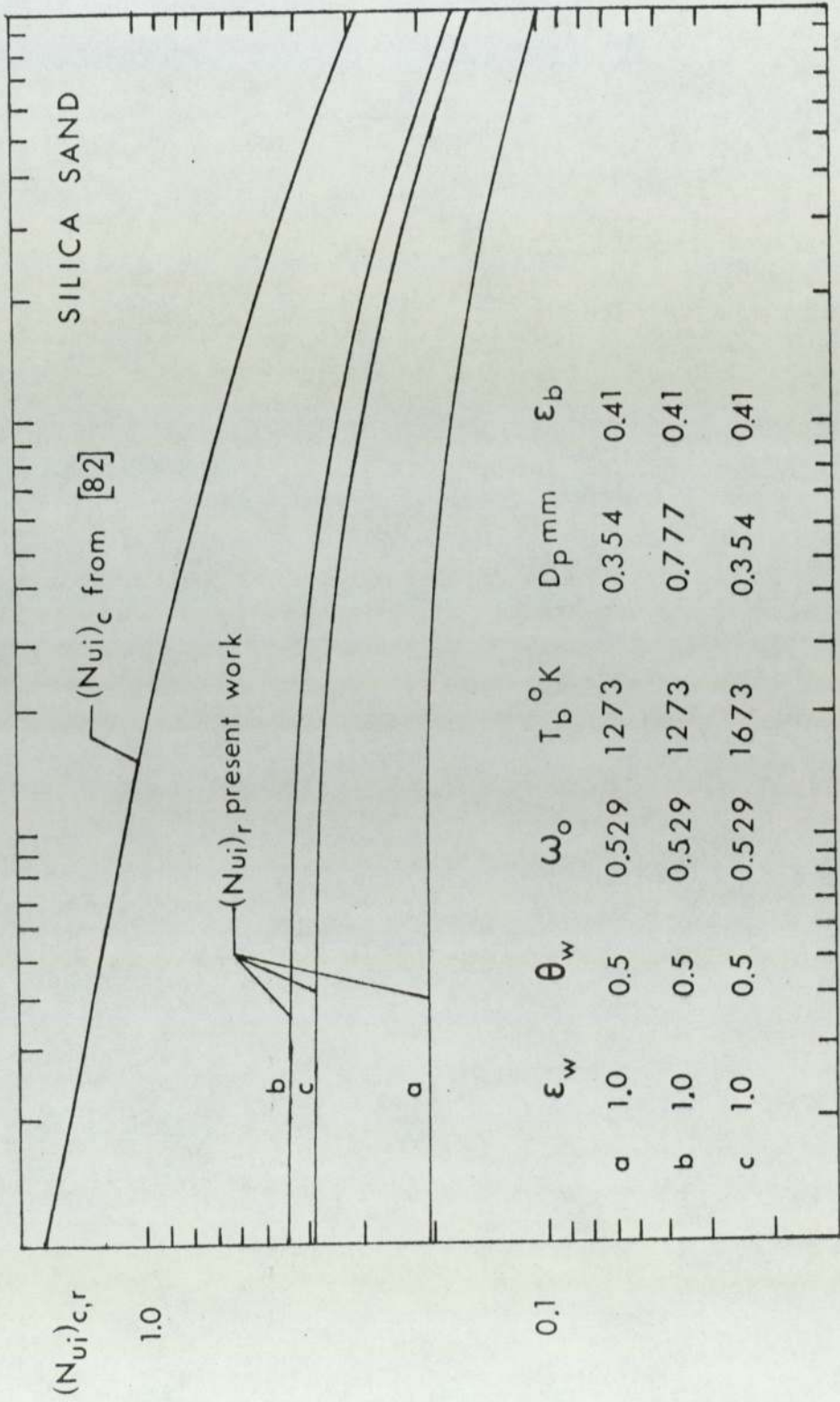


FIG 7.1

THERMAL CONDUCTIVITY OF A
POROUS MEDIUM from [86]

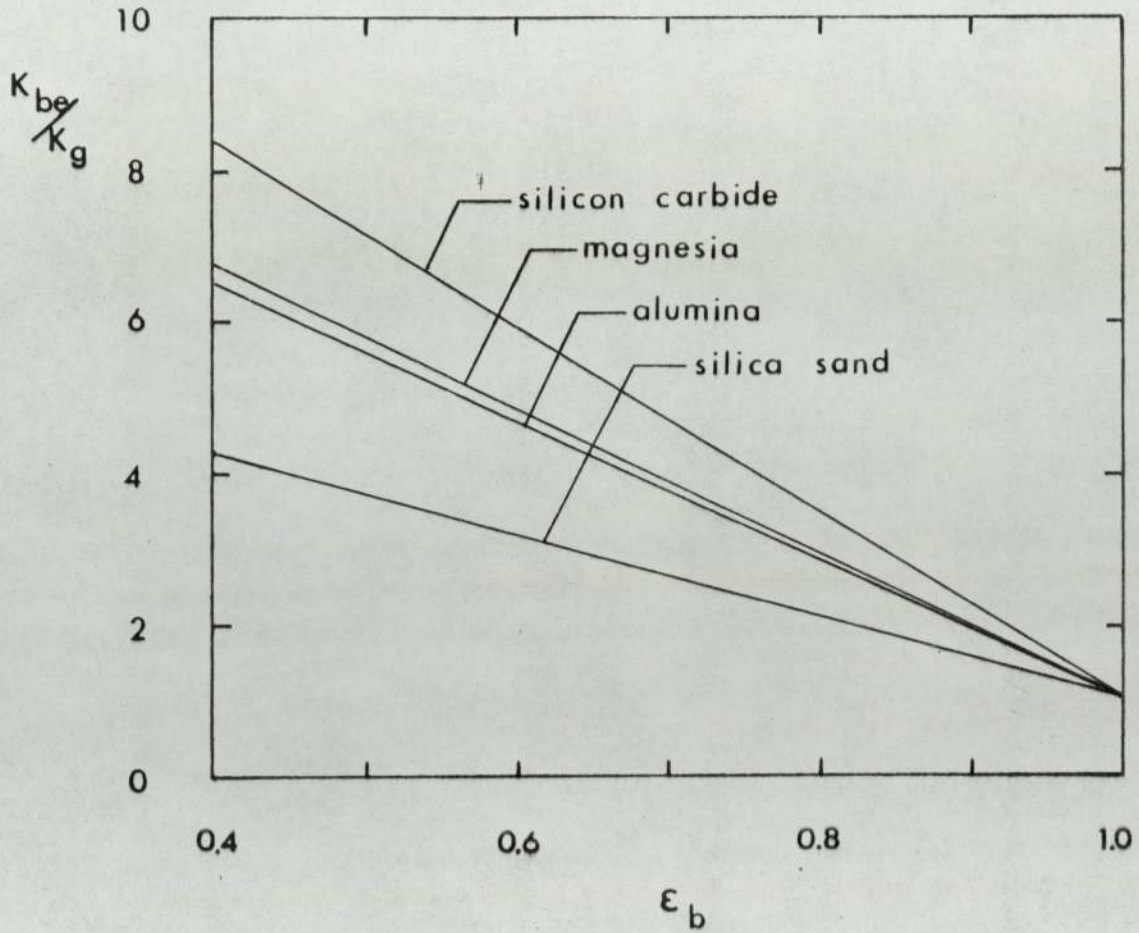
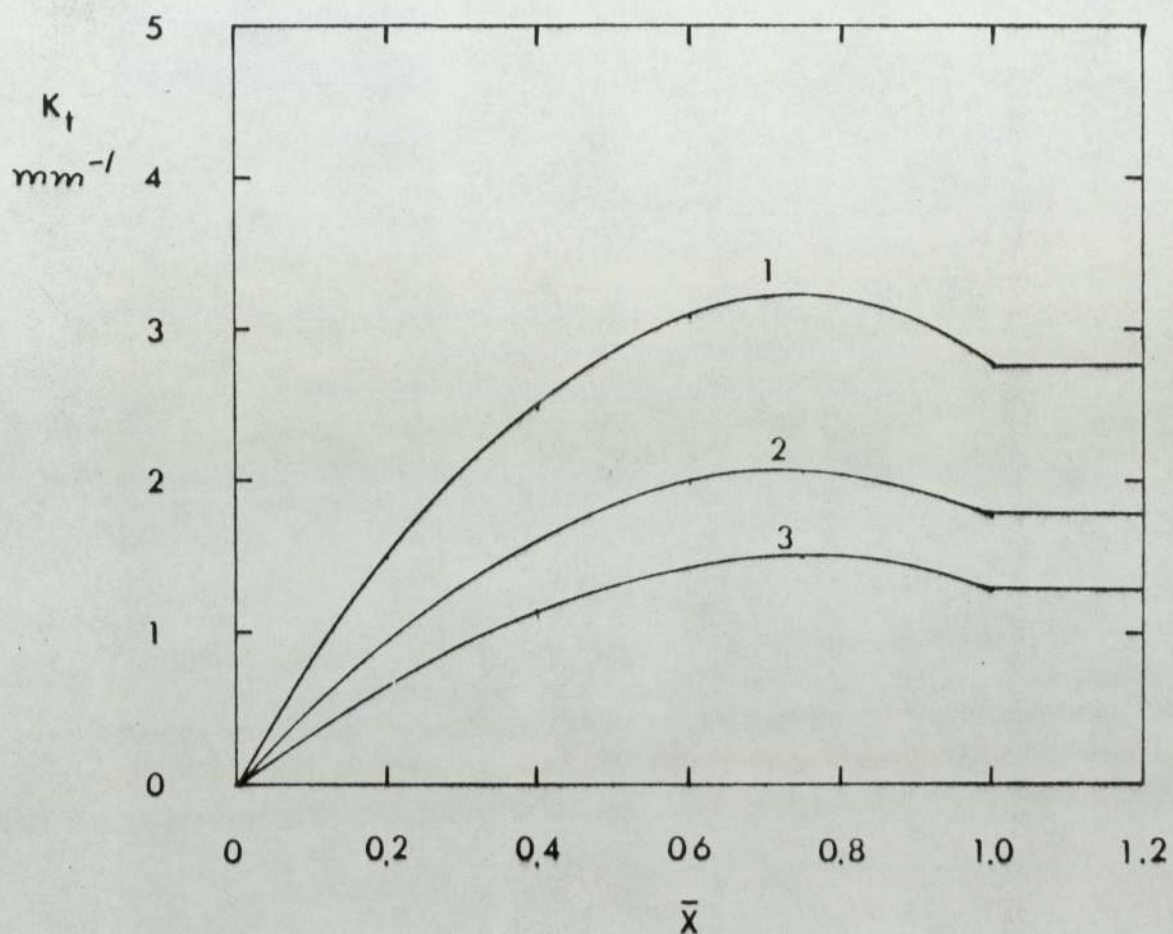


FIG 7.2

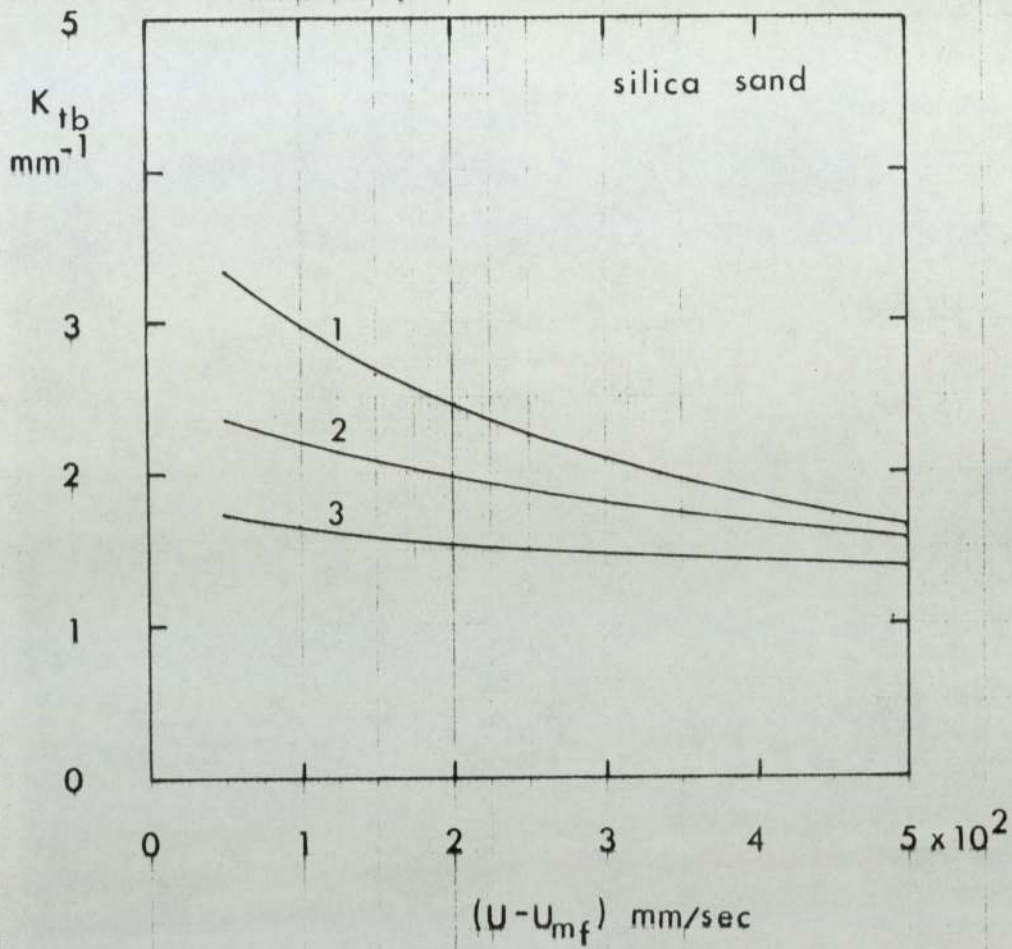
VARIATION OF EXTINCTION COEFFICIENT
AT A WALL



	MAT ^L	D _p mm	ε _p	ε _b
1	ALUMINA	0.354	0.37	0.58
2	—//—	0.55	—//—	—//—
3	—//—	0.777	—//—	—//—

FIG 7.3

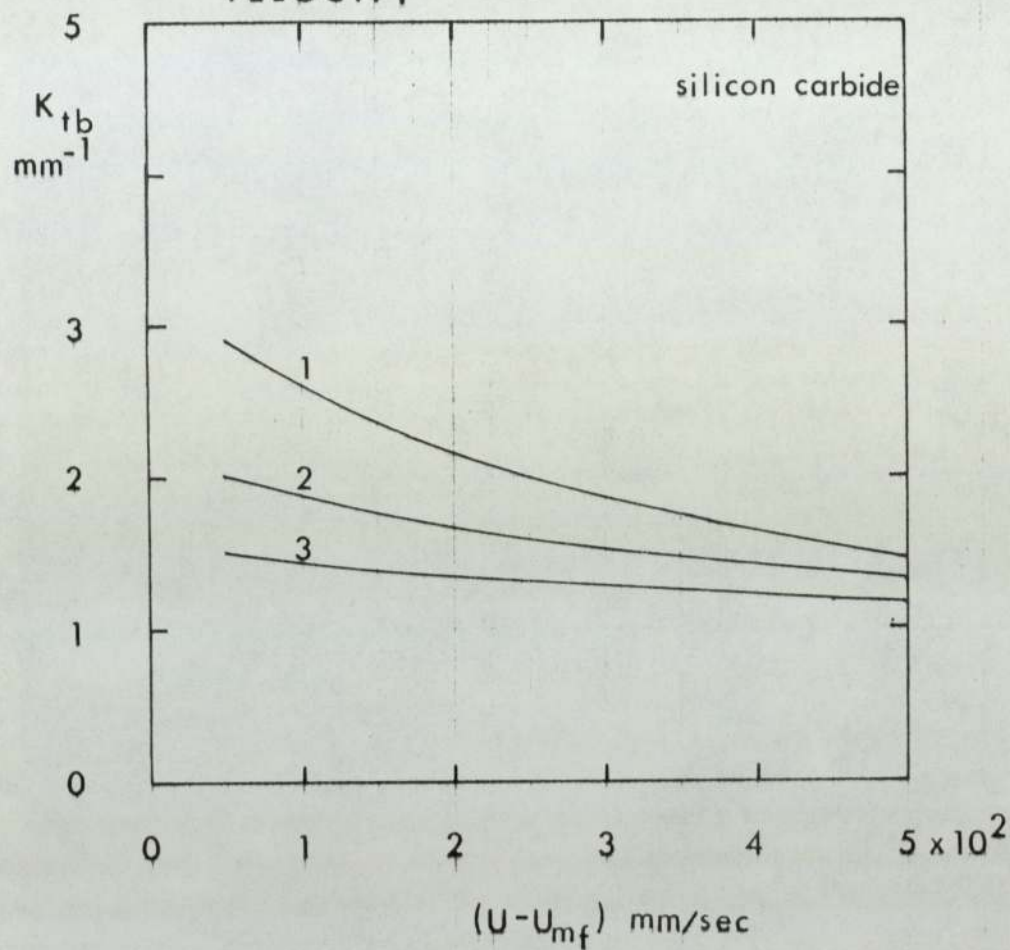
VARIATION OF EXTINCTION COEFFICIENT
(IN EMULSION PACKET) WITH EXCESS GAS
VELOCITY



	ϵ_p	D_p mm
1	0.64	0.354
2	--	0.55
3	--	0.777

FIG 7.4

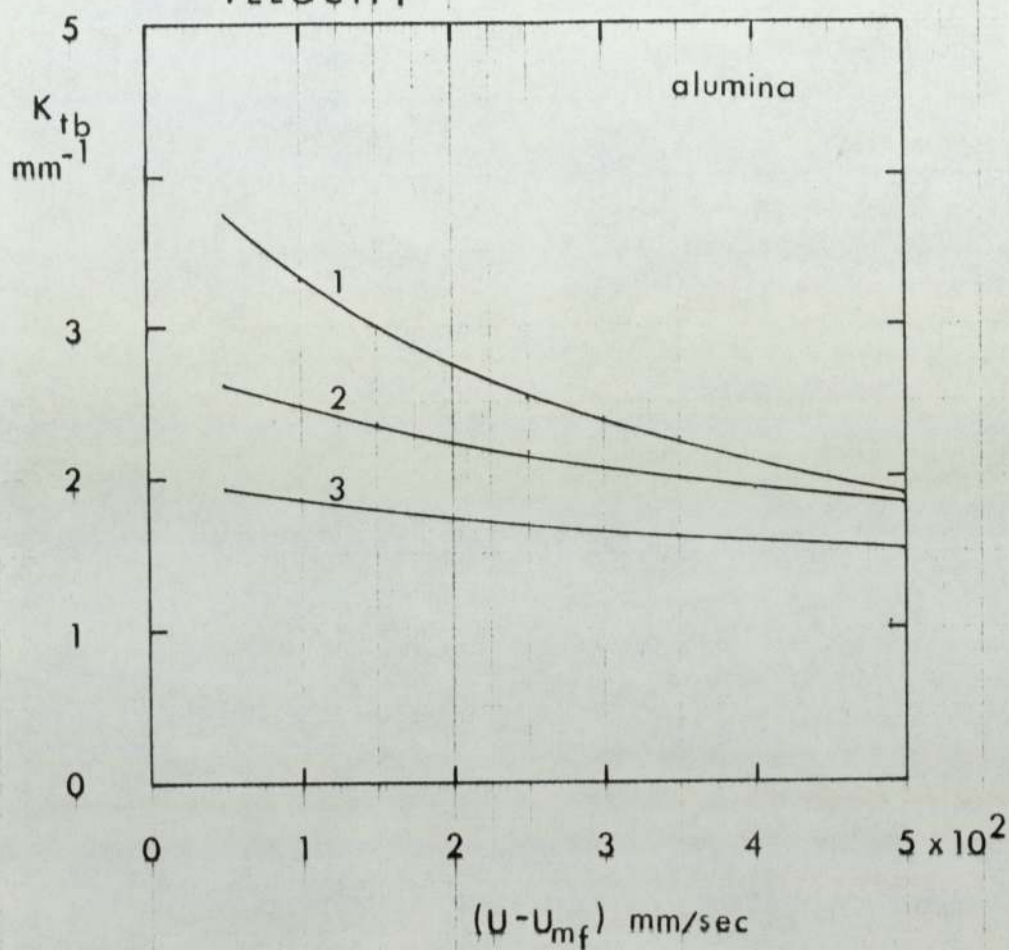
VARIATION OF EXTINCTION COEFFICIENT
(IN EMULSION PACKET) WITH EXCESS GAS
VELOCITY



	ϵ_p	D_p mm
1	0.77	0.354
2	--	0.55
3	--	0.777

FIG 7.5

VARIATION OF EXTINCTION COEFFICIENT
(IN EMULSION PACKET) WITH EXCESS GAS
VELOCITY



	ϵ_p	D_p mm
1	0.37	0.354
2	--	0.55
3	--	0.777

FIG 7.6

COMPARISON OF PREDICTED HEAT
TRANSFER COEFFICIENTS WITH EXPERIMENTAL
DATA FROM [83]

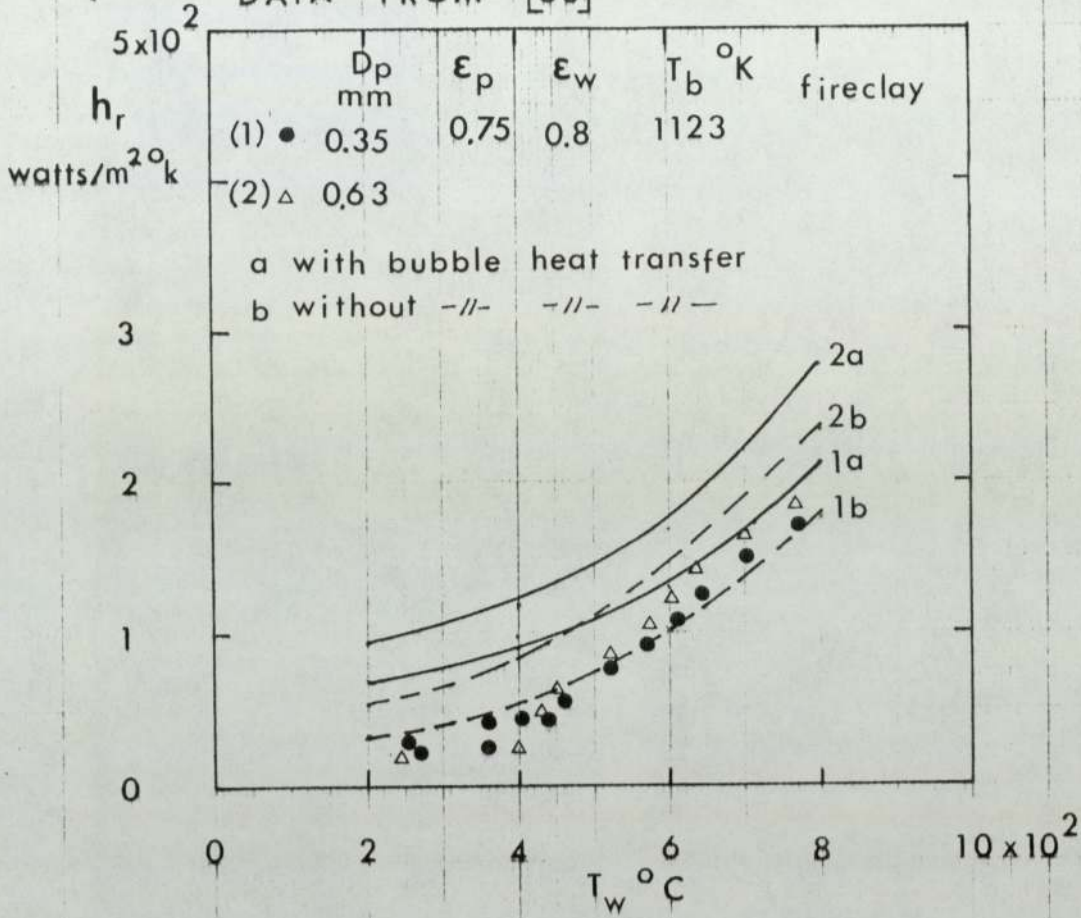


FIG 7.7a

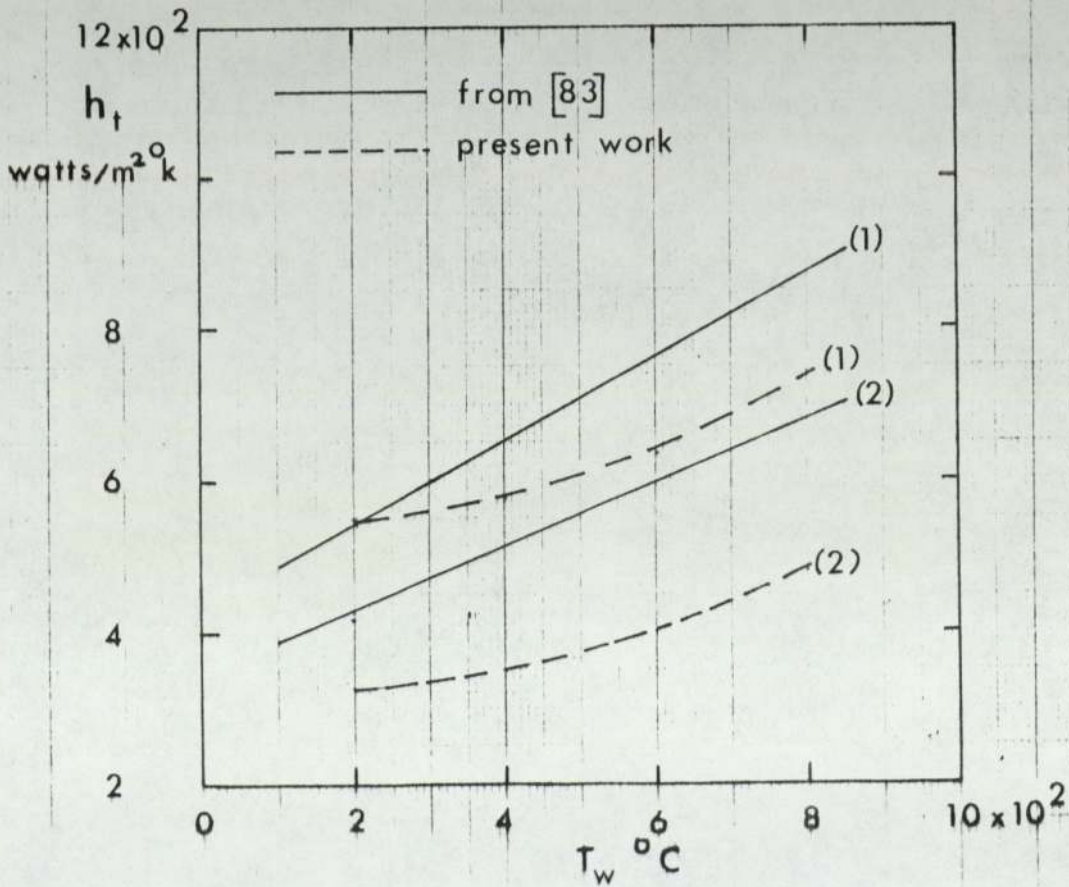


FIG 7.7b

PREDICTED INSTANTANEOUS NUSSELT - FOURIER NUMBER RELATIONSHIP

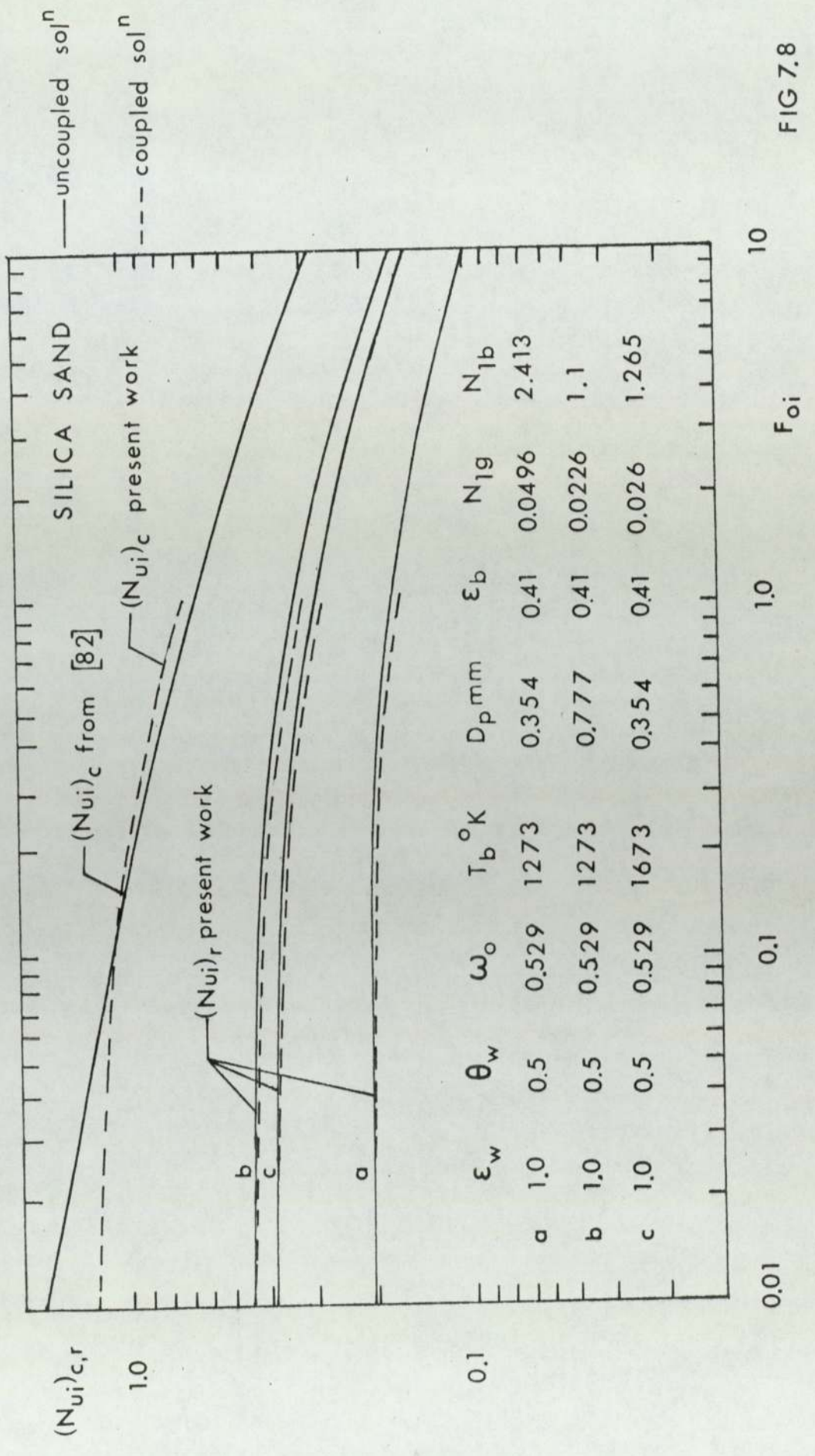


FIG 7.8

PREDICTED INSTANTANEOUS NUSSELT - FOURIER NUMBER RELATIONSHIP

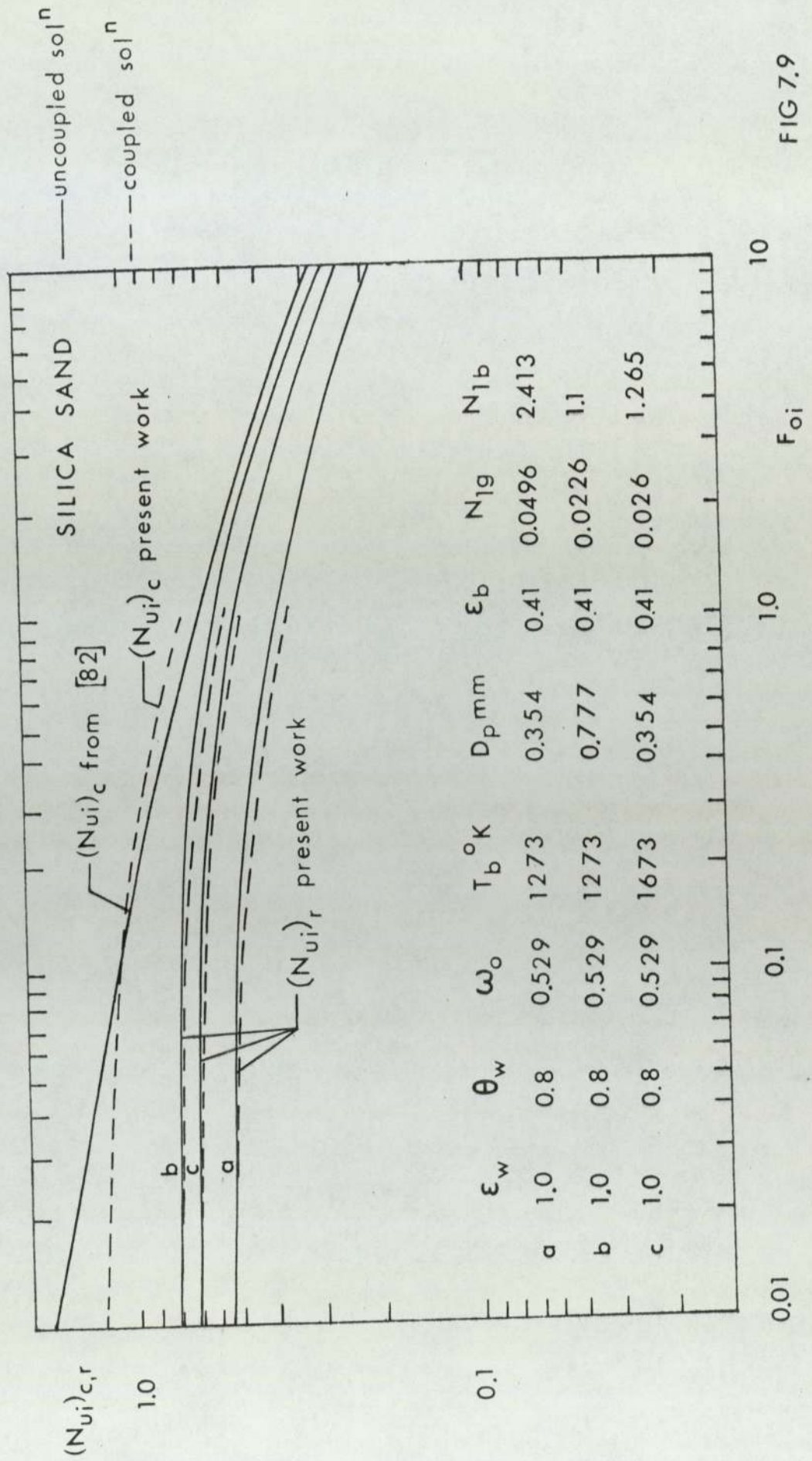


FIG 7.9

PREDICTED INSTANTANEOUS NUSSELT - FOURIER NUMBER RELATIONSHIP

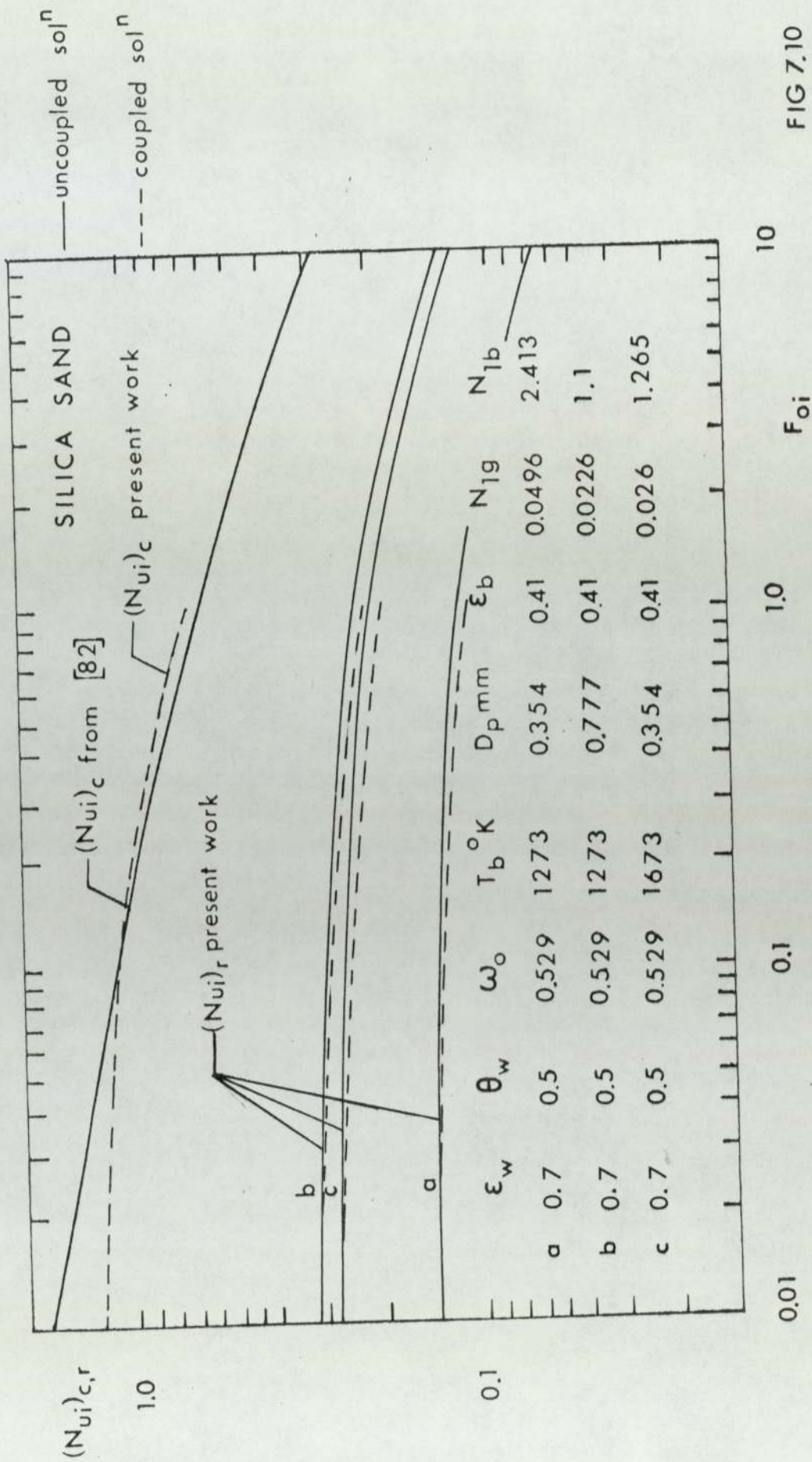


FIG 7.10

PREDICTED INSTANTANEOUS NUSSELT - FOURIER NUMBER RELATIONSHIP

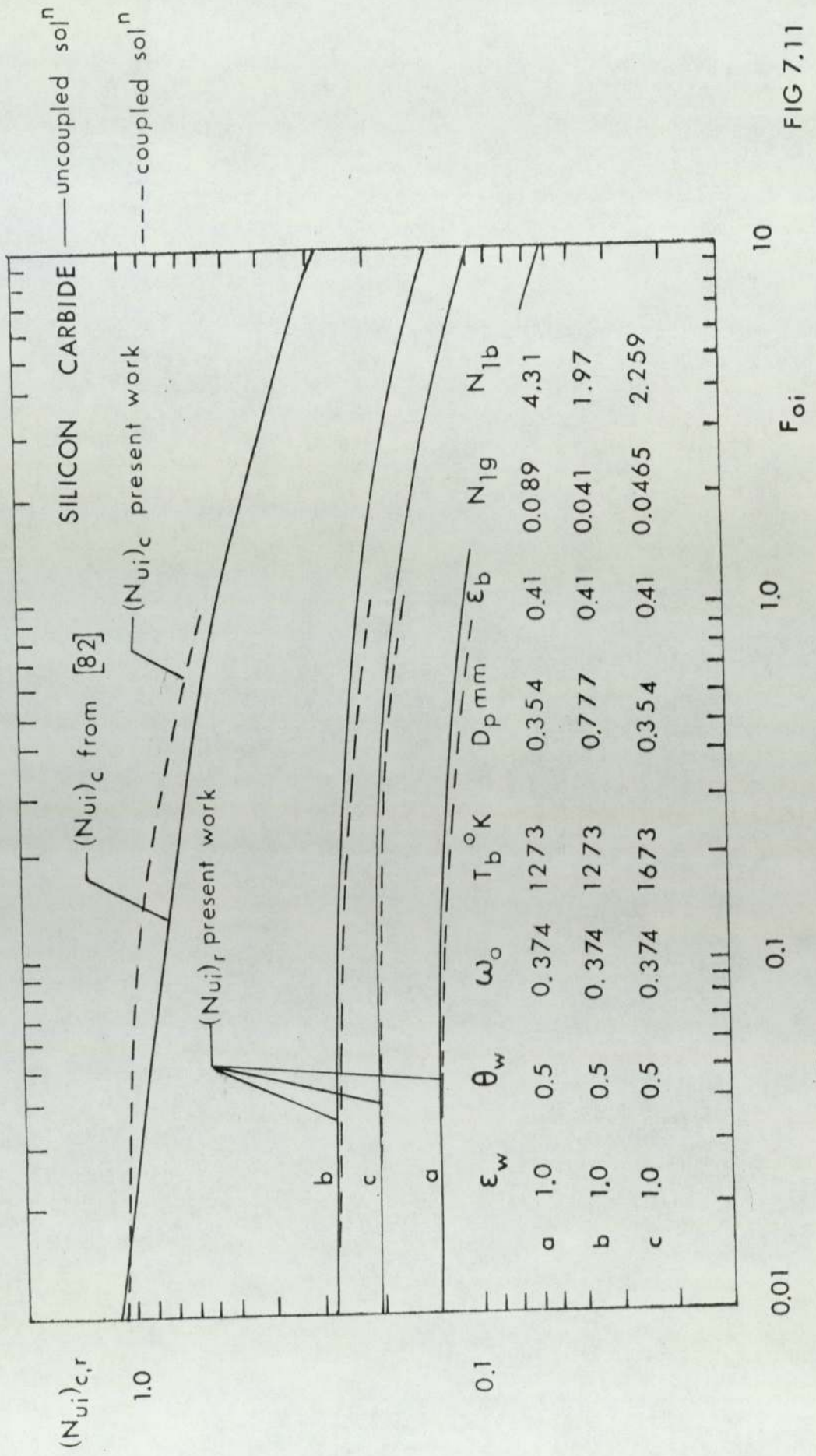


FIG 7.11

TRANSIENT
TEMPERATURE DISTRIBUTION

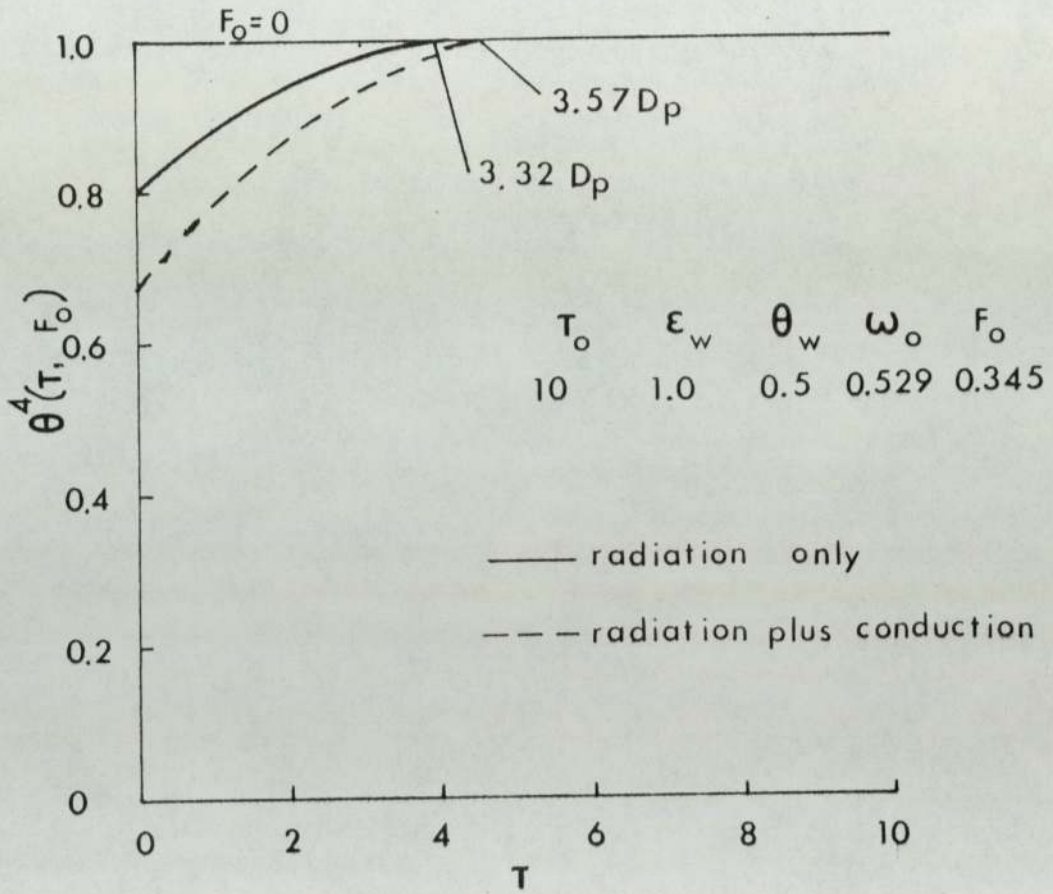
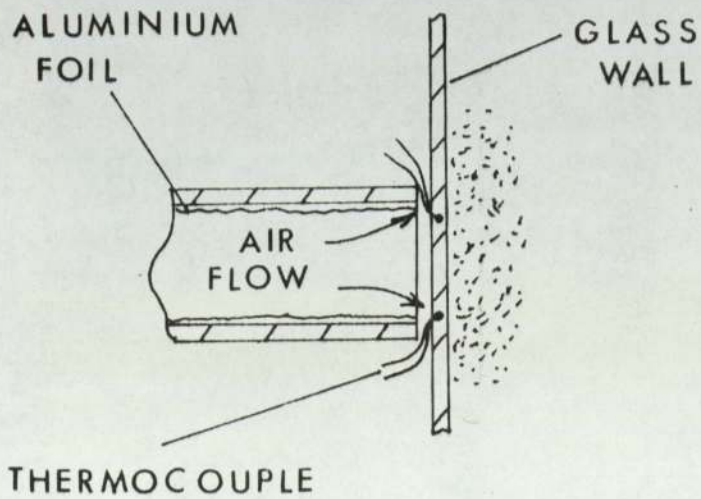
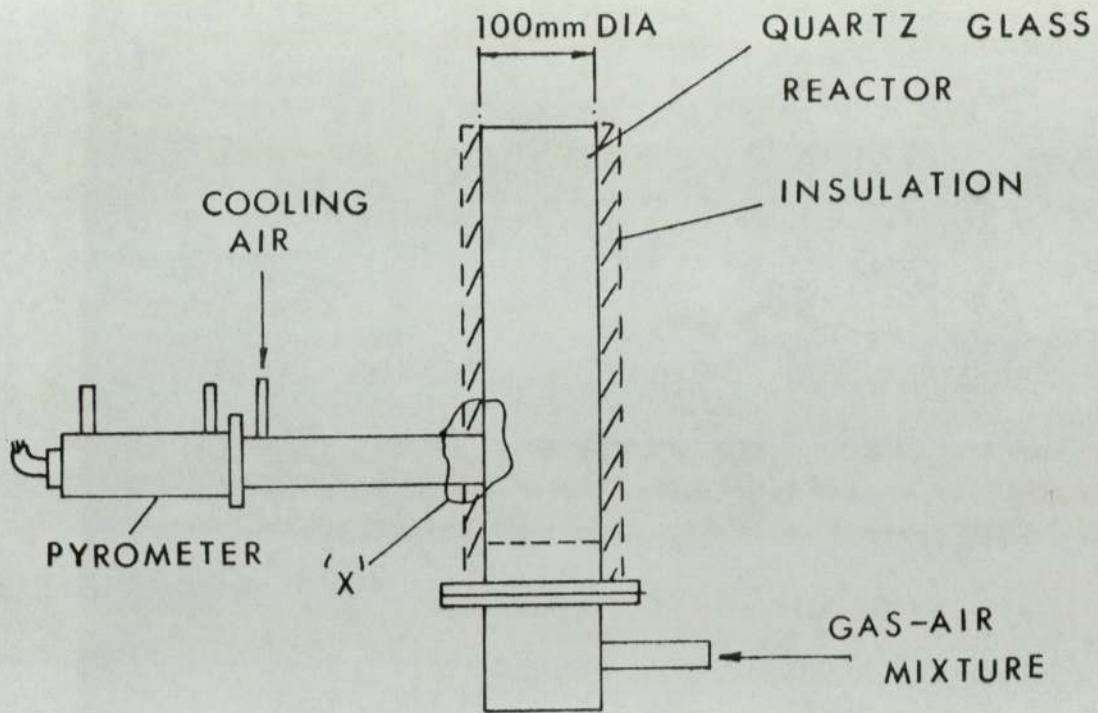


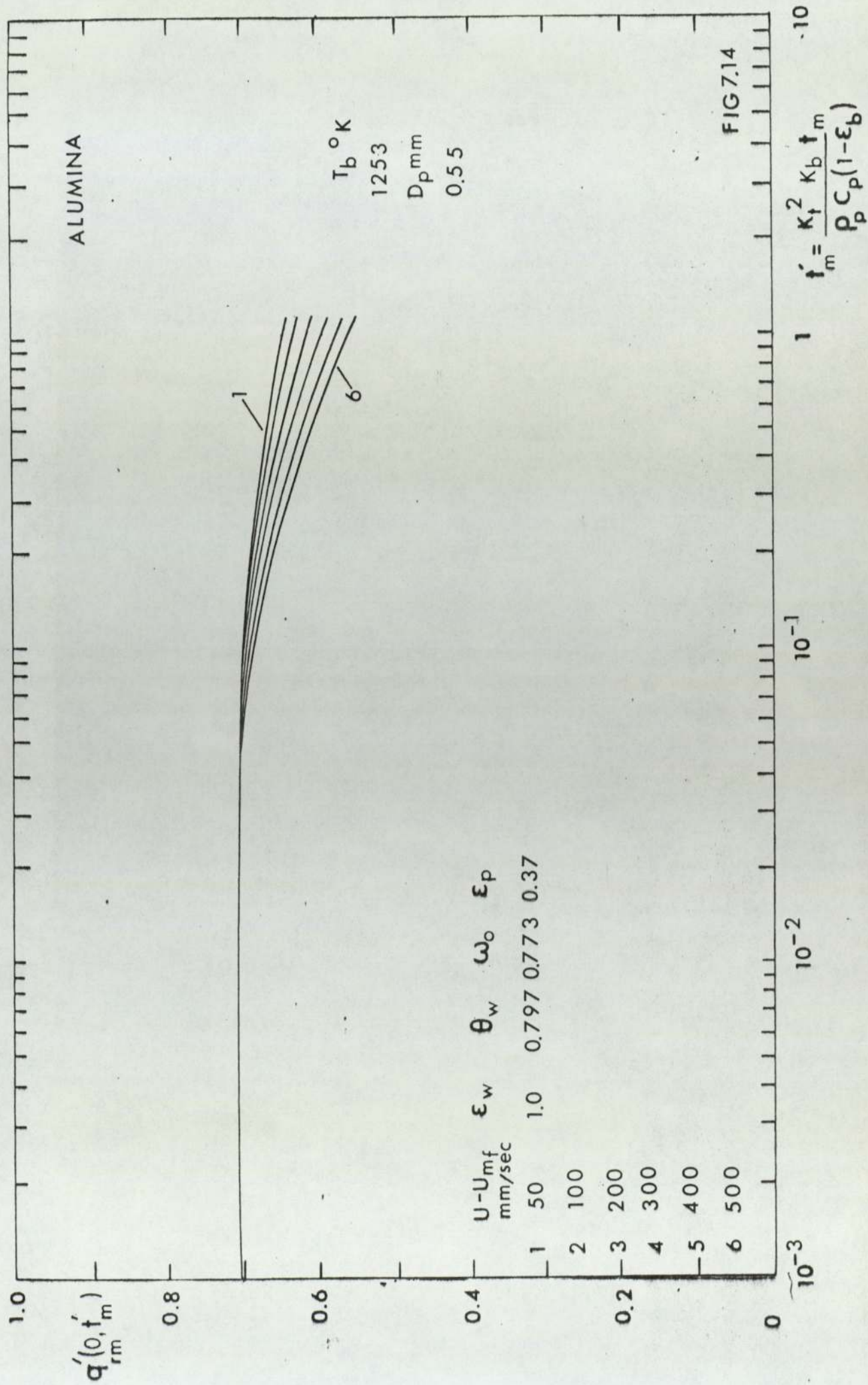
FIG. 7.12

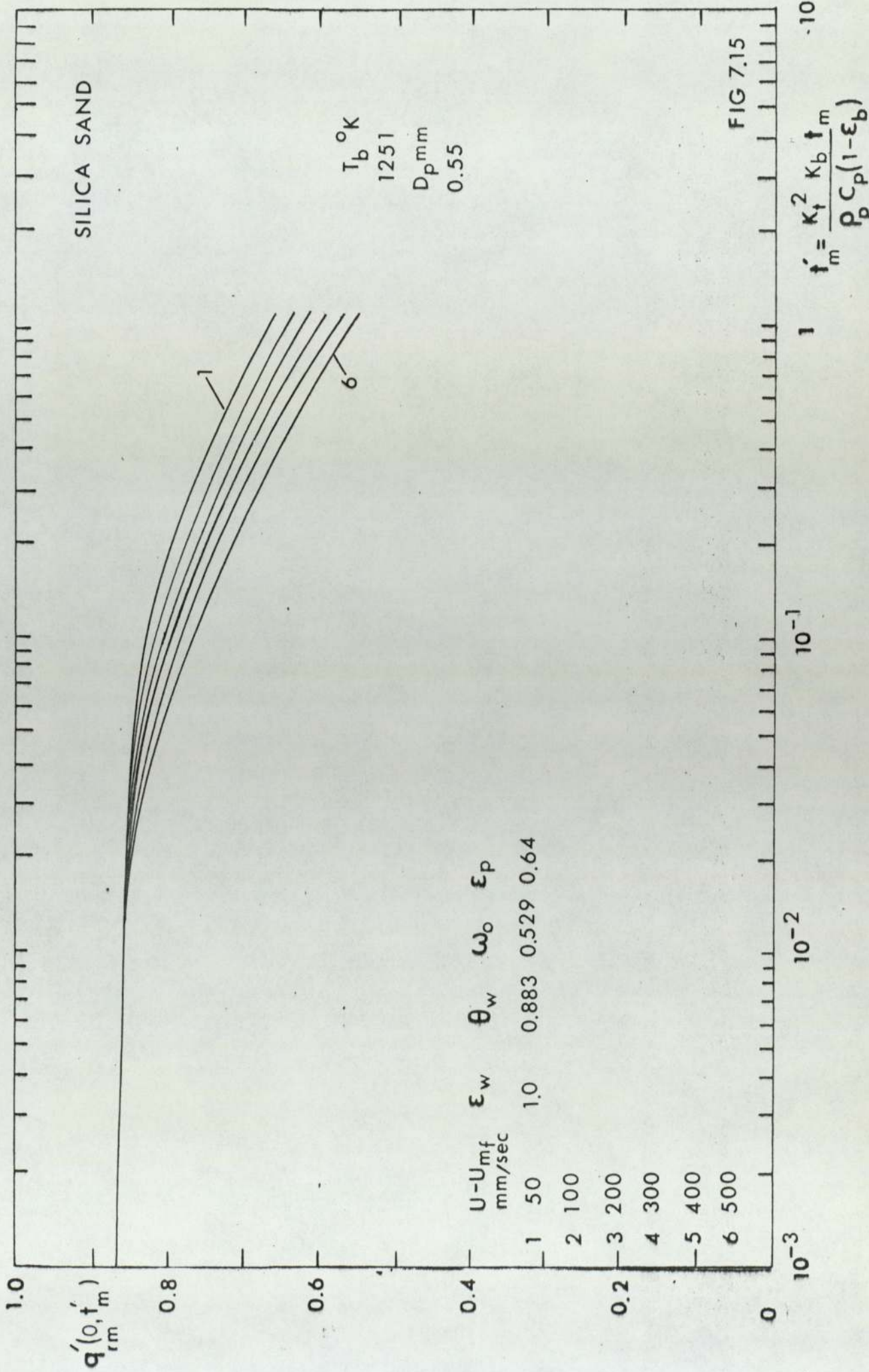
EXPERIMENTAL CONFIGURATION FOR
BED TO WALL RADIATIVE FLUX
MEASUREMENTS

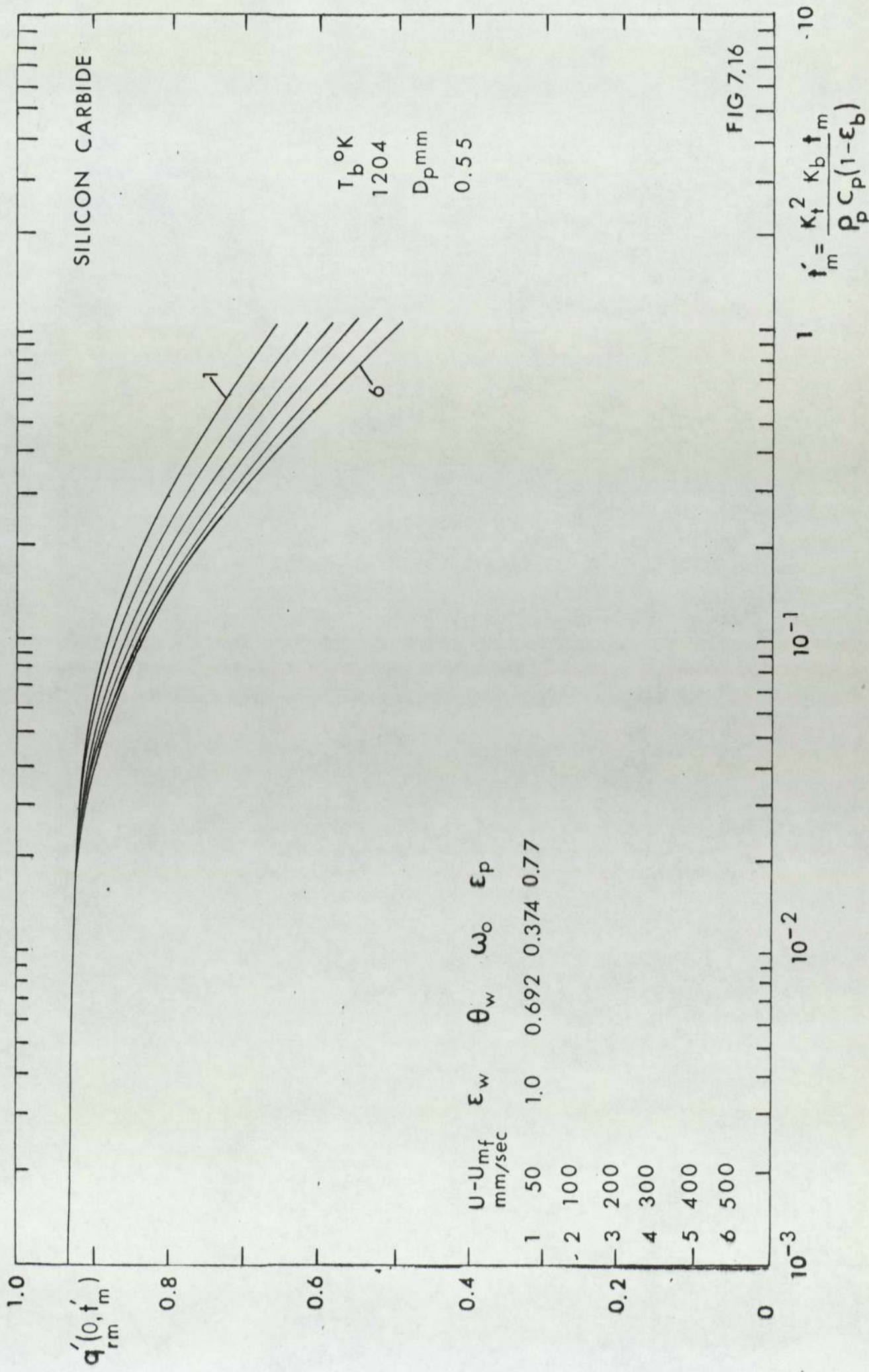


VIEW 'X'

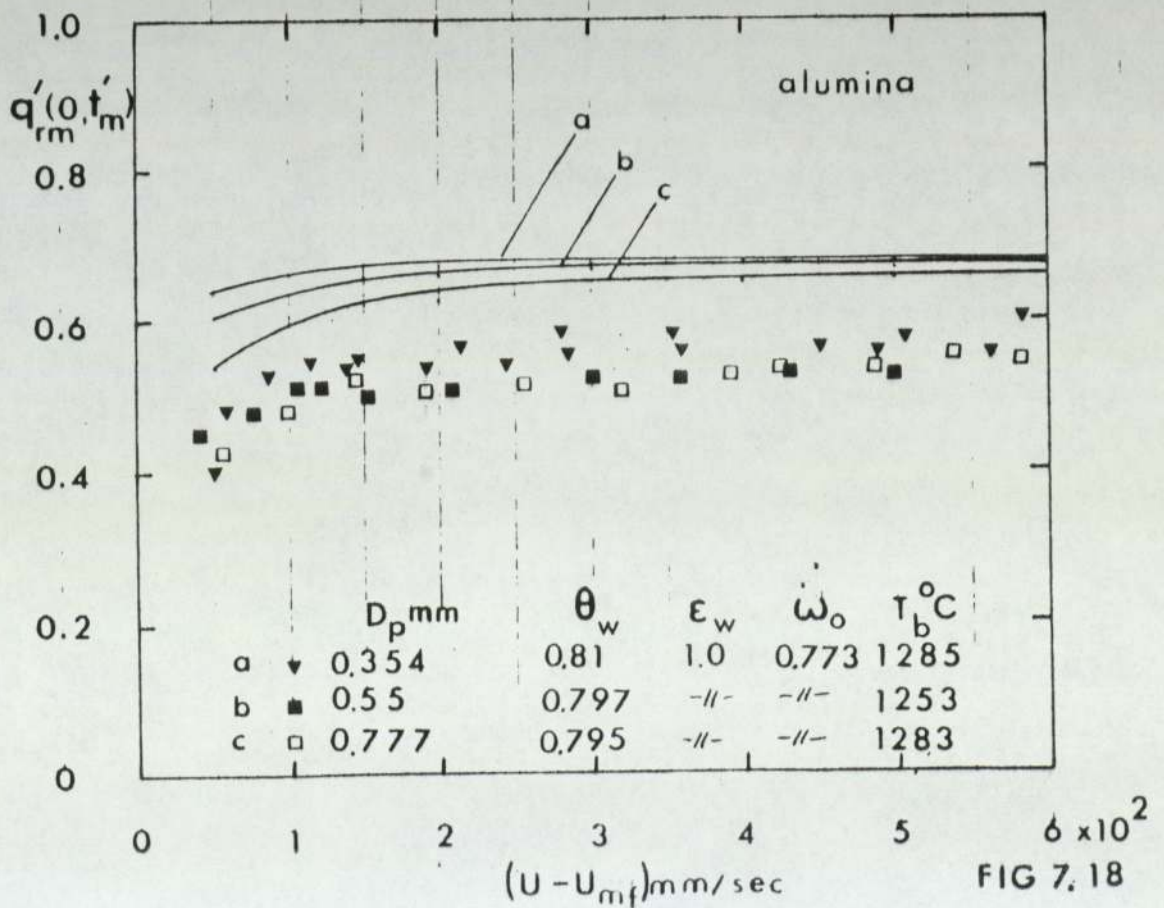
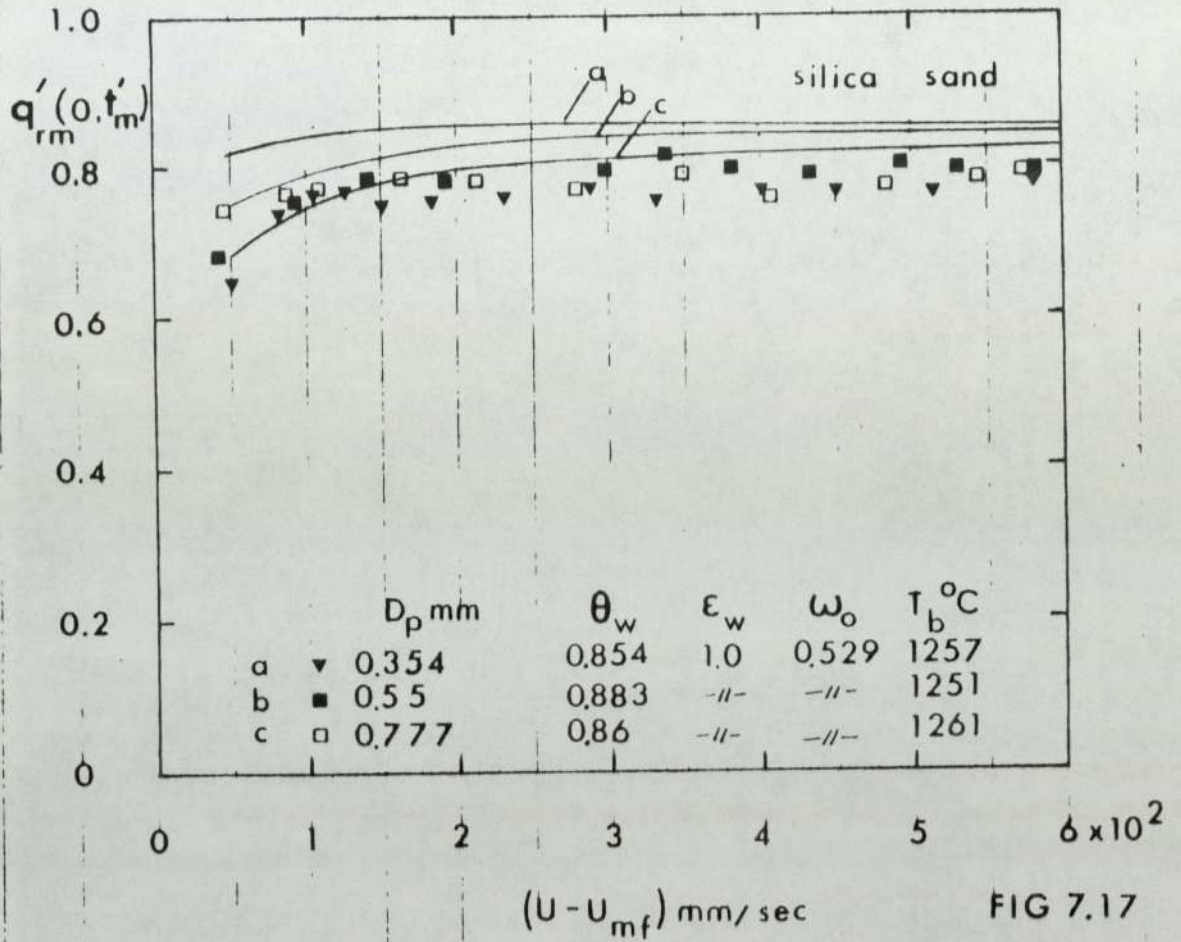
FIG 7.13







EFFECT OF EXCESS GAS VELOCITY ON
TIME MEAN RADIATIVE FLUX



EFFECT OF EXCESS GAS VELOCITY ON
TIME MEAN RADIATIVE FLUX

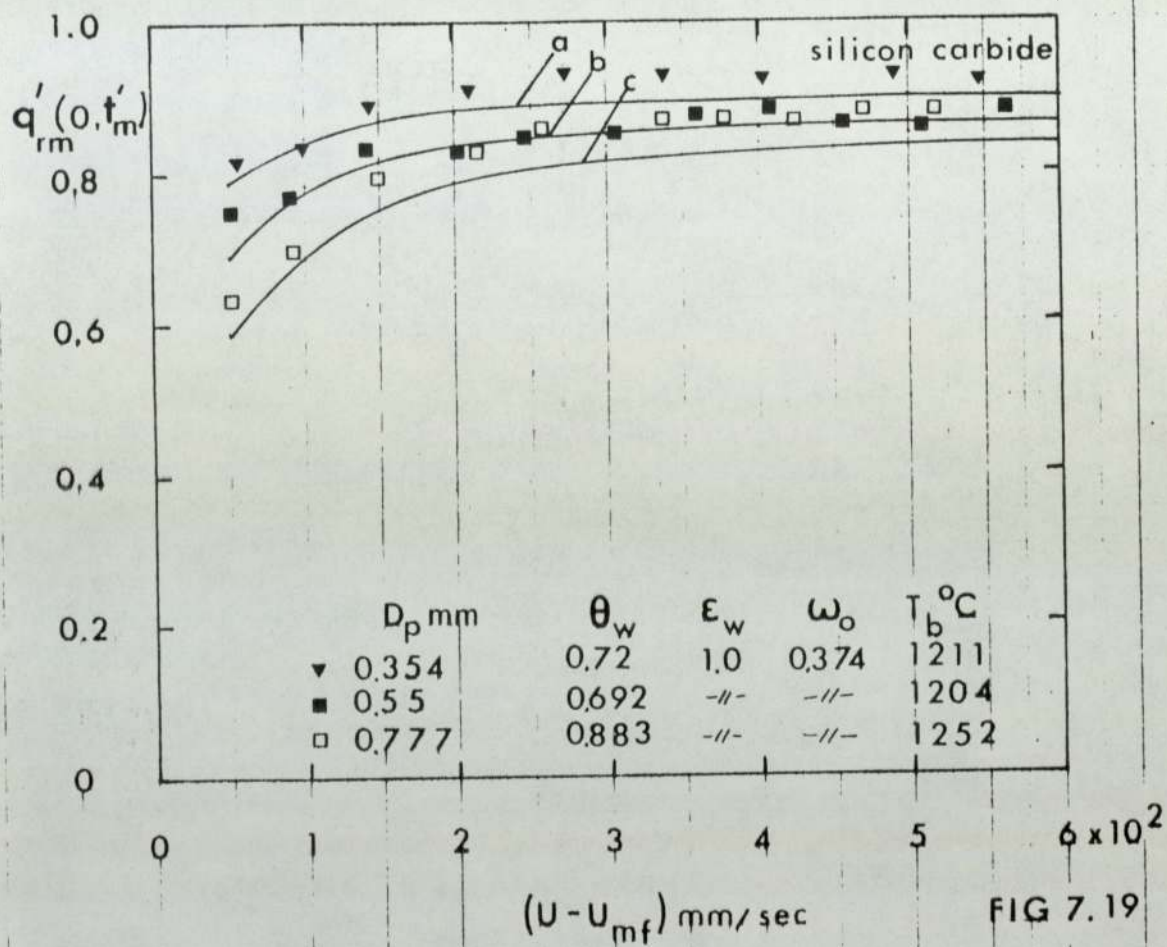


FIG 7.19

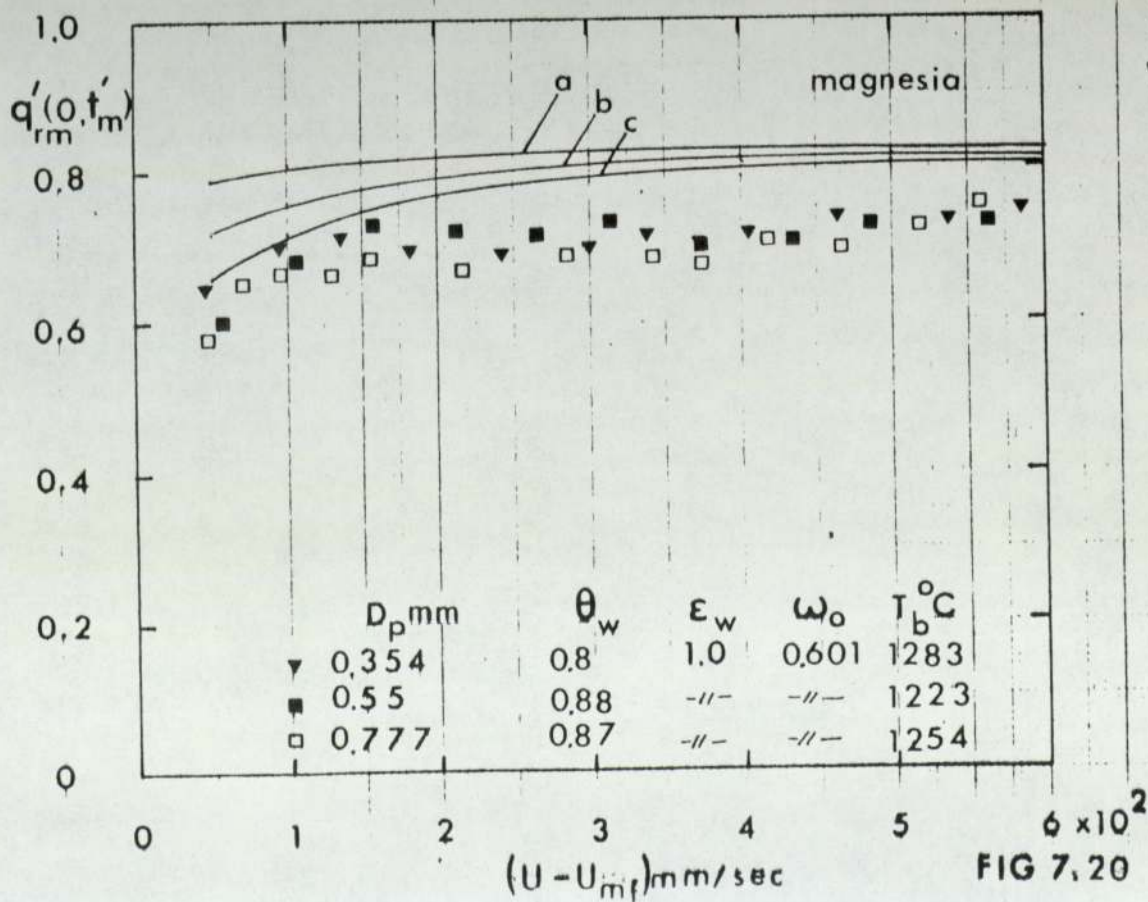


FIG 7.20

A P P E N D I C E S

APPENDIX A

THE EFFECTIVE EMISSIVITY OF A FLUIDIZED BED

From Zabrodsky^[2] the fluidized bed may be approximated by a dusty gas stream, requiring a solution of the classical energy attenuation equation

$$\frac{dI}{dx} = -K_a I \quad (A.1)$$

integrating (A.1)

$$I = I_b e^{-K_a x} \quad \text{or} \quad \frac{I}{I_b} = e^{-K_a x} = \tau_t$$

Now $\tau_t + \alpha = 1$

Hence from Kirchoff's law

$$\alpha = \epsilon_e = 1 - \tau_t = 1 - e^{-K_a x}$$

The constant K_a (absorption coefficient of gas layer) was determined in [2] as

$$K_a = \frac{1.5 (1 - \epsilon_b)}{D_p} \quad (A.2)$$

Hence for a typical fluidized bed with values of $\epsilon_b = 0.65$ and $D_p = 1.5$ mm, then

$$\epsilon_e = 1 - 8.5 \times 10^{-5} \approx 1$$

APPENDIX B

THE EQUATION OF RADIATIVE TRANSFER

Referring to Figure B.1 at the end of this Appendix, the equation of radiative transfer may be written for the one-dimensional case from [17] as:

$$\text{Cos } \theta \frac{dI}{dx} = -K_t I(x, \theta) + \frac{K_s}{4\pi} \int_{4\pi} I(x, \theta') P(\theta, \theta') d\Omega + K_a v^2 I_b(x) \quad (\text{B.1})$$

where θ' and θ refer to the incident and scattered directions respectively using the transforms

$$K_t = K_a + K_s, \quad v^2 = 1$$

$$\tau = \int_0^x K_t(x) dx, \quad \tau_0 = \int_0^L K_t(x) dx$$

with K_t invariant with x

$$\omega_0 = \frac{K_s}{K_t}, \quad 1 - \omega_0 = \frac{K_a}{K_t}, \quad \mu = \text{Cos } \theta$$

Equation (B.1) becomes

$$\mu \frac{dI}{d\tau} = -I + \frac{\omega_0}{4} D(\tau) + (1 - \omega_0) I_b(\tau) \quad (\text{B.2})$$

where

$$D(\tau) = \int_{4\pi} I(\tau, \theta') P(\theta, \theta') d\Omega$$

For the one-dimensional case equation (B.2) may be written as two

simultaneous equations for the positive and negative τ and μ direction as

$$\mu \frac{dI^+}{d\tau} + I^+ = (1 - \omega_0) I_b(\tau) + \frac{\omega_0}{4\pi} D(\tau) \quad (B.3)$$

and

$$\mu \frac{dI^-}{d\tau} + I^- = (1 - \omega_0) I_b(\tau) + \frac{\omega_0}{4\pi} D(\tau) \quad (B.4)$$

with boundary conditions of

$$I^+(\tau, \mu) = I^+(0, \mu), \quad \tau = 0$$

$$I^-(\tau, \mu) = I^-(\tau_0, \mu), \quad \tau = \tau_0$$

using an integrating factor $e^{\tau/\mu}$ then equations (B.3) and (B.4)

becomes

$$I^+(\tau, \mu) = I^+(0, \mu) e^{-\tau/\mu} + \int_0^\tau [(1 - \omega_0) I_b(\tau') + \frac{\omega_0}{4\pi} D(\tau')] e^{-(\tau - \tau')/\mu} \frac{d\tau'}{\mu} \quad (B.5)$$

and

$$I^-(\tau, \mu) = I^-(\tau_0, \mu) e^{(\tau_0 - \tau)/\mu} - \int_\tau^{\tau_0} [(1 - \omega_0) I_b(\tau') + \frac{\omega_0}{4\pi} D(\tau')] e^{-(\tau - \tau')/\mu} \frac{d\tau'}{\mu} \quad (B.6)$$

where τ' is used as a dummy argument to distinguish from τ . The

Radiative Flux may be defined as

$$q_r(\tau) = 2\pi \int_0^1 I^+ \mu d\mu - 2\pi \int_0^1 I^- \mu d\mu \quad (B.7)$$

Then substitution of (B.5), (B.6) into (B.7)

$$\begin{aligned}
 q_r(\tau) &= 2\pi \int_0^1 I^+(0, \mu) e^{-\tau/\mu} d\mu - 2\pi \int_0^1 I^-(\tau_0, \mu) e^{-(\tau_0 - \tau)/\mu} d\mu \\
 &+ 2\pi \int_0^\tau [(1 - \omega_0) I_b(\tau') + \frac{\omega_0}{4\pi} D(\tau')] E_2(\tau - \tau') d\tau' \\
 &- 2\pi \int_\tau^{\tau_0} [(1 - \omega_0) I_b(\tau') + \frac{\omega_0}{4\pi} D(\tau')] E_2(\tau' - \tau) d\tau' \quad (B.8)
 \end{aligned}$$

and similarly

$$D(\tau) = 2\pi \int_0^1 I^+(\tau, \mu) d\mu - 2\pi \int_0^1 I^-(\tau, \mu) d\mu$$

Hence

$$\begin{aligned}
 D(\tau) &= 2\pi \int_0^1 I^+(0, \mu) e^{-\tau/\mu} d\mu + 2\pi \int_0^1 I^-(\tau_0, \mu) e^{-(\tau_0 - \tau)/\mu} d\mu \\
 &+ 2\pi \int_0^\tau [(1 - \omega_0) I_b(\tau') + \frac{\omega_0}{4\pi} D(\tau')] E_1(|\tau - \tau'|) d\tau' \quad (B.9)
 \end{aligned}$$

where $E_n(\tau)$ are exponential integrals.

Non-dimensionalizing with

$$q_r'(\tau) = \frac{q_r(\tau)}{\sigma T_b^4},$$

$$D'(\tau) = \frac{D(\tau)}{\sigma T_b^4}$$

$$\frac{T_1^4}{T_b^4} = \theta_1^4,$$

$$\frac{T_2^4}{T_b^4} = \theta_2^4$$

$$I^+(0, \mu) = \frac{F_1}{\pi},$$

$$I^-(\tau_0, \mu) = \frac{F_2}{\pi}$$

$$2\pi \int_0^1 I^+(0, \mu) e^{-\tau/\mu} d\mu = 2F_1 E_3(\tau)$$

$$2\pi \int_0^1 I^-(\tau_0, \mu) e^{-(\tau_0 - \tau)/\mu} d\mu = 2F_2 E_3(\tau_0 - \tau)$$

$$2\pi \int_0^1 I^+(0, \mu) e^{-\tau/\mu} d\mu = 2F_1 E_2(\tau)$$

$$2\pi \int_0^1 I^-(\tau_0, -\mu) e^{-(\tau_0 - \tau)/\mu} d\mu = 2F_2 E_2(\tau_0 - \tau)$$

$$\theta^4(\tau) = \frac{\pi I_b(\tau)}{\sigma T_b^4}$$

then equations (B.8) and (B.9) may be written

$$\begin{aligned} q_r'(\tau) &= 2F_1 E_3(\tau) - 2F_2 E_3(\tau_0 - \tau) \\ &+ 2 \int_0^\tau [(1 - \omega_0) \theta^4(\tau') + \frac{\omega_0}{4} D'(\tau')] E_2(\tau - \tau') d\tau' \\ &- 2 \int_\tau^{\tau_0} [(1 - \omega_0) \theta^4(\tau') + \frac{\omega_0}{4} D'(\tau')] E_2(\tau' - \tau) d\tau' \end{aligned} \quad (B.10)$$

and

$$\begin{aligned} D'(\tau) &= 2F_1 E_2(\tau) + 2F_2 E_2(\tau_0 - \tau) \\ &+ 2 \int_0^{\tau_0} [(1 - \omega_0) \theta^4(\tau') + \frac{\omega_0}{4} D'(\tau')] E_1(|\tau - \tau'|) d\tau' \end{aligned} \quad (B.11)$$

Equations (B.10) and (B.11) are known as the 'radiative flux equations'.

In equation (B.10) the first two terms on the right-hand side of the equation are the contributions to the radiative flux $q_r'(\tau)$ from the two boundaries. The third and fourth terms are the contributions from the absorbing, emitting and scattering medium. For plane parallel boundaries appropriate radiative boundary conditions become from [26]

$$F_1 = \epsilon_1 \theta_1^4 + (1 - \epsilon_1) (F_1 - q_r'(0)) \quad (B.12)$$

and

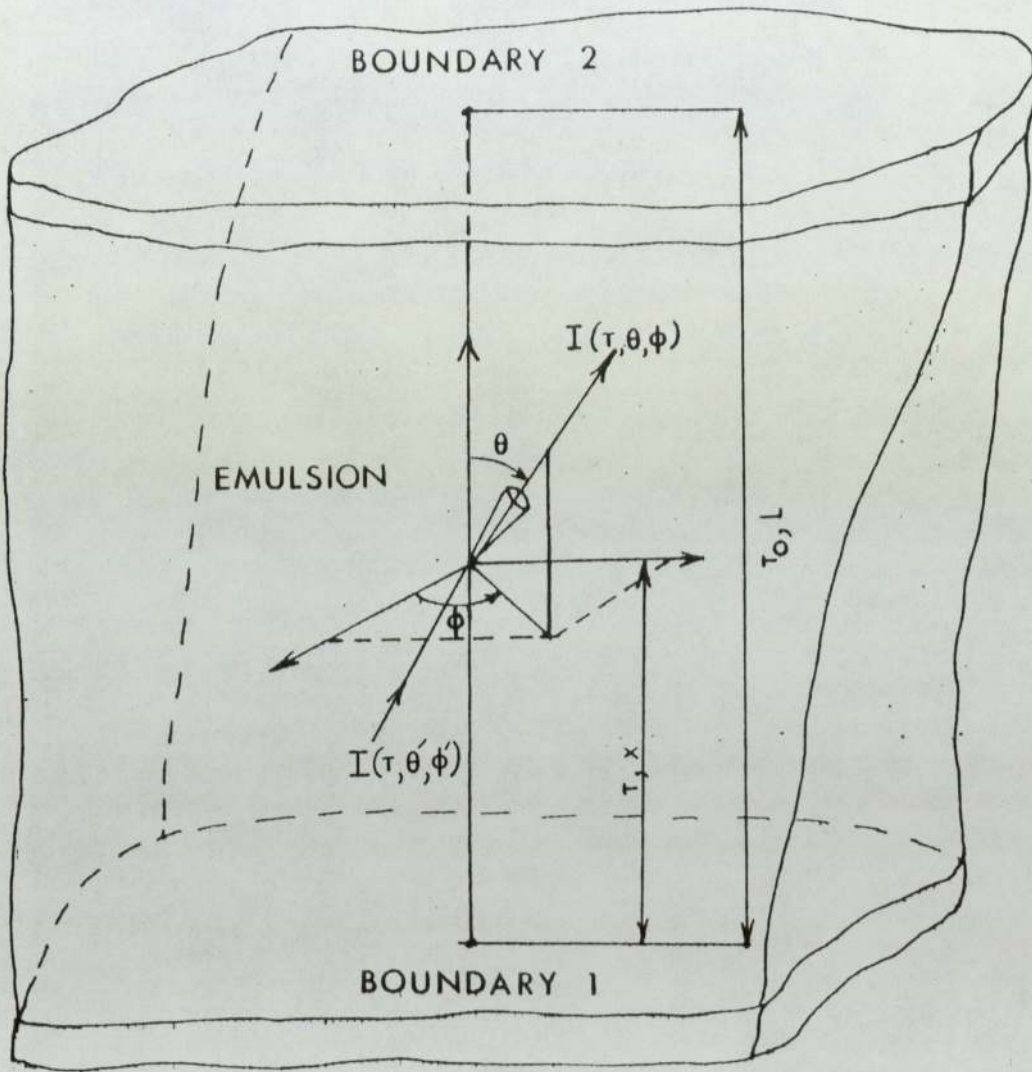
$$F_2 = \epsilon_2 \theta_2^4 + (1 - \epsilon_2)(F_2 + q_r(\tau_0)) \quad (\text{B.13})$$

then at $\tau = 0$

$$F_1 = \epsilon_1 \theta_1^4 + 2(1 - \epsilon_1)\{F_2 E_3(\tau_0) + \int_0^{\tau_0} [(1 - \omega_0)\theta^4(\tau') + \frac{\omega_0}{4} D'(\tau')] E_2(\tau') d\tau'\} \quad (\text{B.14})$$

and at $\tau = \tau_0$

$$F_2 = \epsilon_2 \theta_2^4 + 2(1 - \epsilon_2)\{F_1 E_3(\tau_0) + \int_0^{\tau_0} [(1 - \omega_0)\theta^4(\tau') + \frac{\omega_0}{4} D'(\tau')] E_2(\tau_0 - \tau') d\tau'\}$$



GEOMETRIC CONFIGURATION OF RADIATIVE TRANSFER
 OF AN EMULSION BETWEEN PARALLEL BOUNDARIES

FIG. B1

APPENDIX C

THE TWO FLUX APPROXIMATION OF THE EQUATION OF RADIATIVE
TRANSFER APPLIED TO AN ISOTHERMAL MEDIUM

From Appendix B the equation of radiative transfer in non-dimensional form is

$$\mu \frac{dI}{d\tau} = -I + \frac{\omega_0}{4\pi} \int_{4\pi} IP(\theta') d\Omega + (1-\omega_0)I_b \quad (C.1)$$

and may be transformed by assuming that radiation is scattered in the direction of the incident beam or at 180° to this direction. Hence from [10]

$$\frac{\omega_0}{4\pi} \int_{4\pi} IP(\theta') d\Omega = \omega_0 [fI^+ + bI^-] \quad (C.2)$$

For isotropic scattering $P(\theta') = 1$ and

$$f = \int_0^1 P(\theta') d\mu \quad b = \frac{1}{2} \int_{-1}^0 P(\theta') d\mu$$

Hence equation (C.1) becomes

$$\mu \frac{dI^+}{d\tau} = (f\omega_0 - 1)I^+ + \omega_0 bI^- + (1 - \omega_0)I_b \quad (C.3)$$

and

$$\mu \frac{dI^-}{d\tau} = (1 - f\omega_0)I^- - \omega_0 bI^+ - (1 - \omega_0)I_b \quad (C.4)$$

The solution of (C.3) and (C.4) from [20] is:

$$I^+(\tau) = A(1 - m)e^{n\tau} + B(1 + m)e^{-n\tau} + I_b \quad (C.5a)$$

$$I^-(\tau) = A(1 + m)e^{n\tau} + B(1 - m)e^{-n\tau} + I_b \quad (C.5b)$$

for $f = b = \frac{1}{2}$, where

$$n = [a(a + 2s)]^{\frac{1}{2}} \quad (C.6)$$

and

$$m = \frac{n}{a + 2s} \quad (C.7)$$

where

$$a = (1 - f\omega_0)/\mu, \quad (C.8)$$

$$s = \omega_0 b/\mu \quad (C.9)$$

subject to boundary conditions of

$$\tau = 0, \quad I^+ = 0 \quad (C.10)$$

$$\tau = \tau_0, \quad I^- = 0 \quad (C.11)$$

Hence

$$B = I_b \frac{\left[\frac{1}{(1 + m)e^{n\tau_0}} - \frac{1}{(1 - m)} \right]}{\left[\frac{1 + m}{1 - m} - \frac{1 - m}{1 + m} \frac{1}{e^{2n\tau_0}} \right]} \quad (C.12)$$

and

$$A = \frac{-B(1 + m) - I_b}{(1 - m)} \quad (C.13)$$

By assuming that I^+ and I^- are the total one dimensional hemispherical fluxes across the reference plane rather than intensities, then $\mu = 1$. According to [10] the optical depth for any one dimensional slab may be modified using $\tau = 2\tau$.

APPENDIX D

A SOLUTION OF THE RADIATIVE FLUX EQUATION FOR STEADY
STATE HEAT TRANSFER

The steady state energy equation may be written, for pure radiation (neglecting conduction and convection), as

$$\frac{dq_r}{d\tau} = f(\tau) \neq 0$$

to remain consistent with the first differential of equation (B.10) when an arbitrary temperature distribution is imposed. The Radiative Flux equations (B.10) and (B.11) of Appendix B are:

$$\begin{aligned} q_r'(\tau) &= 2F_1 E_3(\tau) - 2F_2 E_3(\tau_0 - \tau) \\ &+ 2 \int_0^\tau [(1 - \omega_0)\theta^4(\tau') + \frac{\omega_0}{4} D'(\tau')] E_2(\tau - \tau') d\tau' \\ &- 2 \int_0^{\tau_0} [(1 - \omega_0)\theta^4(\tau') + \frac{\omega_0}{4} D'(\tau')] E_2(\tau' - \tau) d\tau' \quad (D.1) \end{aligned}$$

and

$$\begin{aligned} D'(\tau) &= 2F_1 E_2(\tau) + 2F_2 E_2(\tau_0 - \tau) \\ &+ 2 \int_0^{\tau_0} [(1 - \omega_0)\theta^4(\tau') + \frac{\omega_0}{4} D'(\tau')] E_1(|\tau - \tau'|) d\tau' \quad (D.2) \end{aligned}$$

A solution of equations (D.1) and (D.2) may be obtained by firstly considering equation (D.2). Approximating

$$\theta^4(\tau') = \sum_{i=1}^n C_i \tau'^{(i-1)} \quad (D.3)$$

and

$$D'(\tau') = \sum_{i=1}^n d_i \tau'^{(i-1)} \quad (D.4)$$

With the coefficients C_i , $i=1\dots n$, initially known then substitution of equations (D.3) and (D.4) into equation (D.2) enables the integrals to be solved analytically term by term and the unknown coefficients d_i , $i=1\dots n$, to be obtained by satisfying equation (D.2) at 'n' locations.

This may be achieved by recasting the modified form of equation (D.2) as a matrix equation. Then equation (D.2) becomes

$$[V] \cdot [d] = [W] + [X] + [Y] + [Z] \cdot [d] \quad (D.5)$$

Hence

$$[U] \cdot [d] = [P] \quad (D.6)$$

where

$$[U] = [V] - [Z]$$

and

$$[P] = [W] + [X] + [Y]$$

with $[V] = \begin{bmatrix} \tau_1, & \tau_1^2, & \tau_1^3, & \dots, & \dots, & \tau_1^{(n-1)} \\ \tau_2, & \tau_2^2, & \tau_2^3, & \dots, & \dots, & \tau_2^{(n-1)} \\ \cdot & \cdot & \cdot & \cdot & \cdot & \cdot \\ \cdot & \cdot & \cdot & \cdot & \cdot & \cdot \\ \cdot & \cdot & \cdot & \cdot & \cdot & \cdot \\ \tau_n, & \tau_n^2, & \tau_n^3, & \dots, & \dots, & \tau_n^{(n-1)} \end{bmatrix}$

$$[W] = \begin{bmatrix} 2F_1 E_2 (\tau_1) \\ 2F_1 E_2 (\tau_2) \\ \cdot \\ \cdot \\ \cdot \\ 2F_1 E_2 (\tau_n) \end{bmatrix}$$

$$[X] = \begin{bmatrix} 2F_2 E_2 (\tau_0 - \tau_1) \\ 2F_2 E_2 (\tau_0 - \tau_2) \\ \cdot \\ \cdot \\ \cdot \\ 2F_2 E_2 (\tau_0 - \tau_n) \end{bmatrix}$$

$$[Y] = \begin{bmatrix} I_1, & I_2 \tau'_1, & I_3 \tau'^2_1, & \cdot & \cdot & \cdot & I_n \tau'^{(n-1)}_1 \\ I_1, & I_2 \tau'_2, & I_3 \tau'_2, & \cdot & \cdot & \cdot & I_n \tau'^{(n-1)}_2 \\ \cdot & \cdot & \cdot & \cdot & \cdot & \cdot & \cdot \\ \cdot & \cdot & \cdot & \cdot & \cdot & \cdot & \cdot \\ \cdot & \cdot & \cdot & \cdot & \cdot & \cdot & \cdot \\ I_1, & I_2 \tau'_n, & I_3 \tau'_n, & \cdot & \cdot & \cdot & I_n \tau'^{(n-1)}_n \end{bmatrix} \begin{bmatrix} C_1 \\ C_2 \\ \cdot \\ \cdot \\ \cdot \\ C_n \end{bmatrix}$$

$$[Z] = \begin{bmatrix} J_1, & J_2 \tau'_1, & J_3 \tau'_1, & \cdot & \cdot & \cdot & J_n \tau'^{(n-1)}_1 \\ \cdot & \cdot & \cdot & \cdot & \cdot & \cdot & \cdot \\ \cdot & \cdot & \cdot & \cdot & \cdot & \cdot & \cdot \\ \cdot & \cdot & \cdot & \cdot & \cdot & \cdot & \cdot \\ J_1, & J_2 \tau'_n, & J_3 \tau'_n, & \cdot & \cdot & \cdot & J_n \tau'^{(n-1)}_n \end{bmatrix}$$

$$[d] = \begin{bmatrix} d_1 \\ d_2 \\ \cdot \\ \cdot \\ \cdot \\ d_n \end{bmatrix}$$

where $I_i, i=1\dots n$

and $J_i, i=1\dots n$

are obtained from a solution of the integrals in equation (D.2).

It remains to solve equation (D.6) for the unknowns $d_i, i=1\dots n$.

This is achieved by transforming $[U]$ into an upper and lower matrix. Hence

$$[U] \cdot [d] = [P]$$

becomes

$$[U]^L \cdot [U]^U \cdot [d] = [P]$$

or

$$[U]^L \cdot [b] = [P] \tag{D.7}$$

and

$$[U]^U \cdot [d] = [b] \tag{D.8}$$

Hence $[b]$ is solved from (D.7), substituted in (D.8) and solved for $[d]$.

With a solution for $D'(\tau)$ on substituting in equation (D.1), $q_r'(\tau)$ may then be determined.

APPENDIX E

(a) Determination of Extinction Coefficient from Bed Pressure Drop Distribution

Consider a unit volume of a gas/solid emulsion.

$$V_p \rho_p N = \bar{\rho} \quad \text{bulk mass/unit volume} \quad (\text{E.1})$$

$$\therefore N = \frac{\bar{\rho}}{V_p \rho_p} \quad \text{particles/unit volume} \quad (\text{E.2})$$

Across volume ΔV the pressure difference

$$\Delta P = \frac{g V_p \rho_p N \Delta V}{A} \quad (\text{E.3})$$

with $\Delta V = A \Delta x$; then

$$\frac{\Delta P}{\Delta x} = g V_p \rho_p N \quad (\text{E.4})$$

and

$$L_t \lim_{\Delta x \rightarrow 0} \frac{\Delta P}{\Delta x} = \frac{dP}{dx} = V_p \rho_p N g \quad (\text{E.5})$$

For a distribution of particles/unit volume $N(x)$, equation (5) may be written

$$N(x) = \frac{1}{g V_p \rho_p} \frac{dP(x)}{dx} \quad (\text{E.6})$$

with

$$V_p = \frac{\pi}{6} D_p^3$$

$$N(x) = \frac{6}{\pi D_p^3 \rho_p g} \frac{dP(x)}{dx} \quad (E.7)$$

Extinction cross-section

$$K_t' = \frac{\pi D_p^2}{4} [\epsilon_p + 2(1 - \epsilon_p)]$$

Hence optical depth $\tau(x)$ is defined

$$\tau(x) = \int_0^x K_t' N(x) dx \quad (E.8)$$

$$\tau(x) = \frac{3}{2} D_p \frac{1}{\rho_p g} [\epsilon_p + 2(1 - \epsilon_p)] \int_0^x \frac{dP}{dx}(x) \cdot dx \quad (E.9)$$

As $P(x)$ is obtained experimentally. A least squares polynomial fit may be used to obtain the form of

$$P(x) = \sum_{i=1}^n C_i x^{(i-1)} \quad (E.10)$$

Then $\tau(x) = f_n(x)$ may be found. A value of $K_t(x)$ may then be obtained from the relationship.

$$K_t(x) = K_t' N(x) = \frac{d\tau(x)}{dx} \quad (E.11)$$

(b) Determination of Extinction Coefficient at a Plane Surface

From (a) it was established that

$$N(x) = \frac{\bar{\rho}(x)}{V_p \rho_p} \quad (E.12)$$

where

$$\bar{\rho}(x) = \rho_p(1 - \epsilon_b(x)) \quad (\text{E.13})$$

Hence

$$N(x) = \frac{(1 - \epsilon_b(x))}{V_p} = \frac{6(1 - \epsilon_b(x))}{\pi D_p^3} \quad (\text{E.14})$$

with $\bar{x} = \frac{x}{D_p}$; then

$$N(\bar{x}) = \frac{6}{\pi D_p^3} (1 - \epsilon_b(\bar{x})) \quad (\text{E.15})$$

and

$$K_t' = \frac{\pi D_p^2}{4} [\epsilon_p + 2(1 - \epsilon_p)] \quad (\text{E.16})$$

Hence

$$K_t(\bar{x}) = K_t' N(\bar{x}) \quad (\text{E.17})$$

$$K_t(\bar{x}) = \frac{K_t' 6}{\pi D_p^3} [1 - \epsilon_b(\bar{x})] \quad (\text{E.18})$$

From [82]:

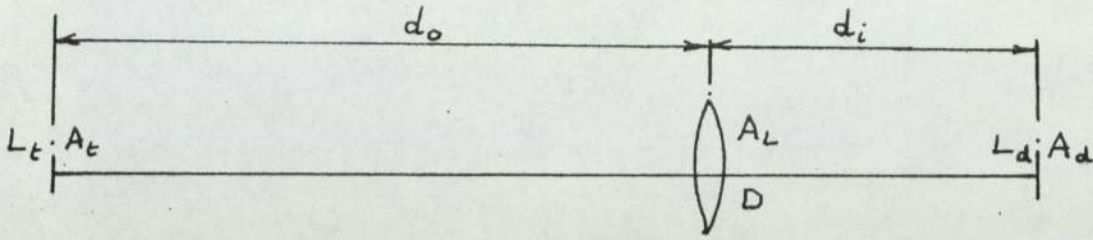
$$\epsilon_b(\bar{x}) = 1 - 3(1 - \epsilon_b) \left(\bar{x} - \frac{2}{3} \bar{x}^2 \right), \quad \bar{x} \leq 1 \quad (\text{E.19})$$

and

$$\epsilon_b(\bar{x}) = \epsilon_b, \quad \bar{x} > 1 \quad (\text{E.20})$$

APPENDIX F

OPERATION OF A RADIATION PYROMETER (RADIOMETER) SYSTEM



For a thin lens f = focal length.

$$\frac{1}{d_o} + \frac{1}{d_i} = \frac{1}{f} \quad \text{(F.1)}$$

The focal length depends upon lens material and its curvature.

Target area which fills the detector A_d is

$$A_t = A_d \quad \text{(F.2)}$$

From (F.1) and (F.2):

$$A_t = A_d \frac{(d_o - f)^2}{f^2} \quad \text{(F.3)}$$

and for $d_o \gg f$

$$A_t \approx A_d \frac{d_o^2}{f^2} \quad \text{(F.4)}$$

For a detector diameter = L_d then

$$L_t \approx L_d \frac{d_o}{f} \quad (F.5)$$

When the target dimensions are equal to or greater than the size in equation (F.4) or (F.5), the target is resolved, therefore requirement for target resolution is:

$$L_t \geq L_d \frac{d_o}{f} \quad (F.6)$$

Irradiance of the Detector

The irradiance G_L received at the radiometer lens decreases with the square of the distance to the target. Hence total radiation received is

$$A_L G_L = \frac{A_L A_t \epsilon_t}{\pi d_o^2} \int_{\lambda_1}^{\lambda_2} N_\lambda d\lambda \quad \text{watts/steradian} \quad (F.7)$$

$$= \frac{D A_t \epsilon_t}{4 d_o^2} \int_{\lambda_1}^{\lambda_2} N_\lambda d\lambda \quad \text{" / " } \quad (F.8)$$

with λ = wavelength

ϵ_t = target emissivity

N_λ = target radiance

and the radiation incident on the detector is

$$G_d = \frac{G_L A_L \tau_t}{A_d} = \frac{A_t \tau_t D^2 \epsilon_t}{4 d_o^2 A_d} \int_{\lambda_1}^{\lambda_2} N_\lambda d\lambda \quad \text{watts/steradian } -m^2 \quad (F.9)$$

where τ_t is the transmission of the optical lens. The signal voltage from the detector is proportional to G_d . For a resolved target

$$\frac{A_t}{d_o^2 A_d} = \frac{1}{f^2}$$

therefore irradiance at the detector is

$$G_d = \frac{\tau_t D^2 \epsilon_t}{4f^2} \int_{\lambda_1}^{\lambda_2} N_\lambda d\lambda \text{ watts/steradian -m}^2 \quad (\text{F.10})$$

and

$$G_d = \frac{\tau_t D^2 \epsilon_t \pi}{4f^2} \int_{\lambda_1}^{\lambda_2} N_\lambda d\lambda \text{ watts/steradian -m}^2 \quad (\text{F.11})$$

Although signal strength V (mv) tends to decrease with the square of target distance, the area of the resolved target increases with square of target distance, resulting in an invariance of the signal with distance and size. Hence

$$V = \frac{K \tau_t D^2 \epsilon_t \pi}{4f^2} \int_{\lambda_1}^{\lambda_2} N_\lambda d\lambda \quad (\text{m volts}) \quad (\text{F.12})$$

Constant K includes the responsivity (volts/watt) of the detector and the gain of amplifier. Hence

$$V = K \cdot G_d \quad (\text{F.13})$$

and K may be found for black body calibration at relevant temperatures.

For a wide spectral range

$$N(T_t) = \int_{\lambda_1}^{\lambda_2} N_\lambda d\lambda \quad (\text{F.14})$$

$$\therefore V = \frac{K\tau_t D^2 \epsilon_t \pi}{4f^2} N(T_t^4) \quad (\text{F.15})$$

From calibration with recorded temperature T_c

$$V = \frac{K\tau_t D^2 \epsilon_d \pi}{4f^2} N(T_c^4) \quad (\text{F.16})$$

from (F.15) and (F.16) with $\epsilon_d = 1$

$$\epsilon_t = \frac{N(T_c^4)}{N(T_t^4)} \approx \frac{T_c^4}{T_t^4} \quad (\text{F.17})$$

APPENDIX G

A SOLUTION OF THE RADIATIVE FLUX EQUATION FOR UNSTEADY
HEAT TRANSFER

The unsteady energy equation for an emulsion (packet) of fluidized particles in contact with a plane surface is:

$$\bar{\rho} \bar{C}_p \frac{\partial T}{\partial t} = - \frac{\partial q_r}{\partial x} \quad (G.1)$$

where $\bar{\rho} \bar{C}_p = \rho_p C_p (1 - \epsilon_b)$ and may be non-dimensionalised to

$$\frac{\partial \theta}{\partial t'} = - \frac{\partial q'_r}{\partial \tau} \quad (G.2)$$

where

$$t' = \frac{K_t \sigma T_b^3 t}{\rho_p C_p (1 - \epsilon_b)}$$

subject to boundary conditions of

$$\tau = 0, \quad \theta(0, t') = \theta_1, \quad t' \geq 0 \quad (G.3)$$

$$\tau = \tau_0, \quad \theta(\tau_0, t') = 1, \quad t' \geq 0 \quad (G.4)$$

and initial conditions of

$$t' = 0, \quad \theta(\tau, 0) = \left\{ \begin{array}{l} 1 \\ \theta(\tau) \end{array} \right\}, \quad \tau \geq 0 \quad (G.5)$$

A solution of equation (G.2) may be obtained using the analysis described in Appendix D. In this case the polynomial approximations become:

$$\theta^4(\tau, t') = \sum_{i=1}^n C_i(\tau, t') \tau^{(i-1)} \quad (G.6)$$

and

$$D(\tau, t') = \sum_{i=1}^n d_i(\tau, t') \tau^{(i-1)} \quad (G.7)$$

Referring to Appendix D, the matrix equation was solved for d_i , $i=1 \dots n$ and a solution for $q'_r(\tau, t')$ obtained initially at $t' = 0$ subject to appropriate boundary conditions. Equation (G.2) may then be written in finite difference form, i.e.

$$\left[\frac{\theta_n^{p+1} - \theta_n^p}{\Delta t'} \right] = - \left[\frac{q'_{r\ n+1} - q'_{r\ n-1}}{2\Delta\tau} \right]^p \quad (G.8)$$

where n refers to the nodal spacial position and p refers to the nodal position of instantaneous time. A temperature profile may then be predicted for the next time increment from equation (G.8). At any instant of time the coefficients $C_i(\tau, t')$ are obtained by a least squares method.

The matrix equation is then resolved, the flux equation determined and the procedure repeated for a new time increment. In order to start the solution at the boundary $n = 1$, for each new time increment, the approximation $q'_{r\ n-1} \approx q'_{r\ n}$ was used and equation (G.8) becomes at $\tau = 0$, i.e. $n = 1$

$$\left[\frac{\theta_1^{p+1} - \theta_1^p}{\Delta t'} \right] = - \left[\frac{q'_{r\ 2} - q'_{r\ 1}}{\Delta\tau} \right]^p \quad (G.9)$$

APPENDIX H

A COMPUTER PROGRAM TO SOLVE THE STEADY STATE &
TRANSIENT RADIATIVE FLUX EQUATION

The following program solves the simultaneous equations (B.10) and (B.11) of Appendix B, initially for the steady state approximation. An extension is included to solve the transient energy equation (G.1) and, in finite difference form, equation (G.8) described in Appendix G. Simply the steady state solution of equations (B.10) and (B.11) with a described temperature distribution is given by the initial solution at time zero.

The important variables encountered in the program are described below.

(a) Input Variables

FL1 = θ_1^4 , the wall temperature to bed temperature ratio raised to the fourth power at boundary 1.

FL2 = θ_2^4 , the wall temperature to bed temperature ratio raised to the fourth power at boundary 2. In this analysis $\theta_2^4 = 1$.

WO is the scattering albedo

EW is the emissivity of boundary 1

EW2 is the emissivity of boundary 2

C(I), I = 1....m are the coefficients of the (m-1) degree polynomial describing the initial fourth power temperature distribution, i.e.

$$\theta^4(\tau) = \sum_{i=1}^m C_i \tau^{(i-1)}$$

(b) Output Variables

$D(I)$, $I = 1 \dots m$ are the coefficients of the $(m-1)$ degree polynomial describing the incident radiative flux, i.e.

$$D(\tau) = \sum_{i=1}^m d_i \tau^{(i-1)}$$

$Q(I)$, $I = 1 \dots n$ are the radiative flux levels at the corresponding spacial position across the field. $Y1(I,J)$, $I = 1 \dots n$, $J = m$ are the values of temperature across the field at position (I) and time (J). ML is a counter.

(c) Important Variables in the Main Body of the Program

$Z(I)$, $I = 1 \dots n$ designates spacial position across the field.

S13AAF is a NAG subroutine used to determine the first exponential integral, i.e. $E_1(x)$

DELX is the spacial step size

DELT is the temporal step size

LESQUT is a least squares curve fitting subroutine

DEES is a subroutine to determine the coefficients

$D(I)$, $I = 1 \dots m$

GAUSS is a subroutine called from subroutine LESQUT.

```

PROGRAM LEWN(INPUT,OUTPUT,TAPE1=INPUT,TAPE2=OUTPUT)
DIMENSION P(6,6),S1(8),U3(6,6),C(10)
DIMENSION U4(6,6),U5(6,6),U6(6,6)
DIMENSION QC(505),QT(505)
DIMENSION D(8),Q(505),Y1(505,3),Y(505),X(10,505),YE(505)
DIMENSION Z(505),ZZ(505),R(505),A(8,8),DD(8),U(505,6),S(505,6)
COMMON Y1
LEVEL 2,Y1
REAL J1,J2,J3,J4,J5
READ(1,*)FL1,FL2,W0,FW,FW2
READ(1,*)(C(I),I=1,5)
WRITE(2,22)FL1,FL2,W0,FW,FW2
22 FORMAT(5F12.4)
DELX=0.02
DFLT=0.0001
NX=1
BL1=FL1
BL2=FL2
N=501
ML=0
NN=N+1
Z(1)=0.0
DO 53 K=2,NN
53 Z(K)=Z(K-1)+0.02
DO 3 K=1,NN
X(1,K)=1.0
X(2,K)=Z(K)
DO 3 J=3,10
3 X(J,K)=X(J-1,K)*Z(K)
DO 56 I=1,NN
56 Y(I)=C(1)+(C(2)*Z(I))+(C(3)*Z(I)*Z(I))+(C(4)*Z(I)*Z(I)*Z(I))
1+(C(5)*(Z(I)**4))
39 CONTINUE
FL1=BL1
FL2=BL2
DO 55 I=5,5
L=N+1
CALL LESQUT (I,10,L,X,Y,C,YE,R,RR)
55 CONTINUE
DO 57 I=1,NN
57 Y(I)=C(1)+(C(2)*Z(I))+(C(3)*Z(I)*Z(I))+(C(4)*Z(I)*Z(I)*Z(I))
1+(C(5)*(Z(I)**4))
BD=Z(N)
E1A=S13AAF(BD,IFAIL)
E2A=(1.0/EXP(Z(N)))-(Z(N)*E1A)
E3A=(1.0/2.0)*((1.0/EXP(Z(N)))-(Z(N)*E2A))
E4A=(1.0/3.0)*((1.0/EXP(Z(N)))-(Z(N)*E3A))
E5A=(1.0/4.0)*((1.0/EXP(Z(N)))-(Z(N)*E4A))
E6A=(1.0/5.0)*((1.0/EXP(Z(N)))-(Z(N)*E5A))
E7A=(1.0/6.0)*((1.0/EXP(Z(N)))-(Z(N)*E6A))
H1=C(1)*(0.5-E3A)
J1= (0.5-E3A)
H2=C(2)*(0.333-E4A-(Z(N)*E3A))
J2= (0.333-E4A-(Z(N)*E3A))
H3=C(3)*(0.5-(2.0*E5A)-(2.0*Z(N)*E4A)-(Z(N)*Z(N)*E3A))
J3= (0.5-(2.0*E5A)-(2.0*Z(N)*E4A)-(Z(N)*Z(N)*E3A))
H4=C(4)*(1.2-(6.0*E6A)-(6.0*Z(N)*E5A)-(3.0*Z(N)*Z(N)*E4A)

```

```

1-( (Z(N)**5)*E3A))
J4= (1.2-(6.0*E6A)-(6.0*Z(N)*E5A)-(3.0*Z(N)*Z(N)*E4A)
1-( (Z(N)**5)*E3A))
H5=C(5)*(4.0-(24.0*E7A)-(24.0*Z(N)*E6A)-(12.0*Z(N)*Z(N)*E5A)
1-(4.0*(Z(N)**3)*E4A)-((Z(N)**4)*E3A))
J5= (4.0-(24.0*E7A)-(24.0*Z(N)*E6A)-(12.0*Z(N)*Z(N)*E5A)
1-(4.0*(Z(N)**3)*E4A)-((Z(N)**4)*E3A))
W1=C(1)*(0.5-E3A)
V1= (0.5-E3A)
W2=C(2)*((Z(N)*0.5)-0.333+E4A)
V2= ((Z(N)*0.5)-0.333+E4A)
W3=C(3)*((Z(N)*Z(N)*0.5)-(2.0*Z(N)*0.333)+0.5-(2.0*E5A))
V3= ((Z(N)*Z(N)*0.5)-(2.0*Z(N)*0.333)+0.5-(2.0*E5A))
W4=C(4)*(((Z(N)**3)*0.5)-(3.0*Z(N)*Z(N)*0.333)+(6.0*Z(N)*0.25)
1-(6.0*0.2)+(6.0*E6A))
V4= (((Z(N)**3)*0.5)-(3.0*Z(N)*Z(N)*0.333)+(6.0*Z(N)*0.25)
1-(6.0*0.2)+(6.0*E6A))
W5=C(5)*(((Z(N)**4)*0.5)-(4.0*(Z(N)**3)*0.3333)+(12.0*Z(N)*Z(N)
1)*0.25)-(24.0*Z(N)*0.2)+4.0-(24.0*E7A))
V5= (((Z(N)**4)*0.5)-(4.0*(Z(N)**3)*0.3333)+(12.0*Z(N)*Z(N)
1)*0.25)-(24.0*Z(N)*0.2)+4.0-(24.0*E7A))
FL1=(EW*BL1)+(2.0*(1.0-EW)*((BL2*EW2*E3A)+((1.0-WU)*(H1+H2+H3+H4
1+H5))))+(4.0*(1.0-EW)*(1.0-EW2)*E3A*(W1+W2+W3+W4+W5))
FL1=FL1/(1.0-(4.0*(1.0-EW)*(1.0-EW2)*E3A*E3A))
FL2=(BL2*EW2)+(2.0*(1.0-EW2)*BL1*EW*E3A)+(2.0*(1.0-EW2)*(1.0-WU)
1*(W1+W2+W3+W4+W5))+(4.0*(1.0-EW2)*(1.0-EW)*(1.0-WU)*E3A*(H1+H2+
2H3+H4+H5))
FL2=FL2/(1.0-(4.0*(1.0-EW)*(1.0-EW2)*E3A*E3A))
XZ=(1.0-(4.0*(1.0-EW)*(1.0-EW2)*E3A*E3A))
DO 58 I=1,5
U3(I,1)=(1.0-EW)*W0*0.5*J1/XZ
U3(I,2)=(1.0-EW)*W0*0.5*J2/XZ
U3(I,3)=(1.0-EW)*W0*0.5*J3/XZ
U3(I,4)=(1.0-EW)*W0*0.5*J4/XZ
U3(I,5)=(1.0-EW)*W0*0.5*J5/XZ
58 CONTINUE
DO 59 I=1,5
U4(I,1)=E3A*(1.0-EW)*(1.0-EW2)*W0*V1/XZ
U4(I,2)=E3A*(1.0-EW)*(1.0-EW2)*W0*V2/XZ
U4(I,3)=E3A*(1.0-EW)*(1.0-EW2)*W0*V3/XZ
U4(I,4)=E3A*(1.0-EW)*(1.0-EW2)*W0*V4/XZ
U4(I,5)=E3A*(1.0-EW)*(1.0-EW2)*W0*V5/XZ
59 CONTINUE
DO 60 I=1,5
U5(I,1)=(1.0-EW2)*(1.0-EW)*W0*E3A*J1/XZ
U5(I,2)=(1.0-EW2)*(1.0-EW)*W0*E3A*J2/XZ
U5(I,3)=(1.0-EW2)*(1.0-EW)*W0*E3A*J3/XZ
U5(I,4)=(1.0-EW2)*(1.0-EW)*W0*E3A*J4/XZ
U5(I,5)=(1.0-EW2)*(1.0-EW)*W0*E3A*J5/XZ
60 CONTINUE
DO 61 I=1,5
U6(I,1)=0.5*(1.0-EW2)*W0*V1/XZ
U6(I,2)=0.5*(1.0-EW2)*W0*V2/XZ
U6(I,3)=0.5*(1.0-EW2)*W0*V3/XZ
U6(I,4)=0.5*(1.0-EW2)*W0*V4/XZ
U6(I,5)=0.5*(1.0-EW2)*W0*V5/XZ
61 CONTINUE

```

```

D040 I=1,N
GG=Z(N)-Z(I)
IF(Z(I).EQ.0.0) GO TO 560
BF=Z(I)
F1A=S13AAF(BF,IFAIL)
E2A=(1.0/EXP(Z(I)))-(Z(I)*F1A)
GO TO 561
560 F2A=1.0
561 CONTINUE
IF(GG.EQ.0.0) GO TO 562
F1B=S13AAF(GG,IFAIL)
F2B=(1.0/EXP(GG))-(GG*F1B)
GO TO 563
562 F2B=1.0
563 CONTINUE
43 E3A=(1.0/2.0)*((1.0/EXP(Z(I)))-(Z(I)*F2A))
62 F3B=(1.0/2.0)*((1.0/EXP(GG))-(GG*E2B))
F4A=(1.0/3.0)*((1.0/EXP(Z(I)))-(Z(I)*E3A))
F4B=(1.0/3.0)*((1.0/EXP(GG))-(GG*E3B))
E5A=(1.0/4.0)*((1.0/EXP(Z(I)))-(Z(I)*E4A))
F5B=(1.0/4.0)*((1.0/EXP(GG))-(GG*E4B))
F6A=(1.0/5.0)*((1.0/EXP(Z(I)))-(Z(I)*E5A))
E6B=(1.0/5.0)*((1.0/EXP(GG))-(GG*E5B))
E7A=(1.0/6.0)*((1.0/EXP(Z(I)))-(Z(I)*E6A))
F7B=(1.0/6.0)*((1.0/EXP(GG))-(GG*E6B))
S(1,1)=(((2.0*E2A-E2B)*(2.0*(1.0-W0)))*C(1))+(2.0*FL1*E2A)+
1(2.0*FL2*E2B)
S(1,2)=(((2.0*Z(I))+E3A-(Z(N)*E2B)-E3B)*(2.0*(1.0-W0)))*C(2))
S(1,3)=(((2.0*Z(I)*Z(I))+1.333-(2.0*E4A)-(Z(N)*Z(N)*E2B)
1-(2.0*Z(N)*E3B)-(2.0*E4B))*(2.0*(1.0-W0)))*C(3))
S(1,4)=(((2.0*Z(I)*Z(I)*Z(I))+4.0*Z(I)+(6.0*E5A)-(6.0*E5B)-
1Z(N)*Z(N)*Z(N)*E2B)-(3.0*Z(N)*Z(N)*E3B)-(6.0*Z(N)*E4B))
2*(2.0*(1.0-W0)))*C(4))
S(1,5)=(((2.0*(Z(I)**4))+8.0*Z(I)*Z(I))+9.6-(24.0*E6A)-(4.0*
1(Z(N)**3)*F3B)-(Z(N)**4)*E2B)-(12.0*Z(N)*Z(N)*E4B)-(24.0*
2Z(N)*E5B)-(24.0*E6B))*(2.0*(1.0-W0)))*C(5))
U(1,1)=(2.0-E2A-E2B)*W0/2.0
U(1,2)=((2.0*Z(I))+F3A-(Z(N)*E2B)-E3B)*W0/2.0
U(1,3)=((2.0*Z(I)*Z(I))+1.333-(2.0*E4A)-(Z(N)*Z(N)*E2B)
1-(2.0*Z(N)*E3B)-(2.0*E4B))*W0/2.0
U(1,4)=((2.0*Z(I)*Z(I)*Z(I))+4.0*Z(I)+(6.0*E5A)-(6.0*E5B)-
1Z(N)*Z(N)*Z(N)*E2B)-(3.0*Z(N)*Z(N)*E3B)-(6.0*Z(N)*E4B))*W0/2.0
U(1,5)=((2.0*(Z(I)**4))+8.0*Z(I)*Z(I))+9.6-(24.0*E6A)-(4.0*
1(Z(N)**3)*E3B)-(Z(N)**4)*E2B)-(12.0*Z(N)*Z(N)*E4B)-(24.0*
2Z(N)*E5B)-(24.0*E6B))*W0/2.0
40 CONTINUE
Z(1)=0.0
D0 966 L=2,NN
966 Z(L)=Z(L-1)+0.02
D0 90 I=1,5
D0 90 J=2,5
P(1,1)=1.0
90 P(1,J)=0.0
D0 91 I=2,5
D0 91 J=2,5
I1=(125*I)-124
YW=Z(I1)

```

```

    YYY=YW***(J-1)
91 P(I,J)=YYY
    DO 92 I=2,5
    DO 92 J=1,5
92 U(I,J)=U(((125*I)-124),J)
    DO 94 I=1,5
    DO 94 J=1,5
94 A(I,J)=P(I,J)-U(I,J)-U3(I,J)-U4(I,J)-U5(I,J)-U6(I,J)
    DO 95 I=2,5
    DO 95 J=1,5
95 S(I,J)=S(((125*I)-124),J)
    DO 98 I=1,5
98 S1(I)=S(I,1)+S(I,2)+S(I,3)+S(I,4)+S(I,5)
    CALL DFES(S1,A,DD)
    DO 82 I=1,5
82 D(I)=DD(I)
    FL1=FL1+(D(1)*U3(1,1))+(D(2)*U3(1,2))+(D(3)*U3(1,3))+(D(4)*
1U3(1,4))+(D(5)*U3(1,5))+(D(1)*U4(1,1))+(D(2)*U4(1,2))+(D(3)*U4
2(1,3))+(D(4)*U4(1,4))+(D(5)*U4(1,5))
    FL2=FL2+(D(1)*U5(1,1))+(D(2)*U5(1,2))+(D(3)*U5(1,3))+(D(4)*
1U5(1,4))+(D(5)*U5(1,5))+(D(1)*U6(1,1))+(D(2)*U6(1,2))+(D(3)*U6
2(1,3))+(D(4)*U6(1,4))+(D(5)*U6(1,5))
    DO 133 I=1,N
    GG=Z(N)*Z(I)
    IF(Z(I).EQ.0.0)GO TO 565
    BF=Z(I)
    E1A=S13AAF(BF,IFAIL)
    E2A=(1.0/EXP(Z(I)))-(Z(I)*E1A)
    GO TO 566
565 E2A=1.0
566 CONTINUE
    IF(GG.EQ.0.0) GO TO 567
    E1B=S13AAF(GG,IFAIL)
    E2B=(1.0/EXP(GG))-(GG*E1B)
    GO TO 568
567 E2B=1.0
568 CONTINUE
    F3A=(1.0/2.0)*((1.0/EXP(Z(I)))-(Z(I)*E2A))
    E3B=(1.0/2.0)*((1.0/EXP(GG))-(GG*E2B))
    F4A=(1.0/3.0)*((1.0/EXP(Z(I)))-(Z(I)*E3A))
    F4B=(1.0/3.0)*((1.0/EXP(GG))-(GG*E3B))
    E5A=(1.0/4.0)*((1.0/EXP(Z(I)))-(Z(I)*E4A))
    E5B=(1.0/4.0)*((1.0/EXP(GG))-(GG*E4B))
    E6A=(1.0/5.0)*((1.0/EXP(Z(I)))-(Z(I)*E5A))
    E6B=(1.0/5.0)*((1.0/EXP(GG))-(GG*E5B))
    E7A=(1.0/6.0)*((1.0/EXP(Z(I)))-(Z(I)*E6A))
    E7B=(1.0/6.0)*((1.0/EXP(GG))-(GG*E6B))
    F1=C(1)*(E3B-E3A)
    G1=D(1)*(E3B-E3A)
    F2=C(2)*(E4A-0.666+(Z(N)*E3B)+F4B)
    G2=D(2)*(E4A-0.666+(Z(N)*E3B)+F4B)
    F3=C(3)*((2.0*E5B)+(2.0*Z(N)*E4B)+(Z(N)*Z(N)*E3B)-(2.0*E5A)
1-(1.333*Z(I)))
    G3=D(3)*((2.0*E5B)+(2.0*Z(N)*E4B)+(Z(N)*Z(N)*E3B)-(2.0*E5A)
1-(1.333*Z(I)))
    F4=C(4)*((6.0*E6B)+(6.0*Z(N)*E5B)+(3.0*Z(N)*Z(N)*E4B)+((Z(N)
1**3)*E3B)+(6.0*E6A)-2.4-(2.0*Z(I)*Z(I)))

```

```

G4=D(4)*((6.0*F6B)+(6.0*Z(N)*F5B)+(3.0*Z(N)*Z(N)*E4B)+((Z(N)
1**5)*E3B)+(6.0*E6A)-2.4-(2.0*Z(I)*Z(I)))
F5=C(5)*((24.0*E7B)+(24.0*Z(N)*E6B)+(12.0*Z(N)*Z(N)*F5B)+
1(4.0*(Z(N)**3)*E4B)+((Z(N)**4)*E3B)-(24.0*E7A)-(9.6*Z(I))-(2.66
2*(Z(I)**3)))
G5=D(5)*((24.0*E7B)+(24.0*Z(N)*E6B)+(12.0*Z(N)*Z(N)*E5B)+
1(4.0*(Z(N)**3)*E4B)+((Z(N)**4)*E3B)-(24.0*E7A)-(9.6*Z(I))-(2.66
2*(Z(I)**3)))
133 Q(I)=(2.0*FL1*F3A)-(2.0*FL2*F3B)+(2.0*(1.0-W0)*(F1+F2+F3+F4+F5))
1+((W0/2.0)*(G1+G2+G3+G4+G5))
Q(NN)=Q(NN-2)
MM=2
DO 75 I=1,NN
DO 75 J=MM,MM
75 Y1(I,J-1)=SQRT(SQRT(Y(I)))
DO 70 I=2,N
DO 70 J=MM,MM
Y1(I,J)=Y1(I,J-1)-((Q(2)-Q(1))*DELX/DELX)
70 Y1(I,J)=Y1(I,J-1)-((DELX/DELX)*(Q(I+1)-Q(I-1))/2.0)
Y1(NN,MM)=1.0
DO 71 J=MM,MM
DO 71 I=1,NN
71 Y(I)=Y1(I,J)**4
IF(ML,EQ.0)GOTO 800
NX=NX+1
IF(NX,EQ.10)GOTO 800
GOTO 801
800 CONTINUE
NX=0
WRITE(2,4) (D(I),I=1,5)
4 FORMAT(5E12.4)
WRITE(2,608) (C(I),I=1,5)
608 FORMAT(5F12.4)
WRITE(2,501)ML
501 FORMAT(I5)
WRITE(2,110) (Q(I),I=1,N,50)
110 FORMAT(8E12.4)
74 WRITE(2,6) ((Y1(I,J),J=MM,MM),I=1,N,50)
6 FORMAT((4E20.8))
801 CONTINUE
DO 86 I=1,NN
86 Y1(I,1)=Y1(I,2)
IF(ML,EQ.1005)GOTO 20
ML=ML+1
GOTO 39
20 STOP
END

```

- + -

```
SUBROUTINE GAUSS(M,AA,BB,X)
DIMENSION A(20),AA(20),B(20,20),BB(20,M),X(M)
DO 5 J=1,M
X(J)=0
A(J)=AA(J)
DO 5 K=1,M
5 B(J,K)=BB(J,K)
IF(M.EQ,1)GOTO 20
MY=M-1
DO 10 L=1,MY
LL=M+1-L
MX=M-L
DO 10 J=1,MX
RB=B(J,LL)/B(LL,LL)
A(J)=A(J)-A(LL)*RB
DO 10 K=1,MX
10 B(J,K)=B(J,K)-B(LL,K)*RB
20 DO 40 K=1,M
XB=0
DO 30 J=1,K
30 XB=XB+X(J)*B(K,J)
40 X(K)=(A(K)-XB)/B(K,K)
RETURN
END
```

```
SUBROUTINE LFSQUT (M,MF,N,X,Y,C,YE,R,RR) .  
DIMENSION A(20),B(20,20),X(MF,N),Y(N),C(MF),YE(N),R(N)  
DATA M1/20/  
IF(M.GT,M1)GOTO15.  
M1=M  
DO 5 J=1,MF  
A(J)=0  
DO 5 K=1,MF  
5 B(J,K)=0  
DO 10 I=1,N  
DO 10 J=1,MF  
A(J)=A(J)+X(J,I)*Y(I)  
DO 10 K=1,MF  
10 B(J,K)=B(J,K)+X(J,I)*X(K,I)  
15 CALL GAUSS(M,A,B,C)  
RR=0  
DO 30 I=1,N  
YE(I)=0  
DO 20 J=1,M  
20 YE(I)=YE(I)+C(J)*X(J,I)  
R(I)=Y(I)-YE(I)  
30 RR=RR+R(I)*R(I)  
RETURN  
END
```

```

SURROUTINE DFFS(S1,A,DD)
DIMENSION YY(8),DD(8),L(8,8),U1(8,8),S1(8),A(8,8)
DO 100 I=1,5
DO 100 J=1,5
100 L(I,J)=0.0
DO 101 I=1,5
DO 101 J=1,5
101 U1(I,J)=0.0
L(1,1)=1.0
L(2,2)=1.0
L(3,3)=1.0
L(4,4)=1.0
L(5,5)=1.0
DO 103 I=1,1
DO 103 J=1,5
103 U1(I,J)=A(I,J)
L(2,1)=A(2,1)/U1(1,1)
DO 104 I=2,2
DO 104 J=2,5
104 U1(I,J)=A(I,J)-(L(2,1)*U1(I-1,J))
L(3,1)=A(3,1)/U1(1,1)
L(3,2)=(A(3,2)-(L(3,1)*U1(1,2)))/U1(2,2)
DO 105 I=3,3
DO 105 J=3,5
105 U1(I,J)=A(I,J)-(L(3,1)*U1(I-2,J))-(L(3,2)*U1(I-1,J))
L(4,1)=A(4,1)/U1(1,1)
L(4,2)=(A(4,2)-(L(4,1)*U1(1,2)))/U1(2,2)
L(4,3)=(A(4,3)-(L(4,1)*U1(1,3))-(L(4,2)*U1(2,3)))/U1(3,3)
DO 106 I=4,4
DO 106 J=4,5
106 U1(I,J)=A(I,J)-(L(4,1)*U1(I-3,J))-(L(4,2)*U1(I-2,J))-(L(4,3)*U1
(I-1,J))
L(5,1)=A(5,1)/U1(1,1)
L(5,2)=(A(5,2)-(L(5,1)*U1(1,2)))/U1(2,2)
L(5,3)=(A(5,3)-(L(5,1)*U1(1,3))-(L(5,2)*U1(2,3)))/U1(3,3)
L(5,4)=(A(5,4)-(L(5,1)*U1(1,4))-(L(5,2)*U1(2,4))-(L(5,3)*U1
(3,4)))/U1(4,4)
DO 107 I=5,5
DO 107 J=5,5
107 U1(I,J)=A(I,J)-(L(5,1)*U1(I-4,J))-(L(5,2)*U1(I-3,J))-(L(5,3)*
U1(I-2,J))-(L(5,4)*U1(I-1,J))
YY(1)=S1(1)
YY(2)=S1(2)-(L(2,1)*YY(1))
YY(3)=S1(3)-(L(3,1)*YY(1))-(L(3,2)*YY(2))
YY(4)=S1(4)-(L(4,1)*YY(1))-(L(4,2)*YY(2))-(L(4,3)*YY(3))
YY(5)=S1(5)-(L(5,1)*YY(1))-(L(5,2)*YY(2))-(L(5,3)*YY(3))-(L
(5,4)*YY(4))
DD(5)=YY(5)/U1(5,5)
DD(4)=(YY(4)-(U1(4,5)*DD(5)))/U1(4,4)
DD(3)=(YY(3)-(U1(3,5)*DD(5))-(U1(3,4)*DD(4)))/U1(3,3)
DD(2)=(YY(2)-(U1(2,5)*DD(5))-(U1(2,4)*DD(4))-(U1(2,3)*DD(3))
1/U1(2,2)
DD(1)=(YY(1)-(U1(1,5)*DD(5))-(U1(1,4)*DD(4))-(U1(1,3)*DD(3))
1-(U1(1,2)*DD(2)))/U1(1,1)
RETURN
END

```

FINISH

APPENDIX I

UNSTEADY COMBINED CONDUCTION AND RADIATION HEAT TRANSFER

The energy equation for a one-dimensional plane layer of an absorbing, emitting and scattering medium in which conduction heat transfer is included may be simply described by Figure B.1 and written

$$\frac{\partial}{\partial x} \left[K(x) \frac{\partial T}{\partial x} \right] - \frac{\partial q_r(x)}{\partial x} = \rho(x) C_p(x) \frac{\partial T}{\partial t} \quad (I.1)$$

The solution of equation (I.1) is complicated by the term $q_r(x)$ adding another degree of freedom to the integro-differential equation of radiative flux. Hence this study considers the equation (I.1) with constant properties. Equation (I.1) becomes

$$K_b \frac{\partial^2 T}{\partial x^2} - \frac{\partial q_r}{\partial x} = (\rho C_p)_p \frac{\partial T}{\partial t} \quad (I.2)$$

using the transform $d\tau = K_t dx$ and the non-dimensional groups

$$\theta = \frac{T}{T_b}, \quad N_1 = \frac{K_t K_b}{4\sigma T_b^3}$$

$$t' = \frac{K_t^2 K_b t}{(\rho C_p)_p}$$

and for an emulsion $(\rho C_p)_p = \rho_p C_p (1 - \epsilon_b)$ equation (I.2) becomes

$$\frac{\partial \theta^2}{\partial \tau^2} - \frac{1}{4N_1} \frac{\partial q_r'}{\partial \tau} = \frac{\partial \theta}{\partial t'} \quad (I.3)$$

For two adjacent regions x and y then we have

$$\frac{\partial^2 \theta}{\partial \tau^2} \Big|_x - \frac{1}{4N_1} \Big|_x \frac{\partial q'_r}{\partial \tau} \Big|_x = \frac{\partial \theta}{\partial t'} \Big|_x \quad (I.4)$$

and

$$\frac{\partial^2 \theta}{\partial \tau^2} \Big|_y - \frac{1}{4N_1} \Big|_y \frac{\partial q'_r}{\partial \tau} \Big|_y = \frac{\partial \theta}{\partial t'} \Big|_y \quad (I.5)$$

which may be solved simultaneously for an equivalent absolute time t, through the relationship

$$t'_x = \frac{K^2_{tx} K_{bx}}{(\rho C_p)_x} \cdot \frac{(\rho C_p)_y t'_y}{K^2_{ty} K_{by}} \quad (I.6)$$

In finite difference form equations (I.4) and (I.5) become

$$\begin{aligned} \frac{(\theta_n^{p+1} - \theta_n^p)}{\Delta t'} \Big|_{x,y} &= \frac{(\theta_{n+1} - 2\theta_n + \theta_{n-1})^p}{\Delta \tau^2} \Big|_{x,y} \\ &- \frac{1}{4N_1} \frac{(q'_{r,n+1} - q'_{r,n-1})^p}{2\Delta \tau} \Big|_{x,y} \end{aligned} \quad (I.7)$$

subject to initial and boundary conditions

$$t' = 0, \quad \theta(\tau, 0) = \begin{Bmatrix} 1 \\ \theta(\tau) \end{Bmatrix}, \quad \tau \geq 0 \quad (I.8)$$

$$\tau = 0, \quad \theta(0, t') = \theta_1, \quad t' \geq 0 \quad (I.9)$$

$$\tau = \tau_0, \quad \theta(\tau_0, t') = 1, \quad t' \geq 0 \quad (I.10)$$

The method of solution is essentially as described in Appendix G and Appendix D. For an optically thin medium the first derivative of equation (B.10) of Appendix B with respect to τ , becomes with $\tau = \tau_0 \ll 1$

$$-\frac{\partial q_r'}{\partial \tau} = 2(1 - \omega_0)[F_1 + F_2 - 2\theta^4(\tau, t')] \quad (I.11)$$

where F_1 and F_2 are the non-dimensional boundary fluxes, i.e. $F_1 = F_w$ and $F_2 = F_e$ (at the emulsion boundary). Hence equation (I.3) becomes with equation (I.11)

$$\frac{\partial^2 \theta}{\partial \tau^2} + \frac{(1 - \omega_0)}{2N_1} [F_w + F_e - 2\theta^4(\tau, t')] = \frac{\partial \theta}{\partial t'} \quad (I.12)$$

and for the gas layer

$$\tau = \tau_{og} \ll 1, \quad \theta^4(0, t') = \theta_w^4$$

and

$$\theta^4(\tau_{og}, t') = \theta_e^4 \quad (\text{the surface temperature of the emulsion})$$

and (I.12) in finite difference form becomes with $n = 1$ (at the emulsion boundary adjacent to the gas layer)

$$\frac{(\theta_1^{P+1} - \theta_1^P)}{\Delta t'} = \frac{(\theta_2 - 2\theta_1 + \theta_w)^P}{\Delta \tau^2} + \frac{(1 - \omega_0)}{2N_1 g} (F_w + F_e - 2\theta_1^4)^P \quad (I.13)$$

with the conductive flux

$$q_c^1 = -4N_1 \left. \frac{\partial \theta}{\partial \tau} \right|_{x,y}$$

and in finite difference form

$$q_c' = -4N_1 \frac{(\theta_{n+1} - \theta_{n-1})^p}{2 \Delta \tau} \Big|_{g,b} \quad (I.14)$$

APPENDIX J

A COMPUTER PROGRAM TO SOLVE THE TRANSIENT COMBINED
CONDUCTION AND RADIATION ENERGY EQUATION

The important variables are as described in Appendix H along with the following additions.

(a) Input Variables (SI units where appropriate)

- RHOP is the density of the particulate material
CP is the specific heat capacity of the particulate material
RHOG is the density of the fluidizing gas
CPG is the specific heat capacity of the fluidizing gas
XB is the depth of the boundary gas film layer in particle diameters
KG is the thermal conductivity of the fluidizing gas
EB is the bed voidage
DP is the particle diameter
KT is the extinction coefficient of the emulsion
KB is the effective thermal conductivity of the emulsion
TB is the bed temperature
TW is the non-dimensional wall temperature
BB is an averaging constant, i.e. taken as 2.0

(b) Output Variables

- QC(I) I = 1....n is the conductive flux across the field
QT(I) I = 1....n is the sum of the conductive and radiative fluxes across the field
HR is the radiative heat transfer coefficient

HC is the conductive heat transfer coefficient

HT = HR + HC

PERC = HR/HT

COND is the conductive flux kW/m²

RAD is the radiative flux kW/m²

FLUXT = (COND + RAD) kW/m²

N1 is the conduction/radiation number associated with the
emulsion

N2 is the conduction/radiation number association with
the gas layer

KTG is the extinction coefficient of the gas layer

DELT1 is the non-dimensional time associated with N2

```
PROGRAM IEWN(INPUT,OUTPUT,TAPE1=INPUT,TAPE2=OUTPUT)
DIMENSION P(6,6),S1(8),U5(6,6),C(10)
DIMENSION U4(6,6),U5(6,6),U6(6,6)
DIMENSION QC(505),QT(505)
DIMENSION D(8),Q(505),Y1(505,3),Y(505),X(10,505),YE(505)
DIMENSION Z(505),ZZ(505),R(505),A(8,8),DD(8),U(505,6),S(505,6)
COMMON Y1
LEVEL 2,Y1
REAL N2
REAL N1,KT,KB
REAL KG,KS
REAL KTG
REAL J1,J2,J3,J4,J5
READ(1,*)FL1,FL2,W0,EW,EW2,RHOP,CP,RHOG
READ(1,*)CPG,XB,KG,EB,DP,KT,KB,TB,TW
READ(1,*)(C(I),I=1,5),BB
WRITE(2,320)FL1,FL2,W0,EW,EW2,RHOP,CP,RHOG,BB
320 FORMAT(9E12,4)
WRITE(2,325)CPG,XB,KG,EB,DP,KT,KB,TB,TW
325 FORMAT(9E12,4)
SIGMA=56.7E-12
N1=(KT*KB)/(4.0*SIGMA*(TB**3))
DELT=0.02
KTG=DELT/(DP*XB)
KG=(KG+KB)/BB
N2=(KTG*KG)/(4.0*SIGMA*(TB**3))
DELT=((RHOG*CPG)+(RHOP*CP*(1.0-EB))/BB)*KT*KT*KB/
1 (RHOP*CP*(1.0-EB)*KG*KTG*KTG)
DELT1=0.0001/DELT
DELT=0.0001
WRITE(2,702)DELT1,DELT,KTG,N1,N2
702 FORMAT(5E12,4)
IF(DELT1.GT.0.002)GOTO20
CONTINUE
NX=1
BL1=FL1
BL2=FL2
N=501
ML=0
NN=N+1
Z(1)=0.0
DO 53 K=2,NN
53 Z(K)=Z(K-1)+0.02
DO 3 K=1,NN
X(1,K)=1.0
X(2,K)=Z(K)
DO3 J=3,10
3 X(J,K)=X(J-1,K)*Z(K)
DO 56 I=1,NN
56 Y(I)=C(1)+(C(2)*Z(I))+(C(3)*Z(I)*Z(I))+(C(4)*Z(I)*Z(I)*Z(I))
1+(C(5)*(Z(I)**4))
39 CONTINUE
FL1=BL1
FL2=BL2
DO55 I=5,5
L=N+1
CALL LESQUT (1,10,L,X,Y,C,YE,R,RR)
```

```

55 CONTINUE
DO 57 I=1,NN
57 Y(I)=C(1)+(C(2)*Z(I))+(C(3)*Z(I)*Z(I))+(C(4)*Z(I)*Z(I)*Z(I))
1+(C(5)*(Z(I)**4))
HD=Z(N)
E1A=S13AA+(BD,1FAIL)
E2A=(1.0/EXP(Z(N)))-(Z(N)*E1A)
E3A=(1.0/2.0)*((1.0/EXP(Z(N)))-(Z(N)*E2A))
E4A=(1.0/3.0)*((1.0/EXP(Z(N)))-(Z(N)*E3A))
E5A=(1.0/4.0)*((1.0/EXP(Z(N)))-(Z(N)*E4A))
E6A=(1.0/5.0)*((1.0/EXP(Z(N)))-(Z(N)*E5A))
E7A=(1.0/6.0)*((1.0/EXP(Z(N)))-(Z(N)*E6A))
H1=C(1)*(0.5-E3A)
J1=(0.5-E3A)
H2=C(2)*(0.333-E4A-(Z(N)*E3A))
J2=(0.333-E4A-(Z(N)*E3A))
H3=C(3)*(0.5-(2.0*E5A)-(2.0*Z(N)*E4A)-(Z(N)*Z(N)*E3A))
J3=(0.5-(2.0*E5A)-(2.0*Z(N)*E4A)-(Z(N)*Z(N)*E3A))
H4=C(4)*(1.2-(6.0*E6A)-(6.0*Z(N)*E5A)-(3.0*Z(N)*Z(N)*E4A)
1-((Z(N)**3)*E3A))
J4=(1.2-(6.0*E6A)-(6.0*Z(N)*E5A)-(3.0*Z(N)*Z(N)*E4A)
1-((Z(N)**3)*E3A))
H5=C(5)*(4.0-(24.0*E7A)-(24.0*Z(N)*E6A)-(12.0*Z(N)*Z(N)*E5A)
1-(4.0*(Z(N)**3)*E4A)-((Z(N)**4)*E3A))
J5=(4.0-(24.0*E7A)-(24.0*Z(N)*E6A)-(12.0*Z(N)*Z(N)*E5A)
1-(4.0*(Z(N)**3)*E4A)-((Z(N)**4)*E3A))
W1=C(1)*(0.5-E3A)
V1=(0.5-E3A)
W2=C(2)*((Z(N)*0.5)-0.333+E4A)
V2=((Z(N)*0.5)-0.333+E4A)
W3=C(3)*((Z(N)*Z(N)*0.5)-(2.0*Z(N)*0.333)+0.5-(2.0*E5A))
V3=((Z(N)*Z(N)*0.5)-(2.0*Z(N)*0.333)+0.5-(2.0*E5A))
W4=C(4)*(((Z(N)**3)*0.5)-(3.0*Z(N)*Z(N)*0.333)+(6.0*Z(N)*0.25)
1-(6.0*0.2)+(6.0*E6A))
V4=((Z(N)**3)*0.5)-(3.0*Z(N)*Z(N)*0.333)+(6.0*Z(N)*0.25)
1-(6.0*0.2)+(6.0*E6A))
W5=C(5)*(((Z(N)**4)*0.5)-(4.0*(Z(N)**3)*0.3333)+(12.0*Z(N)*Z(N)
1*0.25)-(24.0*Z(N)*0.2)+4.0-(24.0*E7A))
V5=((Z(N)**4)*0.5)-(4.0*(Z(N)**3)*0.3333)+(12.0*Z(N)*Z(N)
1*0.25)-(24.0*Z(N)*0.2)+4.0-(24.0*E7A))
FL1=(EW*BL1)+(2.0*(1.0-EW)*((BL2*EW2*E3A)+((1.0-W0)*(H1+H2+H3+H4
1+H5))))+(4.0*(1.0-FW)*(1.0-EW2)*(1.0-W0)*E3A*(W1+W2+W3+W4+W5))
FL1=FL1/(1.0-(4.0*(1.0-EW)*(1.0-EW2)*E3A*E3A))
FL2=(BL2*EW2)+(2.0*(1.0-EW)*BL1*EW*E3A)+(2.0*(1.0-EW2)*(1.0-W0)
1*(W1+W2+W3+W4+W5))+(4.0*(1.0-EW2)*(1.0-EW)*(1.0-W0)*E3A*(H1+H2+
2H3+H4+H5))
FL2=FL2/(1.0-(4.0*(1.0-EW)*(1.0-EW2)*E3A*E3A))
XZ=(1.0-(4.0*(1.0-EW)*(1.0-EW2)*E3A*E3A))
DO 58 I=1,5
U3(I,1)=(1.0-EW)*W0*0.5*J1/XZ
U3(I,2)=(1.0-EW)*W0*0.5*J2/XZ
U3(I,3)=(1.0-EW)*W0*0.5*J3/XZ
U3(I,4)=(1.0-EW)*W0*0.5*J4/XZ
U3(I,5)=(1.0-EW)*W0*0.5*J5/XZ
58 CONTINUE
DO 59 I=1,5
U4(I,1)=E3A*(1.0-EW)*(1.0-EW2)*W0*V1/XZ

```

```

U4(I,2)=F3A*(1.0-EW)*(1.0-EW2)*W0*V2/XZ
U4(I,3)=F3A*(1.0-EW)*(1.0-EW2)*W0*V3/XZ
U4(I,4)=F3A*(1.0-EW)*(1.0-EW2)*W0*V4/XZ
U4(I,5)=E3A*(1.0-EW)*(1.0-EW2)*W0*V5/XZ
59 CONTINUE
DO 60 I=1,5
U5(I,1)=(1.0-EW2)*(1.0-EW)*W0*F3A*J1/XZ
U5(I,2)=(1.0-EW2)*(1.0-EW)*W0*E3A*J2/XZ
U5(I,3)=(1.0-EW2)*(1.0-EW)*W0*F3A*J3/XZ
U5(I,4)=(1.0-EW2)*(1.0-EW)*W0*F3A*J4/XZ
U5(I,5)=(1.0-EW2)*(1.0-EW)*W0*E3A*J5/XZ
60 CONTINUE
DO 61 I=1,5
U6(I,1)=0.5*(1.0-EW2)*W0*V1/XZ
U6(I,2)=0.5*(1.0-EW2)*W0*V2/XZ
U6(I,3)=0.5*(1.0-EW2)*W0*V3/XZ
U6(I,4)=0.5*(1.0-EW2)*W0*V4/XZ
U6(I,5)=0.5*(1.0-EW2)*W0*V5/XZ
61 CONTINUE
D040 I=1,N
GG=Z(N)-Z(I)
IF(Z(I).EQ.0.0) GO TO 560
BE=Z(I)
E1A=S13AAF(BE,IFAIL)
E2A=(1.0/EXP(Z(I)))-(Z(I)*E1A)
GO TO 561
560 E2A=1.0
561 CONTINUE
IF(GG.EQ.0.0) GO TO 562
E1B=S13AAF(GG,IFAIL)
E2B=(1.0/EXP(GG))-(GG*E1B)
GO TO 563
562 E2B=1.0
563 CONTINUE
43 F3A=(1.0/2.0)*((1.0/EXP(Z(I)))-(Z(I)*E2A))
62 E3B=(1.0/2.0)*((1.0/EXP(GG))-(GG*E2B))
E4A=(1.0/3.0)*((1.0/EXP(Z(I)))-(Z(I)*E3A))
E4B=(1.0/3.0)*((1.0/EXP(GG))-(GG*E3B))
E5A=(1.0/4.0)*((1.0/EXP(Z(I)))-(Z(I)*E4A))
E5B=(1.0/4.0)*((1.0/EXP(GG))-(GG*E4B))
E6A=(1.0/5.0)*((1.0/EXP(Z(I)))-(Z(I)*E5A))
E6B=(1.0/5.0)*((1.0/EXP(GG))-(GG*E5B))
E7A=(1.0/6.0)*((1.0/EXP(Z(I)))-(Z(I)*E6A))
E7B=(1.0/6.0)*((1.0/EXP(GG))-(GG*E6B))
S(I,1)=(((2.0-E2A-E2B)*(2.0*(1.0-W0)))*C(1))+(2.0*FL1*E2A)+
1(2.0*FL2*E2B)
S(I,2)=(((2.0*Z(I))+E3A-(Z(N)*E2B)-E3B)*(2.0*(1.0-W0)))*C(2))
S(I,3)=(((2.0*Z(I)*Z(I))+1.333-(2.0*E4A)-(Z(N)*Z(N)*E2B)
1-(2.0*Z(N)*E3B)-(2.0*E4B))*(2.0*(1.0-W0)))*C(3))
S(I,4)=(((2.0*Z(I)*Z(I)*Z(I))+(4.0*Z(I))+(6.0*E5A)-(6.0*E5B)-
12(Z(N)*Z(N)*Z(N)*E2B)-(3.0*Z(N)*Z(N)*E3B)-(6.0*Z(N)*E4B))
2*(2.0*(1.0-W0)))*C(4))
S(I,5)=(((2.0*(Z(I)**4))+(8.0*Z(I)*Z(I))+9.6-(24.0*E6A)-(4.0*
1(Z(N)**3)*E3B)-(Z(N)**4)*E2B)-(12.0*Z(N)*Z(N)*E4B)-(24.0*
2Z(N)*E5B)-(24.0*E6B))*(2.0*(1.0-W0)))*C(5))
U(I,1)=(2.0-E2A-E2B)*W0/2.0
U(I,2)=((2.0*Z(I))+E3A-(Z(N)*E2B)-E3B)*W0/2.0

```

```
U(1,5) = ((2.0*Z(1)*Z(1))+1.333-(2.0*F4A)-(Z(N)*Z(N)*E2B)
1-(2.0*Z(N)*E3B)-(2.0*F4B)) *W0/2.0
U(1,4) = ((2.0*Z(1)*Z(1)*Z(1))+4.0*Z(1))+6.0*F5A)-(6.0*E5B)-(
1Z(N)*Z(N)*Z(N)*E2B)-(3.0*Z(N)*Z(N)*E3B)-(6.0*Z(N)*E4B)) *W0/2.0
U(1,5) = ((2.0*(Z(1)**4))+8.0*Z(1)*Z(1))+9.6-(24.0*E6A)-(4.0*
1(Z(N)**3)*F3B) -((Z(N)**4)*E2B)-(12.0*Z(N)*Z(N)*E4B)-(24.0*
2Z(N)*F5B) -(24.0*E6B)) *W0/2.0
40 CONTINUE
Z(1)=0.0
DO 966 L=2,NN
966 Z(L)=Z(L-1)+0.02
DO 90 I=1,5
DO 96 J=2,5
P(1,1)=1.0
90 P(1,J)=0.0
DO 91 I=2,5
DO 91 J=2,5
I1=(125*I)-124
YW=Z(I1)
YYY=YW**(J-1)
91 P(I,J)=YYY
DO 92 I=2,5
DO 92 J=1,5
92 U(I,J)=U(((125*I)-124),J)
DO 94 I=1,5
DO 94 J=1,5
94 A(I,J)=P(I,J)-U(I,J)-U3(I,J)-U4(I,J)-U5(I,J)-U6(I,J)
DO 95 I=2,5
DO 95 J=1,5
95 S(I,J)=S(((125*I)-124),J)
DO 98 I=1,5
98 S1(I)=S(I,1)+S(I,2)+S(I,3)+S(I,4)+S(I,5)
CALL DEES(S1,A,DD)
DO 82 I=1,5
82 D(I)=DD(I)
FL1=FL1+(D(1)*U3(1,1))+D(2)*U3(1,2))+D(3)*U3(1,3))+D(4)*
1U3(1,4))+D(5)*U3(1,5))+D(1)*U4(1,1))+D(2)*U4(1,2))+D(3)*U4
2(1,3))+D(4)*U4(1,4))+D(5)*U4(1,5))
FL2=FL2+(D(1)*U5(1,1))+D(2)*U5(1,2))+D(3)*U5(1,3))+D(4)*
1U5(1,4))+D(5)*U5(1,5))+D(1)*U6(1,1))+D(2)*U6(1,2))+D(3)*U6
2(1,3))+D(4)*U6(1,4))+D(5)*U6(1,5))
DO 133 I=1,N
GG=Z(N)-Z(I)
IF(Z(I).EQ.0.0)GO TO 565
BF=Z(I)
E1A=S13AAF(BF,IFAIL)
E2A=(1.0/EXP(Z(I)))-(Z(I)*E1A)
GO TO 566
565 E2A=1.0
566 CONTINUE
IF(GG.EQ.0.0) GO TO 567
E1B=S13AAF(GG,IFAIL)
E2B=(1.0/EXP(GG))-(GG*E1B)
GO TO 568
567 E2B=1.0
568 CONTINUE
E3A=(1.0/2.0)*((1.0/EXP(Z(I)))-(Z(I)*E2A))
```

E3B=(1.0/2.0)*((1.0/EXP(GG))-(GG*E2B))
 E4A=(1.0/3.0)*((1.0/EXP(Z(1)))-(Z(1)*E3A))
 E4B=(1.0/3.0)*((1.0/EXP(GG))-(GG*E3B))
 E5A=(1.0/4.0)*((1.0/EXP(Z(1)))-(Z(1)*E4A))
 E5B=(1.0/4.0)*((1.0/EXP(GG))-(GG*E4B))
 E6A=(1.0/5.0)*((1.0/EXP(Z(1)))-(Z(1)*E5A))
 E6B=(1.0/5.0)*((1.0/EXP(GG))-(GG*E5B))
 E7A=(1.0/6.0)*((1.0/EXP(Z(1)))-(Z(1)*E6A))
 E7B=(1.0/6.0)*((1.0/EXP(GG))-(GG*E6B))

F1=C(1)*(E3B-F3A)

G1=D(1)*(E3B-F3A)

F2=C(2)*(E4A-0.666+(Z(N)*E3B)+F4B)

G2=D(2)*(E4A-0.666+(Z(N)*F3B)+F4B)

F3=C(3)*((2.0*E5B)+(2.0*Z(N)*E4B)+(Z(N)*Z(N)*E3B)-(2.0*E5A)

1-(1.333*Z(1)))

G3=D(3)*((2.0*E5B)+(2.0*Z(N)*E4B)+(Z(N)*Z(N)*F3B)-(2.0*E5A)

1-(1.333*Z(1)))

F4=C(4)*((6.0*E6B)+(6.0*Z(N)*E5B)+(3.0*Z(N)*Z(N)*E4B)+((Z(N)

1**3)*E3B)+(6.0*E6A)-2.4-(2.0*Z(1)*Z(1)))

G4=D(4)*((6.0*E6B)+(6.0*Z(N)*E5B)+(3.0*Z(N)*Z(N)*E4B)+((Z(N)

1**3)*E3B)+(6.0*E6A)-2.4-(2.0*Z(1)*Z(1)))

F5=C(5)*((24.0*E7B)+(24.0*Z(N)*E6B)+(12.0*Z(N)*Z(N)*E5B)+

1(4.0*(Z(N)**3)*E4B)+((Z(N)**4)*E3B)-(24.0*F7A)-(9.6*Z(1))-(2.66

2*(Z(1)**3)))

G5=D(5)*((24.0*E7B)+(24.0*Z(N)*E6B)+(12.0*Z(N)*Z(N)*E5B)+

1(4.0*(Z(N)**3)*E4B)+((Z(N)**4)*E3B)-(24.0*F7A)-(9.6*Z(1))-(2.66

2*(Z(1)**3)))

133 Q(I)=(2.0*FL1*E3A)-(2.0*FL2*E3B)+(2.0*(1.0-W0)*(F1+F2+F3+F4+F5))

1+((W0/2.0)*(G1+G2+G3+G4+G5))

Q(NN)=Q(NN-2)

MM=2

DO 75 I=1,NN

DU 75 J=MM,MM

75 Y1(I,J-1)=SQRT(SQRT(Y(I)))

DO 70 I=2,N

DU 70 J=MM,MM

EWE=-Q(1)

F1=(BL1+((1.0-EW)*(-Q(1))))/(1.0-((1.0-EW)*(1.0-EWE)))

F2=((-Q(1))+((1.0-EWF)*BL1))/(1.0-((1.0-EW)*(1.0-EWE)))

Y1(I,J)=Y1(I,J-1)+((DEL1/(DELX*DELX))*(Y1(2,J-1)-(2.0*Y1(1,J-1))

1+TW))+((DEL1*(1.0-W0)/(2.0*N2))*(F1+F2-(2.0*Y1(1,J-1))))

70 Y1(I,J)=Y1(I,J-1)+((DELT/(DELX*DELX))*(Y1(I+1,J-1)-(2.0*Y1(I,J-1)

1))+Y1(I-1,J-1))-((DELT/(4.0*N1*2.0*DELX))*(Q(I+1)-Q(I-1)))

Y1(NN,MM)=1.0

DO 306 J=MM,MM

DO 306 I=2,N

QC(1)=(4.0*N2)*(TW-Y1(1,J-1))/DELX

306 QC(I)=(4.0*N1)*(Y1(I-1,J-1)-Y1(I+1,J-1))/(DELX*2.0)

DO 310 I=1,N

310 QT(I)=Q(I)+QC(I)

HR=Q(1)*SIGMA*(TB**4)/((TW*TB)-TB)

HC=QC(1)*SIGMA*(TB**4)/((TW*TB)-TB)

HT=HC+HR

PERC=HR/HT

COND=QC(1)*SIGMA*(TB**4)

RAD=Q(1)*SIGMA*(TB**4)

FLUXT=COND+RAD

- f -

```

D071 J=MM,MM
DO 71 I=1,NN
71 Y(I)=Y1(I,J)**4
   IF(ML.EQ.0)GOTO 800
   NX=NX+1
   IF(NX.EQ.10)GO TO 800
   GOTO 801
800 CONTINUE
   NX=0
   WRITE(2,4) (D(I),I=1,5)
   4 FORMAT(5E12.4)
   WRITE(2,608)(C(I),I=1,5)
608 FORMAT(5E12.4)
   WRITE(2,501)ML
501 FORMAT(15)
   WRITE(2,110)(Q(I),I=1,N,50)
110 FORMAT(8E12.4)
   WRITE(2,309)(QC(I),I=1,N,50)
309 FORMAT((8E12.4))
   WRITE(2,311)(QT(I),I=1,N,50)
311 FORMAT((8E12.4))
   WRITE(2,609)HR,HC,HT,PERC,COND,RAD,FLUXT
609 FORMAT(7F12.4)
   74 WRITE(2,6)((Y1(I,J),J=MM,MM),I=1,N,50)
   6 FORMAT((4E20.8))
801 CONTINUE
   DO 86 I=1,NN
   86 Y1(I,1)=Y1(I,2)
   IF(ML.EQ.1005)GOTO 20
   ML=ML+1
   GOTO 39
20 STOP
END

```

```
SUBROUTINE GAUSS(M,AA,BB,X)
DIMENSION A(20),AA(20),B(20,20),BB(20,M),X(M)
DO 5 J=1,M
X(J)=0
A(J)=AA(J)
DO 5 K=1,M
5 B(J,K)=BB(J,K)
IF(M.EQ,1)GOTO 20
MY=M-1
DO 10 L=1,MY
LL=M+1-L
MX=M-L
DO 10 J=1,MX
RB=B(J,LL)/B(LL,LL)
A(J)=A(J)-A(LL)*RB
DO 10 K=1,MX
10 B(J,K)=B(J,K)-B(LL,K)*RB
20 DO 40 K=1,M
XB=0
DO 30 J=1,K
30 XB=XB+X(J)*B(K,J)
40 X(K)=(A(K)-XB)/B(K,K)
RETURN
END
```

- 2 -

```
SUBROUTINE LESQUT (M,MF,N,X,Y,C,YE,R,RR)
DIMENSION A(20),B(20,20),X(MF,N),Y(N),C(MF),YE(N),R(N)
DATA M1/20/
IF(M.GT,M1)GOTO15
M1=M
DO 5 J=1,MF
A(J)=0
DO 5 K=1,MF
5 B(J,K)=0
DO 10 I=1,N
DO 10 J=1,MF
A(J)=A(J)+X(J,I)*Y(I)
DO 10 K=1,MF
10 B(J,K)=B(J,K)+X(J,I)*X(K,I)
15 CALL GAUSS(M,A,B,C)
RR=0
DO 30 I=1,N
YE(I)=0
DO 20 J=1,M
20 YE(I)=YE(I)+C(J)*X(J,I)
R(I)=Y(I)-YE(I)
30 RR=RR+R(I)*R(I)
RETURN
END
```

```

SURROUTINE DEES(S1,A,DD)
DIMENSION YY(8),DD(8),L(8,8),U1(8,8),S1(8),A(8,8)
DO 100 I=1,5
DO 100 J=1,5
100 L(I,J)=0.0
DO 101 I=1,5
DO 101 J=1,5
101 U1(I,J)=0.0
L(1,1)=1.0
L(2,2)=1.0
L(3,3)=1.0
L(4,4)=1.0
L(5,5)=1.0
DO 103 I=1,1
DO 103 J=1,5
103 U1(I,J)=A(I,J)
L(2,1)=A(2,1)/U1(1,1)
DO 104 I=2,2
DO 104 J=2,5
104 U1(I,J)=A(I,J)-(L(2,1)*U1(I-1,J))
L(3,1)=A(3,1)/U1(1,1)
L(3,2)=(A(3,2)-(L(3,1)*U1(1,2)))/U1(2,2)
DO 105 I=3,3
DO 105 J=3,5
105 U1(I,J)=A(I,J)-(L(3,1)*U1(I-2,J))-(L(3,2)*U1(I-1,J))
L(4,1)=A(4,1)/U1(1,1)
L(4,2)=(A(4,2)-(L(4,1)*U1(1,2)))/U1(2,2)
L(4,3)=(A(4,3)-(L(4,1)*U1(1,3))-(L(4,2)*U1(2,3)))/U1(3,3)
DO 106 I=4,4
DO 106 J=4,5
106 U1(I,J)=A(I,J)-(L(4,1)*U1(I-3,J))-(L(4,2)*U1(I-2,J))-(L(4,3)*U1
(I-1,J))
L(5,1)=A(5,1)/U1(1,1)
L(5,2)=(A(5,2)-(L(5,1)*U1(1,2)))/U1(2,2)
L(5,3)=(A(5,3)-(L(5,1)*U1(1,3))-(L(5,2)*U1(2,3)))/U1(3,3)
L(5,4)=(A(5,4)-(L(5,1)*U1(1,4))-(L(5,2)*U1(2,4))-(L(5,3)*U1
(3,4)))/U1(4,4)
DO 107 I=5,5
DO 107 J=5,5
107 U1(I,J)=A(I,J)-(L(5,1)*U1(I-4,J))-(L(5,2)*U1(I-3,J))-(L(5,3)*
U1(I-2,J))-(L(5,4)*U1(I-1,J))
YY(1)=S1(1)
YY(2)=S1(2)-(L(2,1)*YY(1))
YY(3)=S1(3)-(L(3,1)*YY(1))-(L(3,2)*YY(2))
YY(4)=S1(4)-(L(4,1)*YY(1))-(L(4,2)*YY(2))-(L(4,3)*YY(3))
YY(5)=S1(5)-(L(5,1)*YY(1))-(L(5,2)*YY(2))-(L(5,3)*YY(3))-(L
(5,4)*YY(4))
DD(5)=YY(5)/U1(5,5)
DD(4)=(YY(4)-(U1(4,5)*DD(5)))/U1(4,4)
DD(3)=(YY(3)-(U1(3,5)*DD(5))-(U1(3,4)*DD(4)))/U1(3,3)
DD(2)=(YY(2)-(U1(2,5)*DD(5))-(U1(2,4)*DD(4))-(U1(2,3)*DD(3)))
1/U1(2,2)
DD(1)=(YY(1)-(U1(1,5)*DD(5))-(U1(1,4)*DD(4))-(U1(1,3)*DD(3))
1-(U1(1,2)*DD(2)))/U1(1,1)
RETURN
END

```

FINISH
